Assemblies and supramolecular sensors that operate in competitive aqueous solutions and biofluids

by

Meagan Beatty
B.Sc., University of the Fraser Valley, 2014

A Dissertation Submitted in Partial Fulfillment
of the Requirements for the Degree of

DOCTOR OF PHILOSOPHY

in the Department of Chemistry

Supervisory Committee

Assemblies and supramolecular sensors that operate in competitive aqueous solutions and biofluids

by

Meagan Beatty
B.Sc., University of the Fraser Valley, 2014

Supervisory Committee

Dr. Fraser Hof, Department of Chemistry
Supervisor

Dr. Cornelia Bohne, Department of Chemistry
Departmental Member

Dr. Jay Cullen, School of Earth and Ocean Science
Outside Member

Abstract

Supervisory Committee
Dr. Fraser Hof, Department of Chemistry
Supervisor
Dr. Cornelia Bohne, Department of Chemistry
Departmental Member
Dr. Jay Cullen, School of Earth and Ocean Science
Outside Member

Nature has inspired chemists to develop complex assemblies that perform functions in biologically relevant solutions. Yet this is not a trivial task. Not only does water act as a competitive medium but the salts that are inevitably present hamper supramolecular hosts from properly binding and carrying out their programmed function.

This work was inspired by a serendipitous discovery of water-soluble functionalized calix[4]arenes that self-assemble into homodimers in salty water, mock serum and real urine. This thesis aims to explore this homodimerizing motif to learn more about self-assembly in salty water and to develop useful supramolecular tools. First the structural limits of the calixarene motif was explored by the transformation into a clip-like host that assembled similarly in water. NMR titrations revealed that the homodimers responded to hydrophobic cationic guests by dissociating to form new host-guest complexes.

The resilience of the self-assembling motif was then tested against extreme co-solute conditions. In this part of the study, reversible covalent bonds were introduced within the dimer scaffold to afford a dynamic library of exchangeable hosts. Quantitative NMR was used to monitor each host in response to molar concentrations of urea and salt.

This work also reports on a new class of salt-tolerant supramolecular chemosensors, called DimerDyes. These sensors form quenched homodimers in water but dissociate in the presence of hydrophobic cations to form new emissive complexes. Its mode of action was characterized by DOSY, ^{1}H NMR and fluorescence spectroscopy. DimerDyes successfully monitored enzymatic reaction in real-time despite the presence of competitive salts and co-factors. The DimerDye concept was quickly expanded by the parallel synthesis of crude DimerDyes and efficient testing for illicit drugs without the need for purification. “Hit” dimers were then purified, characterized and were able to detect multiple different drug classes in real saliva.

Table of Contents

List of Tables

List of Figures

List of Schemes

Abbreviations

2-OG	2-oxoglutaric acid
6-MAM	6-monoacetylmorphine
A	amphetamine
AA	ascorbic acid
Ach	acetylcholine
AIE	aggregation-induced emission
aRme2	asymmetric dimethylarginine
BSH	decahydro-mercapto-closo-dodecaborate
BZE	benzoylecgonine
CB	cucurbituril
CD	cyclodextrin
CIA	calixarene-induced aggregation
COC	cocaine
D	diffusion coefficient
D1	relaxation delay time
DD	DimerDye
DDA	DimerDye assay
DEX	dextrorphan
DMSO	dimethylsulfoxide
DNA	deoxyribonucleic acid
DOSY	diffusion ordered spectroscopy
DTT	dithiothreitol
EtOH	ethanol
F1	principal component 1
F2	principal component 2
FA	formic acid
FDA	Food and Drug Administration
FT-IR	Fourier-transform infrared spectroscopy
G	field gradient strength
H3K4	lysine 4 on histone 3
H3K4me1	monomethylated lysine 4 on histone 3
H3K4me2	dimethylated lysine 4 on histone 3
H3K4me3	trimethylated lysine 4 on histone 3
H3K9	lysine 9 on histone 3
H3K9me1	monomethylated lysine 9 on histone 3
H3K9me2	dimethylated lysine 9 on histone 3
H3K9me3	trimethylated lysine 9 on histone 3
HER	heroin
Het	heterocycle
HMTA	hexamethylenetetramine
HPLC	high performance liquid chromatography
HR-ESI-MS	high resolution - electron stray ionization - mass spectroscopy

HSQC	heteronuclear single quantum spectroscopy
IDA	indicator displacement assay
IIDA	intramolecular indicator displacement assay
IR	infrared
ITC	isothermal calorimetry
JMJD2D	jumonji domain-containing protein 2D
Kac	*N*-acetyllysine
K_d	dissociation constant
Kme3	trimethyllysine
LC	lidocaine
LDA	linear discriminant analysis
LOD	limit of detection
MA	methamphetamine
MDA	3,4-methylenedioxyamphetamine
MDMA	3,4-methylenedioxymethamphetamine
MeOH	methanol
NICO	nicotine
NMR	nuclear magnetic resonance
NOE	nuclear overhauser effect
NOESY	nuclear overhauser effect spectroscopy
OXY-C	oxycodone
OXY-M	oxymorphone
P1	pulse length
PBS	phosphate-buffered saline
PCA	principal component analysis
ppm	parts per million
PRDM9	PR domain zinc finger protein 9
PTM	post-translation modification
R	arginine
R^2	coefficient of determination
r_H	hydrodynamic radius
RMSE	root mean square error
RSR	receptor-spacer-reporter
SAMPL	statistical assessment of the modelling of protein and ligand
SC4A	*para*-sulfonatocalix[4]arene
sRme2	symmetric dimethylarginine
T1	longitudinal relaxation
TFA	trifluoroacetic acid
Tris	tris(hydroxymethyl)aminomethane
TSP	2,2,3,3-d_4-3-(trimethylsilyl)propionic acid
TY	acetaminophen
UPLC-MS	ultra performance liquid chromatography- mass spectroscopy

Acknowledgments

I would first like to thank my committee for reading and contributing to this thesis. A special thanks to Dr. Cornelia Bohne who continues to be an excellent example of a rigorous scientist.

A huge thank you to my supervisor, Dr. Fraser Hof. Thank you for allowing me to grow into the scientist that I am. Your trust and patience to let me build these projects into what they are is something I appreciate. You have taught me not only how to become a better communicator but also the importance of it. It felt like this has been an unusually fun PhD because you cultivate an engaging and fun environment. RYU.

My love of chemistry really started in my undergraduate program at the University of the Fraser Valley in Abbotsford. I was taught by passionate and extraordinarily smart mentors. Thank you to Dr. Godwin Chow for your captivating explanations of organic chemistry. Thank you Dr. Noham Weinberg for teaching me the know-how of computational chemistry. Thank you to Brandon Wiebe and Paul Foth for being my soundboards throughout those UFV-style chemistry classes. But most importantly to Dr. Cory Beshara who taught me the fundamentals of synthetic chemistry (especially when you have no money). There, I grew crystals, ran air/moisture sensitive chemistry *via* balloon (without the guidance of a working NMR), bummed liquid nitrogen from biology and the most rememberable is synthesizing BODIPY dyes that initiated my interest in fluorescence.

During my PhD, most of my time (it felt like) was downstairs at the 500 MHz and if it were not for Chris Barr's help, I would not be able to carry out a large part of my thesis. Thank you for all the training (including fills – it's pretty neat), putting up with all the titrations and establishing the initial DOSY procedure.

I would like to thank all the students I have supervised over the past years and students that initiated projects before me. In particular: Aidan Pye (so much salt), Allison Selinger (DimerDye's new mother, they'll be in good hands), Jorge Borges-González (DimerDyes at its infancy), Jil Busmann (so many NMR titrations whilst I write my candidacy), Emily Davies (NIM-calix), Cara Gallo (high quality Stopped-flow data), and Yuqi Li (all those alkylations). Your positivity and personality taught me to be a better mentor.

I was extremely fortunate to have some of the smartest, quirkiest and entertaining buddies through out this journey. The Wulff group (as we knew it), Jun Chen and Ronan Hanley – hilarious and helpful. Alok Shaurya for all the mentoring, questions answered, and cruxes solved – thank you. Thank you to Natasha Milosevich for teaching me the importance of a strong community and being a role model for strong female scientists.

I could not have done this without my parents. Thank you for making the sacrifices to set me on the path through post-secondary school. Thank you, Mom (and Jude) for being “students” to my “lessons”. More like rapid fire explanations of all the cool things I was learning in first year. Dad, nose to the grindstone. That work ethic has gotten me this far and I expect it will push me further. You have instilled in me a resilience to environmental pressures that is stronger than DimerDyes.

Thank you to Mathieu Lepage. By far, one of the most impressive scientists I have met (thanks for all the insider tips). You have filled these last two years with so many adventures that it makes it hard to believe I was in a PhD. Merci pour tout l’amour et le soutien. Mais surtout, merci pour croire en moi, même quand je ne le fais pas.

Dedications

To Nature. You are one salty gal.

Chapter 1: Supramolecular chemistry that operates in varying degrees of aqueous complexity

Supramolecular chemistry, or chemistry beyond the molecule, involves the design and study of simple components interacting through non-covalent bonds to form larger, more complex assemblies.[1-2] These assemblies can take on functions and characteristics that differ from the components they comprise. The evidence of supramolecular interactions and complexes was noted in the early 20th century and since then has gained significant recognition with Nobel Prizes in Chemistry in 1987 and 2016. Each achievement has broadened the scope of what is possible. For example, the 2016 prize rewarded the advances in the design of synthetic molecular machines that resemble kinesin proteins that walk along microtubules in cells.[3] This was not only an example of complex assembly but one that carried out a function of motion.

One goal to further develop supramolecular chemistry aims at mimicking Nature's sophisticated assemblies, but with unique characteristics that chemists can program into the system. Although there are many strategies to develop such assemblies one common strategy is to synthesize a 'host' molecule that contains a recognition motif for a specific secondary 'guest' molecule. Upon recognition of the two components, a complex is formed based on the strength of non-covalent bonds that are shared between each component. The medium that solvates each component influences the strength of the non-covalent bonds and in turn the complex. Early supramolecular systems were almost entirely studied in organic solvents. Yet mimicking Nature requires systems to operate in water which interacts with the assembling components much differently than organic solvents. Chemists have reported many systems that mimic different aspects of natural molecular recognition and self-assembly, and from this history we can identify key lessons. This chapter will highlight those key lessons, building towards the creation of organic molecules that function in complex, salty, competitive aqueous media and real biofluids.

1.1 Key lessons of host-guest binding in water

Biology has mastered the art of directing intricate molecular assemblies in water, yet supramolecular chemists are still learning the rules. Within a cell, many types of assemblies carry out functions to propagate itself forward. These assemblies can generate compartments that eventually produce an energy source, or multi-protein complexes that are involved in replication. All such assemblies need to form in aqueous solutions that contain various salts, competitive co-solutes, and other proteins. Although we want to mimic Nature, we also have the synthetic tools to create unique systems that bring their own properties. However, it remains challenging to create molecules that are soluble in water, have limited interactions with salts and co-solutes, and still carry out their programmed binding function.

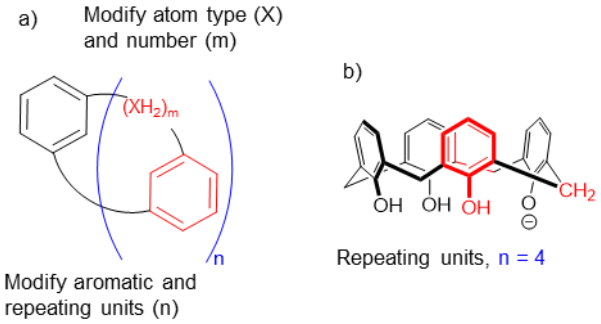

Figure 1. 1 a) Generic structure of a cyclophane-based host and b) calix[4]arene is a popular example of a cyclophane.

There are hundreds of different hosts that are reported in the literature but to limit the scope of this Chapter we will report on an informative subset, including cyclophanes, cucurbiturils, and cyclodextrins. Cyclophanes are macrocyclic hosts consisting of an aromatic repeating unit connected by a bridging component.[4] A general structure of these hosts is illustrated in Figure 1. 1a. This family of cyclophanes contains many members that vary structurally in number and types of bridging components and aromatic repeating units that ultimately change their binding properties. A central member of the cyclophane family are known as calix[n]arenes. Shown in Figure 1. 1b, the calix[4]arene is comprised of phenol units repeated n=4 times and bridged by methylenes. To solidify key lessons and highlight important comparisons, some non-cyclophane hosts such as cucurbiturils and cyclodextrins will be included. Their general structures are illustrated in Figure 1. 2.

Briefly, cucurbiturils (CBs) are cyclic hosts that contain glycoluril units that can be repeated 5 – 8 times to yield larger hosts (**CB6** – **CB8**, respectively) although even larger hosts have been reported. Cyclodextrins (CDs) are cyclic oligosaccharides that contain a repeating glucose molecule joined by a glyosidic bond. The number of glucose units vary from 6 – 8 to afford **α-CD**, **β-CD**, and **γ-CD**, respectively. Examples of each host, **CB7** and **γ-CD** are presented in Figure 1. 2c and Figure 1. 2d.

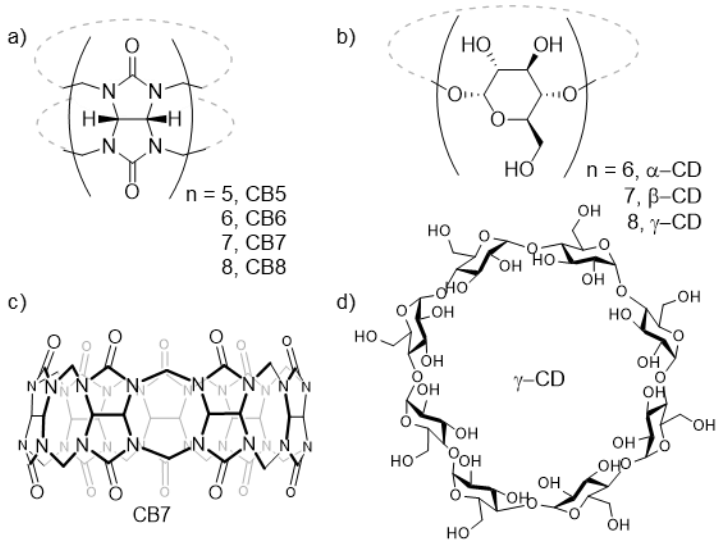

Figure 1. 2 Cucurbiturils and cyclodextrins are non-cyclophane hosts that make notable host-guest complexes. a) Cucurbiturils vary by the number of glycoluril units while b) cyclodextrins are formed from glucose. Examples of each include c) **CB7** and d) **γ-CD**

To further define the scope of this Chapter, we will focus on hosts that interact with guests via 'host-guest' mode instead of a 'scaffold'-mode.[5] An advantage of many hosts is that they offer a pre-organized scaffold to append larger recognition sites. When binding partners interact with these recognition motifs external to the macrocycle's binding pocket, then it is known as the 'scaffold'-mode. When the binding partner binds inside the recognition pocket itself, it is called 'host-guest' mode.

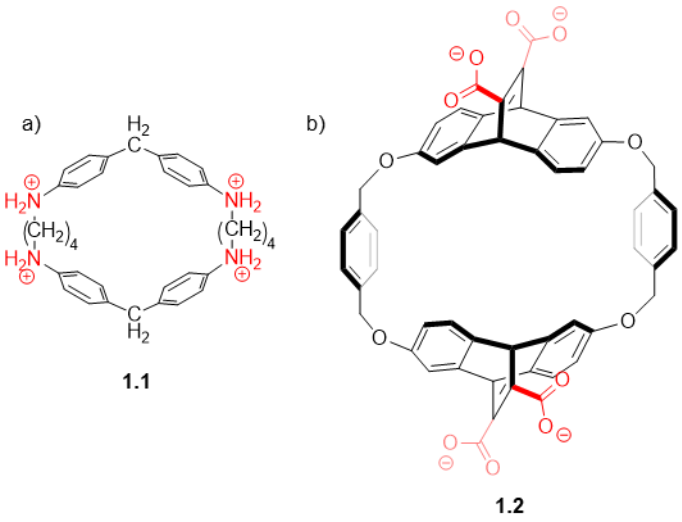

Figure 1. 3 Water solubility of cyclophane hosts are increased with a) tetra-cationic and b) tetra-anionic charged groups.

The first step towards making organic hosts functional in aqueous medium is to ensure they are water-soluble. Early work in host-guest chemistry with cyclodextrins, which are water-soluble by virtue of being completely decorated with hydroxyl groups, demonstrated that a hydrophobic cavity is necessary to bind with organic guests in aqueous solutions.[6] Therefore, cyclophanes became an interesting target as they also provide hydrophobic pockets yet can be synthetically manipulated to form unique recognition sites. Many cyclophane derivatives were then synthesized with varying charged functional groups that successfully rendered them both water-soluble and efficient at encapsulating guests from water. For example, a tetra-cationic cyclophane **1.1** was rendered water-soluble at pH 2 by functionalization of ammonium motifs (Figure 1. 3a),[7] while tetra-anionic cyclophane **1.2** shown in Figure 1. 3b, is decorated with carboxylates and is water-soluble at neutral-basic pH.[8] This latter cyclophane inspired further modifications and invention of various macrocyclic hosts through the formation of dynamic disulfide bonds. Similar carboxylate analogues were cyclized from dithiol monomers through the formation of disulfide bonds illustrated in Figure 1. 3c.[9-11]

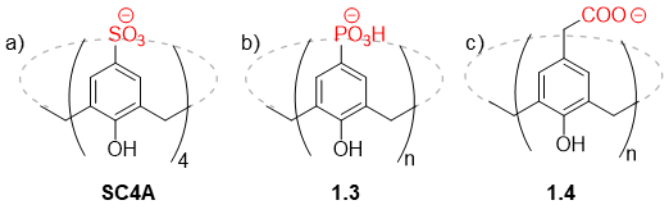

Figure 1. 4 Typical negatively charged functional groups used to render calixarenes water-soluble. a) Sulfonates along the upper rim have created a popular host (**SC4A**) among other hosts that include b) phosphonates, **1.3**, and c) carboxylates, **1.4**.

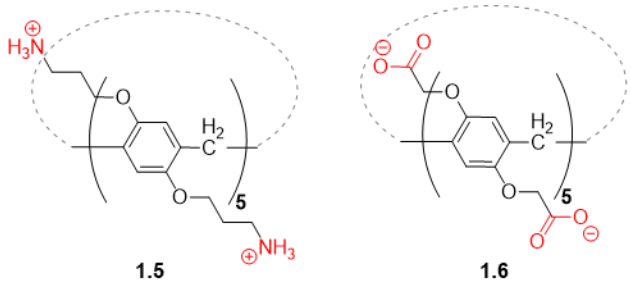

Figure 1. 5 Oppositely charged pillar[5]arenes bear ammonium (**1.5**) and carboxylate groups (**1.6**).

As introduced earlier, calixarenes were first synthesized and used in organic solvents. It was found that sulfonation along the upper rim yielded water-soluble variants. One of these variants, *para*-sulfonatocalix[4]arene (**SC4A**), has found itself in many supramolecular systems and will be re-introduced throughout this thesis (Figure 1. 4a).[12-13] The sulfonates provide both favourable electrostatic interactions and an entropic gain when encapsulating organic cationic guests.[14] Other negatively charged groups have been used to solubilize calixarenes including phosphonates or carboxylates and examples like **1.3** and **1.4** are shown in Figure 1. 4b and c.[15-17] There are also cationic versions of many of these host classes that typically incorporate ammonium, pyridinium and guanidinium groups.[18-19] For example, a pair of oppositely charged pillar[5]arenes (Figure 1. 5), hosts that are structurally related to calixarenes, have been decorated with either ammonium, **1.5**, or carboxylates groups, **1.6**, to render them water-soluble.[20]

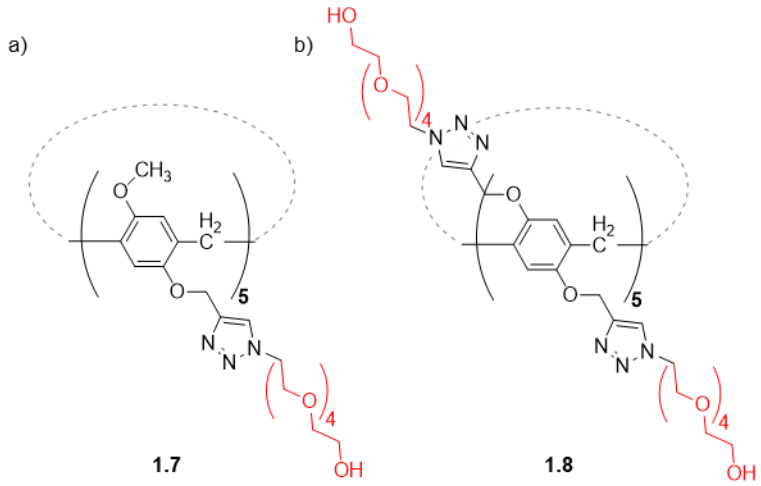

Figure 1. 6 Polyethylene glycol tails improve water-solubility without unfavourable electrostatic interactions from charged functional groups. a) A single glycol tail improves solubility (1 mM with 10% DMSO) while b) two glycol tails renders it completely water-soluble (1 mM).

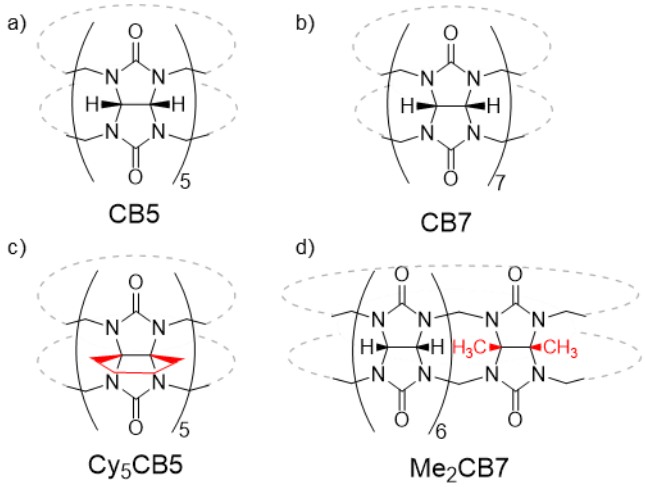

Figure 1. 7 Structurally modifying cucurbiturils improve their water solubility. a) **CB5** and b) **CB7** are moderately water-soluble (10 – 20 mM). c) Cyclohexyl-CB5, **Cy$_5$CB5**, and b) dimethyl-CB7, **Me$_2$CB7** have improved water solubility (200 mM).

Neutral polar functional groups are an alternate strategy to increase water solubility while avoiding potentially unfavourable electrostatic interactions with guests. For example, in Figure 1. 6, when polyethylene glycol tails have been appended to only a single rim of pillar[5]arenes (**1.7**) they become water-soluble with the aid of 10% DMSO.[21] When both rims display polyethene glycol tails (**1.8**) then the host is fully soluble in water without the aid of any organic solvent and assemble into large complexes without electrostatic repulsion. Cucurbiturils contain neutral polar groups they are intrinsically water-soluble.

However, many of these hosts are only moderately water-soluble at best (20 – 30 mM for **CB5** and **CB7**, structures in Figure 1. 7a and b).[22] Although synthetically modifying these hosts is not trivial, there exist functionalized CBs that are more water-soluble in comparison to their unfunctionalized counterparts. For example, cyclohexyl-CB5 (**Cy$_5$CB5**) derivative increased water solubility to ~200 mM, while the addition of two methyl groups on **CB7** (**Me$_2$CB7**) increases the water solubility to 264 mM (Figure 1. 7c, d).[22-23]

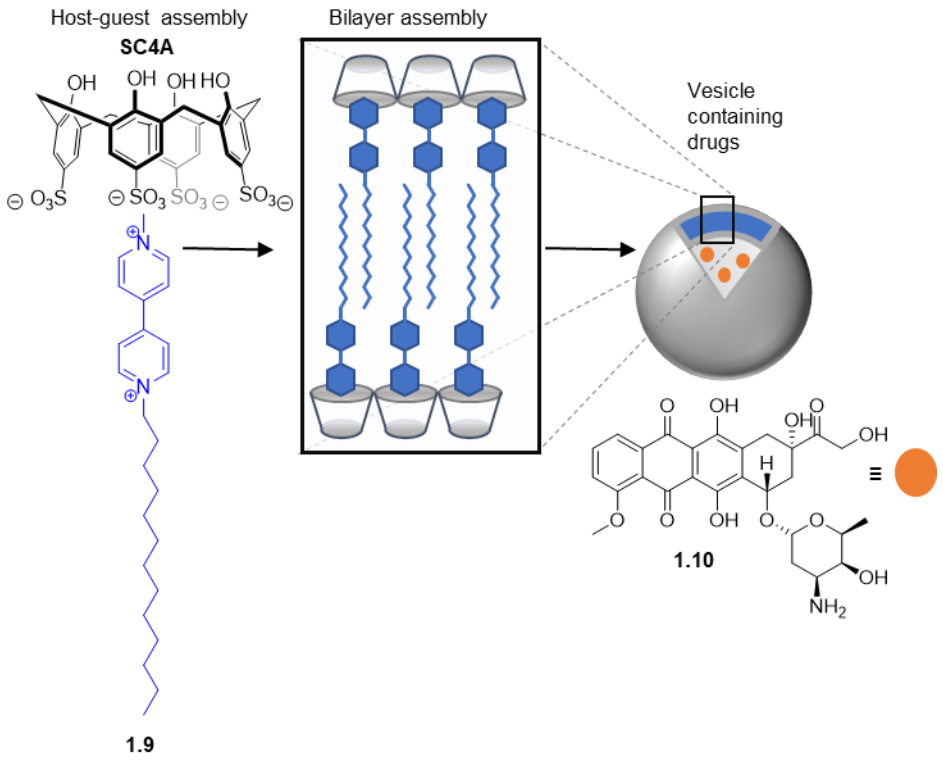

Figure 1. 8 Calixarene-induced aggregation (CIA) has been used to make drug delivery systems.

Hosts that are water-soluble are further challenged by amphiphilic aggregation and charge neutralization. Integrating charged functional groups within a "greasy" organic host improves water solubility but can create an amphiphilic host that is prone to aggregation. At certain concentrations in water, the hydrophobic regions of the host can aggregate into micelles or other structures, while the charged groups maximize their contacts with water. Often the hosts' critical aggregation concentration is determined to ensure that further host-guest studies are conducted under conditions where the monomer is dominant, instead of

studying guest binding by an ill-defined aggregate. However, even at low host concentrations the addition of the guest itself can cause aggregation and precipitation. In one set of examples, it has been observed that guests like fluorescent dyes, drugs, surfactants or proteins form large assemblies with sulfonated calixarenes. This phenomenon is so general that it was given a name: "calixarene-induced aggregation" (CIA).[24-25] In one series of studies, this potential nuisance was transformed into a strategy to form stimuli-responsive drug delivery vesicles among other novel materials. For example, **SC4A** formed a host-guest complex with an amphiphilic guest, **1.9**, and further assembled into a bilayer vesicle that encapsulated the drug doxorubicin, **1.10** (Figure 1. 8).[26] In a related set of challenges, precipitation can occur when charged solubilizing groups encounter certain oppositely charged binding partners that render them effectively neutral and lower the solubility. For example, in Figure 1. 9 tetra-anionic (**1.11**) and tetra-cationic (**1.12**) calixarenes form capsules with each other in polar organic solvents, driven by complementarity of electrostatic charges.[27] Yet, this perfect charge complementarity causes the complex to become water-insoluble and precipitate from aqueous solution. This can be overcome if one of the members of the capsule is modified with a different solubilizing group. For example, by changing the upper-rim sulfonates to carboxylates (**1.13**) while also replacing the lower rim alkyl groups for polyethylene chains (**1.14**) the capsule forms and remains soluble in water.[28] In our own group, we have synthesized unpublished calixarenes that contain a symmetric arrangement of two anionic and two cationic functional groups, and we noticed this internal charge neutralization routinely renders the molecules almost perfectly insoluble in water (See Chapter 2). We have also heard many tales at conferences of work in which the study of a host-guest system in water was impeded because of charge-neutralization-induced precipitation. This work is well known by many, but is almost always unpublished, because of the significant barriers to publishing negative results. The presence of counter-ions from the host, buffer or salt from biological solutions can also changes the solubility of hosts in water. This effect will be explored more in depth in Section 1.3.

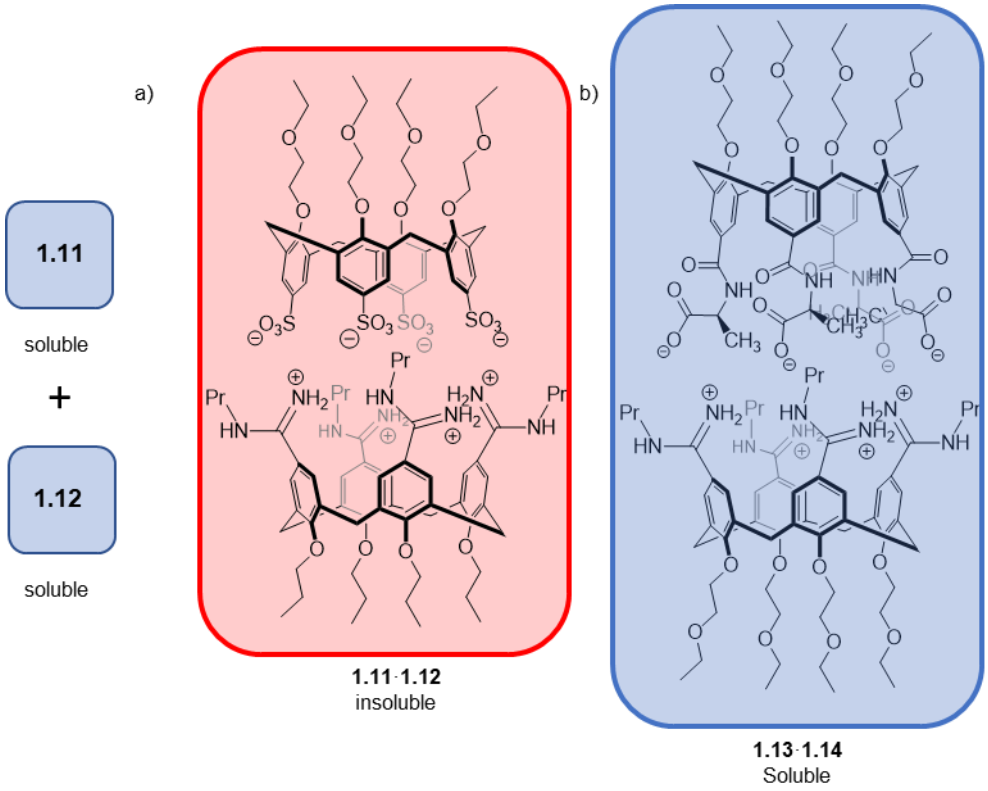

Figure 1. 9 a) Oppositely charged solubilizing groups on **1.11** and **1.12** neutralize each other rendering the assembly insoluble in water. b) Changing the sulfonates for carboxylates and propyl chains for ethyl glycol groups increases the solubility of the assembly of capsule.

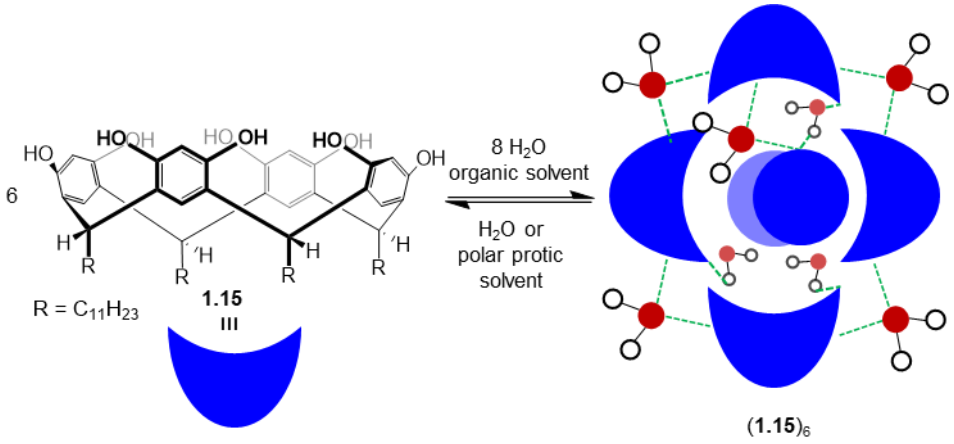

Figure 1. 10 Six resorcinarenes, **1.15**, form a stable capsule, $(\mathbf{1.15})_6$ in wet organic solvent, where 8 water molecules stabilize the hexameric assembly; the latter falls apart in a polar protic solvent.

Water interferes with supramolecular interactions by competing directly for binding interactions. We often look to Nature for guidance as to which interactions are

more prevalent and perhaps most important when forming large assemblies in water. For example, hydrogen bonds are non-covalent interactions that are responsible for nucleotide base pairing in DNA. However, when implemented in synthetic hosts, we don't observe assemblies as strong as predicted. Hexameric resorcinarene, (**1.15**)$_6$, capsules assemble in wet organic solvent, often chloroform, through intermolecular hydrogen bonding between phenol groups and 8 molecules of water (Figure 1. 10).[29-31] Yet, it is hard to find examples where the capsule assembles using similar building blocks that work in polar and/or protic solvents (methanol, DMSO, water). Although the structural integrity of the capsule relies on water-mediated host-host hydrogen bonds, if water is the solvent there is too much competition for hydrogen bonds and the capsule falls apart. Urea and thiourea are motifs commonly used to recognize anionic guests, but they suffer from similar problems.[32-33] In organic solvents strong hydrogen-bond driven association is observed with squaramides, and triazolophanes that sequester inorganic anions,[34-36] but the addition of water (0.5 – 25% by volume) causes a decrease in the binding strength. It seems that, if the receptor relies on a single or a few of the same interactions then it fails in water because it cannot outcompete the solvent. However, if it instead contains multiple recognition motifs displayed as an array in three-dimensional space, then the ability of water to outcompete the host is lessened. For example, we can compare the sulfate binding strengths of two similar receptors that differ by one or two amide-urea motifs (**1.16** and **1.17**) in varying degrees of water in DMSO (Figure 1. 11).[37] The receptor with two motifs, **1.17**, offers 8 coordination sites, and remain able to bind with sulfate in 50% water, although the affinity is considerably weakened (~2000-fold) in comparison to 0.5% water. Yet **1.16** bearing a single motif, which offers half the coordination sites, completely loses affinity for sulfate at 50% water. This highlights the strength of the chelate effect where more recognition sites offered by the host can help combat the competition with water for the guest. A high-level look at these data show that the transition of host-guest chemistry from organic solvent to aqueous medium is not as simple as just solving a solubility problem. Interactions that were once strong in organic solvents become weak in water. One possible remedy is to implement multiple interactions that function in synchronization to yield strong complexes in water.

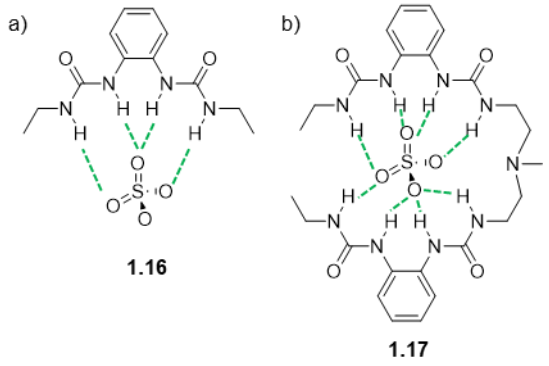

Figure 1. 11 The effect of doubling the recognition motifs stabilizes the sulfonate in water. a) **1.16** loses affinity (no binding detected in 1:1 DMSO:H_2O, K_d = 0.1 mM in DMSO) while b) **1.17** engages weakly with the sulfonate by providing double the coordination sites (K_d = 21 mM in 1:1 DMSO:H_2O, K_d = 0.1 mM in DMSO).

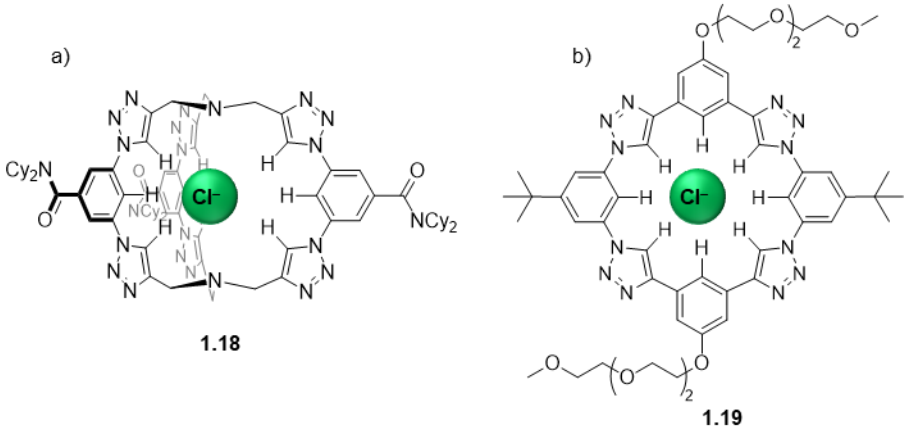

Figure 1. 12 Directional non-covalent interactions of a) the cryptand-like cage aids in the complexation of chloride (K_d = 10 aM in wet dichloromethane) in comparison to b) the planar derivative (K_d = 125 nM in wet dichloromethane).

Topologically enveloping noncovalent interactions help stabilize guest complexes in competitive water. The convergent arrangement of strong non-covalent interactions helps optimize recognition while also shielding the guest from water. For example, a cryptand-like cage, **1.18**, in Figure 1. 12a contains 9 C-H derived hydrogen bonds that all point inwards to sequester Cl^- and successfully transfers the anion from water into dichloromethane (K_d = 10 aM in wet dichloromethane).[38] In contrast, the planar analog, **1.19**, contains 8 C-H derived hydrogen bonds and encapsulates chloride strongly (K_d = 125 nM in dichloromethane) but does not effectively protect the anion from water (Figure 1. 12b). Numerous directional electrostatic interactions are also important when considering guests that bind with CBs. Many highly electronegative ureido groups (5 – 8) all point

inwards at each portal to stabilize polar or positively charged groups. For example, in Figure 1. 13, **CB7** binds to neutral guest diamantane (**1.20**) strongly (K_d = 0.25 nM) but binds to the di-cationic analog, **1.21**, 35-fold stronger (K_d = 7.1 pM).[39] The directional non-covalent interactions between the two ammonium groups and the carbonyls further stabilize the diamantane core when bound inside the cucurbituril. From these two examples, it may be tempting to conclude that directional non-covalent interactions are the key to developing strong, and selective hosts in water. Yet there are countless examples of hosts with similar pre-organization that are not as successful. This could be attributed to many reasons but the competition with water still remains a challenge for both host and guest. New topologies and types of interactions are needed to afford strong complexes that utilize the unique features of water instead of attempting to outcompete water.

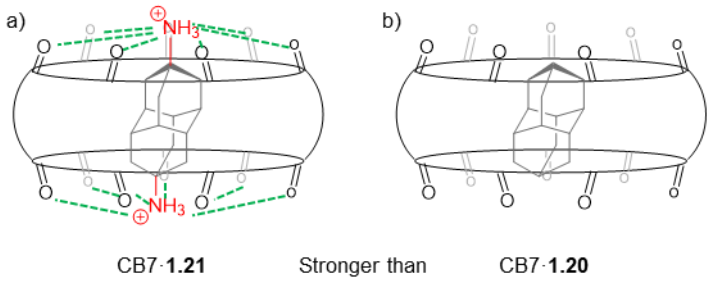

Figure 1. 13 Directional non-covalent interactions provided by cucurbiturils carbonyl portals further stabilizes dicationic guest a) diammonium diamantane, **1.21**, over neutral a guest like the b) diamantane core, **1.20**

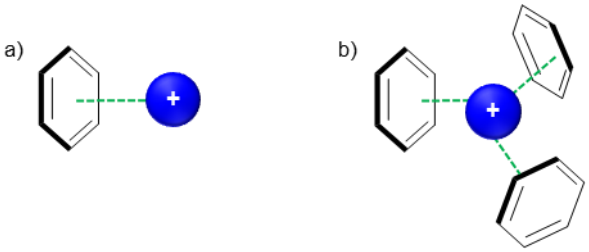

Figure 1. 14 Aromatic faces provide an electron rich surface to interact strongly with cationic guests. a) A simple benzene ring participates in cation-π interactions which can be further stabilized when b) the aromatic rings are arranged in a cyclic array.

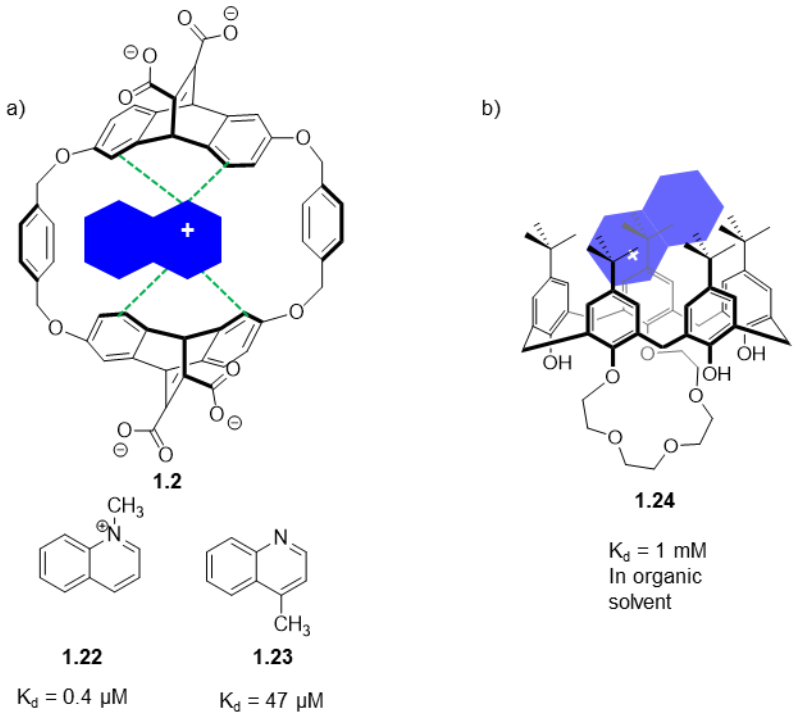

Figure 1. 15 Cation-π interactions are the primary driving force for the selectivity of cationic guests. a) Cyclophane **1.2** binds preferably to **1.22** over the isosteric, non-cationic version **1.23**. b) Calix[5]arene **1.24** sequesters **1.22** in organic solvent despite no assistance of anionic functional groups.

Cation-π interactions are important in cyclophane-based hosts. Aromatic rings provide an electron rich surface for strong non-covalent interactions with organic and alkali metal cations (Figure 1. 14a). This interaction is amplified with cyclophane hosts, as there are multiple aromatic rings arranged in a cyclic array to provide an electron-rich box for the cationic guest to occupy (Figure 1. 14b).[40-41] This inherently provides these hosts powerful selectivity for cationic guests over the many other neutral or anionic guests that could potential interfere with binding. Cyclophane **1.2** introduced previously and others were noted to bind organic cationic guests with moderate affinities. Notably the binding of cationic *N*-methylquinolinium, (**1.22**) was nearly 80-fold stronger than its neutral, isosteric counterpart, 4-methylquinoline (**1.23**) (Figure 1. 15a).[42] This trend extends to other cyclophanes including calix[n]arenes, pillar[n]arenes, resorcin[n]arenes, and cyclotriveratrylenes that are all cable of binding cationic guests more strongly than neutral guests in water.[43-49] For example, **SC4A** binds more strongly with a cationic ethylammonium guest (K_d = 560 μM) than with a similar sized neutral ethanol guest (K_d =

100 mM).[50] It could be argued that the sulfonates are responsible for the additional binding strength through ion-ion interactions. However, a few examples that support the significant contributions of cation-π interactions should be noted. The first is that cationic guests such as **1.22** are complexed by neutral calix[5]arenes like **1.24** in organic solvents, shown in Figure 1. 15b.[51] This eliminates ion-ion interactions as sulfonates are not needed in these hosts and eliminates any hydrophobic driving forces that are common in aqueous systems. Furthermore, comparing the binding affinities of trimethyllysine (Kme3) for penta-anionic **SC4A** with di-anionic carboxycalixarene **1.25** in water shows similar binding affinities (Figure 1. 16).[52] Both examples, do not rely on electrostatic interactions between negatively charged solubilizing groups to sequester cationic guests and only cation-π interactions are responsible.

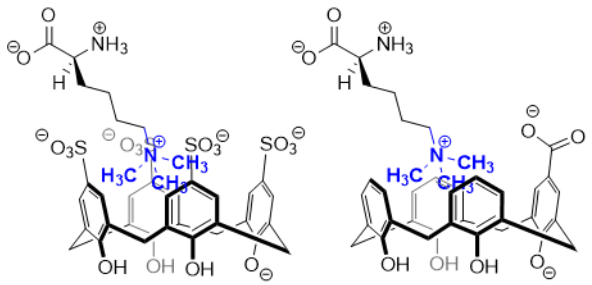

Figure 1. 16 Calix[4]arenes with and without sulfonates both bind to cationic guest, trimethyllysine (Kme3), through cation-π interactions with equimolar affinities.

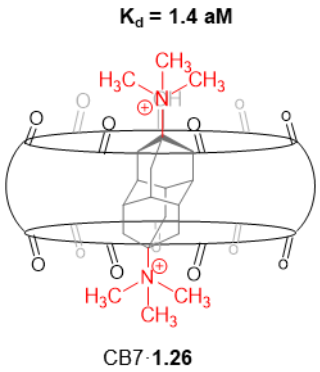

Figure 1. 17 The hydrophobic effect contributes to the extremely strong complex formed between **CB7** and bis(trimethylammonium) diamantine, **1.26**.

The hydrophobic effect is responsible for strong and unlikely assemblies. Unlike the previous topics covered, the hydrophobic effect is not an electrostatic interaction but a

consequence of hydrophobic molecules existing in water, a uniquely cohesive solvent. Because water makes many strong contacts with itself, as well as charged and polar motifs, it is by exclusion from water that neutral and non-polar motifs associate. How water interacts with a guest and host before and after complexation is a major factor in determining how strong the association will be. The cucurbituril family produces some of the strongest synthetic complexes to date. For example, **CB7** associates with bis (trimethylammonium) diamantane, **1.26**, to yield an attomolar complex of K_d 1.4 aM in water (Figure 1. 17).[53] The hydrophobic effect strongly contributes to the strength of this complex as well as important electrostatic interactions. It also heavily influences the formation of electrostatically unfavourable assemblies. For example, **1.27** can assemble into 1:1 homodimer nanocontainers that form despite an overall charge of –16 (Figure 1. 18).[54]

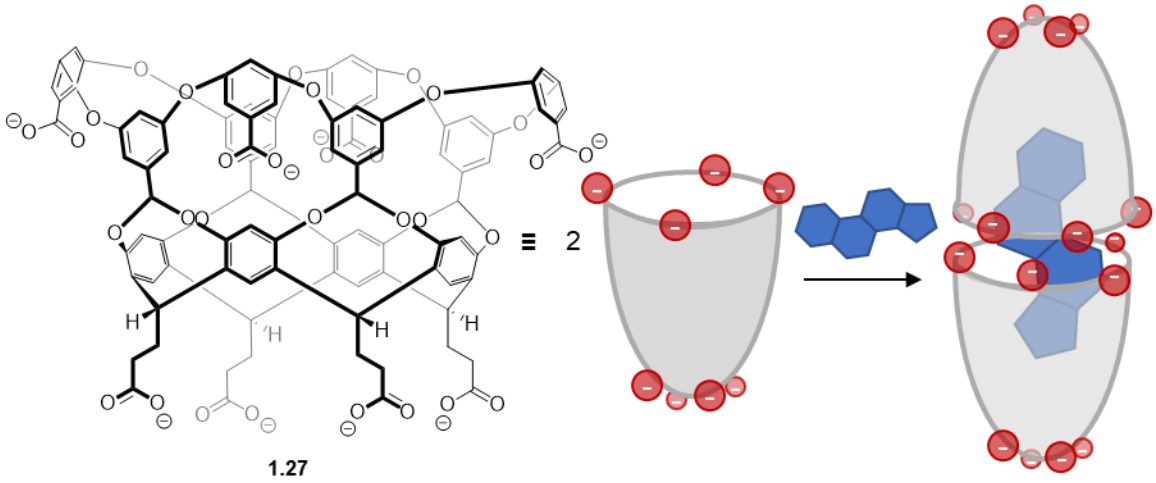

Figure 1. 18 Cavitand **1.27** forms an $^{-}16$ anionic dimeric capsule in the presence of a hydrophobic guest, despite a strong electrostatic repulsion.

One of the first explanations of the hydrophobic effect considered that hydrophobic species often associate to increase entropy of the system.[55] To explain the observed entropic driving force, it was considered that the layer of water solvating hydrophobic surfaces was more rigid and had fewer degrees of freedom in comparison to bulk water. This is a consequence of strengthening adjacent hydrogen bonds in response to a loss of non-covalent interactions with the hydrophobic species. When two hydrophobic species associate the surface area of the complex is smaller than each individual species. This

liberates water back into the bulk and increases entropy, as shown in Figure 1. 19. Typically, this is coupled to little or no change in the enthalpic term upon association. This entropy-driven model is sometimes called the 'classical hydrophobic effect'. However, as more systems were created and tested, the thermodynamic data suggested a second look into the driving forces behind the hydrophobic effect.

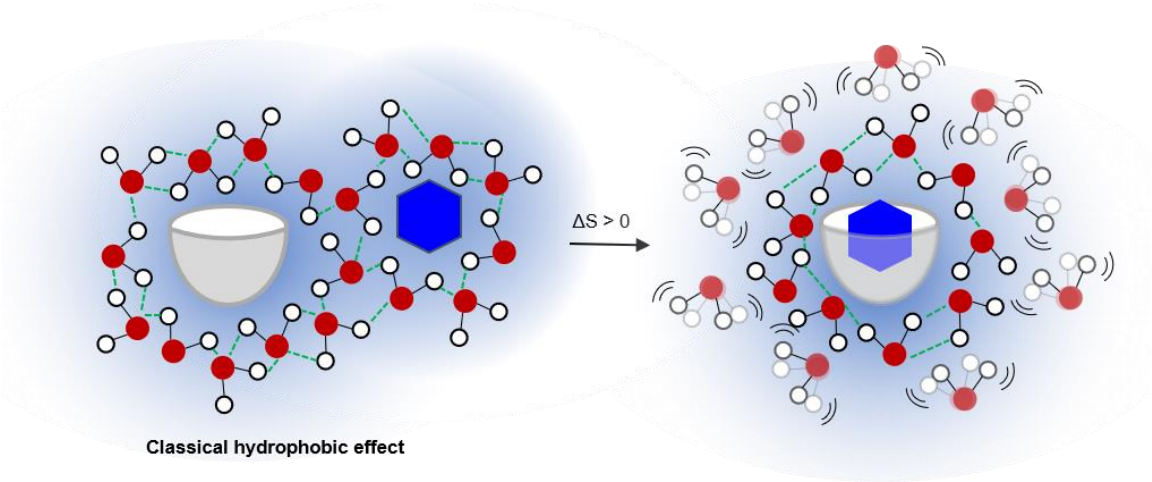

Figure 1. 19 Cartoon illustration of the classical hydrophobic effect between a hydrophobic host and guest. The release of highly ordered water molecules solvating the solutes is released which drives complexation.

There is often also an enthalpic gain when encapsulated water is released from a host's cavity. The few encapsulated water molecules can no longer make the same number of hydrogen bonds as they would in the bulk. This is considered to be a pool of high-energy water molecules, and the displacement of this water back into bulk water by a guest allows more water-water hydrogen bonds to form, giving an explanation for the observed favorable enthalpies of binding. This is illustrated in Figure 1. 20a. Contrary to the interpretation discussed before, this enthalpic-driven association of hydrophobic molecules is called the 'non-classical hydrophobic effect'. Keeping these two definitions in mind – classical vs. non-classical – we will explore the parameters that influence the strength of the hydrophobic effect.

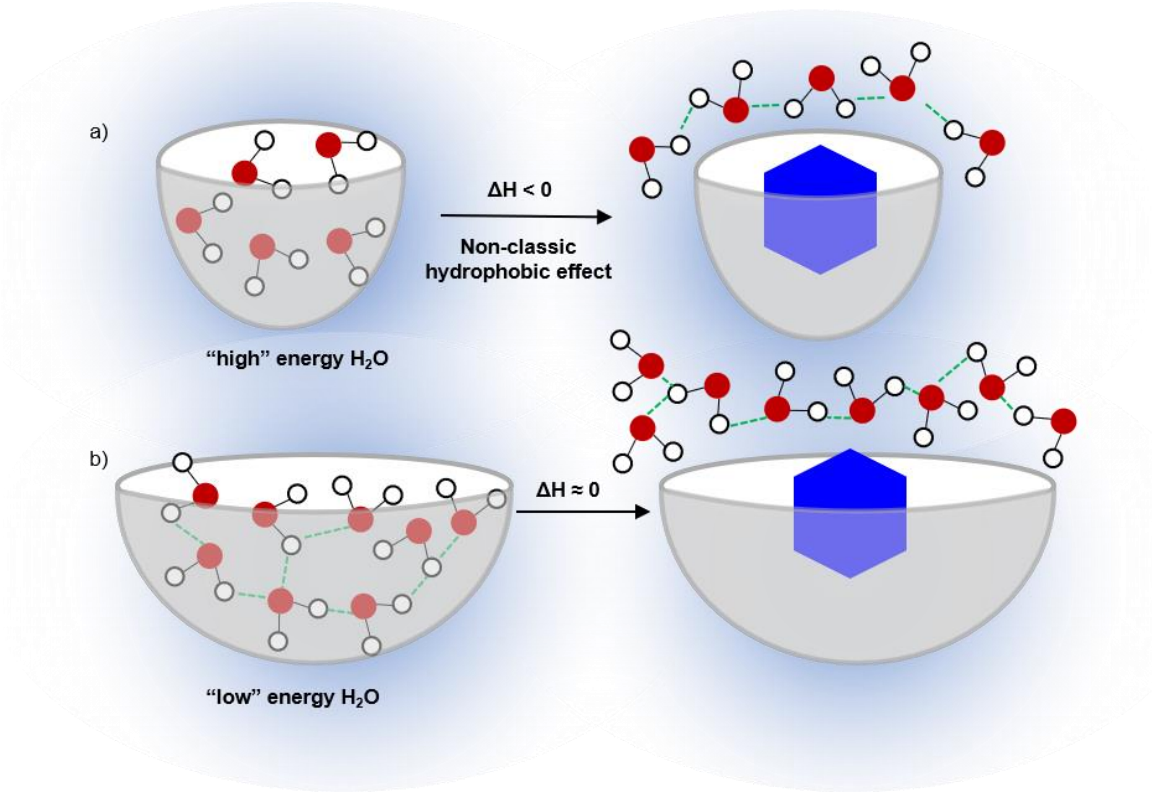

Figure 1. 20 Cartoon illustration of the non-classical hydrophobic effect. a) The release of water encapsulated forms fewer stabilizing hydrogen bonds than in bulk deeming it as "high" energy. b) Larger hosts encapsulate clusters of water molecules that stabilize each other rendering them as "low" energy by comparison.

The volume and topology of the host can influence solvation and in turn modulate the strength of guest complexation.[56] The volume within the cavity influences the number of these high-energy water molecules. If a cavity is large enough to contain many "high-energy" water molecules, then the enthalpic gain when releasing them will be significant and can give rise to strong association with a guest. The size of the cavity depends on the depth and diameter – approximately 8 high-energy water molecules is optimal.[57] However, a large cavity doesn't necessarily lead to a proportionally strong association due to a large enthalpic gain. Once the diameter of the portal becomes too large (~10 Å), the water inside the cavity can start making stabilizing hydrogen bonds with neighbouring encapsulated water molecules, as illustrated in Figure 1. 20b. The release of this water leads to a much smaller gain in hydrogen bonds, and therefore a smaller enthalpic driving force. On the other hand, if the hosts volume becomes so small that not even a single water molecule can be encapsulated this then creates a vacuum or a void within the host. At this point, the host

is considered prematurely "de-solvated" from water and welcomes a suitably sized guest. It has been proven both experimentally and computationally that **CB5** – the smallest member of the cucurbituril family – is too small to encapsulate any water molecules and that only a vacuum exists within the cavity.[58] This was shown to help in the encapsulation of noble gases in water. Although there is a de-solvation penalty to transfer the noble gas from bulk water into the cavity, this is greatly made up for as **CB5** is already considered "de-solvated" illustrated in Figure 1. 21. Interestingly, similar sized hosts like **SC4A** and **α-CD** were not able to sequester noble gases. Both **SC4A** and **α-CD** cavities are more exposed to bulk water and do not have "de-solvated" empty cavities like **CB5** (Figure 1. 21). This is an example of how different host topologies change host solvation and ultimately control binding properties.

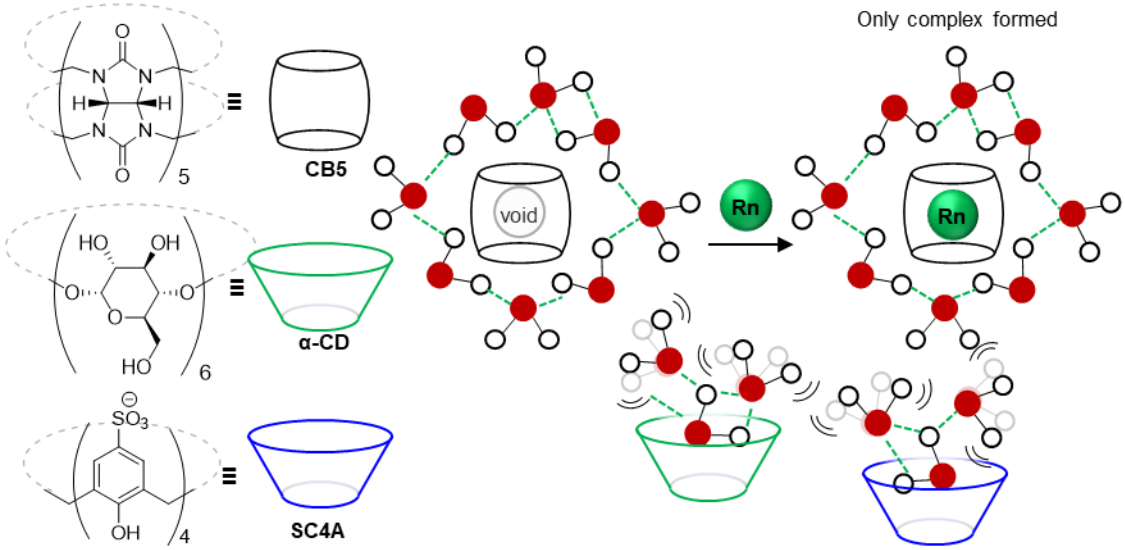

Figure 1. 21 **CB5** is the only host that sequesters Radon from water. **CB5** contains an empty de-solvated cavity that is filled perfectly when noble gases complex. Similar sized hosts, **α-CD** and **SC4A**, have different topologies and make favourable interactions with water and not with Radon.

The hydrophobic effect is also responsible for the selectivity towards "greasier" guests. We previously discussed that the cation-π interaction is responsible for the selectivity of cationic over anionic guests for cyclophane hosts. However, when comparing the binding strengths between two cations like tetramethylammonium, $N(CH_3)_4^+$ and ammonium, NH_4^+, many cyclophanes prefer the "softer" hydrophobic cation, $N(CH_3)_4^+$ over its "harder" hydrophilic counterpart, NH_4^+.[13, 18, 47, 59-62] For example, **SC4A** binds to

$N(CH_3)_4^+$ with a dissociation constant of 40 μM while the more hydrophilic counterpart, $N(CH_3)H_3^+$, bound much more weakly (K_d = 1.8 mM), as shown in Figure 1. 22a and b.[50] This trend extends to biologically relevant cations. For example, in Figure 1. 22 **SC4A** is 70-times more selective for a greasy cation, trimethyllysine (Figure 1. 22c) over the un-methylated counterpart, lysine in Figure 1. 22d.[63] This trend cannot be explained by the cation-π interaction alone, as the this interaction decreases as the ionic radius of a guest increases, hence the hydrophobic effect is the best explanation for this observed selectivity.

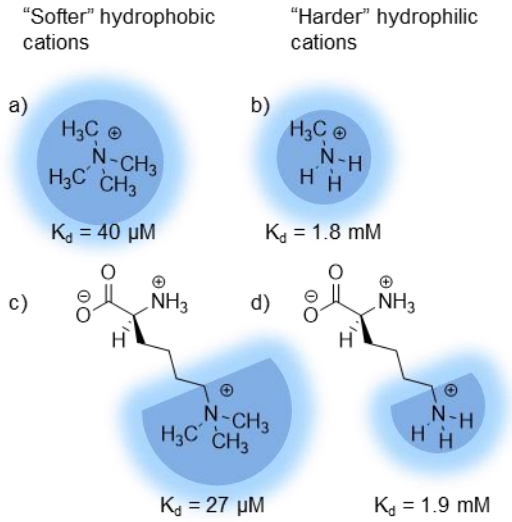

Figure 1. 22 **SC4A** binds more strongly to "softer" hydrophobic cations a) $N(CH_3)_4^+$ and c) trimethyllysine over their "harder" hydrophilic counterparts b) $N(CH_3)H_3^+$ and d) lysine.

1.2 A note on host flexibility and shape matching

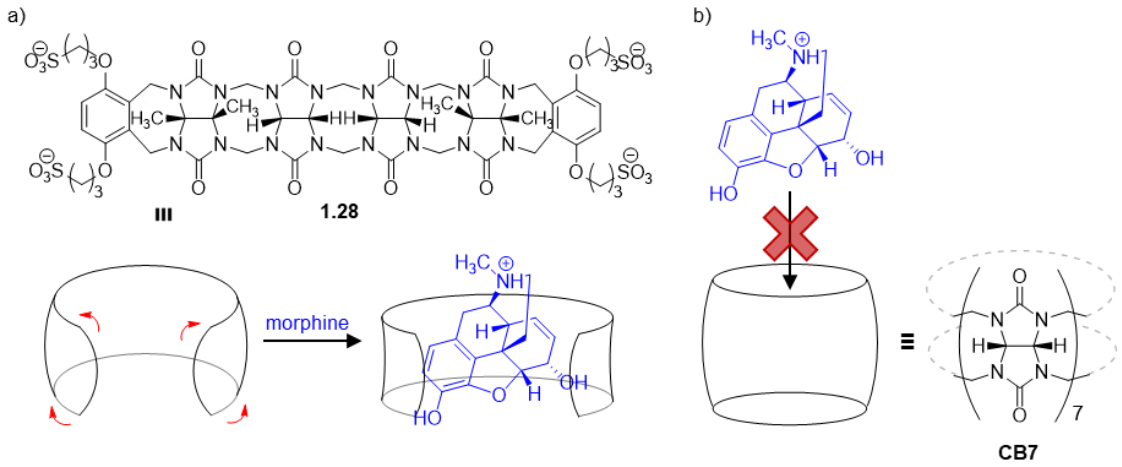

Figure 1. 23 Host flexibility facilitates an induced fit for larger guests. a) Acyclic cucurbituril, **1.28**, can flex to bind with large guests like morphine whereas b) cyclic cucurbiturils are inflexible and bind poorly to morphine.

Increased host flexibility governs the types of guests that will form strong complexes. Creating rigid hosts is thought to help guest selectivity and limits the differential loss of degrees of freedom between free host and host complexed.[64] Yet, there are advantages in making hosts more flexible to encourage an induced fit with the guest. For example, acyclic CB are U-shaped derivatives of their respective cyclic parents that bind strongly to a diverse suite of larger guests. In Figure 1. 23, **1.28** binds to morphine with micromolar affinities (K_d = 2 μM) whereas **CB7** does not associate at all.[65] The contraction of the acyclic hosts backbone allows them to accommodate guests that would not be as easily retained by their cyclic counterparts.[66] **SC4A** provide a rigid, well-defined pocket that is known to bind strongly to organic cations such as trimethyllysine (K_d = 28 μM) and lucigenin, **1.29** (K_d = 35 nM).[63, 67] Increasing the flexibility of these hosts is achieved by increasing the cavity size to afford 6- and 8- membered calixarenes. This ultimately changes the binding topology which is reflected in the binding strengths to the same guests. In Figure 1. 24, **SC6A**, the 6-membered variant, does not bind strongly with trimethyllysine (K_d = 1.1 mM) yet has a strong affinity with **1.29** (K_d = 52 nM).[68] **SC6A** easily interconverts to adopt many conformations which changes guest selectivity and affinity.

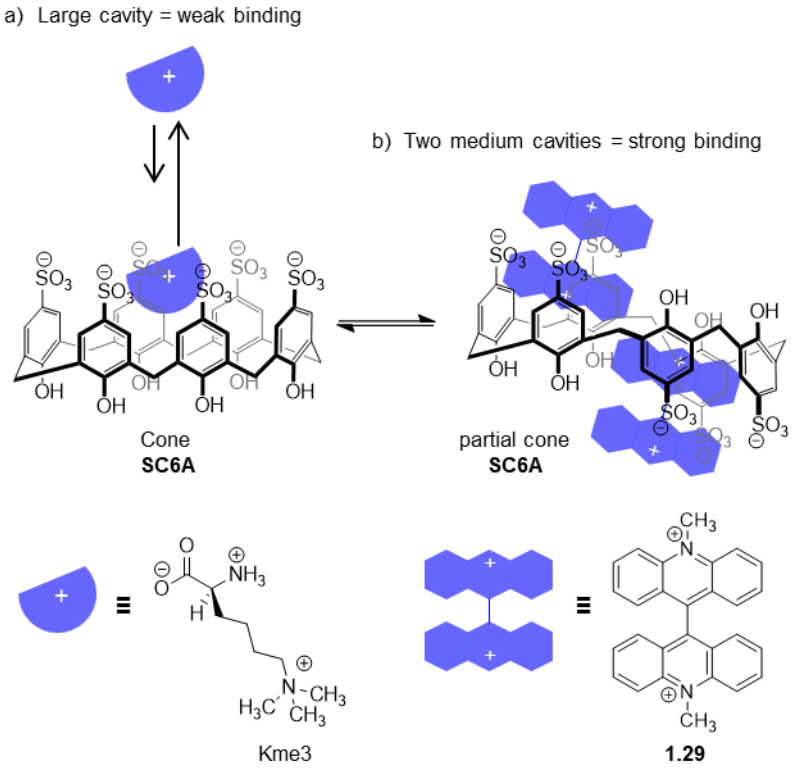

Figure 1. 24 **SC6A** offers two binding topologies when either in cone or partial cone conformation which modulates the size of guest that binds. a) Trimethllysine (Kme3) is too small to bind effectively to the cone conformation while b) lucigenin, **1.29**, is large enough to occupy both cone (not shown) and partial cone.

If it fits, it sits. Complementary host-guest shape aids in the formation of strong complexes. Although a lot of emphases have been placed on host design, the guest shape is also an important consideration. A great example is a pair of cyclophanes, **1.30** and **1.31**, that vary in size and hydrophobicity which creates different binding cavities for closely related guests (Figure 1. 25).[69] **1.30** contains a single carboxyphenyl linker that selectively binds to trimethyllysine (Kme3), a spherical cation. While **1.31** contains a carboxynaphthyl linker instead and selectively binds to asymmetric dimethylarginine (aRme2), a more rectangular-shaped cation. The slight change in cavity shape increases the selectivity by 2.5-fold for aRme2 over Kme3.

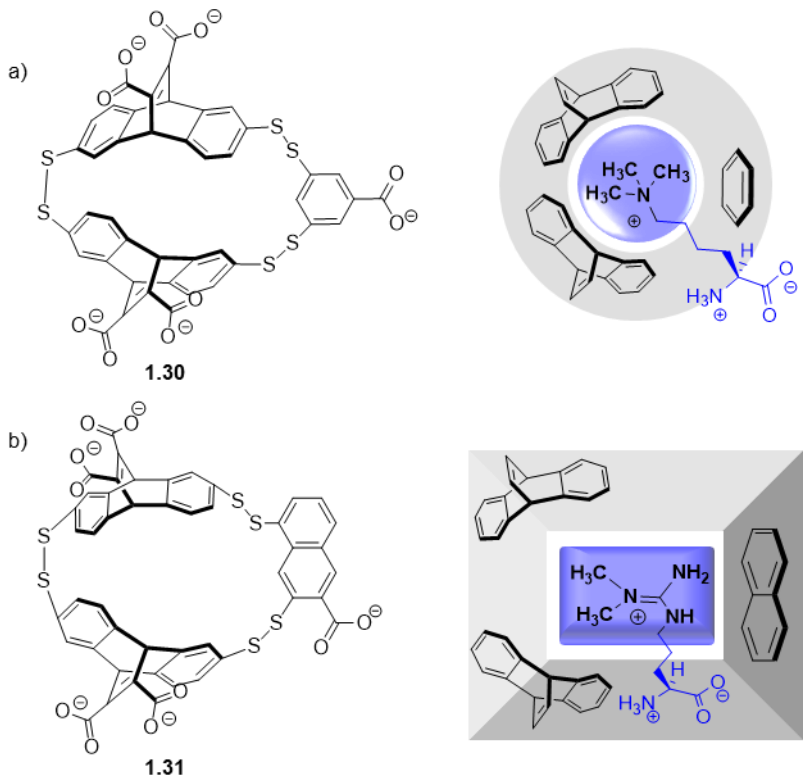

Figure 1. 25 Different cavity shapes influence guest binding. a) **1.30** displays a spherical cavity that complements Kme3 while b) **1.31** yields a rectangular cavity that is more ideal for a planar guest like aRme2.

Despite improvements, computational methods are still not able to fully understand or predict host-guest chemistry in water – especially where salt is involved. Computational and supramolecular chemists have collaborated to model binding interactions through the SAMPL (Statistical Assessment of the Modelling of Protein and Ligand) host-guest blind challenge exercises. SAMPL aims to evaluate and improve existing computational tools by asking computational chemists to predict binding energies for a set of pre-determined experimental values that are kept blinded until the predictions are submitted for evaluation. The initial efforts of the first and second SAMPL challenges were aimed toward predicting drug structures for protein targets. However, in the third challenge (SAMPL3) host molecules were included as these structures were less complex than proteins and had faster binding dynamics.[70] Since then, three more SAMPL challenges have been initiated: SAMPL4 in 2014,[71] SAMPL5 in 2017,[72] and SAMPL6 in 2018,[73] with the intention of improving computational tools to better predict binding energies of established host-guest systems. This work is necessary to further understand how water and co-solutes interact

with hosts and guests. Overall these exercises show improvements in predicting binding affinities of a suite of guests with selected hosts. In both SAMPL5 and SAMPL6 challenges, hosts **1.32** and **1.27** (Figure 1. 26) were used as model hosts (but with different guests) which helped to evaluate computational improvements. For example, the range of predicted binding affinities by SAMPL5 and SAMPL6 decreased for both hosts. In order to evaluate the quality of the predicted free energies of binding many statistical analyses were performed including root mean square error (RMSE) and coefficient of determination (R^2). When considering the binding energies of both hosts to their full suite of guests, the RMSE decreased from 3.00 kcal/mol to 2.76 kcal/mol and the median R^2 improved from 0.0 to 0.5. Further challenges remain to accurately define a host-guest system computationally that considers buffers, salts, and protonation states. For example, the predictive power weakened and the RMSE increased for both hosts **1.32** and **1.27** with a method that included the same ionic strength as reported experimentally. Yet, the opposite was true when considering a neutral host, **CB8**. This highlights the need to further develop methods that accurately describe the effects of salt. The goals for future SAMPL challenges are to consider not only different hosts, but also efforts to predict the effects of common biological salts and cosolvents that modulate the hydrophobic effect. As we will see in the next sections, these different factors can have a tremendous impact on the strength of host-guest interactions.

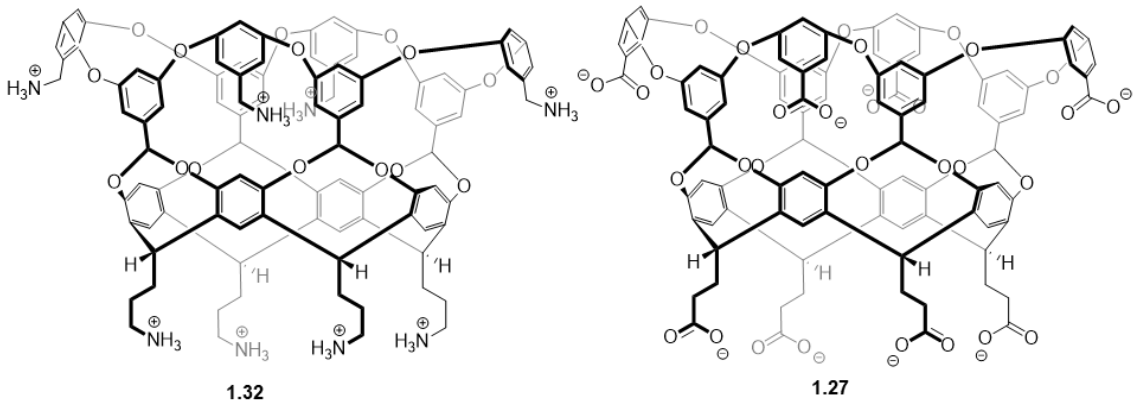

Figure 1. 26 Two hosts used in both SAMPL5 and 6 that were used to predict the free energies of binding.

1.3 Salts perturb host-guest systems in aqueous solution

The type and concentrations of salts often negatively impact host-guest systems. In order to design hosts that will eventually function in biological medium, the system is typically studied in buffered water to mimic the pH levels (and sometimes ionic strength) of the natural solution. The type of salt and the choice of buffer used can drastically change how the host behaves. Understanding how salts and buffers interact may help to design a system that will have a better chance at functioning in biological solutions.

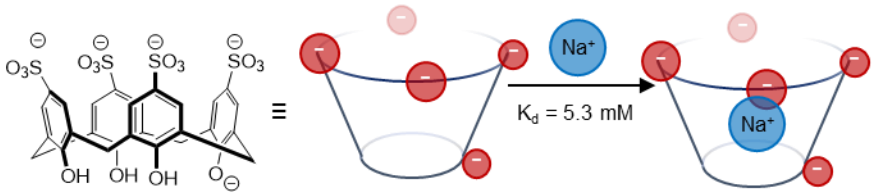

Figure 1. 27 High concentrations of Na^+ from buffers act as guests for **SC4A**.

Metal cations act as competitive guests for supramolecular cavities. The counter-cation in most buffers is often overlooked but can bind to hosts especially those with anionic solubilizing groups or electron-rich motifs. **SC4A** is best known to bind with cationic ammonium guests, but also binds Na^+ with K_d = 5.3 mM.[74] Although this is a weaker association constant than other ammonium guests, if one considers the buffer concentration to be at least 10-times the concentration of **SC4A** (100 – 150 mM), then nearly every host can be occupied by Na^+, as illustrated in Figure 1. 27. The addition of salt or acid (H_3O^+) helps increase the solubility of cucurbiturils in water because the cation binds to the electronegative ureido carbonyls.[75] It is evident from extensive mechanistic studies that Na^+ and other simple cations can bind to both carbonyl portals and modulate guest encapsulation.[76-78] This is accomplished by either weakening the complex when the cation acts as a competitive guest or acting as a lid, increasing the strength of host-guest complex. For example, **CB7** binds with a ditopic guest, **1.33**, *via* the phenyl or naphthyl ring but prefers the latter.[79] At high concentrations of Na^+, the cation acts as a competitor and weakens the naphthyl inclusion yet when Na^+ ions are bound, it acts as a stabilizing cap for the phenyl inclusion complex (Figure 1. 28). To avoid negative interactions of salt with various hosts, a lower buffer concentration is ideal. However, when translating these

systems to real biological solutions, it is hard to escape the 100's of mM concentrations of various salts that exist in Nature.

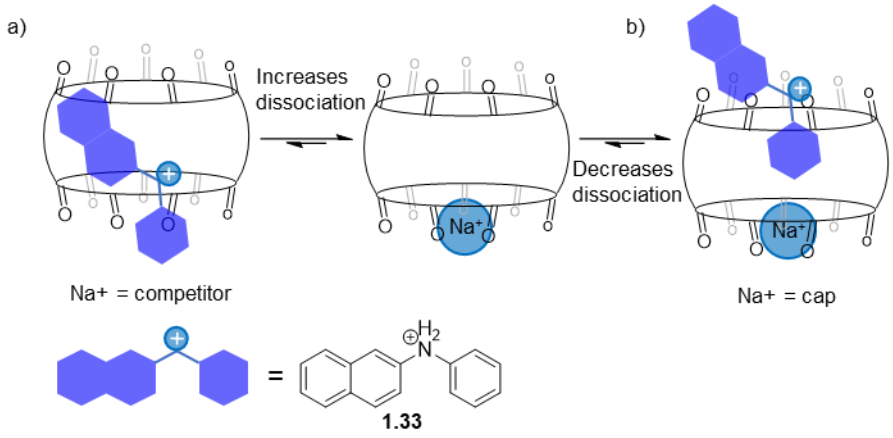

Figure 1. 28 Na^+ binds with the carbonyl portals of cucurbiturils and modulates guest binding orientation. a) Na^+ acts as a competitor and increases the dissociation of the naphthyl motif in **1.33** and b) acts like a cap which stabilizes the phenyl motif.

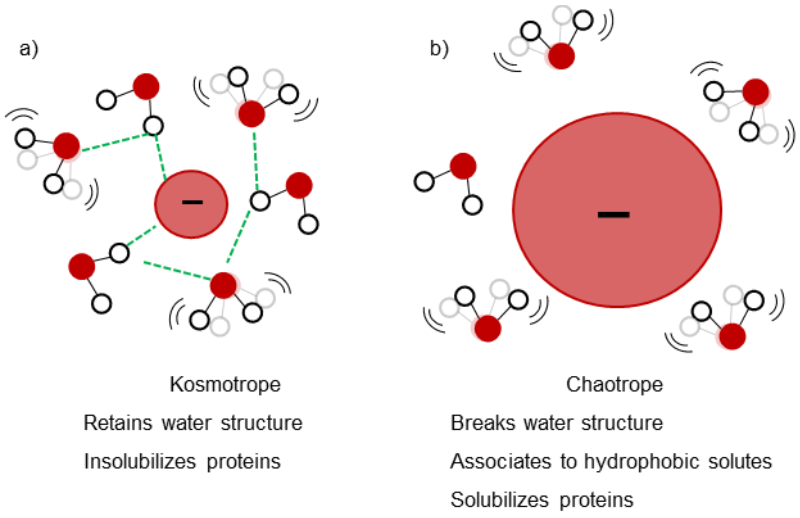

Figure 1. 29 Cartoon illustrating the Hofmeister anions effect on solvated water. a) Kosmotropes are small and preserve water structure while b) chaotropes are large and disrupt water structure.

Soft polarizable anions act as direct competitors for hydrophobic cavities. These anions are a subset of the Hofmeister anion series that were first described to change the solubility of proteins. The anions are ranked either by rendering proteins insoluble (kosmotropes) or soluble (chaotropes) in water: F^-, SO_4^{2-}, AcO^-, Cl^-, Br^-, NO_3^-, ClO_3^-, I^-, ClO_4^-, SCN^-. This observation has been extended to include salt effects on polymers, peptides, hydrophobic solutes and hosts.[80-83] The combination of interactions between the

anion-water and anion-solute help explain their effects on solutes. The early anions in the series are charge dense and preserve the solvated water structure hence their name as kosmotropes (kosmo = good order) (Figure 1. 29a). The later anions in the series are polarizable and disrupt water structure, giving them the name chaotropes (khaos = chaos) (Figure 1. 29b). Chaotropes also associate with hydrophobic surfaces and can outcompete for the binding pocket with native guests. For example, the host-guest system **1.27** and **1.34** weakens in the presence of NaI, $NaClO_4$, and NaSCN (Figure 1. 30). Notably, in the presence of $NaClO_4$ there is an unfavourable binding enthalpy yet a greater but opposite gain in entropy which weakens the complex by 1.5 kcal/mol.[84] This was explained by NMR studies that indicate perchlorate was encapsulated within the **1.27**, preventing **1.34** from binding. This effect becomes more dramatic when chaotropic anions increase in size and polarizability and are referred to as super-chaotropic.[85]

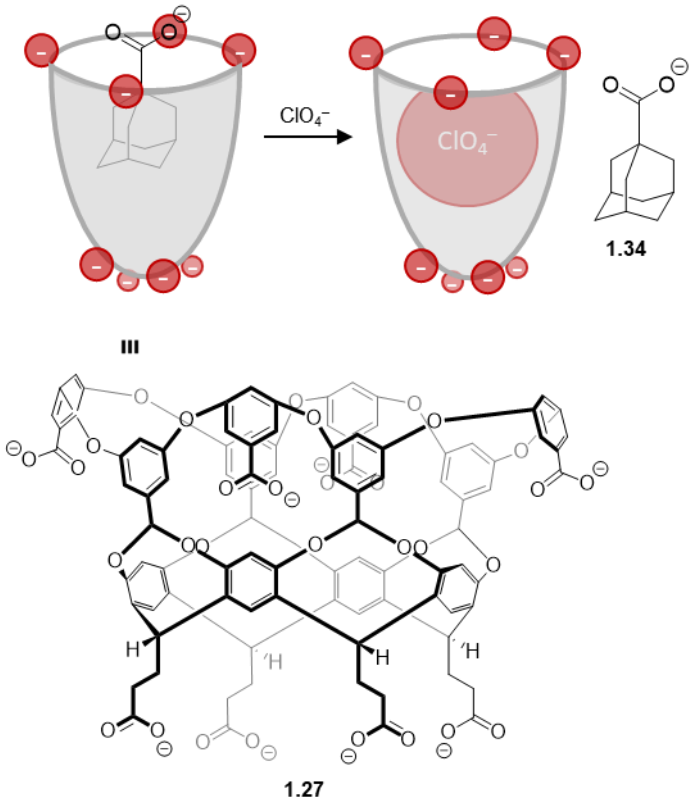

Figure 1. 30 The association between **1.27** and **1.34** is perturbed by chaotropes like ClO_4^- as it directly competes for the hydrophobic binding pocket.

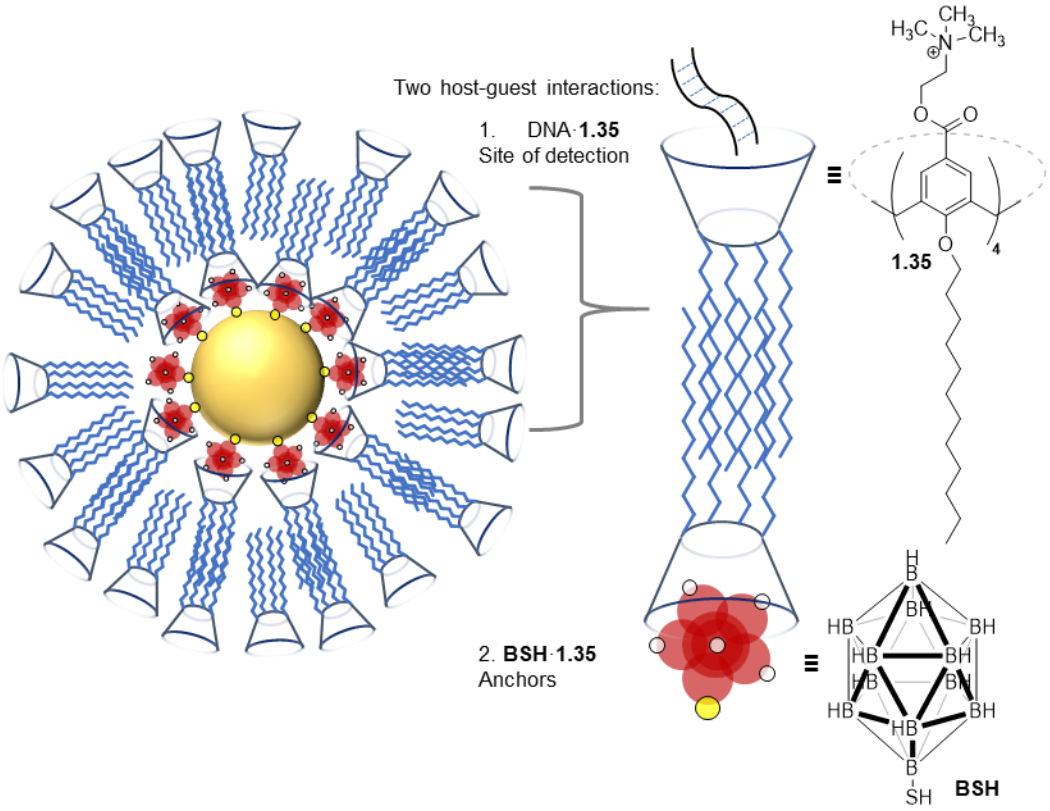

Figure 1. 31 Super-chaotropic anion, **BSH**, binds strongly to **1.35** providing an anchor between a Gold surface and the supramolecular bilayer that detects DNA in complex mixtures.

Super-chaotropic anions have been utilized to generate functional hierarchal supramolecular materials. As the anionic size increases, so does the entropy from the surrounding dis-ordered water molecules and in turn an even greater gain upon association with a hydrophobic surface. These anions include borate clusters, like $B_{10}H_{10}^{2-}$, and polyoxometalates, like $P_2W_{18}O_{62}^{6-}$, which are 2- to 3-fold larger than the former chaotropic anions. Although the competition of chaotropic anions for a hydrophobic cavity has been considered a problem, others have utilized this association to create materials for biological purposes. For example, the superchaotropic anion, decahydro-mercapto-closo-dodecaborate (**BSH**), coated and stabilized gold nanoparticles while also providing a host-guest anchor point for an amphiphilic cationic calixarene, **1.35**, that further assembled into a bilayer structure (Figure 1. 31).[86] This assembly remained stable and able to detect biological cations such as DNA and enzymatic reactions. The chaotropic effect is considered relatively new yet is already responsible for developing complex

supramolecular structures that function in water and is anticipated to lead to more advances in the near future.

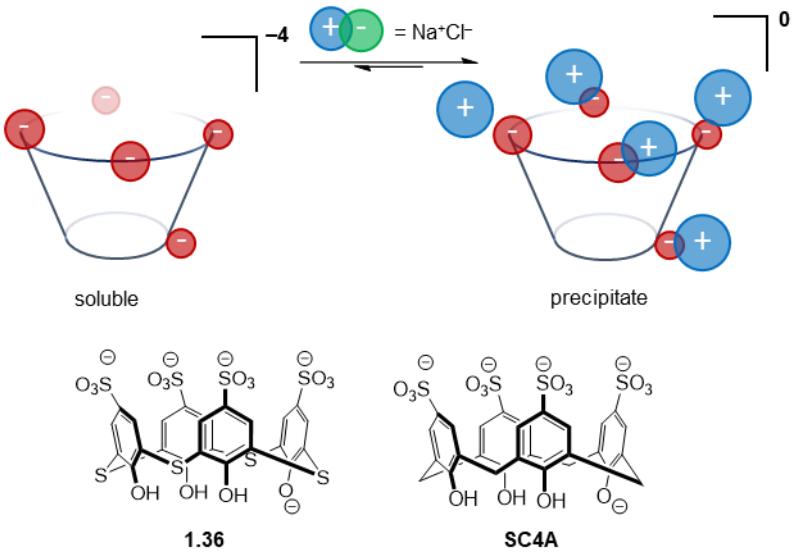

Figure 1. 32 Millimolar concentrations of salt neutralize the charge on highly charged hosts rendering them insoluble in water. **1.36** and **SC4A** both precipitate from solution by varying degrees of added NaCl.

High concentrations of salt induce precipitation when ions condense on charged hosts. Earlier in section 1.2, there was discussion regarding precipitation of charged species upon the association of a guest or an oppositely charged molecule. Host solubility in water can also be affected by salt when the buffer or solution counterions neutralize the charge on the host (Figure 1. 32). The addition of large excess of salt to precipitate both sulfonated thio-calixarenes and **SCnA** have been reported.[87-89] The Na^+ ions condense on the sulfonates which neutralizes the host rendering it insoluble in water. For example, **SC4A** and its corresponding thio-derivative (**1.36**) were used to encapsulate ketones and alcohols guests in water and then a 100-fold excess of NaCl was added to precipitate the host-guest complex (Figure 1. 32).[90] In this case the neutralization of **SC4A** by Na^+ was used as a successful technique to isolate a host-guest complex but it is difficult to predict how different hosts with behave in the presence of salt. From the same example, it was clear there was a preference for **1.36** to capture guests and salt-out more readily than **SC4A** despite both bearing four sulfonates along the upper rim. This suggests that it is not as

simple as translating these observations into reasonable predictions of how one class of host will behave given a certain concentration of a salt.

1.4 Exemplary systems that operate in the presence of salts and buffers

Supramolecular tools have been developed to function in aqueous mixtures of buffer and salts. The current understanding of how hosts behave in salty water aids in the design of supramolecular systems that carry out a function in a biological context. There are many examples of hosts that bind with protein surfaces to inhibit protein function,[91-92] increase stability,[93-96] and induce crystallization.[15] There are hosts that form responsive supramolecular polymers,[97] micelles and vesicles with targeted guests.[97-98] Some act as nanoreactors by facilitating photochemical reactions in buffered water.[99-101] Other biologically aimed tools are those that enable peptide enrichment,[102] and there are also sensors that detect various biological analytes.[103-105] These sensors are particularly interesting for the current discussion, as the supramolecular systems that target biological analytes need to generate a detectable output for the user while using mechanisms that are resistant to salts.

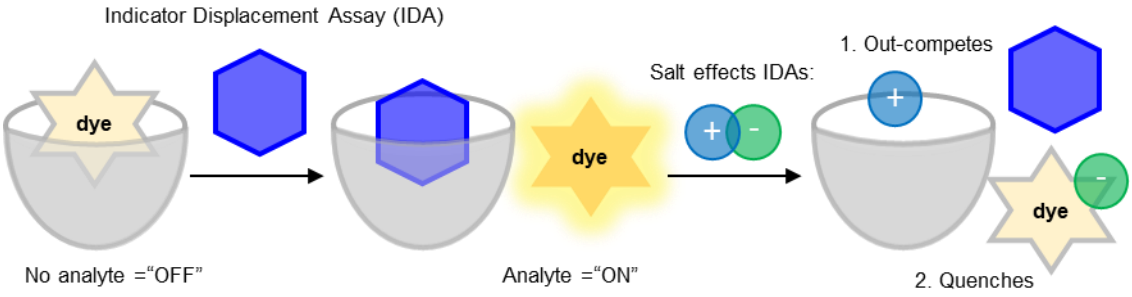

Figure 1. 33 Indicator Displacement Assay (IDA) is used to detect analytes by displacement of a quenched dye. Salt can affect IDAs either acting as a competitor or quenching the dye.

Transforming a host into a chemosensor requires the integration of a reporter motif or molecule that communicates when an analyte has been bound by the host. Dyes are common reporters as their optical properties can be sensitive to the environment and to the presence of other molecules. There are various photophysical mechanisms that modulate the response of dyes, but one common strategy is through indicator displacement, as illustrated in Figure 1. 33. The dye/indicator is encapsulated by the host which creates an

"analyte absent" optical state. Once an analyte is present, it displaces the indicator (dye) into the bulk water, which induces another optical state of "analyte present".[106-107] When supramolecular systems detect an analyte through this mechanism it is referred to as an Indicator Displacement Assay (IDA). Some examples of hosts exist in which the hosts have been structurally modified to include this dye molecule tethered covalently to their structure. However, many more supramolecular sensors simply use an added, external dye molecule to avoid the synthetic challenges of creating dye-integrated hosts. Although these sensors are often easily constructed, they suffer from the same challenges as any aqueous supramolecular system: chemosensors that target biological analytes must work in salty water. Salts can not only act as competitors, but also can directly perturb the photophysical properties of the indicators.

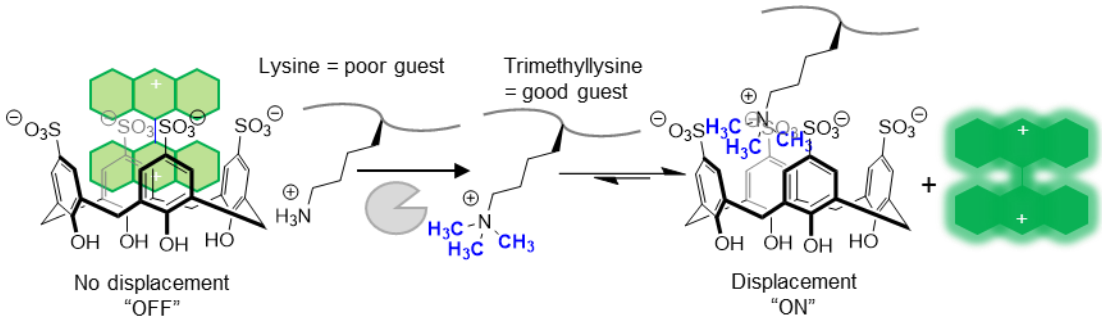

Figure 1. 34 **SC4A** and **1.29** are used to monitor a methyltransferase reaction with a turn-on fluorescence response when trimethyllysine is formed. The reaction is conducted in low salt concentrations to eliminate any negative effects.

In spite of these challenges, there are some examples of supramolecular sensors that teach key lessons about compatible buffers and how to use salt effects as an advantage. For example, **SC4A** was used to detect the product formation of an enzymatic reaction in real-time when combined with lucigenin (**1.29**) as the dye component in an indicator displacement assay. **SC4A** binds to **1.29** and quenches its emission. One **SC4A**-**1.29** assay monitored **1.29**'s fluorescence increase as the dye was displaced from the **SC4A** cavity by a trimethyllysine-containing peptide, which was the product of an enzymatic methylation reaction. A glycine buffer (5 mM, pH 10) was chosen to avoid the presence of large amounts of Na^+ and Cl^- (Figure 1. 34).[108] As discussed previously, **SC4A** binds weakly with Na^+. More importantly, Cl^- and other halides bind to **1.29** directly and quench its fluorescence.[109] The enzyme worked well in the chosen buffer, and the assay proceeded

smoothly. A different example shows how salt effects can provide a functional advantage. In this case a deep-walled cavitand, **1.37**, was paired with a trimethylamine-fluorescein conjugate, **1.38**, as the displaceable indicator and was used to detect an enzymatic demethylation reaction (Figure 1. 35).[62] In this case the IDA works as a turn-off sensor: **1.37** first binds the trimethyllysine substrate peptide, leaving **1.38** uncomplexed and emissive, once the enzyme creates the unmethylated counterpart, **1.38** associates with the host. However, **1.38** is not quenched when encapsulated by **1.37**; instead the amphiphilic dye-host complex forms micelles in which the dye is quenched by aggregation effects. The complex assembly strength was tested in the presence of various chaotropes and kosmotropes. Each salt had a unique influence on the sensor's aggregation, which in turn can affect the sensitivity. For example, NaI decreased the stability of the quenched aggregate while chloride promoted its formation. In both examples, the effects of buffer and salt were considered and evaluated to yield supramolecular chemosensors that can operate in a complex aqueous mixture.

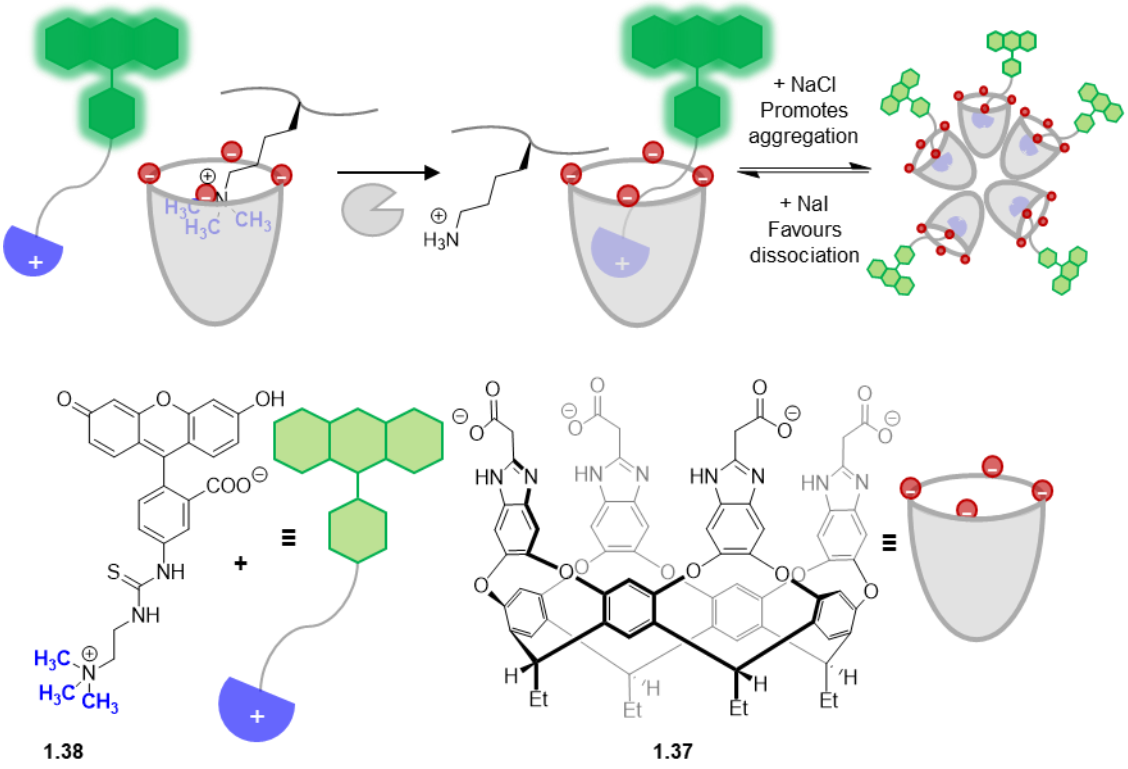

Figure 1. 35 Aggregation quenched IDA detects a demethyltransferase reaction. The sensitivity is influenced by Hofmeister anions that modulate the formation of the quenched aggregate.

1.5 Systems that function in real biological media

The goal for most water-compatible supramolecular systems is to operate in real biological solutions. But such solutions can be both complex and unpredictable. Supramolecular hosts offer selective and potent recognition sites that mimic those of biomolecules in Nature. However, an additional challenge for these supramolecular tools is to operate in solutions that are even more complex and less controlled than the salty, buffered aqueous solutions that have been discussed above. Biofluids such as serum and urine contain a mixture of different salts, proteins, and organic analytes that vary in concentrations between individuals.[110-111] This complexity and heterogeneity is further amplified in cells and whole organisms. Examples of biofluid-compatible chemosensors and medicinally relevant systems that operate in cells and whole organisms are discussed below.

1.5.1 Chemosensors that function in biofluids

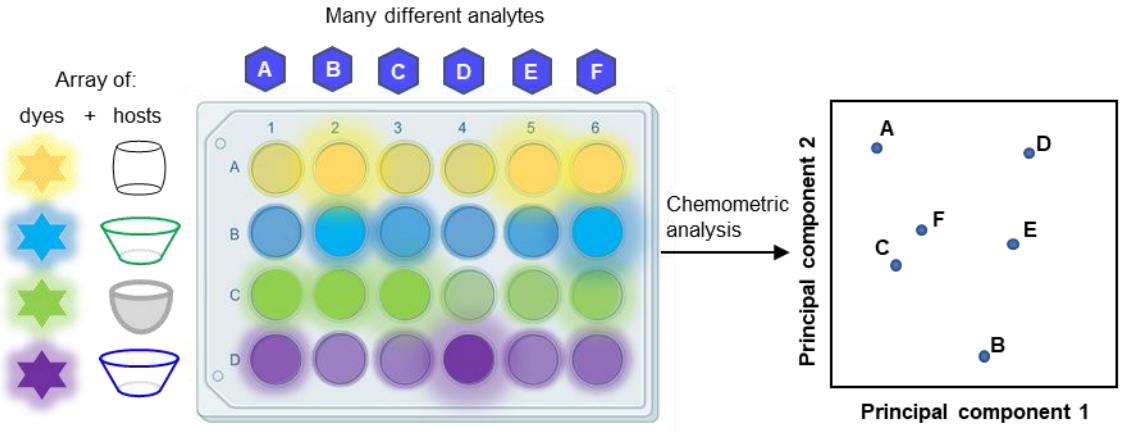

Figure 1. 36 An array of different dyes and hosts detect many different analytes producing a complex output which is simplified through chemometric analysis to distinguish each analyte.

Chemosensors become more powerful when implemented as an array of related sensor elements. Often, a single chemosensor is not enough to selectively target one analyte in a complex mixture that contains a number of structurally similar analytes and co-solutes. Instead of re-designing a chemosensor to improve selectivity, the original IDA can be

expanded to form an array of promiscuous chemosensors that detect many analytes but to different extents. The output is a unique pattern or fingerprint for a given analyte, that is simplified and visualized through chemometric analyses. The most common methods (principal component analysis and linear discriminant analysis) each can provide a dimensionally reduced scores plot that distinguishes different analytes from one another (Figure 1. 36). Anslyn popularized this approach to take advantage of the inherent cross-reactivity of supramolecular chemosensors, while avoiding pain-staking synthetic efforts to yield a single, selective receptor.[112]

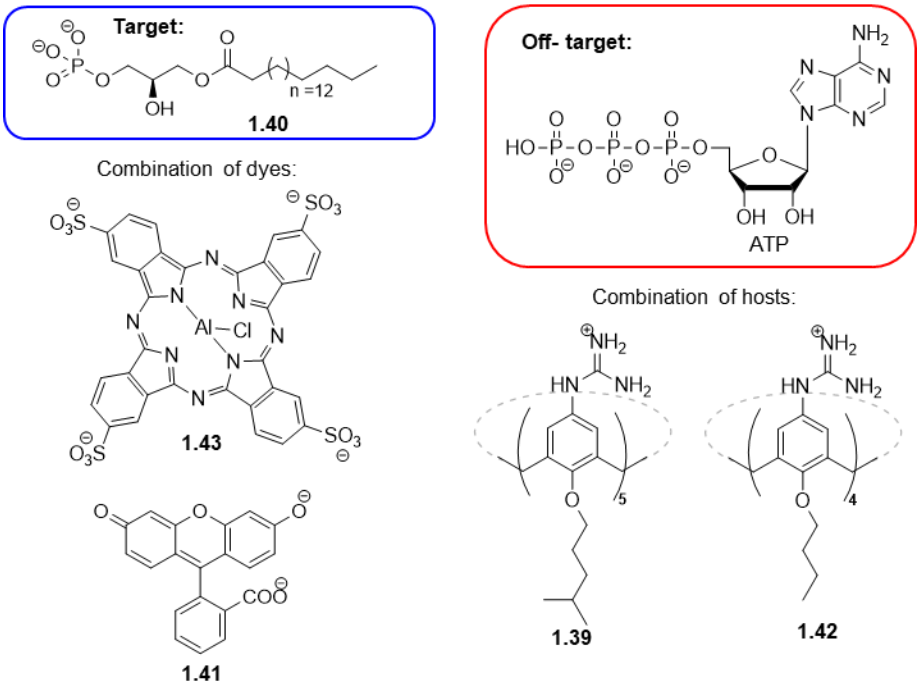

Figure 1. 37 A combination of two different calixarenes (**1.39**, **1.42**) and dyes (**1.41**, **1.43**) detect and discriminate a cancer biomarker, lysophosphatidic acid (**1.40**), from an off-target molecule, adenosine triphosphate, ATP, in plasma.

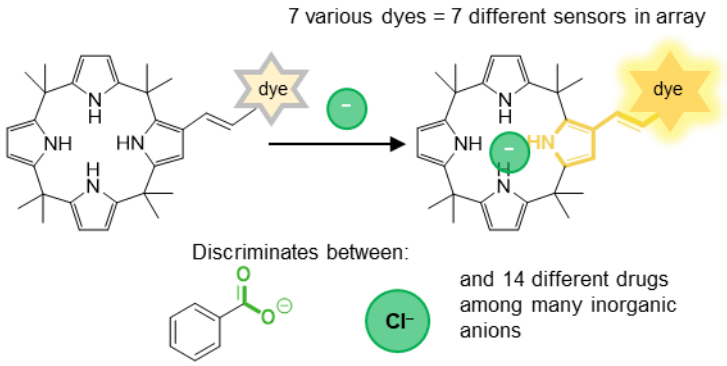

Figure 1. 38 An array of 7 dye-integrated calix[4]pyrrole chemosensors detect over-the-counter carboxylate drugs in urine despite high detection fidelity with inorganic anions.

Many published chemosensors that function in biofluids operate within a sensor array to overcome the challenges of sensing in competitive solutions. For example, a guanidinium-modified calix[5]arene, **1.39**, was able to detect an ovarian cancer marker, lysophosphatidic acid (**1.40**), at nM concentrations in plasma through the displacement of a fluorescein dye, **1.41** (Figure 1. 37).[113] Despite high selectivity over most other co-solutes, ATP was found to be a major competitor. An array of similar calixarenes (**1.42**) and different dyes (**1.43**) were used in combination with chemometrics to distinguish ATP from the desired biomarker, **1.40**. In another example, a library of dye-conjugated calix[4]pyrroles detected and discriminated between different over-the-counter carboxylate drugs in urine (Figure 1. 38).[114] Once a drug is bound to the pyrrole, the dye turns on through an intramolecular partial charge transfer. The authors initially found that each calix[4]pyrrole chemosensor bound more strongly to competitive biological anions like Cl^- and $H_2PO_4^-$ than with benzoate, a structural similar compound to the tested over-the-counter drugs. However, the library of calix[4]pyrroles in combination of chemometrics was able to detect and successfully discriminate between the carboxylate drugs in urine.

1.5.2 Hosts that operate in whole cells and cell lysates

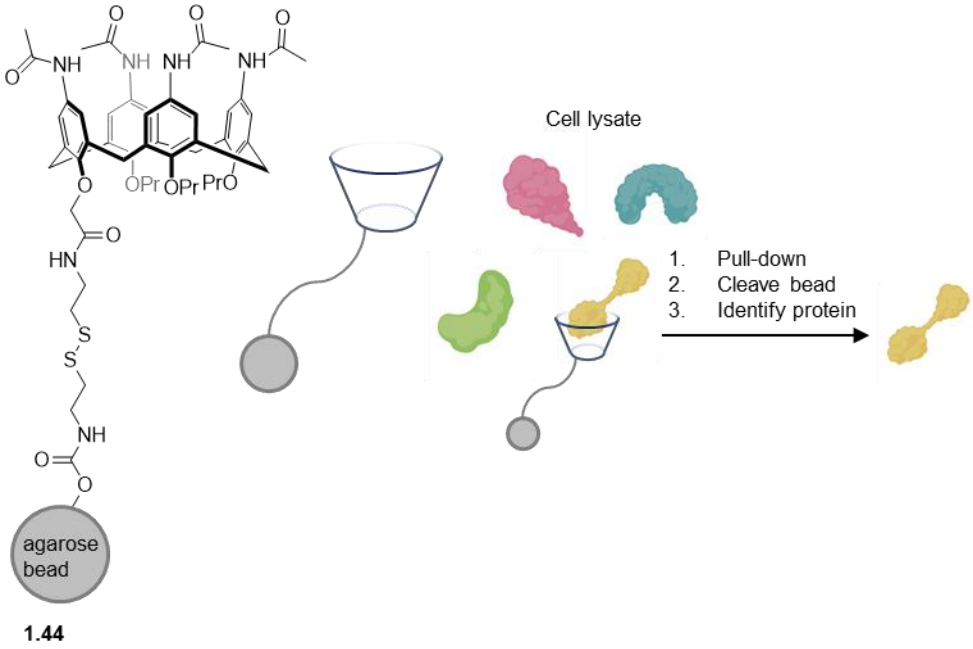

Figure 1. 39 An acetamidocalix[4]arene conjugated to an agarose bead, **1.44**, is used to "fish" proteins from a cancer cell lysate to discover high binding proteins.

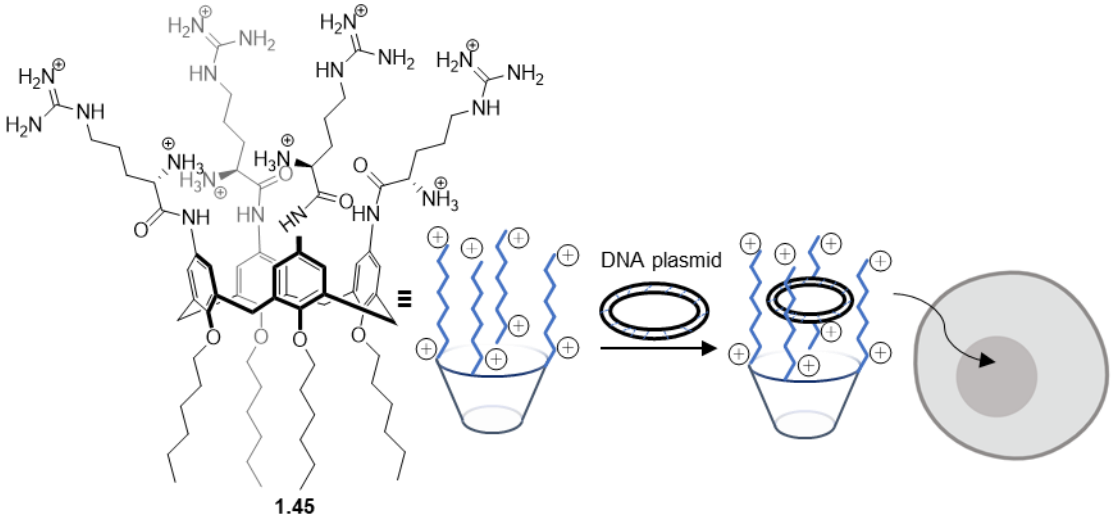

Figure 1. 40 An arginine-functionalized calix[4]arene, **1.45**, encapsulates DNA plasmids and successfully transfects cells.

Some supramolecular hosts can function in whole cells and cell lysates, in spite of the variation of salts, metabolites and other biomolecules that exist in living systems. In one example, a host was used as a biomolecular enrichment tool that functioned in a cell lysate to "fish out" a protein from a complex mixture (Figure 1. 39).[115] An acetamidocalix[4]arene, **1.44**, was conjugated to an agarose bead and mixed with HeLa

cell lysate. The goal was to allow the calixarene to form complexes with a few strong protein partners from the thousands of proteins contained in the cancerous cell. “Hit” proteins were identified after a pull-down, cleavage from the bead, and proteomics analysis. Subsequent re-testing confirmed the biological activity of the calixarene on its newly discovered protein target.

Cells have lipid bilayers and other barriers that prevent foreign substances from entering, yet there are supramolecular hosts that successfully pass membranes. For example, an arginine-functionalized calix[4]arene, **1.45**, was able to encapsulate nucleic acids such as DNA plasmids and transfect cells (Figure 1. 40).[116] The arginine groups assisted in DNA condensation and are also known to assist with internalization of cargo inside cells. These cell-penetrating motifs are not always necessary, as demonstrated by the pre-formed complex of **SC4A** and lucigenin dye (**1.29)** penetrating and working as an IDA sensor within live cells (Figure 1. 41).[117] The sensing abilities were strongly affected by the chloride-containing cell medium (binding strength decreased 100-fold, quenching efficiency decreased 5-fold) yet the differential response was enough to detect guests such as acetylcholine. **CB7**s are known to bind with *N*-terminal phenylalanine residues on full proteins such as insulin with nM affinity (Figure 1. 42).[93] Many protein unfolding diseases such as Alzheimer’s and amyloidosis contain hydrophobic residues, like phenylalanine, that form β-sheets which promote unfolding and sequential formation of toxic fibrils. **CB7** was able to prevent this mechanism by sequestering phenylalanine residues on insulin and amyloid proteins in cells.

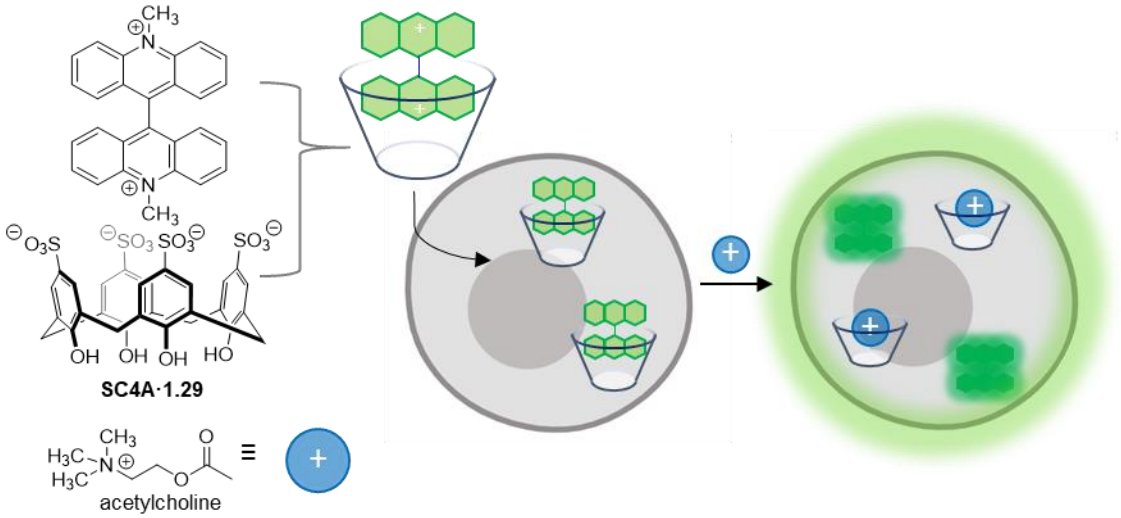

Figure 1. 41 **SC4A** and **1.29** enter cells and detect acetylcholine.

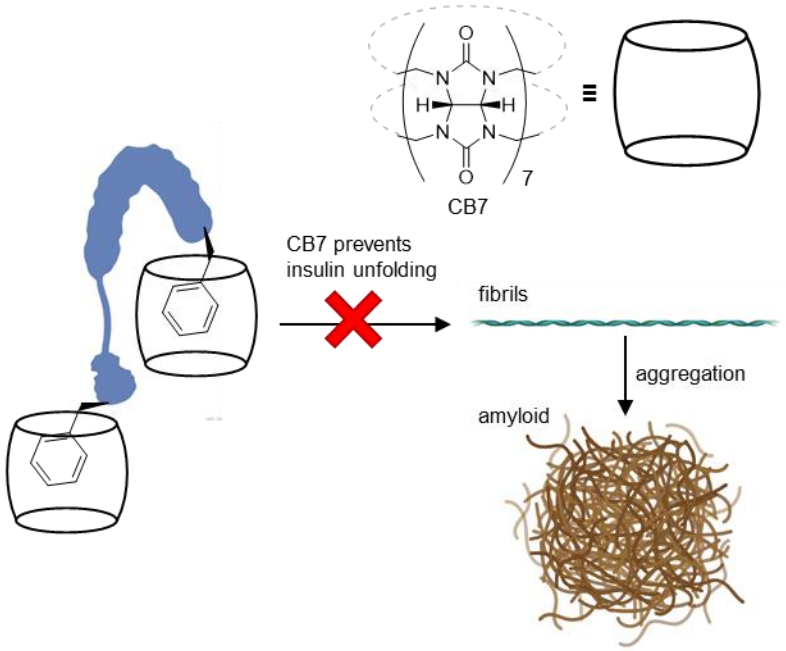

Figure 1. 42 **CB7** encapsulates terminal phenylalanine on insulin preventing toxic fibril and amyloid formation in cells.

1.4.3

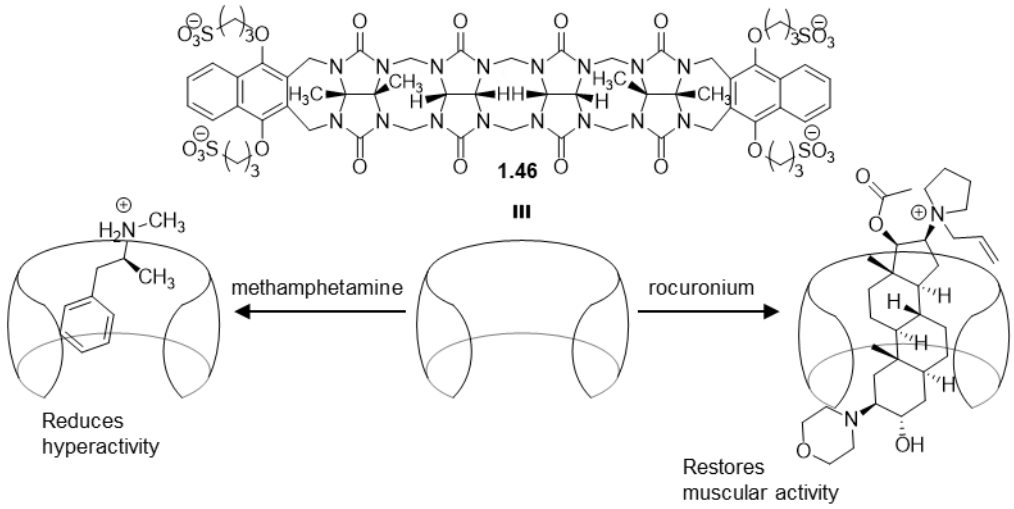

Figure 1. 43 Acyclic cucurbituril, **1.46**, binds to methamphetamine to reduce hyperactivity in rats and rocuronium to restore muscular activity in mice.

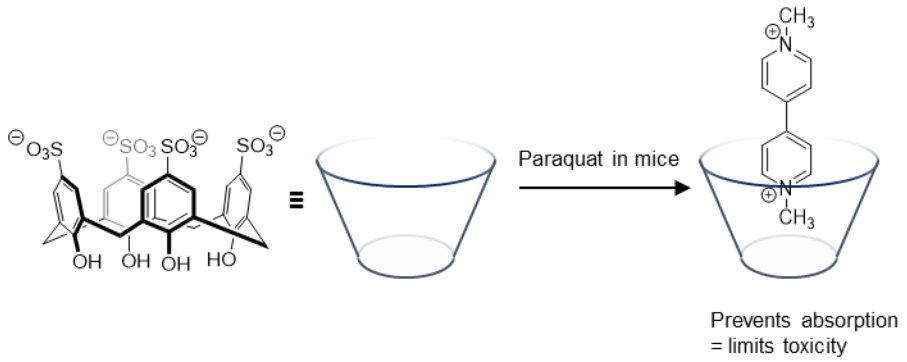

Figure 1. 44 **SC4A** binds with paraquat and prevents the toxic herbicide from absorption in the body of mice.

1.5.3 Supramolecular systems can function in whole organisms

For a supramolecular system to be successful in a whole organism requires the host to be both tolerant to co-solutes and to behave well pharmacokinetically. When a synthetic drug is introduced within an organism, the location, biochemical pathway and waste product must be considered safe. The same expectations are necessary when introducing a supramolecular host in an organism. Cucurbiturils, **SC4A** and γ-cyclodextrin all have shown to be non-toxic to mice at concentrations up to 250 mg/kg, 100 mg/kg, and even 16 000 mg/kg, respectively.[118-120] **SC4A** showed rapid clearance through the urine and no accumulation in vital organs. While, the fast clearance of CBs indicates that the macrocycle exits the body by excretion or by metabolism. Since these macrocycles seem to be

relatively inert in the body, many hosts can act as drug carriers, aid in bioimaging, act as disease inhibitors, and drug reversal agents.

Supramolecular hosts can act as drug reversal agents. Many hosts including **SC4A**, cyclodextrins, cyclic and acyclic cucurbiturils form strong complexes with various illicit drugs in water with association constants ranging from 0.1 mM to 10 nM.[65] **1.46** was successful at binding and removing methamphetamine in rats and reducing its hyperactivity effects.[65] It was also successfully able to bind and remove rocuronium, a neuromuscular blockade agent from mice, to restore normal muscular control (Figure 1. 43).[121] Yet there is currently a FDA approved cyclodextrin drug called Sugammadex that also removes rocuronium and restores muscular activity in humans.[122] Similarly, **SC4A** has been shown to act as a drug reversal agent by lowering the concentration of a toxic herbicide, paraquat, from rats (Figure 1. 44).[123-124]

Hosts can also act as carriers for beneficial drugs and therapies.[125-130] This helps reduce harmful side-effects, improves drug stability and solubility, and the host can sometimes release the drug at the diseased site due to an environmental change. For example, carboxylatopill[6]arene (**1.47**) encapsulated and transported a toxic cancer drug, oxaliplatin, to tumor cells in mice (Figure 1. 45).[131] The release of the drug is triggered by a pH drop in cancer tissue as oxaliplatin loses affinity for protonated **1.47**. In another strategy, a host can encapsulate a reactive molecule *in vivo* rendering it temporarily inert. A specific biomarker localized at a diseased site can then displace the reactive guest from the host in order to kill the diseased cells. An example of this used a modified calixarene, **1.48**, which formed a strong complex with a photosensitizer (**1.43**), rendering it photochemically inert (Figure 1. 46).[132] The large abundance of ATP present in those cells displaces **1.43**. Here free **1.43** is irradiated by a localized source of light where it converts inert triplet oxygen to highly toxic singlet oxygen to kill the tumor cells in mice. This biomarker displacement technique is similar to indicator displacement in sensing but in this case was used to improve phototheranotics.

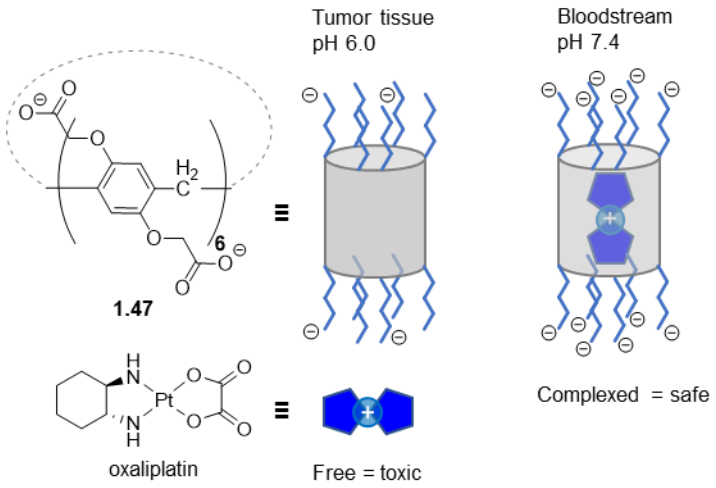

Figure 1. 45 Carboxypillar[6]arene, **1.47**, complexes a potent cancer drug, oxaliplatin, when deprotonated in the bloodstream but releases the drug in acidic tumour tissue.

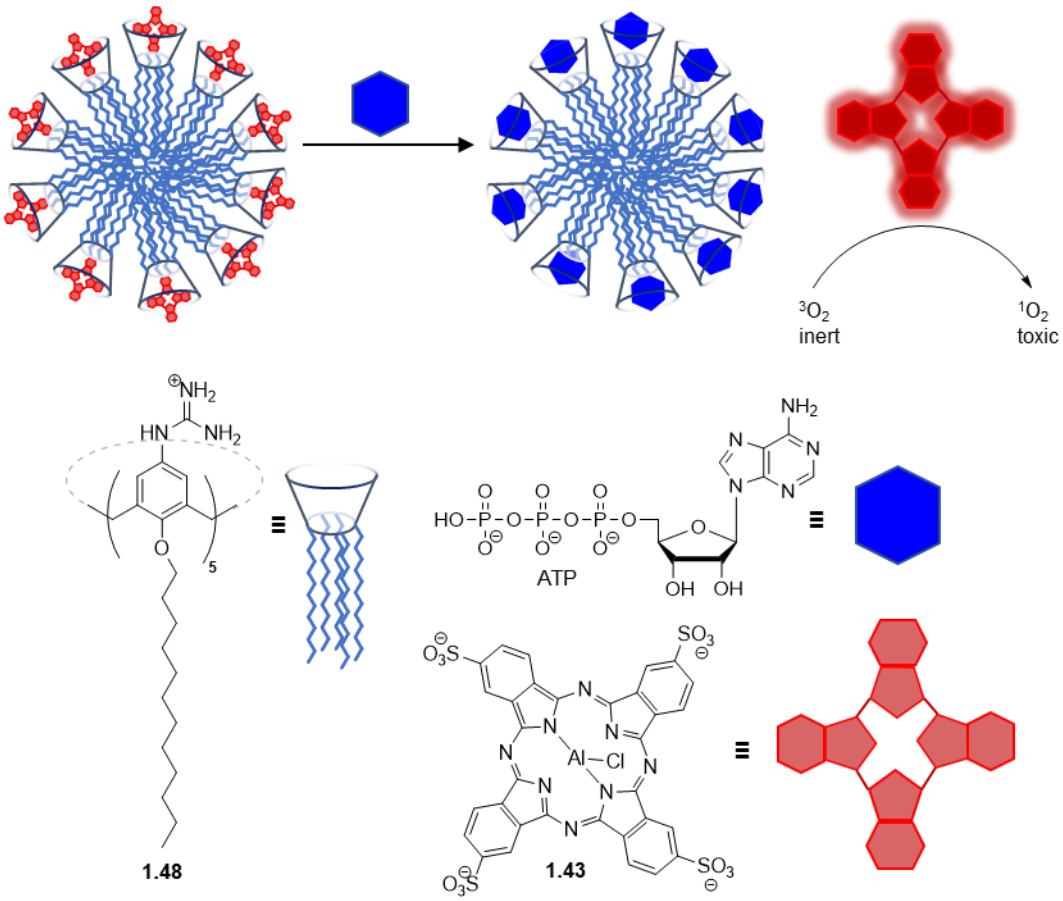

Figure 1. 46 An amphiphilic calix[5]arene, **1.48**, quenches a photosensitizer, **1.43**, when bound and forms stable micelles that remain inert in mice. **1.43** is displaced by ATP and converts inert triplet oxygen into the reactive singlet oxygen, killing cancer cells.

1.6 A serendipitous discovery of a salt tolerant self-assembly

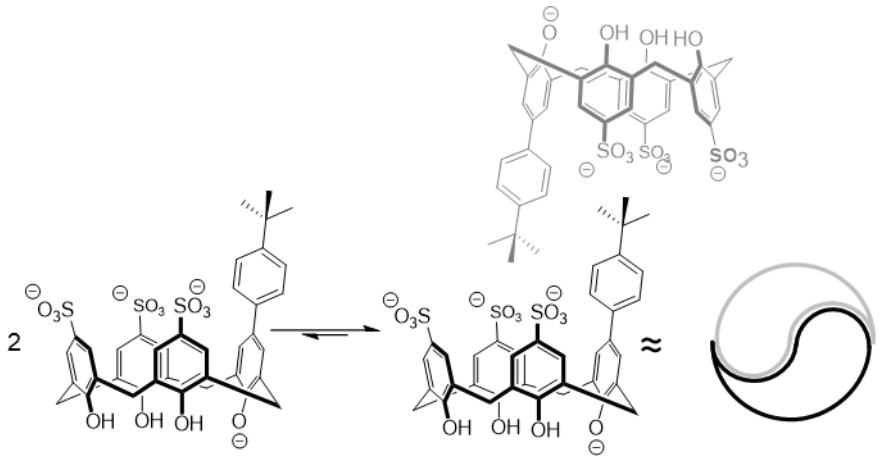

Figure 1. 47 Two copies of ***tBu*$_1$-SC4A** form yin-yang like homodimer assemblies in water.

Much of this thesis work grows from a serendipitous discovery that occurred while creating water-soluble calixarenes to target certain guest proteins. The goal was to synthesize different functionalized water-soluble calix[4]arenes for the purpose of selective recognition of post-translationally methylated proteins and peptides.[133] During this process, a mono-aryl tri-sulfonated calixarene was synthesized and yielded an unexpected ^{1}H spectrum in D_2O — aromatic resonances were shifted significantly upfield and were broadened.[134] The explanation that supported this observation was a self-assembly of two copies of the host molecule. The pocket of one host encapsulated the aromatic pendant group of the other, yielding a yin-yang type structure shown in Figure 1. 47. Following this initial discovery, seven analogues were synthesized and tested in order to characterize the scope of the assemblies. The dimers can dissociate upon dilution. ^{1}H NMR resonances of encapsulated protons sharpen and shift downfield towards their expected chemical shifts upon dilution. The heat of dimer dissociation can be measured with ITC dilution experiments, and an equilibrium constant can be derived. ***tBu*$_1$-SC4A** was the strongest dimer that formed with a dissociation constant of 1.1 mM in sodium phosphate buffer. Further evidence to support self-assembly came from an X-ray crystal structure that showed the pendant group of one calixarene occupying the recognition pocket of another (Figure 1. 48). The measured radius from the X-ray crystal structure

(11.1 Å) also matched Diffusion-Ordered Spectroscopy (DOSY)-derived hydrodynamic radius of 11.3 Å.

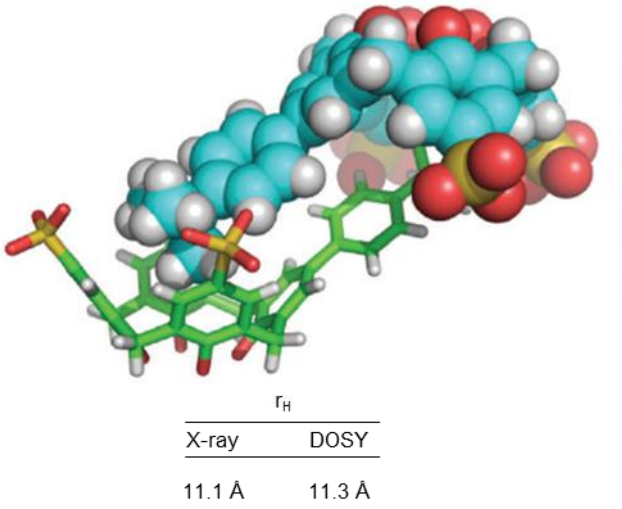

Figure 1. 48 X-ray crystal structure further confirms ***tBu*$_1$-SC4A** dimerizes with a measured radius of 11.1 Å which matches the DOSY- derived r_H of 11.3 Å.

The yin-yang dimers are stabilized by the hydrophobic effect and destabilized by mutual electrostatic repulsion. A single calixarene, with three sulfonates and one deprotonated phenol, carries an overall –4 charge at neutral pH. Hence the dimer is a –8 assembly. Despite this electrostatic repulsion from the sulfonates along the upper rim, the hydrophobic effect overcomes this. The role of hydrophobicity is made even clearer when comparing the ^{1}H spectra of ***tBu*$_1$-SC4A** in D_2O and CD_3OD shown in Figure 1. 49. The upfield and broadened resonances that indicate self-assembly in D_2O are not found in CD_3OD. Instead, an expected ^{1}H spectrum is observed with sharp aromatic resonances found between 7 – 9 ppm. ITC data revealed a significant favourable enthalpic contribution and an unfavourable entropic contribution upon assembly. Clearly, there is a significant energy gain upon de-solvation of water from each calixarene drives the assembly. Although over-interpretation of thermodynamic should be avoided, this suggests that the self-assembly can be governed by the non-classical hydrophobic effect.

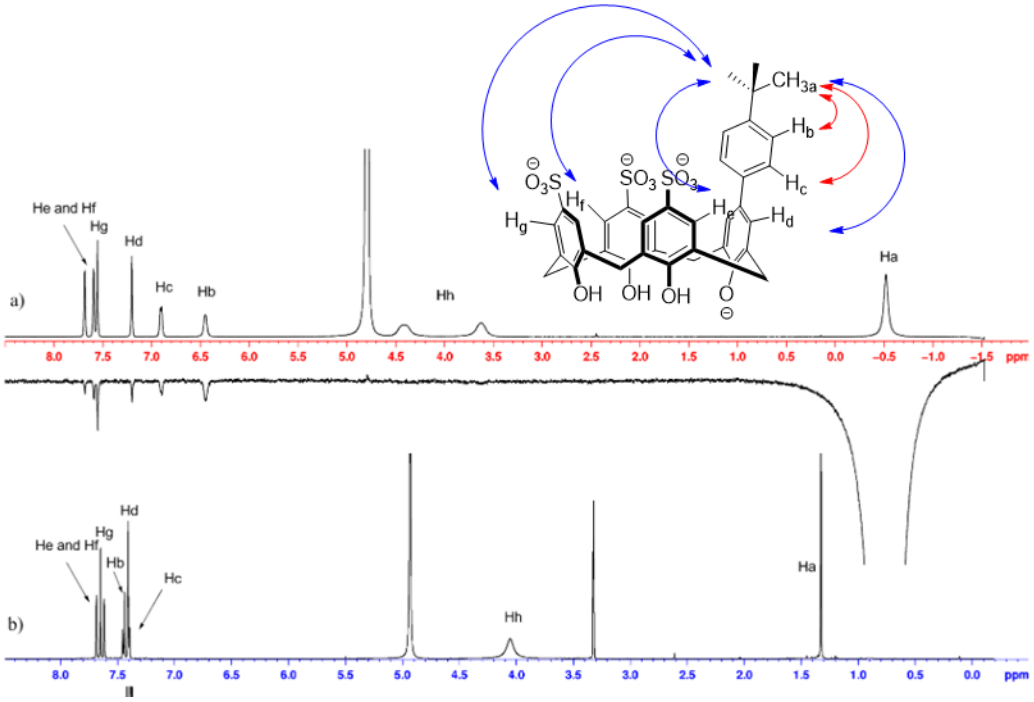

Figure 1. 49 ^{1}H NMR supports homodimerization of ***tBu*$_1$-SC4A**. a) In water ***tBu*$_1$-SC4A** dimerizes with characteristic upfield shifts and broadening of pendant group resonances while b) in organic solvent this does not occur, and resonances are in expected chemical shifts. 1D NOE further confirms self-assembly with intermolecular correlations (blue arrows) between dimers are observed along with intramolecular correlations (red arrows)

The homodimers remain stable to salt and co-solutes. Dimers become stronger in the presence of salts from a PBS buffer that contains added NaCl, KCl and $MgCl_2$. Comparing the thermodynamic data of ***tBu*$_1$-SC4A** between buffer with and without these extra salts shows a decrease in the enthalpic contribution from –11.0 kcal/mol to –10.3 kcal/mol. However, there is an opposite but greater compensating change in entropy from –6.9 kcal/mol to –5.9 kcal/mol, ultimately creating a stronger dimer (K_d = 0.73 mM). The assemblies were further tested and were even resilient to real urine which contains salts (total ~200 mM), urea (~137 mM), and other organic co-solutes (up to 15 mM).

1.7 Summary of thesis

The calixarene dimers described in Section 1.6 are the starting point for my research and thesis. I was interested in pursuing three goals in order to further understand and extend their yin-yang mode of self-assembly.

The first goal involves modifying the calixarene to expand the scope of structures that can dimerize in water. Chapter 2 explores the overall topology of the calixarene to form clip-like calixarene-based assembles. These assemblies are also tested for their responsiveness to the presence of various guests.

The second goal is to explore the limits of solute tolerance. Chapter 3 explores modifying the upper rim to include a dynamic covalent bond that allows exchangeable hosts to form from four distinct components, yet still assemble in the overall yin-yang topology of the parent compounds. The four-component hosts are systematically tested in the presence of solutes and shown to survive in molar concentrations of salt and urea.

The third goal involves transforming the self-assembly into systems that carry out a sensing function in real biological solutions. In Chapter 4, I integrate a solvatochromic dye within the calixarene pocket to form a chemosensor, coined DimerDye, that can monitor enzymatic reactions in real-time by a novel disassembly-induced supramolecular sensing mechanism. In Chapter 5, I expanded the DimerDye by developing a parallel synthesis and screening method to afford a small library of new DimerDye derivatives that can detect illicit drugs in aqueous buffer and in saliva.

Chapter 2: A clip-like host that undergoes self-assembly and competitive guest-induced disassembly in water

This work was adapted from a previously published paper.

Meagan A. Beatty, Jil A. Busmann, Noah G. Fagen, Graham A. E. Garnett, Fraser Hof *Supramol. Chem.*, **2019**, 31, 101-107

GG and FH conceived of the molecular design and MB conceived the idea of guest responsiveness. NF first synthesized and characterized the calixarenes and performed ITC experiments. JB and MB conducted NMR guest titrations. MB designed, conducted and analysed data for variable temperature-NMR, 1D DOSY and UV-Vis/fluorescence experiments. MB and FH co-wrote the paper.

2.1 Foreword

Soon after the discovery of calixarene-based dimers discussed in Chapter 1.6, we wanted to explore the structural limits of calixarenes that were prone to dimerize. It was noted that there was a balance between hydrophobicity, charge and complementary shape that drove the self-assembly, and that these parameters could be tested by varying the calixarenes' upper rim functionality. The new design added a second aryl group, and in doing so took on a different clip-like host topology that is often found in the literature to have unique recognition properties.

I was also interested in testing the responsiveness of the homodimers to good guests. The previous dimers were tested for their resilience to urine and mock serum but not to the presence of hydrophobic cationic guests. I hypothesized that a guest could cause dimer disassembly and the formation of new calixarene-guest complexes.

2.2 Introduction

Molecular clips and tweezers are important motifs for molecular recognition in water. The combination of a rigid, U-shaped hydrophobic surface with peripheral solubilizing groups creates a poorly hydrated concave surface that is predisposed to strong

binding of hydrophobic partners in water. For example, a U-turn topology has been achieved using acyclic cucurbiturils discussed throughout Chapter 1 [135-137] that have strong affinities towards hydrophobic cationic drugs *in vivo*.[138] There are examples of norbornene-derived structures that recognize biologically relevant guests such as neurotransmitters, nucleotide derivatives, peptides and even lysine residues that disrupt important protein-protein interactions.[139-141] Yet in aqueous solution, both types of clips are involved self-complementary assemblies that form homo- or heterodimers.[142-144] Often these two binding modes – self-association and host-guest binding – compete. For example, norbornene clip **2.1** forms a strong homodimer, (**2.1**)$_2$, in water which diminishes the fluorescence of the two anthracene motifs. Once a guest is present such as the acetylcholine (ACh), the dimer disassembles to form a new **2.1**•ACh complex that is strongly fluorescent in pure, unbuffered water (Figure 2. 1).[145]

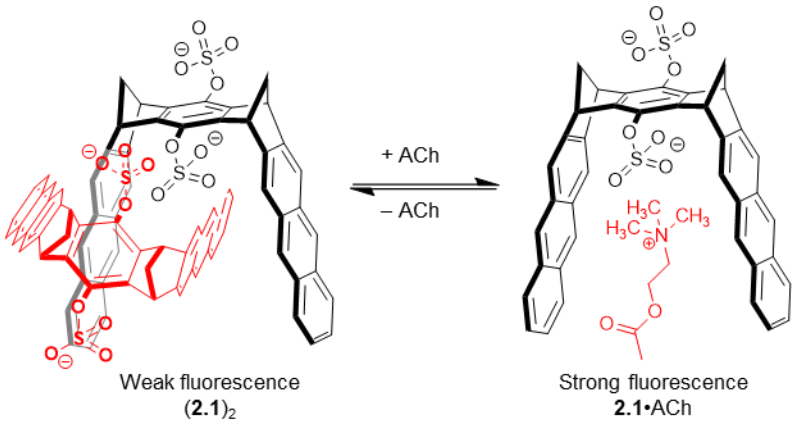

Figure 2. 1 Clip **2.1** assembles into a weakly fluorescent homodimer in water. The addition of acetylcholine induces dis-assembly of the homodimer and assembly of a strongly fluorescent **2.1**•ACh complex.

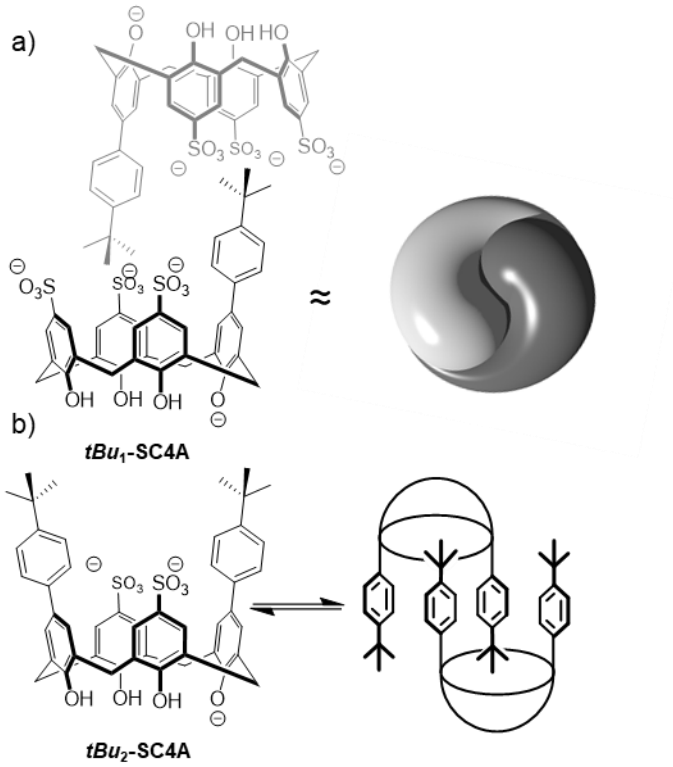

Figure 2. 2 a) Previously reported dimeric monofunctionalized calix[4]arene, ***tBu*$_1$-SC4A**, and b) the new difunctionalized clip-like calix[4]arene, ***tBu*$_2$-SC4A**.

We converted the original yin-yang calixarene homodimer into a new structure that has both clip-like character and a higher level of symmetry. We were interested in modifying our strongest dimer, ***tBu*$_1$-SC4A**, that included a single *t*-butylphenyl group and carried a total charge of –4 (Figure 2. 2a). By adding a second *t*-butylphenyl group to ***tBu*$_1$-SC4A**, we produced a clip-like calixarene with a net charge of –3 at neutral pH. This created an overall C_{2v} symmetry with two opposing similar arms and increased hydrophobic surface area in the form of an extended cleft (***tBu*$_2$-SC4A**, Figure 2. 2b). Unlike prior water-soluble clips and tweezers, the clip incorporates a sulfonated calix[4]arene binding pocket of a type that offers an unique recognition site for biological guests [146-149]. As mentioned in Chapter 1, calixarenes have been documented to bind with protein surfaces, peptides, drugs and other biological analytes. This provides a multifaceted clip that has the potential to self-assemble yet engage to form a complex in the presence of a "good guest."

We report here our studies of the new molecule's homodimerization in water. We also report the response of this homodimer to a variety of guests in competitive buffered water solutions.

2.3 Results and Discussion

The synthesis of ***tBu$_2$*-SC4A** is achieved through selective upper-rim functionalization reactions. It starts with the selective dibromination of 1,3-dibenzoyl calix[4]arene (**2.2**) [150] which occurs selectively at the two positions *para* to unprotected phenols to give **2.3**. The benzoyl groups are removed (**2.4**) and the newly exposed phenols are *para* sulfonated along the upper rim upon treatment with H_2SO_4 to yield the key precursor **2.5**. The final compound, ***tBu$_2$*-SC4A**, is obtained by a double Suzuki coupling with *t*-butylphenyl boronic acid and obtained in 40% yield after HPLC purification (Scheme 2. 1). Compound ***tBu$_2$*-SC4A** is most soluble in slightly basic water, at which it is expected to have a net charge of –3 due to the low pKa for the first phenol deprotonation in calix[4]arenes [151]. We decided to study only clip ***tBu$_2$*-SC4A** as a previously synthesized clip **2.6**, obtained from similar Suzuki coupling conditions contained two methylammonium groups was found to be insoluble in water. As mentioned in Chapter 1, the symmetric arrangement of two cationic and two anionic functional groups renders the molecule insoluble in water due to an internal charge neutralization.

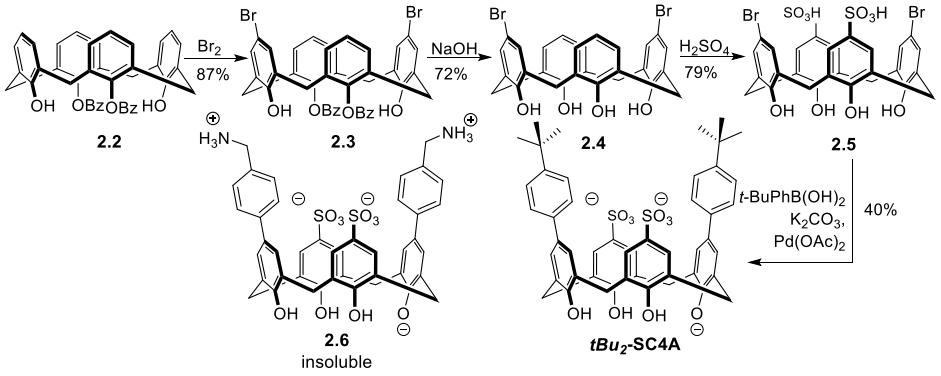

Scheme 2. 1 The synthesis of the calix[4]arene clip, ***tBu$_2$*-SC4A**.

Dimerization of ***tBu$_2$*-SC4A** was apparent when comparing the ^{1}H NMR spectra in CD_3OD and D_2O. In CD_3OD, the pendant phenyl and *t*-butyl resonances were found as sharp peaks at 7.45 ppm, 7.40 ppm and 1.32 ppm, as expected for an unaggregated

monomeric state. In D_2O both the phenyl and *t*-butyl resonances broadened and shifted upfield to 7.25 ppm, 7.0 ppm and 0.33 ppm, respectively (Figure 2. 3). This pattern of upfield shifts is diagnostic for encapsulation of a *t*-butylphenyl substituent within a calix[4]arene's electron-rich pocket [134]. The fact that this is not observed in pure CD_3OD (or even upon addition of small amounts of CD_3OD) indicates that the dimerization is primarily driven by the hydrophobic effect.

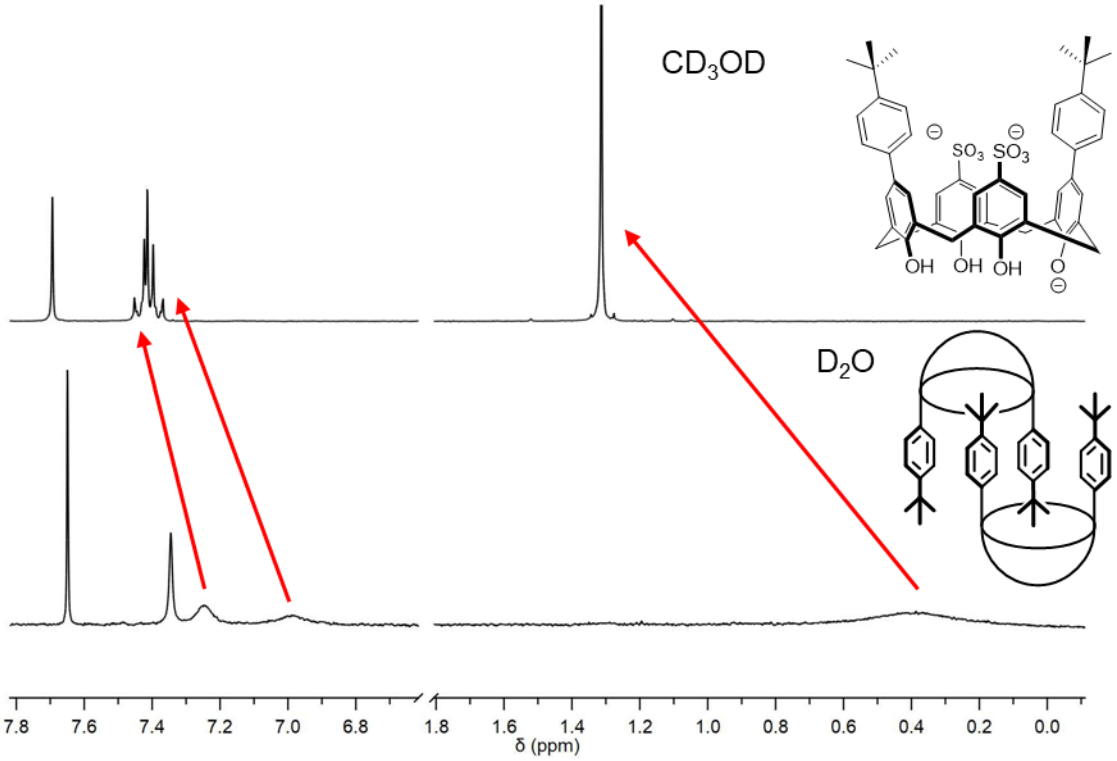

Figure 2. 3 ***tBu₂*-SC4A** in CD_3OD (top) as a monomer and in D_2O (bottom) as a dimer. The upfield shift and sharpening of the *t*-butyl singlet, and Ph doublets are diagnostic of encapsulation.

The existence of dimer in solution was confirmed by DOSY. The diffusion coefficient of monomeric ***tBu₂*-SC4A** was obtained by 1D DOSY in 20% CD_3OD in Na_2HPO_4/NaH_2PO_4 (50 mM, pD 8.5) buffer—conditions under which 1D chemical shifts show that pure monomer is present. The Stokes-Einstein equation was used to determine the monomer's hydrodynamic radius as 8.51 Å (Table 2.1 and Supp. Info.). This value is similar to the value determined in the same CD_3OD/buffer conditions for the control compound *para*-sulfonatocalix[4]arene (**SC4A**), which can't undergo dimerization. In 100% aqueous Na_2HPO_4/NaH_2PO_4 (50 mM, pD 8.5) buffered solution the hydrodynamic

radius of the dimer was found to be 11.31 Å consistent with the value observed for its thoroughly characterized dimeric analogue ***tBu*$_1$-SC4A.**[134]

Table 2. 1 Diffusion coefficients (D) obtained by 1D DOSY and corresponding hydrodynamic radii (r_H)

	D (m^2/s)	r_H (Å)
SC4A[(a)] (monomer control)	2.20 x 10^{-10}	7.1
***tBu*$_2$-SC4A**[(a)] (monomer)	(1.92 ± 0.03) x 10^{-10}	8.2 ± 0.4
***tBu*$_2$-SC4A**[(b)] (dimer)	(2.18 ± 0.02) x 10^{-10}	11.2 ± 0.3

(a) 20% CD_3OD in Na_2HPO_4/NaH_2PO_4 (50 mM, pD 8.5) buffer, [**SC4A**] or [***tBu*$_2$-SC4A**] = 1 mM. (b) Na_2HPO_4/NaH_2PO_4 (50 mM, pD 8.5) buffer (c) previously reported data [134], in D_2O.

ITC dilution titrations show that compound ***tBu*$_2$-SC4A** forms stronger dimers than ***tBu*$_1$-SC4A**, with different enthalpic and entropic contributions. The K_d decreased from 1.0 mM (***tBu*$_1$-SC4A**) to 0.54 mM (***tBu*$_2$-SC4A**) with the addition of a second *t*-butylphenyl group (Table 2. 2). In spite of the relatively small structural change, the association of ***tBu*$_1$-SC4A** was less enthalpically favoured while ***tBu*$_2$-SC4A** was more entropically driven. NMR data suggest dimers of similar structures, so we attribute the slight differences mainly to the swap of a sulfonate for a second *t*-butylphenyl group. Additional hydrophobic surface area must be de-solvated upon dimerization of ***tBu*$_2$-SC4A**. The increase in entropic driving force follows the classical view of the hydrophobic effect, which is appropriate considering that the new appended hydrophobic group is not in a confined space and is largely exposed to solvent in the free state.

Table 2. 2 ITC-derived thermodynamic parameters for homodimerization of ***tBu*$_1$-SC4A** and ***tBu*$_2$-SC4A**.[(a)]

	K_d (mM)	ΔG (kcal/mol)	ΔH (kcal/mol)	TΔS (kcal/mol)
***tBu*$_1$-SC4A** [(b)]	1.0	−4.2	−11	−6.9
***tBu*$_2$-SC4A**	0.57	−4.5	−5.5	−0.98

(a) ITC dilution titrations in H_2O containing Na_2HPO_4/NaH_2PO_4 (100 mM, pH 7.4). (b) Data taken from literature.[134]

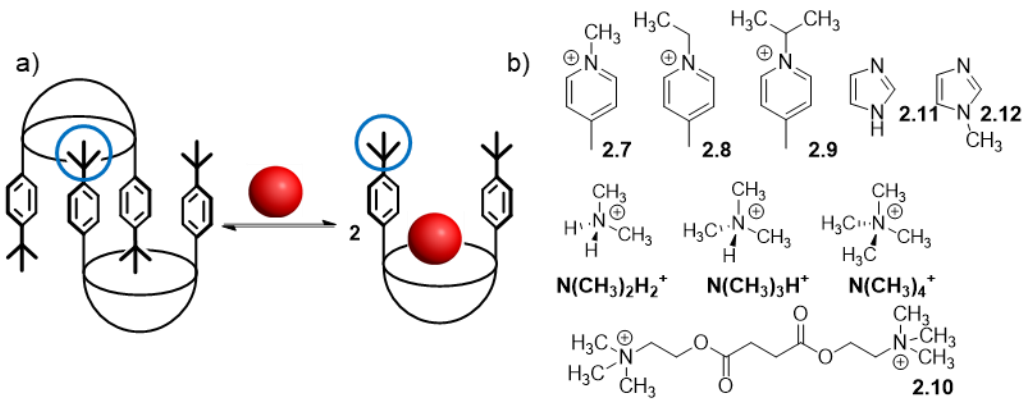

Figure 2. 4 a) Cartoon depiction of dimeric ***tBu*$_2$-SC4A** dissociating to form new host-guest complex which can be observed by the change in chemical shift of the *t*-butyl singlet (blue circle) with b) various hydrophobic cationic guests.

Table 2. 3 Guest-induced chemical shift perturbation of resonances for ***tBu*$_2$-SC4A** away from the positions observed in the pure ***tBu*$_2$-SC4A** homodimer.

Guest	Δδ of resonances from ***tBu*$_2$-SC4A** (ppm)[(a)]	
	t-butyl	*ortho*-aryl
2.7	0.71	0.18
2.8	0.79	0.24
2.9	0.80	0.26
$N(CH_3)_2H_2^+$	0.01	0.01
$N(CH_3)_3H^+$	0.39	0.24
$N(CH_3)_4^+$	0.67	0.40
2.10[(b)]	0.83	0.48
2.11	0.03	0.06
2.12	0.15	0.06

(a) All solutions are 1:1 mixtures of ***tBu*$_2$-SC4A** and guest at 1 mM in Na_2HPO_4/NaH_2PO_4 (50 mM, pD 8.5)-buffered D_2O. See Supporting Information for full titrations and spectra for selected guests. (b) This ditopic guest was studied at a ratio of 0.5:1 for **2.10**:***tBu*$_2$-SC4A** ([***tBu*$_2$-SC4A**] = 1 mM).

Upon guest addition, ^{1}H NMR proved the formation of host-guest complexes with concomitant dimer dissociation (Figure 2. 4). All resonances for these simple guest binding studies were in fast exchange. Under these conditions, the position of the chemical shift between the extremes expected for free and bound states qualitatively indicate the relative amounts of each state (Table 2. 3). The diagnostic position and shape of the *t*-butyl singlet was used to track monomer-dimer equilibrium: a strong hydrophobic guest like *N*-ethyl-4-methyl-pyridinium (**2.8**) caused the *t*-butyl singlet of ***tBu*$_2$-SC4A** to sharpen and shift

downfield (blue diamonds, Δδ +0.76 ppm) to the position expected for monomeric ***tBu*$_2$-SC4A** (Figure 2. 5). The guest's CH_3 triplet broadened and shifted upfield (red circle, Δδ –0.25 ppm). This indicated that while the dimer dissociated, the guest was encapsulated to form a host-guest complex of the type that is well known for sulfonated calix[4]arenes [50, 152]. Similar observations were made with other *N*-alkylated pyridinium guests (Figure 2. 14, Figure 2. 15 and Table 2. 3). Complete NMR titrations showing the evolving response upon addition of selected guests are shown in the Supp. Info.

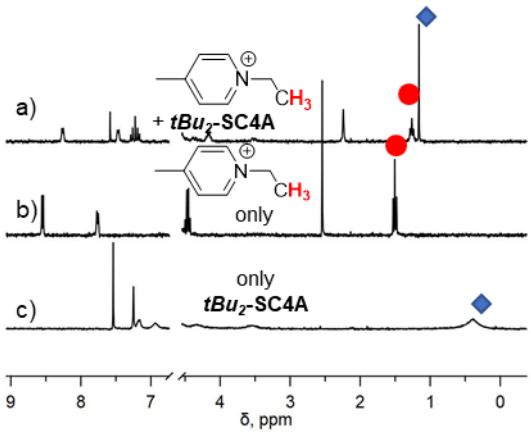

Figure 2. 5 NMR spectra demonstrate competition between ***tBu*$_2$-SC4A** homodimerization and host-guest binding. a) 1:1 (1 mM) host-guest complex formed with *N*-ethyl-4-methyl-pyridinium (**2.8**) indicated with an upfield shift of guest protons (red dot) from its b) unbound resonance and the downfield shift of ***tBu*$_2$-SC4A** (blue diamond) c) from its dimeric state. Buffer = Na_2HPO_4/NaH_2PO_4 (50 mM, pD 8.5) in D_2O.

Comparison of simple methylammonium ion guests showed that more hydrophobic guests are more effective at disrupting dimerization. The *t*-butyl singlet of ***tBu*$_2$-SC4A** travels from 0.4 ppm (Figure 2. 6c) to 0.79 ppm (2.6b) and to finally 1.06 ppm (2.6a) when treated with the same concentrations of di-, tri- and tetramethylammonium, respectively (blue diamonds). Similarly, the guest methyl resonances show upfield shifts from their free chemical shifts that are proportional to the expected strength of guest binding: 2.39 ppm (dimethylammonium), 1.88 ppm (trimethylammonium), and 1.49 ppm (tetramethylammonium). Weaker guests like imidazole (**2.11**) did not perturb the dimer at all (Figure 2. 6g, Figure 2. 16 and Table 2. 3). Yet its methylated counterpart, *N*-CH_3-imidazole (**2.12**), partially formed a complex, as supported by the methyl singlet shifting Δδ –0.37 ppm and the *t*-butyl shifting Δδ +0.2 ppm (Figure 2. 6e and Table 2. 3). A bis-(trimethylammonium) guest, suxamethonium (**2.10**), also induced dissociation of

***t*Bu$_2$-SC4A** by Δδ +0.83 and the guest protons upfield shifted and broadened by Δδ –1.44 ppm at 0.4 eq. (Figure 2. 17 and Table 2. 3)

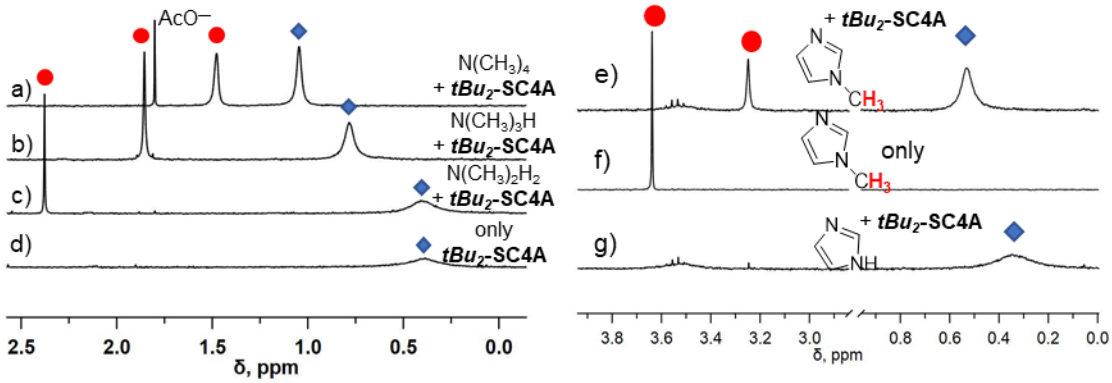

Figure 2. 6 NMR spectra show that more hydrophobic guests disrupt ***t*Bu$_2$-SC4A** homodimer more effectively. The downfield shift of ***t*Bu$_2$-SC4A** (blue diamonds) upon dimer disruption, and the upfield shift (red dot) of guests upon host-guest complex formation are apparent. a) $N(CH_3)_4^+$; b) $N(CH_3)_3H^+$; c) $N(CH_3)_2H_2^+$; d) no guest added; while e) *N*-methyl imidazole (**2.12**) shifts upfield in comparison to f) **2.12** alone and g) imidazole (**2.11**). Each spectrum contains a 1:1 (1 mM) mixture of ***t*Bu$_2$-SC4A** and guest in Na_2HPO_4/NaH_2PO_4 (50 mM, pD 8.5) in D_2O.

Lucigenin (**1.29**), a quinaldinium dye, showed unusual host-guest behaviour with ***t*Bu$_2$-SC4A** and allowed fluorescence characterization of the complexes. **1.29** is quenched upon binding sulfonated calixarenes.[106] A 1:1 mixture of **1.29** and ***t*Bu$_2$-SC4A**, each at 1 mM, yielded a perfectly flat ^{1}H NMR spectrum — all host and guest resonances are in intermediate exchange, and the solution is clear and homogeneous, suggesting the formation of an undefined soluble aggregate (Figure 2. 7b). The **1.29** emission is mostly quenched in a 1:1 solution prepared at lower concentrations that are appropriate for fluorescence measurements ([**1.29**] = [***t*Bu$_2$-SC4A**] = 1 μM), as ≤10% of the intensity of free **1.29** emission is observed in this sample. Upon changing the stoichiometry only ≥20% away from 1:1 ratio in either direction, resonances for whichever species is in excess start to appear alongside an otherwise flat NMR spectrum. This indicates that the soluble aggregate, although not structurally understood, is something that requires a 1:1 ratio of ***t*Bu$_2$-SC4A** and **1.29**. When ***t*Bu$_2$-SC4A** is in excess the resonances for homodimeric ***t*Bu$_2$-SC4A** are observed in the NMR spectrum (Figure 2. 7a). Fluorescence is completely quenched under these conditions, showing that the **1.29** is fully engaged in an aggregate with ***t*Bu$_2$-SC4A** (Figure 2. 7a). Conversely, when **1.29** is in excess, the NMR

resonances for the uncomplexed dye are observed emerging from the flat NMR spectrum that arises from the ***t*Bu$_2$-SC4A •1.29** aggregate. Partial (30%) fluorescence intensity is observed, as expected for a solution containing a small amount of free **1.29**. Upon heating the solution, we observed at 80°C by NMR the appearance of resonances of monomeric ***t*Bu$_2$-SC4A** and free **1.29**, as both the soluble aggregate and the homodimer dissociate (Figure 2. 7d).

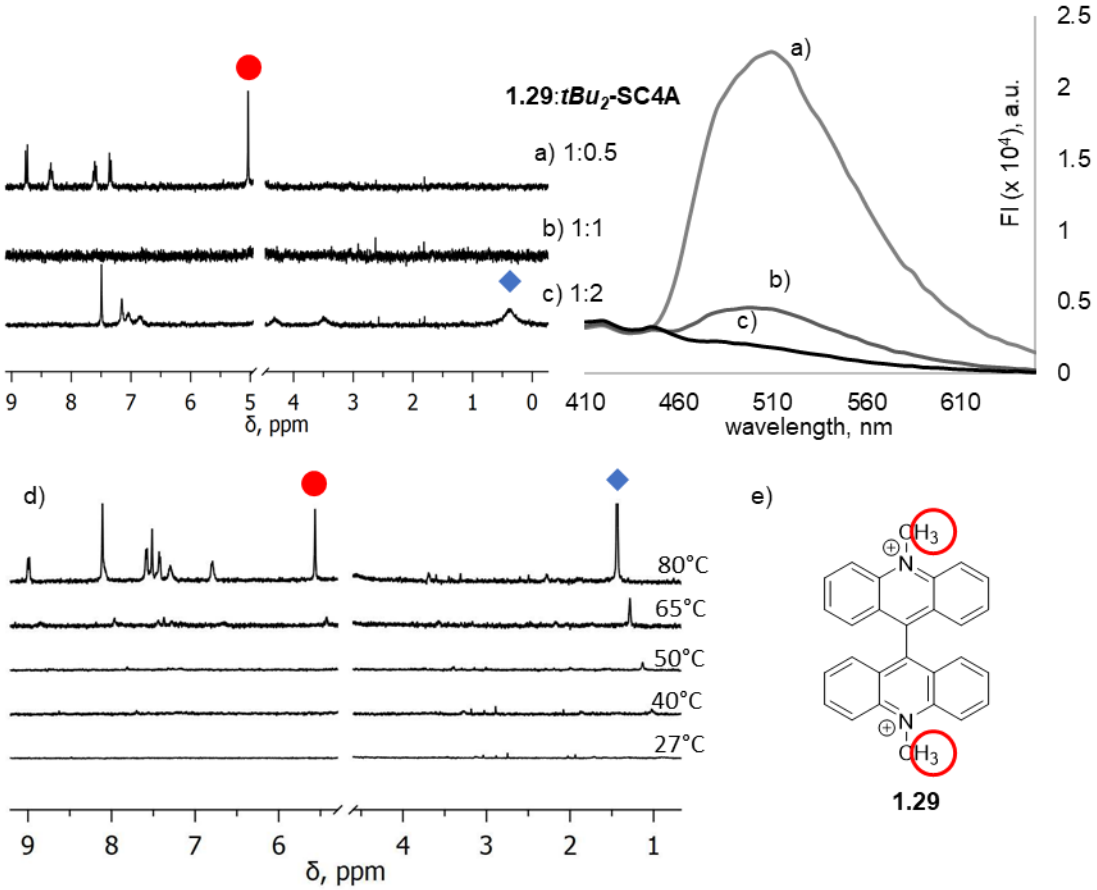

Figure 2. 7 Aggregation behaviour of **1.29** and ***t*Bu$_2$-SC4A** monitored by ^{1}H NMR and fluorescence spectroscopy. a) At **1.29**:***t*Bu$_2$-SC4A** ratio of 1:0.5 – free **1.29** resonances observed in the NMR, with significant fluorescence emission observed to arise from free **1.29**. b) At **1.29**:***t*Bu$_2$-SC4A** ratio of 1:1, no NMR resonances are observed which indicates a soluble aggregate undergoing intermediate exchange with complete line broadening. Low fluorescence emission is observed, showing that most **1.29** is bound to calixarene under these conditions. c) At **1.29**:***t*Bu$_2$-SC4A** ratio of 1:2, homodimer ***t*Bu$_2$-SC4A** is observed by NMR and no free **1.29** emission is seen by fluorescence spectroscopy. d) The flat ^{1}H spectra of the 1:1 **1.29**:***t*Bu$_2$-SC4A** complex fully dissociates at 80°C and resonances appear from the unbound dye (red dot) and monomeric ***t*Bu$_2$-SC4A** (blue diamond) in Na_2HPO_4/NaH_2PO_4 (50 mM, pH 8.5).

Data suggesting a similar hetero-aggregate behaviour was also observed for mixtures of ***t*Bu$_2$-SC4A** and Brooker's merocyanine (**2.13**) – another cationic pyridinium dye. The NMR spectrum of a 1:1 mixture of **2.13**: ***t*Bu$_2$-SC4A** was completely flat which suggested **2.13** also formed soluble aggregates with ***t*Bu$_2$-SC4A** in solution as it did with **1.29**. Although the fluorescent quenching effects were not as drastic because calixarenes do not effectively quench merocyanines to the same extent as for **1.29** (Figure 2. 8b). A 2:1 mixture of **2.13**:***t*Bu$_2$-SC4A** showed only resonances for **2.13**, as a mixture of *trans* and *cis* isomers, and no resonances from ***t*Bu$_2$-SC4A**. The fluorescence spectrum of the mixture showed a slight increase in comparison to the 1:1 (Figure 2. 8a).

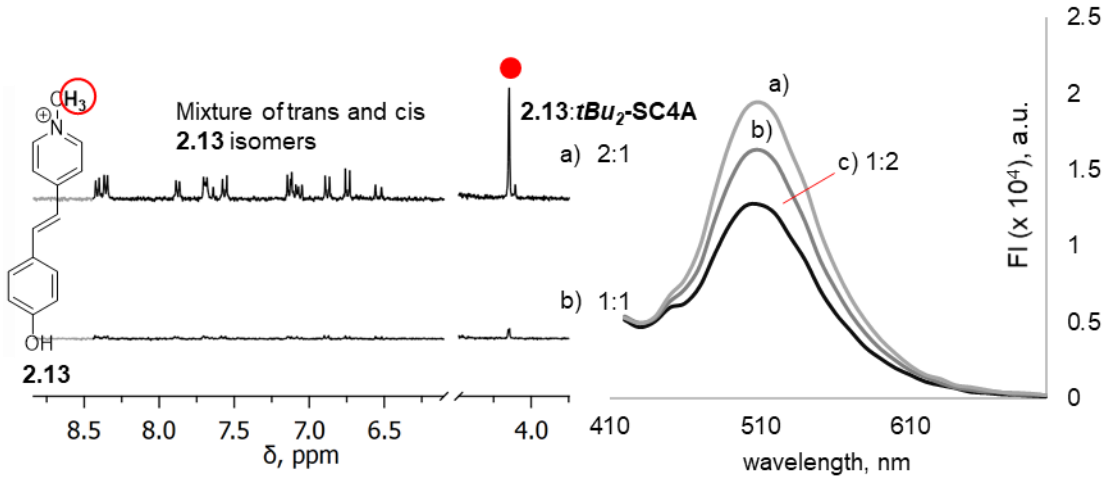

Figure 2. 8 Aggregation behaviour of **2.13** and ***t*Bu$_2$-SC4A** monitored by ^{1}H NMR and fluorescence spectroscopy. a) At **2.13**:***t*Bu$_2$-SC4A** ratio of 2:1 (2 mM:1 mM) – free **2.13** resonances observed in the NMR, as a mixture of *cis* and *trans* isomers, with strong fluorescence observed. b) At **2.13**:***t*Bu$_2$-SC4A** ratio of 1:1 ([***t*Bu$_2$-SC4A**] = [**2.13**] = 1 mM), no NMR resonances are observed which indicates a soluble aggregate undergoing intermediate exchange with complete line broadening. The fluorescence intensity decreases slightly. [**2.13**] = 10 μM, ($\lambda_{ex.}$ 382 nm, $\lambda_{em.}$ 420 – 700 nm) in Na_2HPO_4/NaH_2PO_4 (10 mM, pH 8.5) buffered H_2O for fluorescence experiments and in Na_2HPO_4/NaH_2PO_4 (50 mM, pH 8.5) buffered D_2O for the NMR experiments.

2.4 Conclusions

We synthesized a new calix[4]arene clip, ***t*Bu$_2$-SC4A**, characterized its homodimeric self-assembly in buffered water, and studied the effects of competing guests. The addition of a second *t*-butylphenyl pendant group was tolerated. The expected dimerization occurred and was stronger than its analogue ***t*Bu$_1$-SC4A**. The dimer was also

responsive to various guests and in particular hydrophobic cations. The synthesis of difunctionalized ***tBu*$_2$-SC4A** involves a Suzuki coupling that could be applied to several other binding arms in order to expand on these new topologies that undergo self-assembly [133]. Multiple research groups have used trisulfonated calixarenes with a single upper-rim functionalization to modulate guest binding, and/or to impart many different functionalities to the host structure [91, 147, 153-156]. This work opens the door to a wide variety of clip-like hosts that combine self-assembly and guest responsiveness in competitive aqueous solutions.

2.5 Supplementary Information

2.5.1 General information and materials

^{1}H, ^{13}C, 1D DOSY and variable temperature-NMR experiments were recorded on a Bruker Avance 500 MHz spectrometer unless otherwise indicated and processed with MestReNova by Mestrelab Research S.L. All reported chemical shifts were reported in ppm with respect to an internal standard: *cis*-butenedioic acid at 6.2 ppm. Deuterated solvents were purchased from Sigma Aldrich and NaH_2PO_4/Na_2HPO_4 (50 mM, pD 8.5) in D_2O were prepared in lab and the pD was adjusted with 5% NaOD/DCl solutions. Isothermal calorimetery experiments were conducted at 303 K in buffered water on a MicroCal VP-ITC and fitted to include heat of dilution outlined below. Mass spectra of novel compounds were collected on a Thermo Scientific Ultimate 3000 ESI-Orbitrap Exactive. All UV-Vis and fluorescence spectra were collected on a Molecular Device Spectra M5 spectrometer in NUNC 96-well black walled plate. Infrared (IR) spectra were obtained using a Perkin Elmer 1000 FT-IR spectrometer. Data are represented as follows: frequency of absorption (cm^{-1}), intensity of absorption (s = strong, m = medium, w =weak, br = broad). Melting points were collected on a Gallenkamp Melting Point apparatus. Compound ***tBu*$_2$-SC4A** was purified using a Shimadzu Prominence HPLC system on a 9.4 mm x 250 mm semi-preparative Agilent Eclipse XDB-C18 5 μm with UV detection at 280 nm.

2.5.2 Synthesis of novel compounds

5,17-dibromo-26,28-dibenzoyloxy-calix[4]arene (2.3). Compound **2.2** (0.9 g, 1.5 mmol) was dissolved in $CHCl_3$ (30 mL) and Br_2 (0.8 mL, 15 mmol) was added. The mixture was stirred at room temperature for 4 h. The mixture was then diluted with CH_2Cl_2, the organic layer was washed with $Na_2S_2O_3$ (5 g/100mL) aqueous solution, followed by water, brine and dried over Na_2SO_4. The solution was decanted, reduced under pressure to a pure yellow solid (0.99 g, 83%). Mp: decomposed > 230 °C. FT-IR (cm^{-1}): 3537 (br.), 1733 (m), 1706 (m), 1451 (m), 1265 (s), 1173 (s), 1023 (m), 1056 (m), 861 (w), 754 (m), 709 (s). ^{1}H NMR (300 MHz, $CDCl_3$): δ 8.24 (dd, *J* = 8.5 Hz, 1.5 Hz, 4H), 7.77 (tt, *J* = 7.4 Hz 1.4 Hz, 2H), 7.62 (t, 7.9 Hz, 4H), 7.11 (s, 4H), (m, 6H), 5.22 (s, 2H), 3.85 (d, *J* = 14.6 Hz, 4H), 3.53 (d, *J* = 14.6 Hz, 4H). ^{13}C NMR (125 MHz, $CDCl_3$): δ 164.6, 152.0, 146.1, 134.0, 132.0, 131.7, 130.5, 129.8, 129.7, 129.3, 126.8, 111.8, 33.1. HR-ESI-MS ($[M-H]^-$, *m/z*): Calculated for $C_{42}H_{29}Br_2O_6^-$ 787.03364, Found 787.03363

5,17-dibromo-25,26,27,28-tetrahydroxy-calix[4]arene (2.4). Compound **2.3** (1 g, 1.25 mmol) was dissolved in MeOH (50 mL) and NaOH (1 g, 18 mmol) was added. The mixture was heated to reflux for 4 h. The product was precipitated out of solution by the addition of 1 M HCl. The solid was vacuum filtered and washed with hexanes to afford a light yellow solid (530 mg, 72%). Mp: decomposed > 230 °C. FT-IR (cm^{-1}): 3141 (br), 1448 (s), 1209 (s), 856 (w), 828 (w), 750 (s), 665 (m) 514 (m). ^{1}H NMR (500 MHz, $CDCl_3$): δ 10.06 (s, 4H), 7.17 (s, 4H), 7.08 (d, *J* = 7 Hz, 4H), 6.80 (t, *J* = 6.8 Hz, 2H), 4.20 (br. s, 4H), 3.52 (br. s., 4H). ^{13}C (125 MHz, $CDCl_3$): δ 148.8, 147.9, 131.6, 130.2, 129.3, 127.5, 122.52, 114.0, 31.5. HR-ESI-MS ($[M-H]^-$, *m/z*): Calculated for $C_{28}H_{21}Br_2O_4^-$ 578.98121, Found 578.98106.

5,17-dibromo-25,26,27,28-tetrahydroxy-11,23-disulfonatocalix[4]arene (2.5). Compound **2.4** (50 mg, 86 μmol) was dissolved in CH_2Cl_2 (2 mL) followed with conc. H_2SO_4 (100 μL). The reaction was heated to reflux for 24 h to afford a residue. The CH_2Cl_2 was decanted, and the residue was rinsed with fresh CH_2Cl_2. The solid was suspended in EtOAc, transferred into a conical tube and diluted with cold Et_2O. The suspension was centrifuged to a pellet, the supernatant was decanted and the resuspension/centrifugation/decanting process was repeated three times. The pellet was left

to air dry overnight to afford a gray solid (51 mg, 81%). Mp: decomposed > 178 °C. IR (KBr disc) (cm^{-1}): 2408 (br), 3221 (br), 2961 (w), 1651 (m), 1204 (m), 1163 (m), 1036 (m), 625 (m). ^{1}H NMR (500 MHz, d_6-DMSO): δ 9.62 (br. s, 7H), 7.43 (s, 4H), 7.28 (s, 4H), 3.89 (br. s, 8H). ^{13}C NMR (125 MHz, d_6-DMSO): δ 151.6, 149.8, 140.0, 131.5, 131.3, 127.6, 127.0, 112.3, 41.0, 30.6. HR-ESI-MS ($[M-2H]^{2-}$, *m/z*): Calculated for $C_{28}H_{20}Br_2O_{10}S_2^{2-}$ 368.94378, Found 368.94376.

5,17-di(4-*t*-butylphenyl)-25,26,27,28-tetrahydroxy-11,23-disulfonatocalix[4]arene (*tBu*$_2$-SC4A). Compound **2.5** (50 mg, 67 μmol), tert-butyl-phenylboronic acid (20 mg, 148 μmol), K_2CO_3 (74 mg, 0.51 mmol) and $Pd(OAc)_2$ (5 mg, 22 μmol) were dissolved in a microwave vial with 3 mL of 1:1 EtOH:deionized water. The reaction was irradiated to a temperature of 150 °C for 5 min with cooling air and stirring on (Biotage Initiator Microwave Reactor). After, thiourea (1 M, 0.5 mL) was added and the reaction stirred at 90°C for 1 h. The solution was filtered through a PDVF syringe filer (0.45 um), and concentrated until solution became cloudy. The slurry was re-dissolved with small amounts of CH_3CN and purified by HPLC purification with a gradient running from 90% H_2O (+ 0.1% TFA)/10% CH_3CN (+ 0.1% TFA) to 40% H_2O (+ 0.1% TFA)/60% CH_3CN (+ 0.1% TFA) over 18 min. Lyophilization of collected fractions afforded a white powder in 40% yield (0.022 g). Mp: decomposed > 190 °C. FT-IR (cm^{-1}): 3398 (br), 2962 (m), 2874 (w), 1456 (m), 1268 (m), 1153 (m), 1038 (s), 832 (m), 750 (s), 629 (s), 542 (s). ^{1}H NMR (500 MHz, CD_3OD): δ 7.69 (s, 4H), 7.44 (s, *J* = 7.4 Hz, 4H), 7.41 (s, 4H), 7.39 (d, *J* = 7.4 Hz, 4H), 4.07 (br. s, 8H), 1.31 (s, 18H). ^{13}C NMR (125 MHz, d_6-DMSO): δ 151.0, 149.52, 149.50, 140.2, 137.5, 133.7, 129.2, 128.3, 127.5, 126.9, 126.4, 125.9, 34.6, 31.6, 31.1. HR-MS ($[M-2H]^{2-}$, *m/z*): Calculated for $C_{48}H_{46}O_{10}S_2^{2-}$423.12717, Found 423.12712.

2.5.3 ^{1}H and ^{13}C spectra of novel compounds

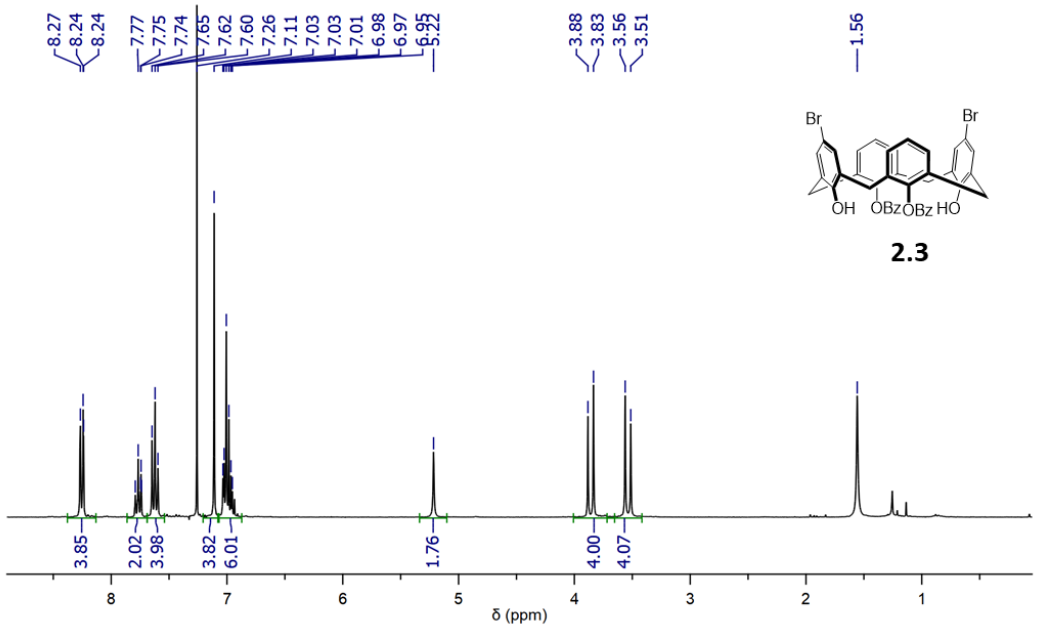

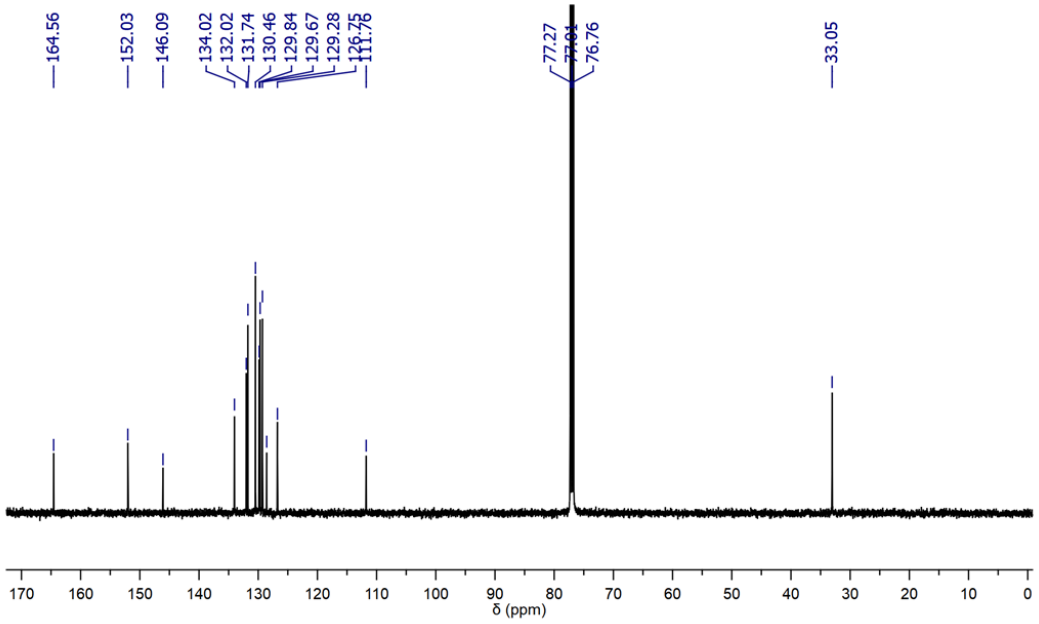

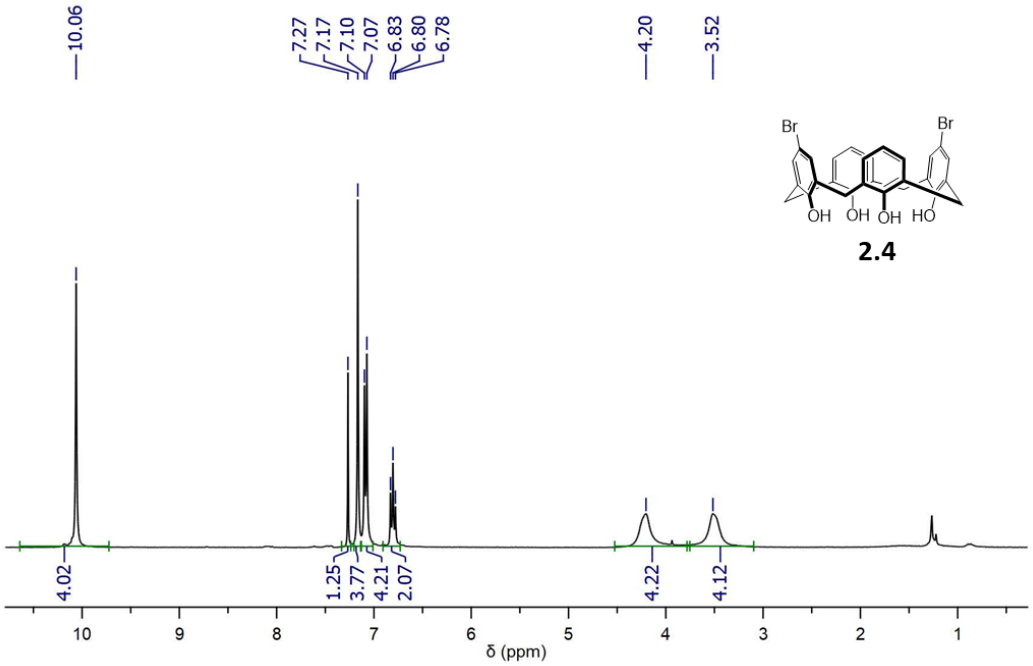
10.06
7.27
7.17
7.10
7.07
6.83
6.80
6.78
4.20
3.52
Br
Br
OH
OH
OH
HO
4.02
1.25
3.77
4.21
2.07
4.22
4.12
10
9
8
7
6
5
4
3
2
1
δ (ppm)

2.4

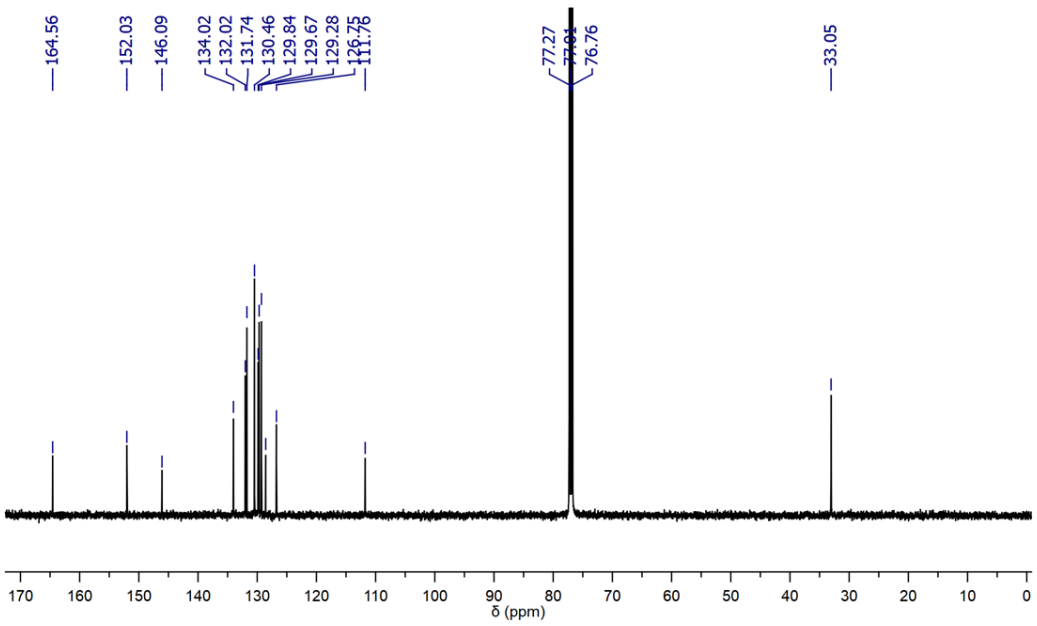
164.56
152.03
146.09
134.02
132.02
131.74
130.46
129.84
129.67
129.28
126.75
111.78
77.27
77.01
76.76
33.05
170
160
150
140
130
120
110
100
90
80
70
60
50
40
30
20
10
0
δ (ppm)

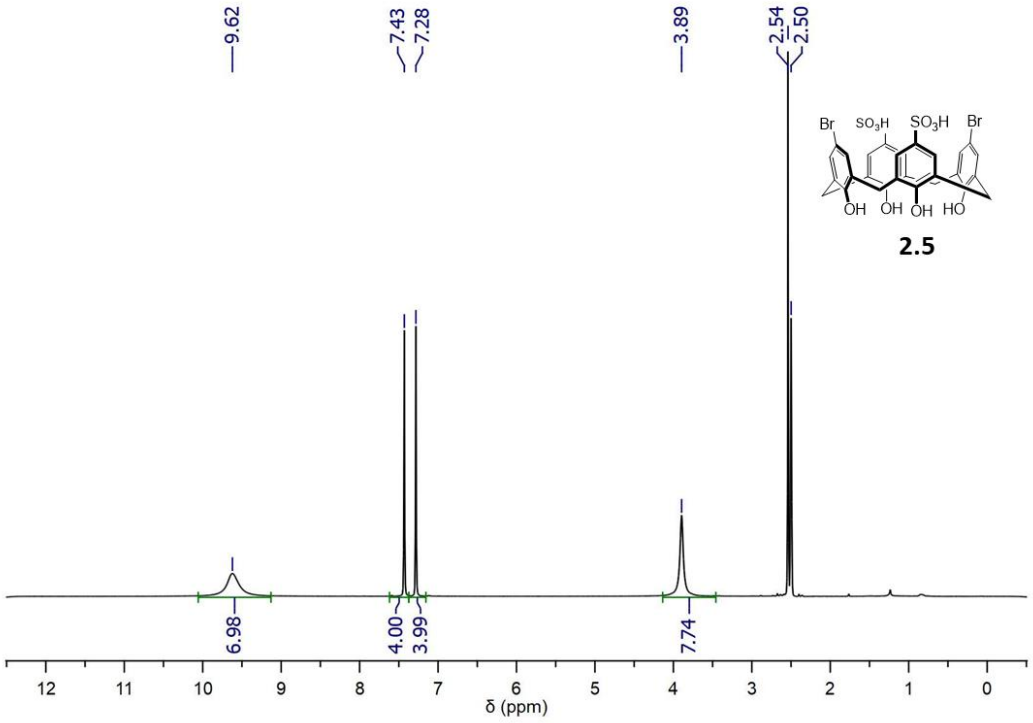
9.62
7.43
7.28
3.89
2.54
2.50
Br
SO3H
SO3H
Br
OH
OH
OH
HO
2.5
6.98
4.00
3.99
7.74
δ (ppm)

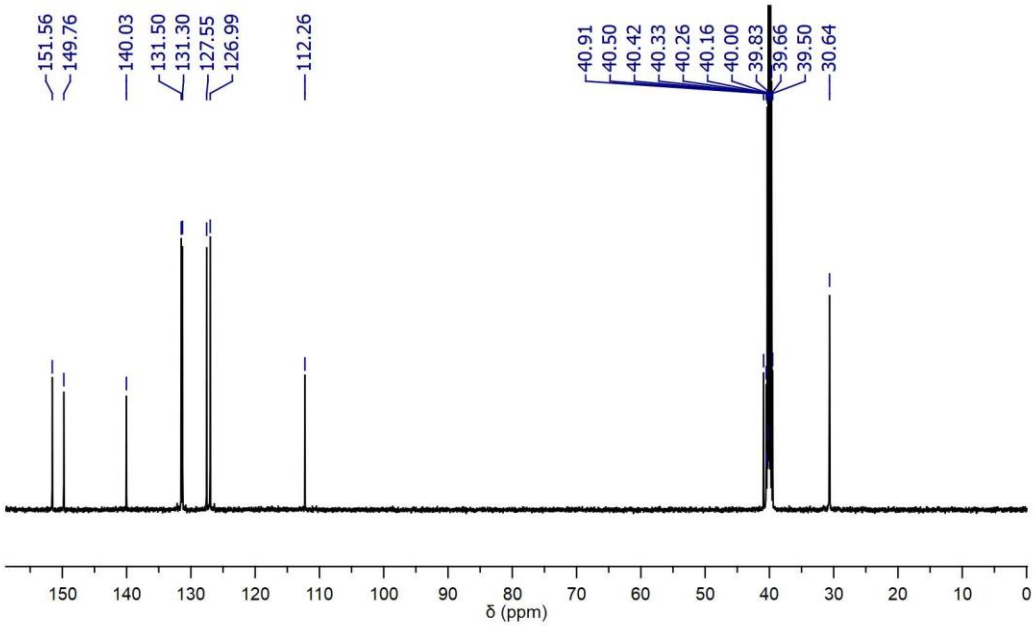
151.56
149.76
140.03
131.50
131.30
127.55
126.99
112.26
40.91
40.50
40.42
40.33
40.26
40.16
40.00
39.83
39.66
39.50
30.64
δ (ppm)

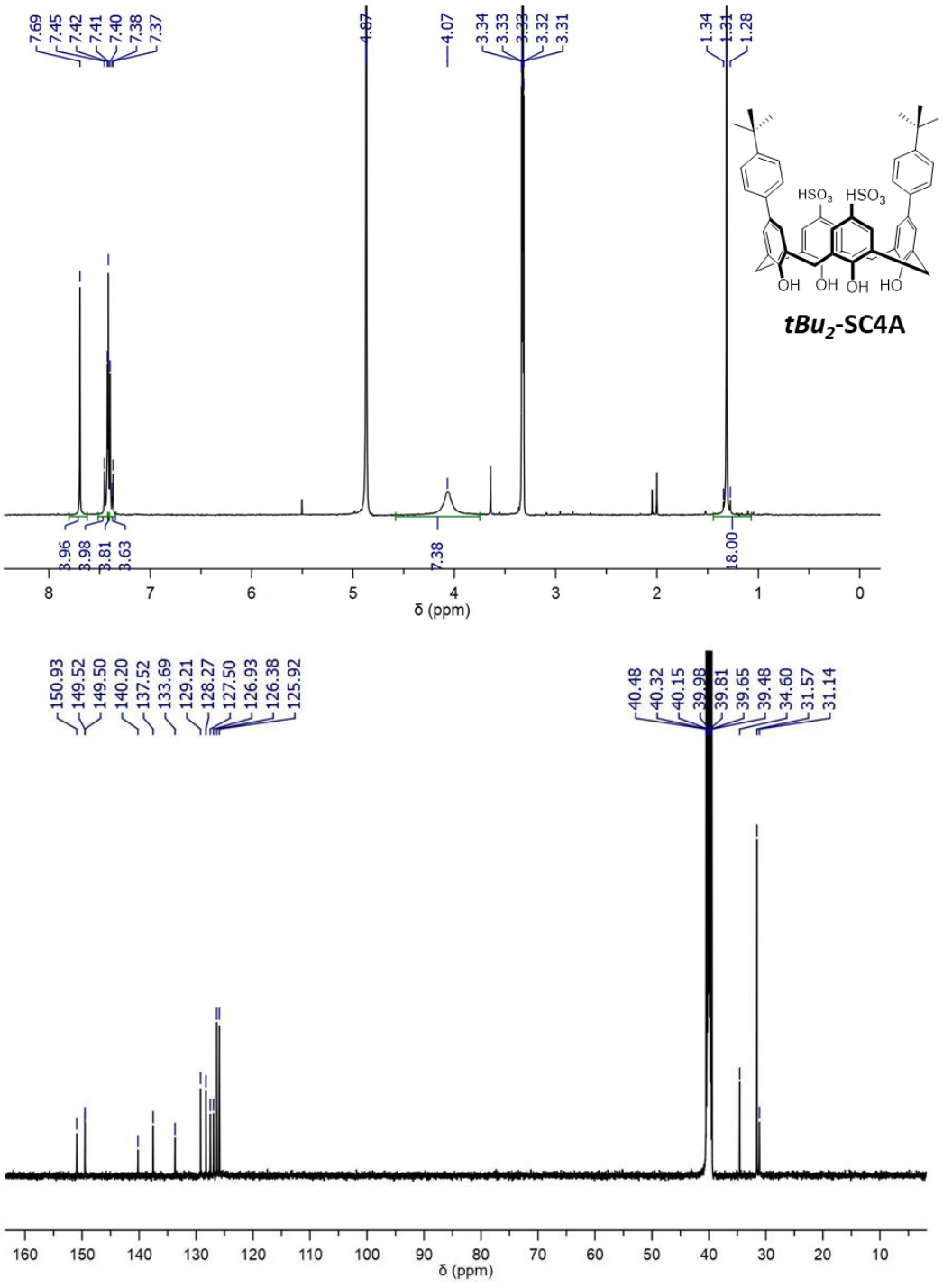
7.69
7.45
7.42
7.41
7.40
7.38
7.37
4.87
4.07
3.34
3.33
3.33
3.32
3.31
1.34
1.31
1.28
HSO3 HSO3
OH OH OH HO
tBu2-SC4A
3.96
3.98
3.81
3.63
7.38
18.00
δ (ppm)
150.93
149.52
149.50
140.20
137.52
133.69
129.21
128.27
127.50
126.93
126.38
125.92
40.48
40.32
40.15
39.98
39.81
39.65
39.48
34.60
31.57
31.14
δ (ppm)

2.5.4 ITC characterisation of *tBu*$_2$-SC4A

$$NDH = (Qd) + (dH) \times \left(\frac{(-\sqrt{K} + \sqrt{K + (8 \times (syringe\_C\_\%Q)^2)}}{16} \times (0.001 \times injv) \right) - dH \times \left(\frac{\left((-\sqrt{K} + \sqrt{K + (8 \times xt)}\right)^2}{16} \times \left((ITC\_CELL\_VOL) + \left(\frac{0.001 \times injv}{2} \right) \right) \right)$$

The modified dimer dissociation equation used with a second heat term (highlighted yellow) to account for the heat of dilution, (Qd). Normalized heat change for injection (NDH), heat resulting from injections (dH), syringe concentration (syringe_C_%Q), volume injected (injv), concentrations of injected solute in sample cell (xt), the sample cell volume (ITC_CELL_VOL).

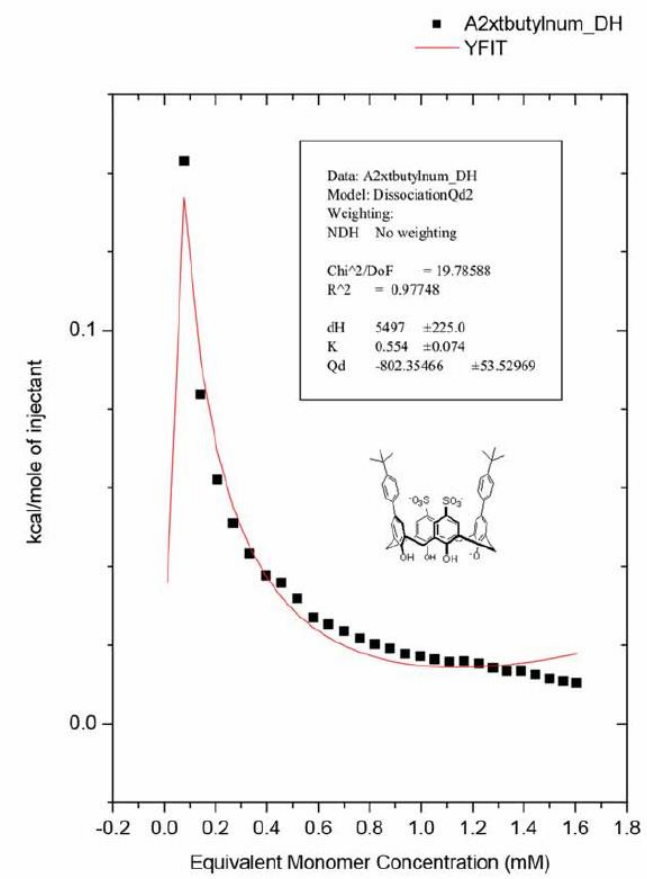

Figure 2. 9 ITC dilutions of ***tBu*$_2$-SC4A** fitted with the above dimer dissociation model.

2.5.5 General protocol for all 1D DOSY in thesis

For each DOSY experiment, the 90° pulse is determined by measuring the pulse length (P1) at 360° by a zg pulse sequence and divided by four. The longitudinal relaxation (T1) was estimated through an inversion recovery (t1ir1d) pulse sequence. The relaxation delay time (D1) for each experiment was set to be 10-times the estimated T1. For each experiment, the big delta, Δ, was set to 50 or 100 ms. The small delta, δ, was determined by finding a 90-95% intensity difference between the first and last spectra in the power array via a stebpgp1s1d pulse program. The pulse sequences used for 1D DOSY was stebpgp1s. After pre-processing through TopSpin, the area under the peaks of interest was selected and plotted as a function of the field gradient (G). These points were fitted to the below equation to extract the diffusion coefficient, (D).

$$I = I(0)exp^{(-\gamma^2 G^2 \delta^2 \left(\Delta - \frac{\delta}{3}\right) D)}$$

The average diffusion coefficient was calculated along with an uncertainty. The hydrodynamic radius (r_H) is calculated using the Stokes-Einstein equation (shown below) along with an uncertainty. The Stokes-Einstein equation assumes the particle is a sphere which are assumptions in these cases. k_B is the Boltzmann constant, temperature (T) is 297 K ± 1 K and viscosity (η) of water at 297 K is $8.94 \times 10^{-4} \pm 2.78 \times 10^{-5}$ Pa·s or the viscosity of 20% methanol in water at 297 K is $1.39 \times 10^{-3} \pm 2.78 \times 10^{-5}$ Pa·s either are used when appropriate throughout the thesis.[157]

$$r_H = \frac{k_B T}{6\pi\eta D}$$

2.5.5a 1D DOSY analysis for *t*Bu$_2$-SC4A (monomer and dimer)

Solution prep: **SC4A** and ***tBu*$_2$-SC4A** were mixed together (1 mM ea.) in 20% CD_3OD in Na_2HPO_4/NaH_2PO_4 (50 mM, pD 8.5) buffer to ensure the diffusion coefficients obtained for both hosts came from the same sample conditions.

Table 2. 4 Parameters used for diffusion analysis of ***t*Bu$_2$-SC4A** (monomer) and **PSC**

Parameters used for diffusion analysis	
used γ:	26752 rad/(s*Gauss)
used δ:	0.0062000 s
used Δ:	0.049950 s
used gradient strength:	variable
Random error estimation of data:	RMS per spectrum (or trace/plane)
Systematic error estimation of data:	worst case per peak scenario
Fit parameter Error estimation method:	from fit using arbitrary uncertainties
Confidence level:	95%
Used peaks:	automatically picked peaks
Used integrals:	area integral
Used Gradient strength:	all values (including replicates) used

Table 2. 5 Diffusion coefficients calculated from indicated resonances in ***tBu*$_2$-SC4A** and **PSC** from 1D DOSY in 20% methanol in water.

Peak name	F2 [ppm]	D [m^2/s]	error
1 (***tBu*$_2$-SC4A**)	7.552	1.92×10^{-10}	1.189×10^{-12}
2 (**PSC**)	7.513	2.20×10^{-10}	1.118×10^{-12}
3 (***tBu*$_2$-SC4A**)	7.409	1.91×10^{-10}	1.912×10^{-12}
7 (***tBu*$_2$-SC4A**)	7.329	1.92×10^{-10}	1.349×10^{-12}
11 (***tBu*$_2$-SC4A**)	1.089	1.92×10^{-10}	7.697×10^{-13}

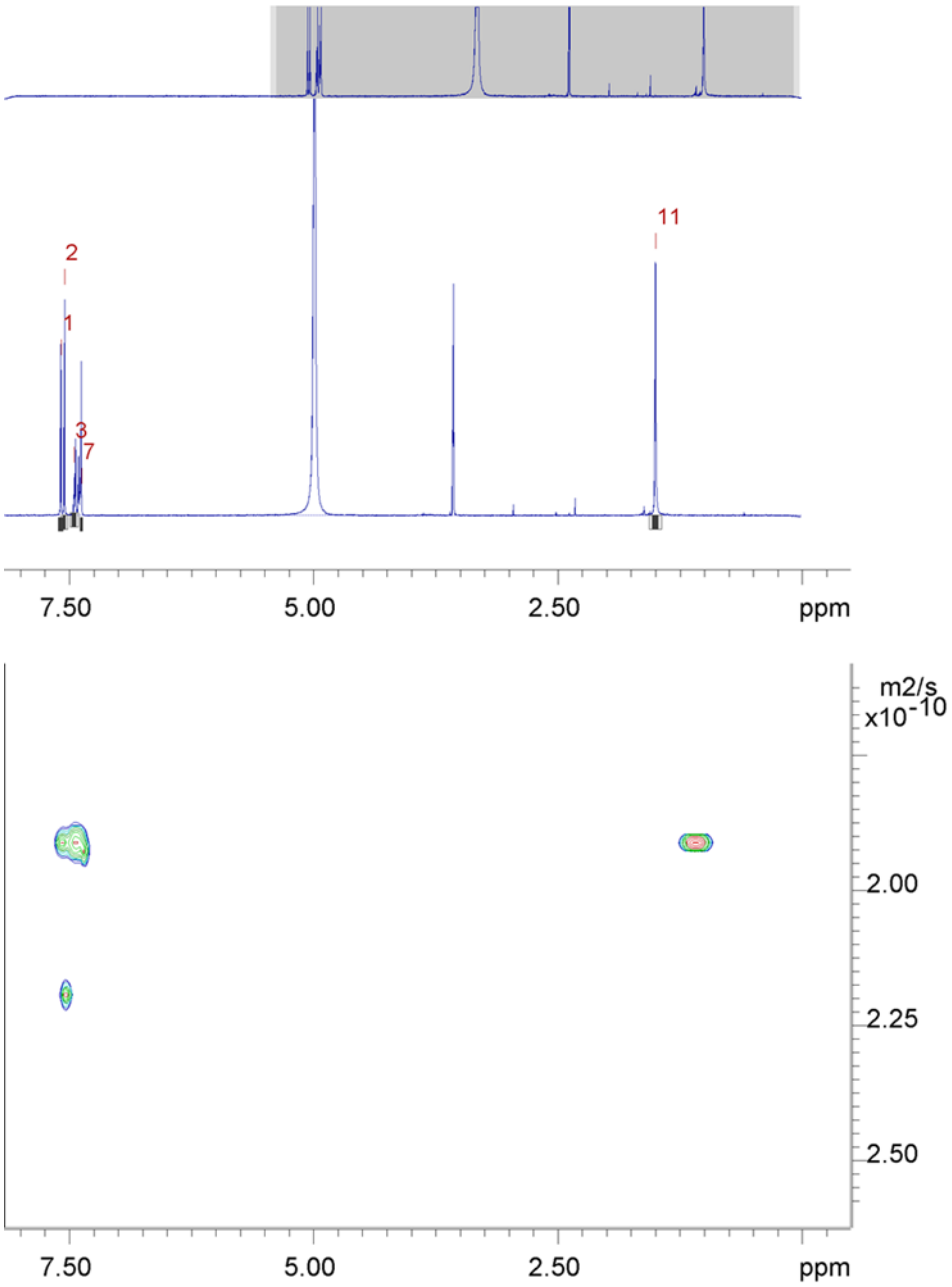

Figure 2. 10 ^{1}H NMR of ***t*Bu$_2$-SC4A** (monomer) and **PSC** mixture with integrals highlighted (gray boxes) used to calculate diffusion coefficients for each resonance along with the corresponding 2D DOSY spectrum.

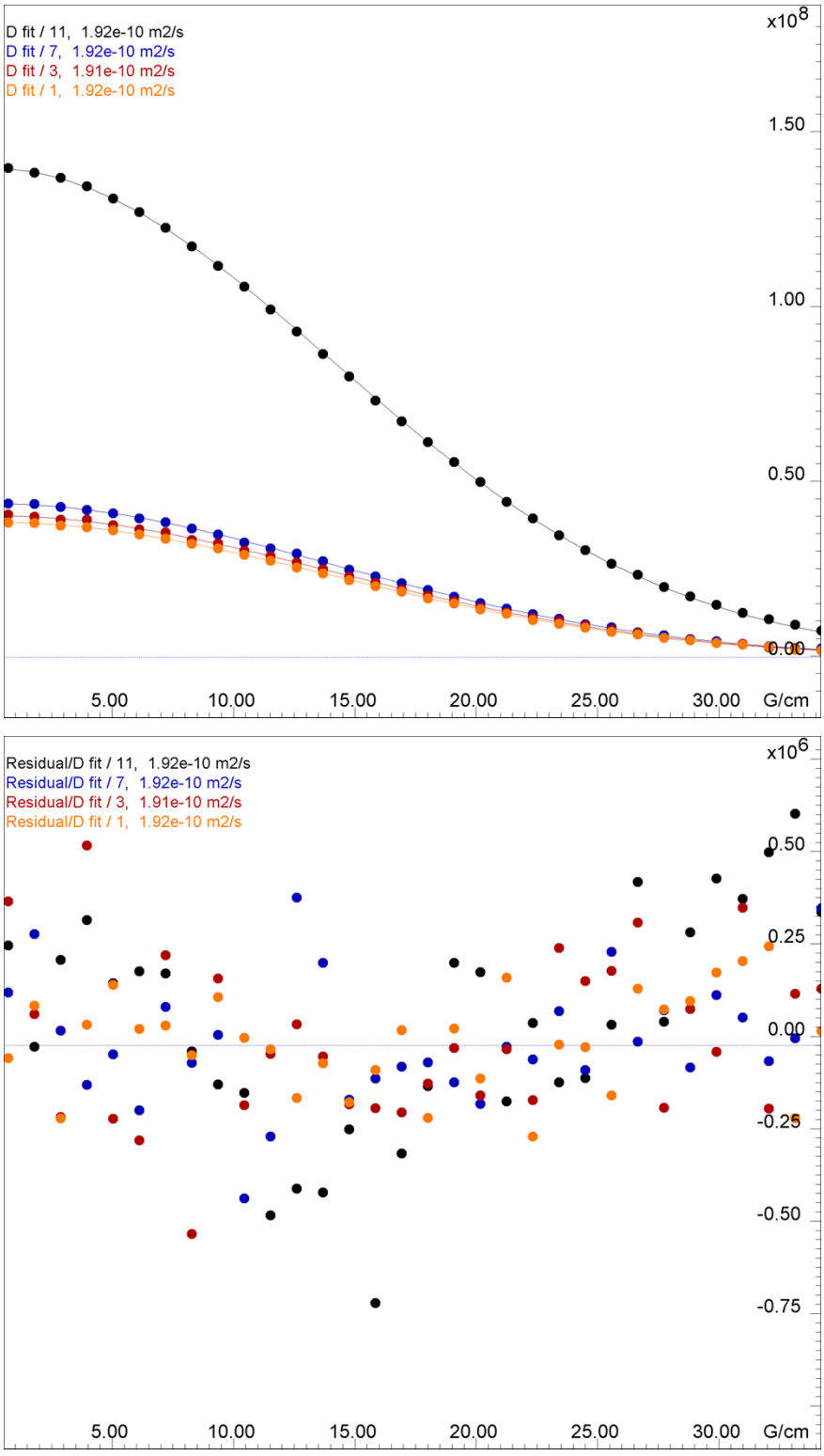

Figure 2. 11 1D DOSY plots of each integral from ***t*Bu$_2$-SC4A** (monomer) and **PSC** mixture along with corresponding residuals.

Table 2. 6 Parameters used for diffusion analysis of ***t*Bu$_2$-SC4A** (dimer)

Parameters used for diffusion analysis	
used γ:	26752 rad/(s*Gauss)
used δ:	0.0054000 s
used Δ:	0.049950 s
used gradient strength:	variable
Random error estimation of data:	RMS per spectrum (or trace/plane)
Systematic error estimation of data:	worst case per peak scenario
Fit parameter Error estimation method:	from fit using arbitrary uncertainties
Confidence level:	95%
Used peaks:	automatically picked peaks
Used integrals:	area integral
Used Gradient strength:	all values (including replicates) used

Table 2. 7 Diffusion coefficients calculated from indicated resonances in ***tBu*$_2$-SC4A** (dimer) in buffered water.

Peak name	F2 [ppm]	D [m^2/s]	error
1	7.651	2.19×10^{-10}	3.235×10^{-12}
4	7.346	2.16×10^{-10}	3.618×10^{-12}

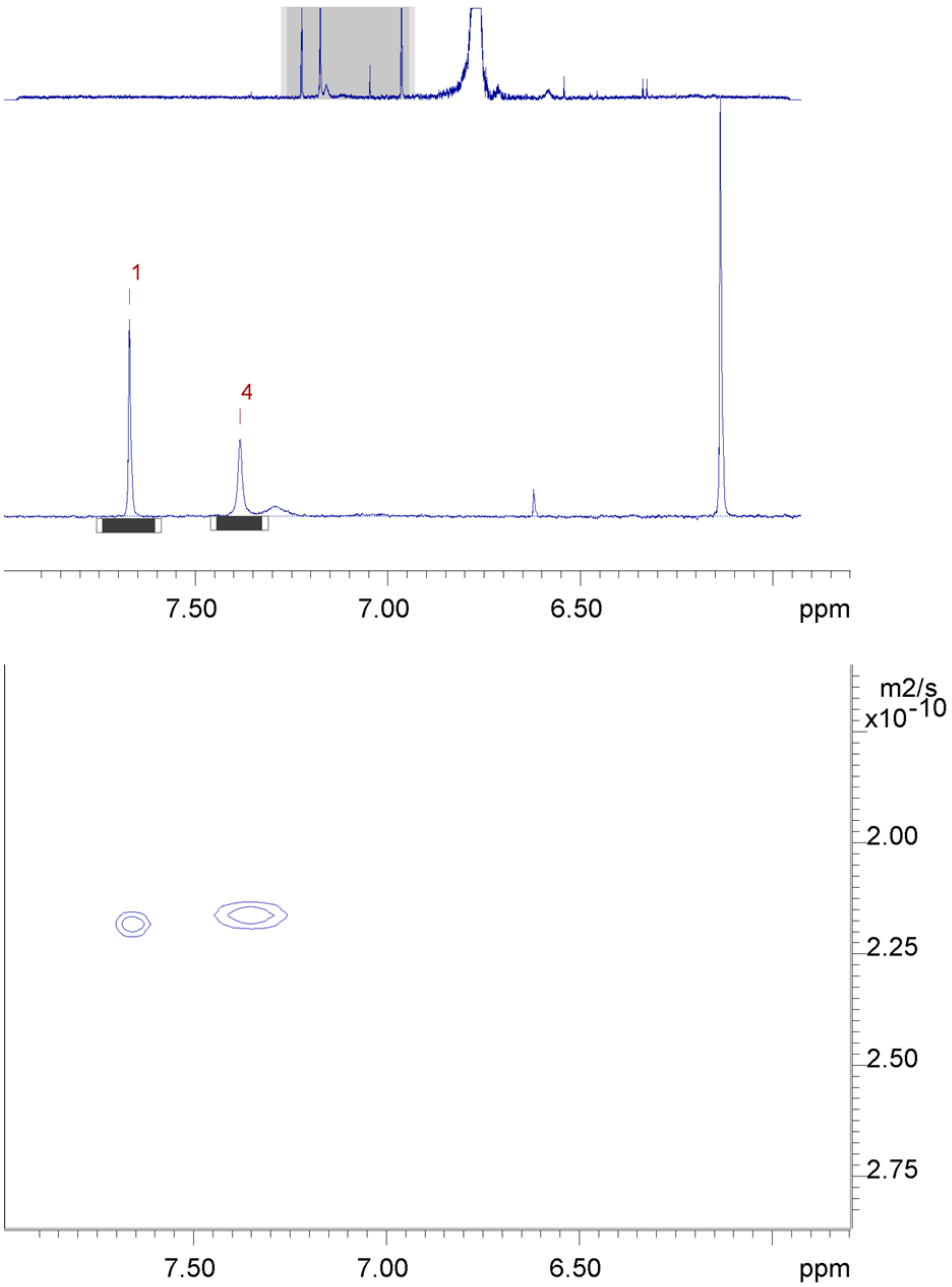

Figure 2. 12 ^{1}H NMR of ***t*Bu$_2$-SC4A** (dimer) with integrals highlighted (gray boxes) used to calculate diffusion coefficients for each resonance along with the corresponding 2D DOSY spectrum.

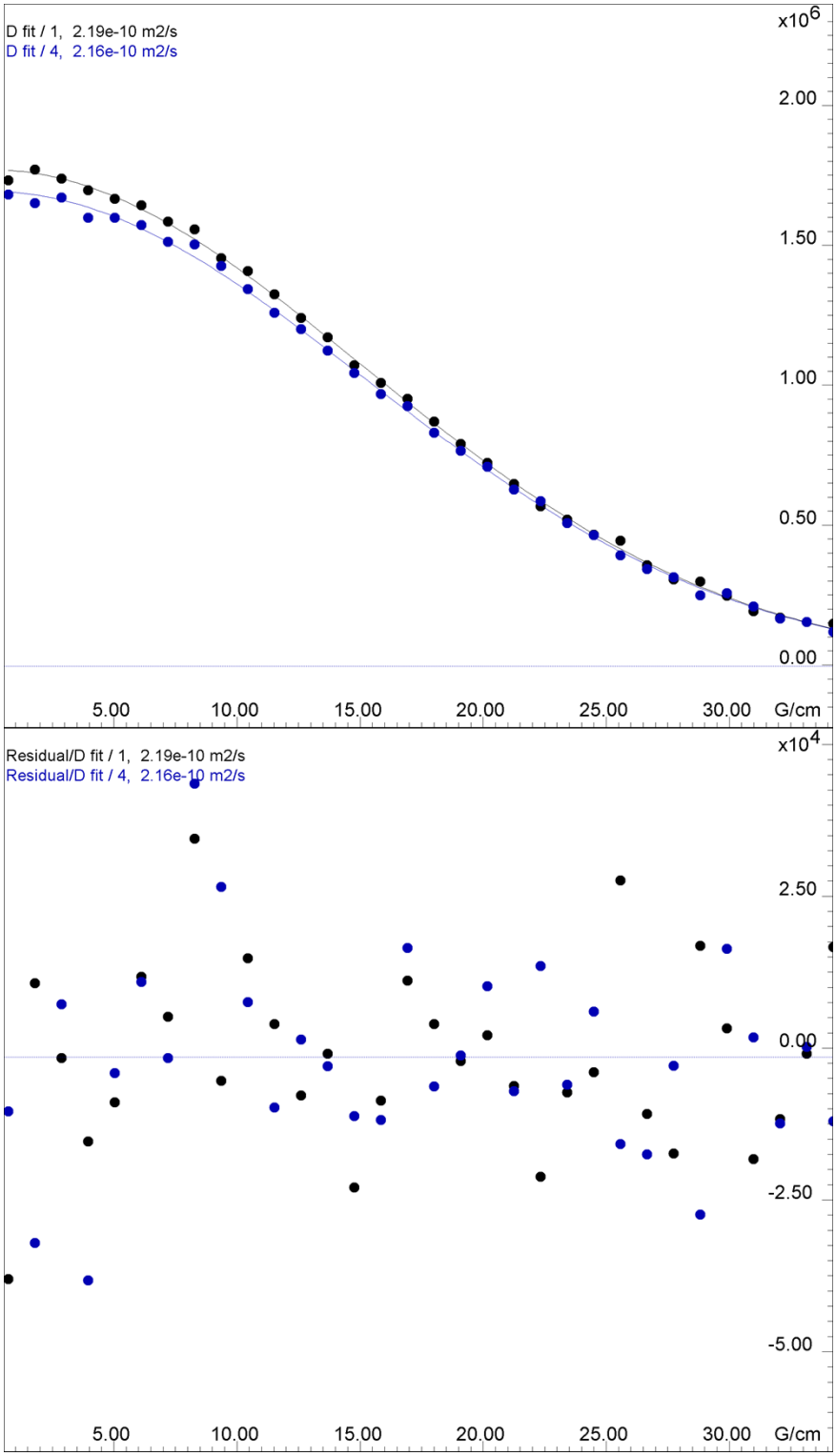

Figure 2. 13 1D DOSY plots of each integral from ***t*Bu$_2$-SC4A** (monomer) and **PSC** mixture along with corresponding residuals.

2.5.6 ^{1}H NMR titrations of guests with *tBu*$_2$-SC4A

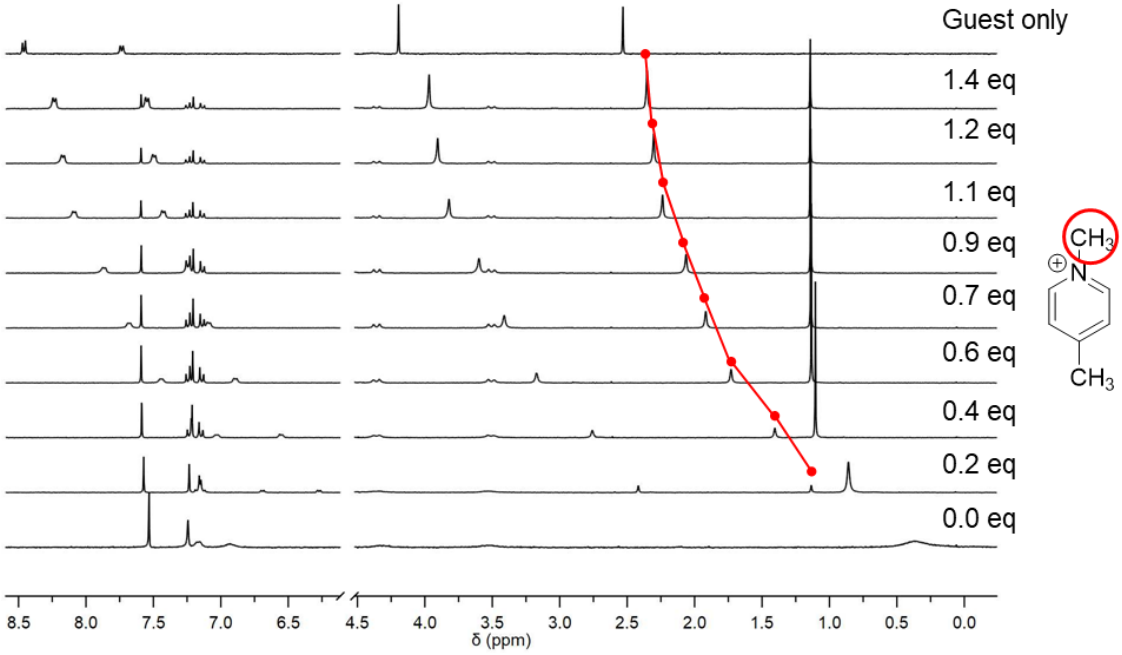

Figure 2. 14 ^{1}H titrations of *N*-methyl-4-methyl-pyridinium (**2.7**) (20 mM) into ***tBu*$_2$-SC4A** (1 mM) shows fast exchange resonances of the methyl singlet (red) travel from encapsulated and upfield towards to unbound state, downfield.

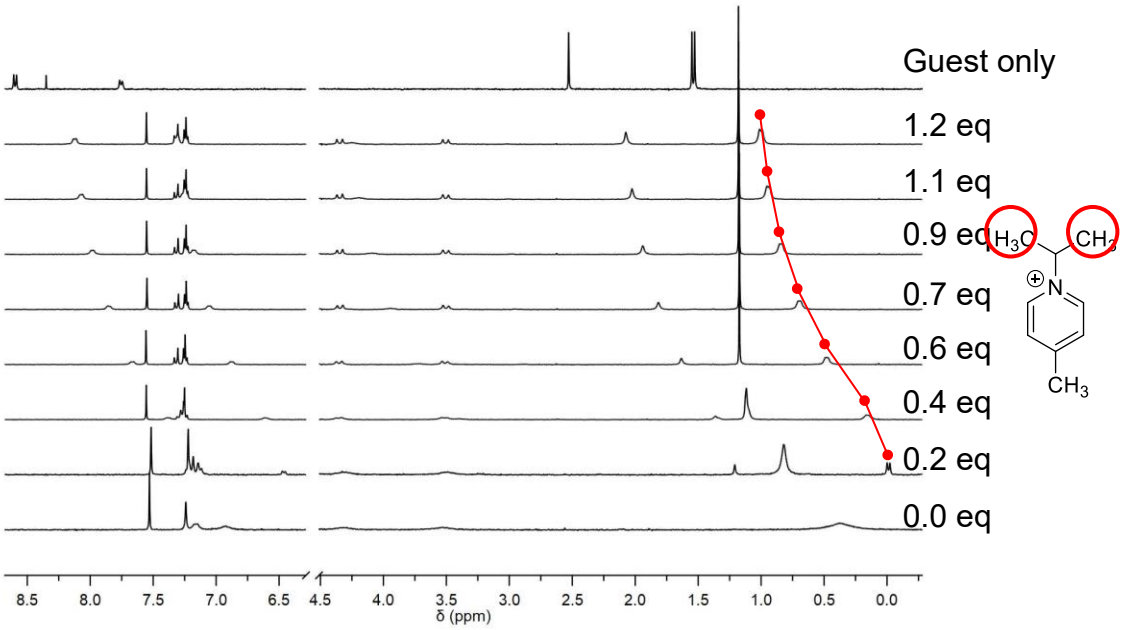

Figure 2. 15 ^{1}H titrations of *iso*-propyl-4-methyl-pyridinium (**2.9**) (20 mM) into ***t*Bu$_2$-SC4A** (1 mM) shows the fast exchange resonances of the *iso*-propyl doublet (red) travel from encapsulated and upfield towards to unbound state, downfield.

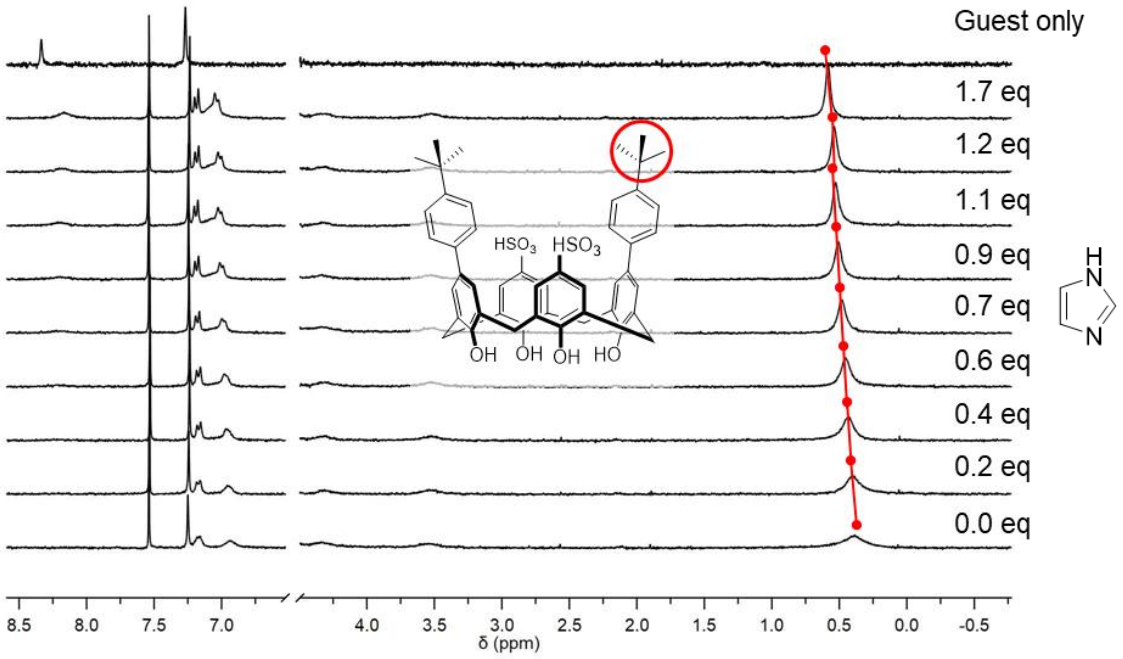

Figure 2. 16 ^{1}H titrations of imidazole (**2.11**) (20 mM) into ***t*Bu$_2$-SC4A** (1 mM) shows slight change in chemical shift of the *t*-butyl singlet (red) even with excess hence imidazole is not a strong guest to dissociate the dimer.

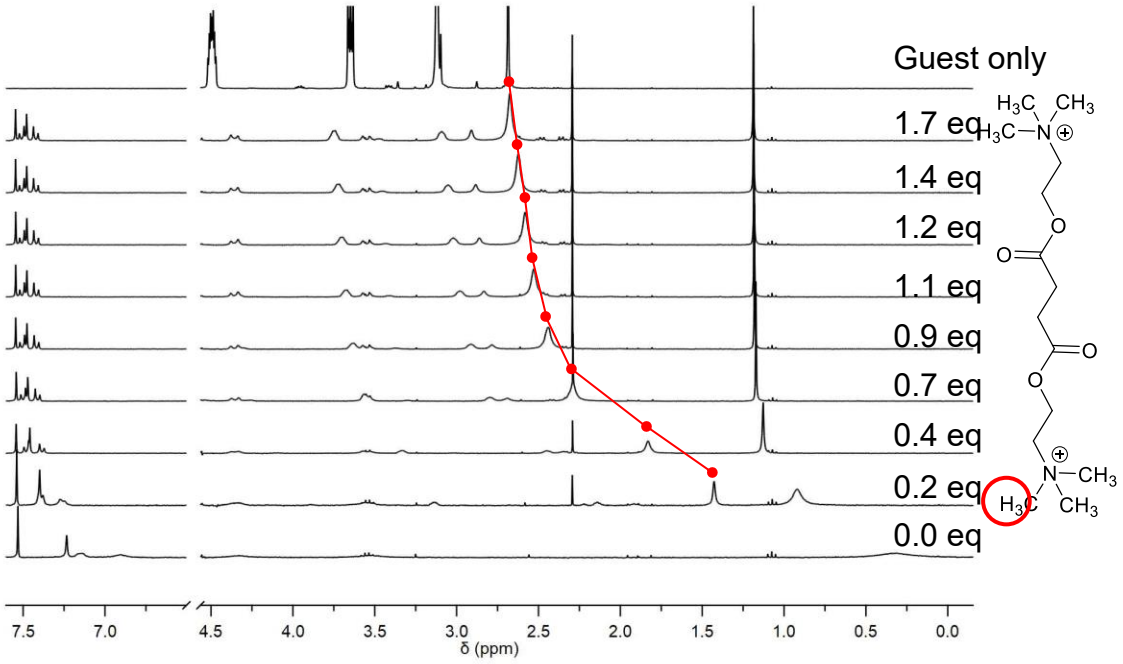

Figure 2. 17 ^{1}H titrations of suxamethonium (**2.10**) (20 mM) into ***t*Bu$_2$-SC4A** (1 mM) shows the fast exchange resonances of the guest's quaternary methyl ammonium singlet (red) travel from upfield as an encapsulated guest towards the unbound state, downfield.

Chapter 3: Using reversible non-covalent and covalent bonds to create assemblies and equilibrating molecular networks that survive 5 molar urea

This work was adapted from a previously published paper.

Meagan A. Beatty, Aidan T. Pye, Alok Shaurya, Belim Kim, Allison J. Selinger, and Fraser Hof
Org. Biomol. Chem., **2019**,17, 2081-2086

MB, AS and FH conceived of the idea. AJS provided starting material, AS provided guidance and MB designed the experiments. BK conducted preliminary NMR experiments. AP and MB conducted the majority of the NMR titrations and competition experiments, while MB analysed and interpreted the data. MB conducted and interpreted the data for 1D DOSY and 1D NOE experiments. FH and MB co-wrote the paper with the initial outline written by FH. MB did additional writing and figures for the Chapter.

3.1 Foreword

In the previous chapter, one lesson we learned was that a calixarene with a clip-like topology can self-assemble into dimers and can even afford a stronger dimer than the previously discussed mono-functionalized series of compounds. These previous dimers remained assembled in highly competitive aqueous mixtures like mock serum and real urine. Some of these derivatives were observed to become stronger in high salt concentrations while others were weakened. This suggested that there were some structures better able to survive competitive co-solutes than others. We wanted to continue to learn, by finding out what structures would self-assemble even under extreme solution conditions.

This motivated two goals for this chapter: The first was to test the resilience of new dimers to ‘extreme’ conditions. The second goal was to introduce reversible covalent bonds within the dimer scaffold to afford a dynamic library of exchangeable hosts that are dependent on the solution conditions.

3.2 Introduction

Molecular recognition and self-assembly in water — once a frontier of discovery — is increasingly well understood. Many examples of systems now exist in which assembly and recognition are predictable and can be used to solve important problems in biochemistry and biology.[97, 158-164] But Nature is a salty place, and the influences of co-solutes on self-assembly remain hard to understand, model, and predict. Mentioned in Chapter 1, Hofmeister anions compete for hydrophobic hosts such as the **1.27** and weaken the binding strengths with native guests.[165-166] Other systems tolerate and function in biological media like urine and plasma that contain millimolar concentrations of various salts and co-solutes.[114, 131, 167-169] Salts are also responsible for dynamic morphology changes between peptide amphiphiles by mediating intermolecular electrostatic peptides.[170] Despite these systematic studies, the programmed assembly of molecules in complex solutions containing mixtures of solutes at high concentrations remain hard or impossible to predict.

This work is motivated by two fundamental questions: 1) How extreme of a condition could a simple host-guest system survive? 2) Which functional groups would be useful for guiding self-assembly under extreme conditions? We were inspired by some extreme solute concentrations that exist in Nature. Mammalian kidney cells generally contain ca. 1.5 M urea,[171-172] and urea can even reach 5 M in the kidneys of certain desert mammals.[173] Halophilic microbes thrive in 100's of millimolar NaCl, and their proteomes contain an overabundance of anionic amino acids as a key adaptation that allows their proteins to stay folded and functional under high-salt conditions.[174] While there is evidence of residual protein structure within a denatured protein when exposed to solutions of 8 M urea.[175]

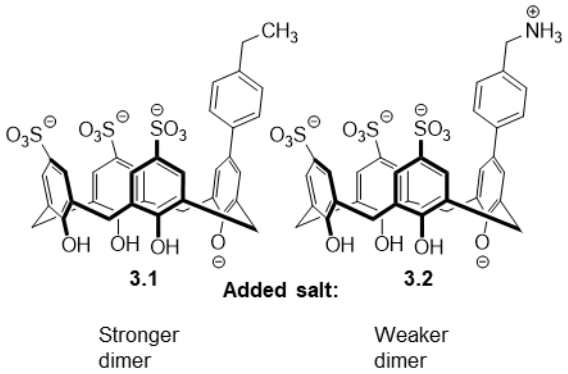

Figure 3. 1 Two previously published calixarenes that differ by an ethyl, **3.1**, and a methyl ammonium group **3.2**, both self-assemble in water but respond differently in the presence of salt.

Our previously reported self-assemblies were tolerant to moderate concentrations of salt and urea. As mentioned in Chapter 1.6, the yin-yang like dimers remained assembled in complex medium that contained NaCl (≤150 mM), creatinine (≤13 mM), and urea (≤220 mM).[134] It seemed so far that some small level of resistance to competing co-solutes is a general feature of molecules in this family. Yet, we noticed different dimers responded differently to the addition of salts. For example, **3.1** which contained an ethylphenyl pendant group became stronger in the presence of salts as the K_d value strengthened from 4.7 mM to 3.3 mM. An isosteric ammonium ion containing analogue, **3.2**, became slightly weaker, with K_d changing from 1.1 mM to 1.4 mM upon addition of salt (Figure 3. 1). We wanted to further explore the salt tolerance of these dimers while exploring the pendant group preference upon exposure to extreme conditions such as molar concentrations of urea and salt.

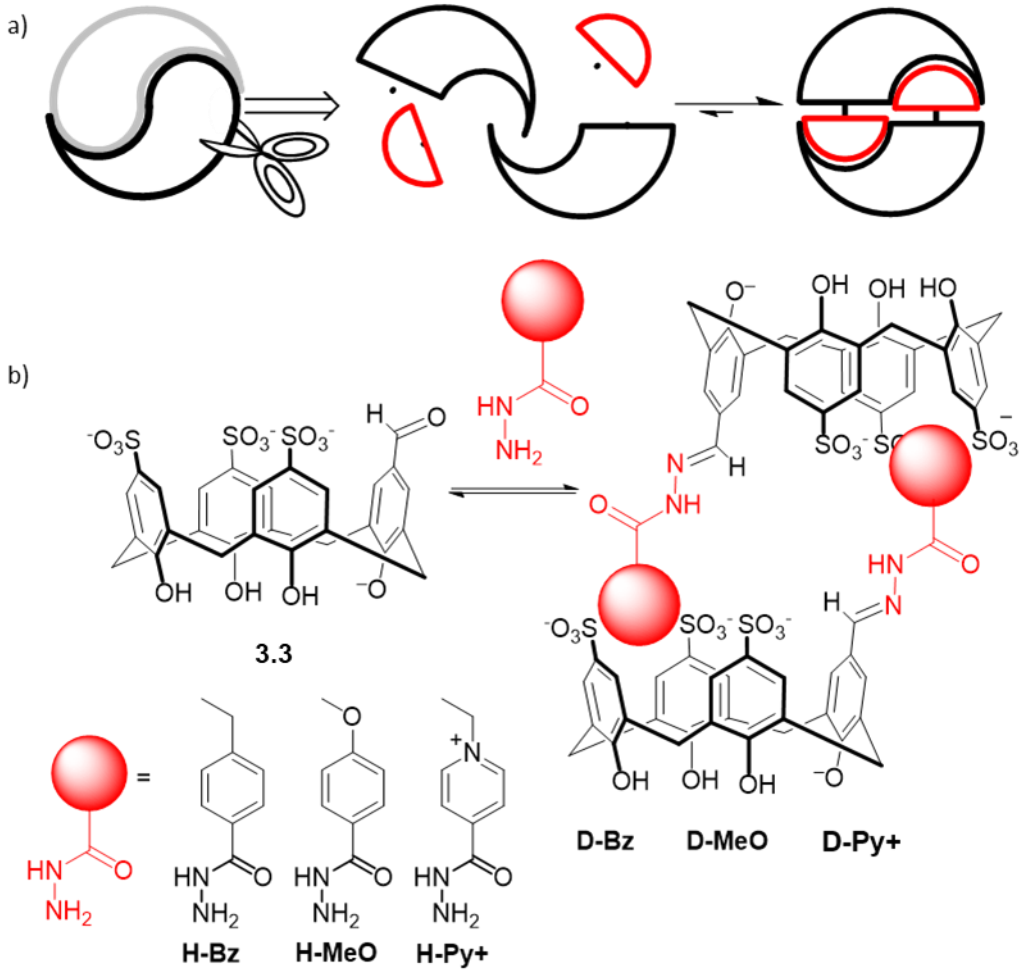

Figure 3. 2 Cartoon illustrating the incorporation of reversible covalent bonds into our yin-yang dimer structures. b) Aldehyde-trisulfonatocalixarene, **3.3**, condenses with various acyl hydrazides to form AB monomers which self-assemble into $(AB)_2$ dimers.

In order to test the limits of these systems, we created a new design in which the aforementioned yin-yang bowl and arm are separate molecules that can be stitched together by dynamic covalent chemistry Figure 3. 2a. This is based on the idea that reversible covalent bonds would tolerate salty and competitive aqueous conditions, while allowing comparison of the non-covalent interactions that different binding arms would confer upon the resulting monomers. We wanted to build from our previous observations of **3.2** and learn how different functional groups (neutral or charged, polar or hydrophobic) would dimerize best while under the influence of competing co-solutes. In order to make these comparisons on an equal footing, we minimized steric effects by choosing three binding arms with nearly isosteric binding elements. Hydrazides **H-Bz**, **H-MeO**, and **H-Py+** have

neutral hydrophobic (CAr-Et), neutral polar (CAr-OMe), and charged hydrophobic (N^+Ar-Et) groups in similar positions, respectively (Figure 3. 2b), each one appended with an acyl hydrazide that could form reversible covalent hydrazone bonds with an aldehyde partner. Condensation with aldehyde-functionalized sulfonated calixarene **3.3** would provide an AB-type monomer, which might then assemble into $(AB)_2$ dimers, **D-Bz**, **D-MeO** and **D-Py+**. We were also interested in establishing a molecular network in which multiple hydrazide building blocks are competing and equilibrating, such that we could observe changes in that network in response to different co-solutes.

3.3 Results and Discussion

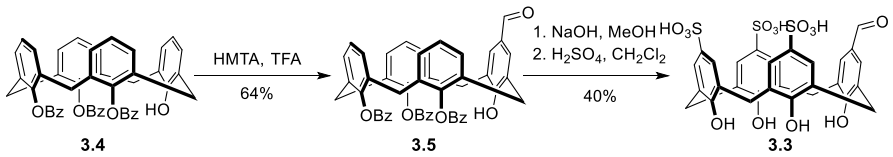

Scheme 3. 1 Synthesis of reactive aldehyde-trisulfonatocalix[4]arene, **3.3**.

The reactive aldehyde-calixarene was efficiently synthesized by site-specific functionalization of the calix[4]arene skeleton. The triprotected calix[4]arene **3.4**[176] was selectively formylated by treatment with hexamethylenetetramine (HMTA) to produce **3.5**. Subsequent ester removal (**3.6**, not shown) and sulfonation produced the aldehyde trisulfonate **3.3** after reverse-phase HPLC purification (Scheme 3. 1).

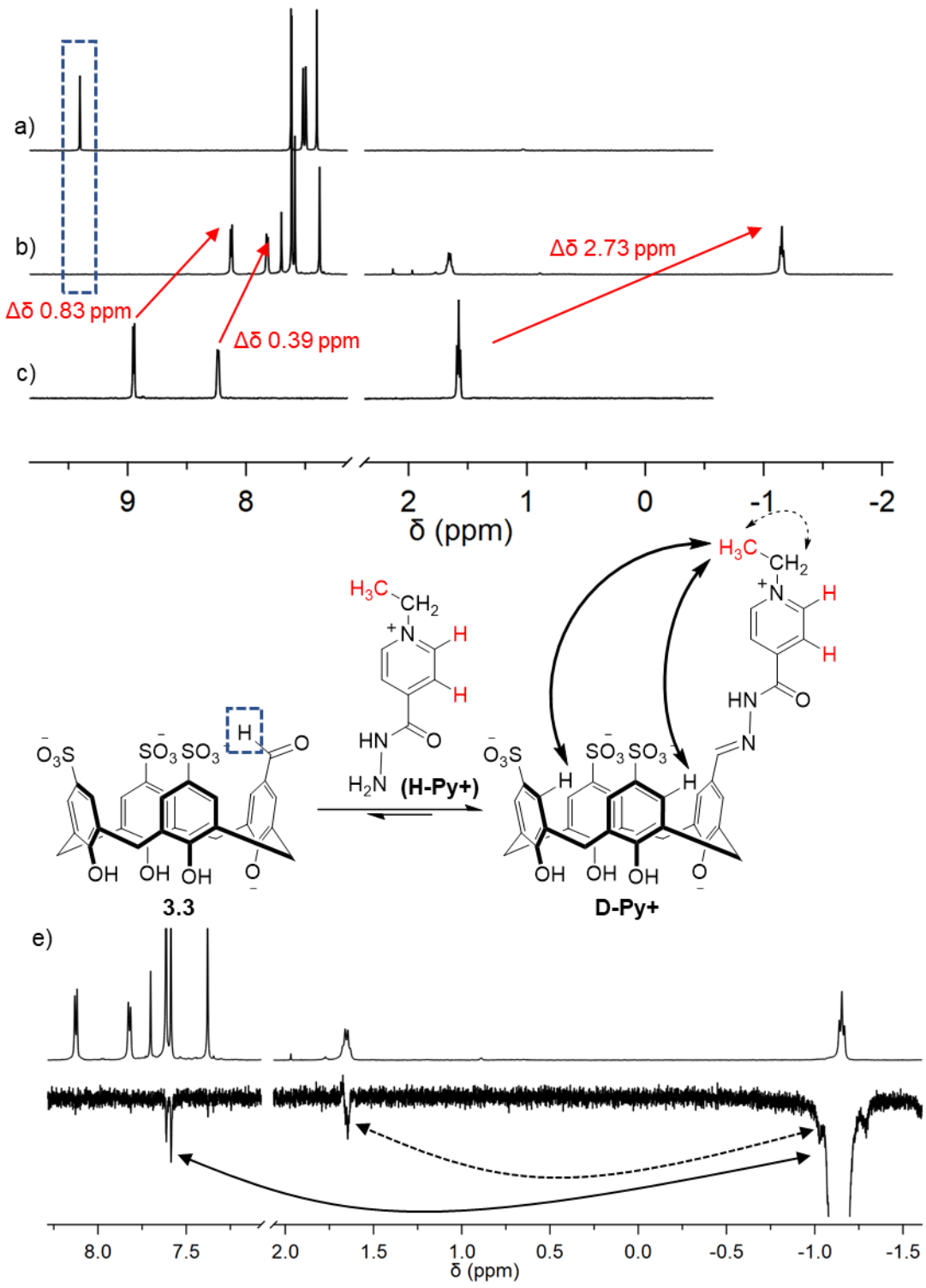

Figure 3. 3 NMR proves formation of hydrazone and subsequent self-assembly in D_2O containing citrate buffer (50 mM pD 5.0). NMR stackplots of a) **3.3** alone, b) 1:1 mixture of **H-Py+**:**3.3**, and c) **H-Py+** alone (all compounds are at 5 mM). The blue box highlights the disappearance of the starting material aldehyde peak confirming hydrazone

formation. The red arrows emphasize the upfield shift of protons of the encapsulated pendant group that indicate self-assembly. d) Intermolecular NOE interactions between the pendant group CH_3 and upper-rim protons are indicated by bold arrows and intramolecular NOE by dotted arrows.

Mixtures of **3.3** and **H-Py+** spontaneously form the predicted four-component, $(AB)_2$ assemblies in buffered water. We chose citrate at pH 5 as the supporting buffer for all solution phase studies, because it allows for rapid exchange of hydrazone components.[177] The disappearance of the aldehyde peak (9.40 ppm, Figure 3. 3a) proves the formation of the expected hydrazone (Figure 3. 3b). The simultaneous upfield shift of resonances on the pendant arm in comparison to the hydrazide arm ($\Delta\delta$: CH_3 +2.73 ppm, CH_2 +2.97 ppm (not shown), *ortho*-protons +0.83 ppm, *meta*-protons +0.40 ppm) strongly support end-on inclusion of the N-Et component into the calixarene pocket, in the form of structure **D-Py+** (Figure 3. 3c).[134, 178] Nuclear Overhauser Effect (NOE) correlations between the pendant arm CH_3 and upper-rim protons further confirm end-on complexation (Figure 3. 3d). Hydrazone dimers were also observed by NMR in both the neutral hydrophobic, **D-Bz**, and neutral polar derivatives, **D-MeO**, although not to the same extent as **D-Py+** (Figure 3. 10, Figure 3. 11). The existence of the assembled dimer, as opposed to a folded-in, self-included monomer, or higher-level aggregates, is proven by Diffusion-Ordered NMR SpectroscopY (DOSY) (Table 3. 1, see Support. Info.). All three dimers had diffusion coefficients (D) and calculated hydrodynamic radii (r_H) close to that of the similarly sized assembly ***tBu*$_1$-SC4A**.[134, 178]

Table 3. 1 1D DOSY-derived parameters for self-assembled components.

Dimer	D (m^2/s)	r_H (Å)
D-Bz	$(2.20 \pm 0.04) \times 10^{-10}$	11.1 ± 0.4
D-MeO	$(2.23 \pm 0.03) \times 10^{-10}$	10.9 ± 0.6
D-Py+	$(2.28 \pm 0.13) \times 10^{-10}$	10.7 ± 0.9

All samples were prepared by combining **3.3** with each respective hydrazide in a 1:1 mixture (5 mM) in D_2O containing citrate buffer (50 mM, pD 5.0)

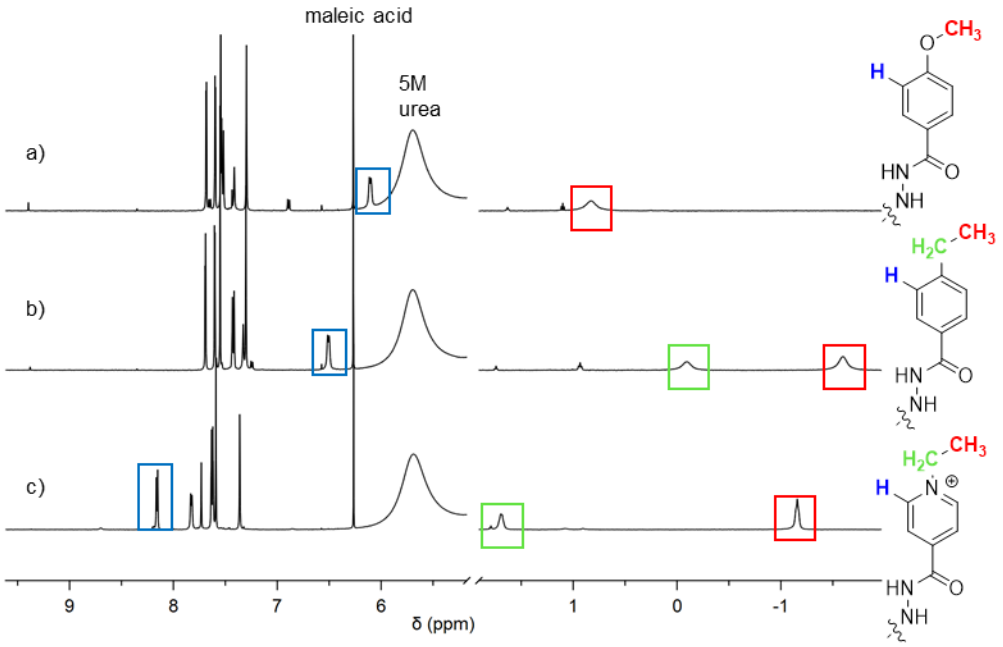

Figure 3. 4 ^{1}H NMR shows a) **D-MeO** b) **D-Bz** c) **D-Py+** all remain assembled in the presence of 5 M urea. Solutions contain 1:1 hydrazide:**3.3** (5 mM, ea.) and maleic acid as the internal standard (3 mM) in D_2O containing citrate buffer (50 mM, pD 5.0).

All three hydrazone dimers remain assembled in solutions containing up to 5 M urea. Quantitative NMR using maleic acid as an internal standard was used to track absolute concentrations of species. Surprisingly, introducing urea up to this level caused insignificant changes in both the covalent and non-covalent equilibria that stitch each dimer together. Figure 3. 4 shows all three hydrazone dimers assembled in the presence of 5 M urea as the chemical shifts of pendant arm resonances indicate dimerization. **D-Py+** remained the strongest assembly with 100% of the hydrazide converted to the hydrazone dimer (Figure 3. 5a, circles), followed by both neutral dimers, **D-MeO** and **D-Bz** existing at 93% and 97%, respectively (Figure 3. 5a, squares and triangles).

The addition of NaCl induced precipitation of varying degrees from each dimer. We were able to use quantitative NMR to determine the amounts of each species remaining in solution, and by mass balance the extent of precipitation. The neutral hydrophobic derivative, **D-Bz**, remained assembled and in solution in the presence of 200 mM NaCl (Figure 3. 5b, triangles). The polar and charged derivatives, **D-MeO** and **D-Py+** partially precipitated, leaving only 22% and 20% in solution, respectively (Figure 3. 5b, squares and circles). The species remaining in solution in each case were intact hydrazone dimers. At

400 mM NaCl both **D-MeO** and **D-Py+** were completely precipitated from solution, while 1 M NaCl was required to cause complete precipitation of **D-Bz** (Supp. Info for all NaCl titrations).

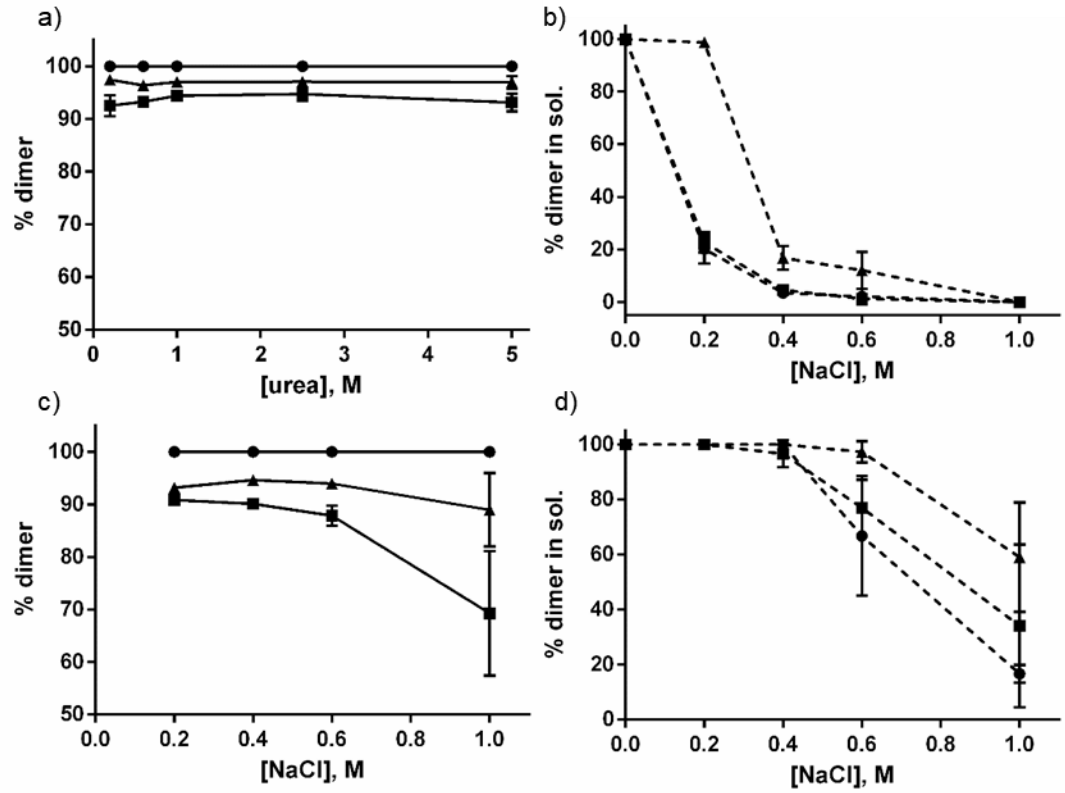

Figure 3. 5 Dimer concentrations and overall solubilities change with increasing concentrations of co-solutes. a) Dimers (5 mM) remain assembled with increased concentrations of urea (0.2 – 5 M). b) Dimers (5 mM) precipitate from solution with increased concentrations of NaCl (0.2 – 1 M). In 5 M urea and increased NaCl concentrations (0.2 – 1 M) c) dimers exist with d) limited precipitation. Solid lines show % dimer (=[dimer]/[dimer+**3.3**]) in solution for **D-Py+** (circles), **D-Bz** (triangles), **D-MeO** (squares). Dashed lines show % dimer in solution (=[dimer]/[dimer]$_0$). All solutions contain **3.3** (5 mM) with **H-Py+**, **H-Bz**, or **H-MeO** (5 mM) in citrate buffer (50 mM, pD 5). TSP (1 mM) was used as an internal standard for 5 M urea experiments, in all other experiments maleic acid (3 mM) was used. Error is calculated from the maximum standard deviation of duplicates.

The coupling between solute effects on non-covalent assembly and hydrazone formation was evident when studies included both NaCl and urea. Precipitation caused by the increasing concentrations of NaCl was limited when 5 M urea was also present. In terms of overall effect on solubility, increasing NaCl in the presence of 5 M urea caused greatest amount of precipitation for Py+ species and the least amount for Bz species (Figure

3. 5c). The neutral hydrophobic dimer, **D-Bz**, decreased from 93% (200 mM NaCl) to 88% (1 M NaCl), and when the amount of dimer decreased the appearance of resonances for **3.3** and **H-Bz** showed that disassembly is accompanied by unstitching of the hydrazone bond (Figure 3. 5c, triangles, spectra in Figure 3. 20). The neutral polar derivative, **D-MeO** decreased from 90% (200 mM NaCl) to 69% (1 M NaCl), also showing that the hydrazone reverted to aldehyde and hydrazide components **3.3** and **H-MeO** (Figure 3. 5c, squares, spectra in Figure 3. 19) The charged hydrophobic dimer, **D-Py+**, remained assembled throughout the addition of NaCl (Figure 3. 5c, circles, spectra in Figure 3. 18), with no changes in the amount of dimer or aldehyde **3.3** in solution. The overall picture shows different coupling between the $(AB)_2$ non-covalent assembly equilibria and the covalent AB formation equilibria for each of the compounds under study.

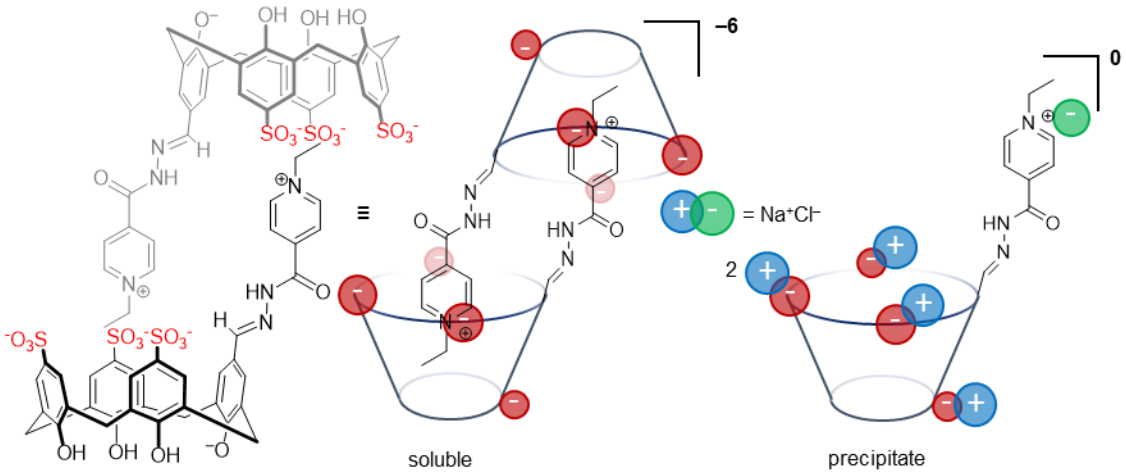

Figure 3. 6 Cartoon illustration of ion condensation around charged groups on **D-Py+** rendering it neutral and insoluble in D_2O.

Solubility changes are best attributed to direct co-solute interactions with the dissolved macrocycles. We propose that ion condensation (ie. ion pairing between Na^+ and sulfonates) and charge neutralization are the major drivers of precipitation.[87, 89, 179] As mentioned in Chapter 1.3, alkali cations bind weakly with calixarene sulfonates (K_d = 5.3 mM).[74, 180-181] This does not likely compete with the much stronger host-guest type binding at the ~50 mM Na^+ concentrations present in the parent buffer, but becomes significant at higher NaCl concentrations (0.2 – 1 M). **D-Py+** is the dimer that is most sensitive to NaCl-induced precipitation. This offers more indirect support for the ion condensation model,

because **D-Py+** is the only molecule with a cationic pendant arm that is subject to ion condensation by excess Cl^- (Figure 3. 6).

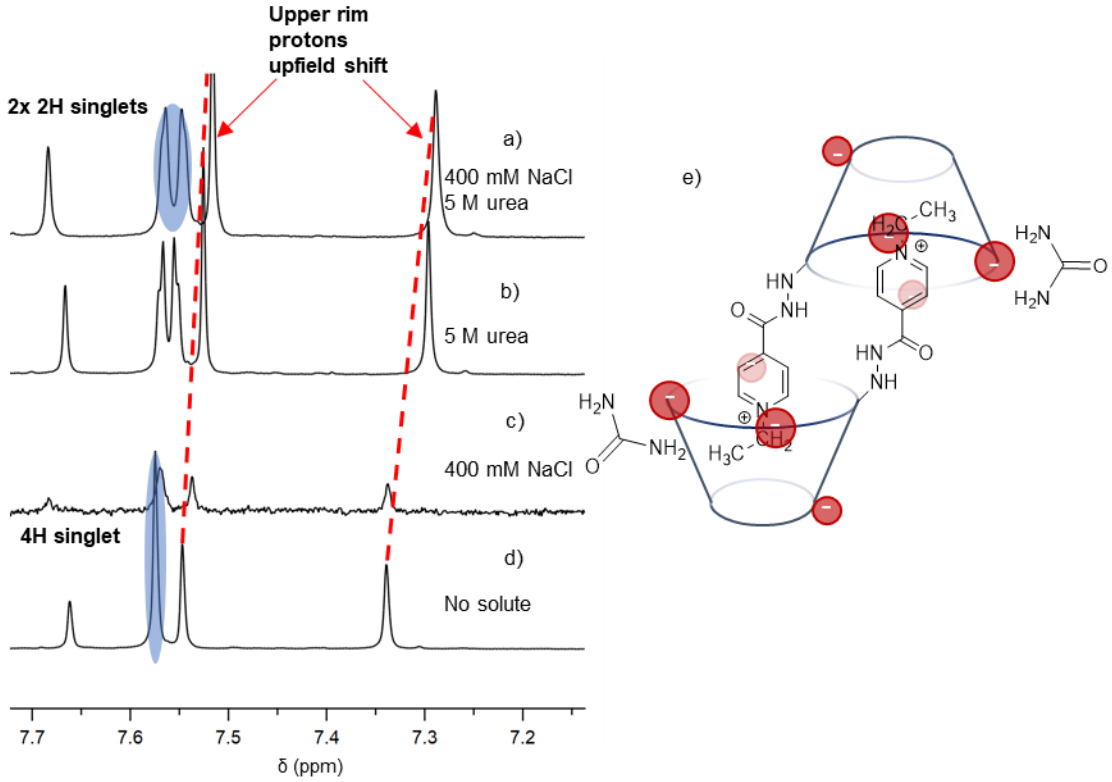

Figure 3. 7 ^{1}H NMR stack plots of **D-Py+** in the presence of a) both NaCl (400 mM) and urea (5 M), b) urea (5 M) only, c) NaCl (400 mM) only, and d) no solute added, suggests urea binds and shields sulfonates from cations and mediates precipitation. This is supported by resonances *ortho* to the sulfonates either upfield shift (dotted red line) or become inequivalent (highlighted in blue) in the presence of both solutions containing urea.

The origin of the urea effects are revealed by NMR. Urea is known to directly bind with sulfonates[182] and with hydrophobic moieties,[183] increasing the solubility. In the ^{1}H NMR spectra containing urea, we observe chemical shift and splitting changes of the upper rim proton resonances, indicating that urea interacts directly with this part of the calixarenes (Figure 3. 7b). Importantly, the NMR spectra in urea/NaCl mixtures have the same characteristic appearance as the urea-only samples (Figure 3. 7a), which suggests strongly that urea engages the sulfonates and upper rim directly, and in doing so prevents Na^+ from condensing onto the sulfonates and causing precipitation, Figure 3. 7e.

Combining **3.3** with two hydrazides in the same tube creates a complex, equilibrating molecular network. We quantified the composition of these dynamic libraries

by NMR and created speciation diagrams that help to view the overall state of each system under a given set of conditions (Figure 3. 8). We used a molar excess of hydrazides relative to aldehyde **3.3** in each tube. This makes the hydrazides compete for a common, scarce resource (**3.3**) to form hydrazone,[184] and ultimately to form self-assembled homodimers. Under these conditions **3.3** is not observed in NMR spectra. Free hydrazone monomers are also not observed, indicating that once a hydrazone forms, its subsequent homodimerization is fast and that dimers are thermodynamically stable relative to hydrazone monomers. Heterodimers are also not observed. In citrate buffer without additional co-solutes, the three pairwise competitions each support the overall order of preference **D-Py+** > **D-Bz** > **D-MeO**. The competition between **H-Py+** and **H-Bz** favours **D-Py+** by 71:29 (Figure 3. 8a) and the competition between **H-Py+** and **H-MeO** again favours **D-Py+** by 84:16 (Figure 3. 8b). The neutral hydrazides were nearly similar in abundance with a slight preference for **D-Bz** by 60:40 (Figure 3. 8c). All species are in solution under these conditions.

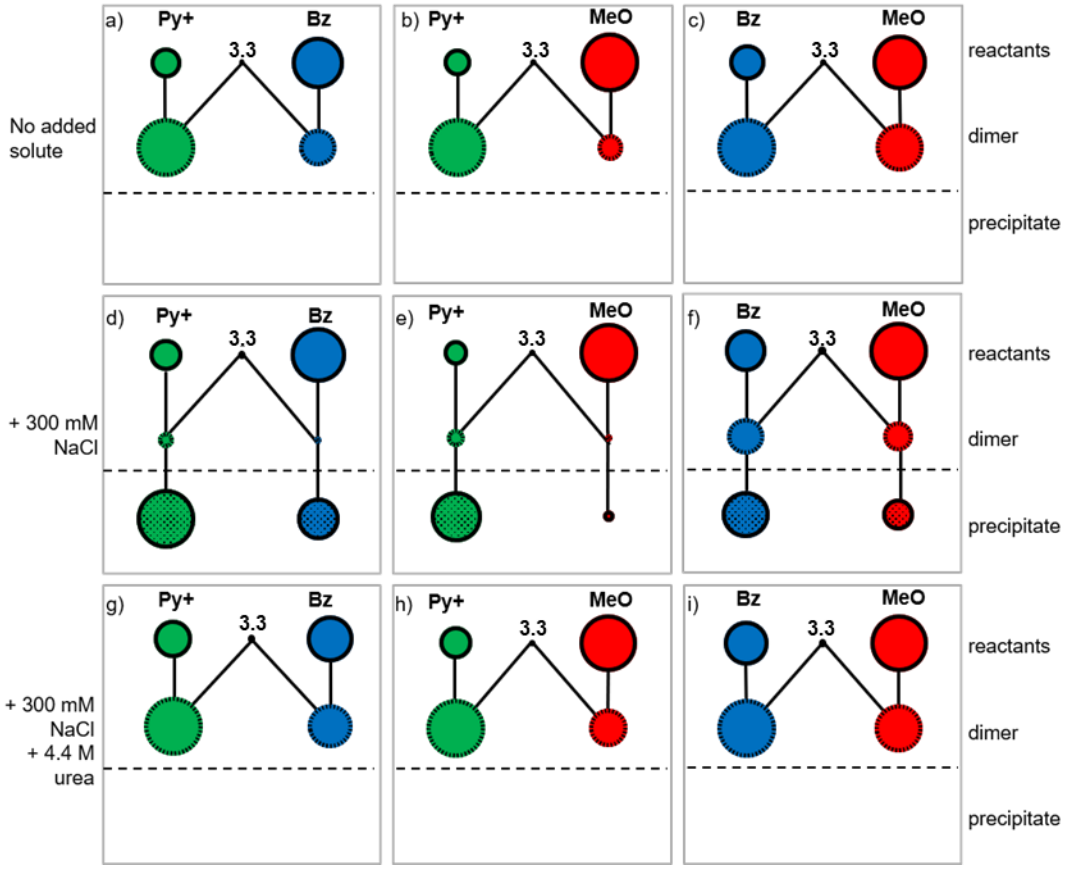

Figure 3. 8 Competition among hydrazides produces complex systems that respond differently to different co-solutes. Speciation diagrams based on quantitative NMR integration data show the composition of different systems and their responses to a – c) no solute; d – f) 300 mM NaCl; g – i) 300 mM NaCl and 4.4 M urea. The area of each circle corresponds to that species' concentration, and the locations of each circle show how different species are linked to others with which they can equilibrate. All solutions contain **3.3** (4 mM) with **H-Py+**, **H-Bz**, or **H-MeO** (4 mM), as indicated, in pH 5 citrate buffer and maleic acid (3 mM) as internal integration standard.

Addition of NaCl leads to varying precipitation from each competitive system. Most significantly affected were the competition experiments involving **D-Py+**, in which most of the precipitate formed was derived from Py+. 65% of the precipitate in the Bz/Py+ competition (Figure 3. 8d) was derived from Py+, while 94% of the precipitate in the MeO/Py+ competition was derived from Py+ (Figure 3. 8e). In both competition experiments involving **D-MeO** (Figure 3. 8e, f) salt induced formation of free, soluble hydrazide, instead of completely precipitating from solution, which was not the case in the salt experiments with **D-MeO** alone.

The presence of 4.4 M urea allowed the dimers to remain in solution upon addition of salt and allowed us to observe the re-distribution of species within the dynamic libraries under conditions where all species are in solution. Only small differences are visible when comparing dynamic libraries in the absence of co-solute (Figure 3. 8a–c) and in the presence of both co-solutes (Figure 3. 8g–i). In each competition experiment involving **D-Py+** with one of the neutral binding arms Bz or MeO, the addition of NaCl and urea caused small increases in **D-Bz** or **D-MeO**, with compensating small decreases in **D-Py+** that necessarily lead to an increase in the free hydrazide **H-Py+** (compare Figure 3. 8a, b to Figure 3. 8g, h). But the overall picture that arises is of two complex networks, each governed by reversible hydrazone formation and reversible dimerization equilibria, that are remarkably unperturbed by the addition of large amounts of NaCl and urea.

Covalent hydrazone formation and subsequent non-covalent dimerization are strongly coupled under all experimental conditions. Hydrazone monomers (AB) are not observed as distinct species in the NMR spectra, and quantitative integration of aldehyde and dimer resonances account for all expected calixarene in any given sample. Hydrazone formation is rapidly reversible at this pH,[177] and to ensure that we were measuring all samples at equilibrium we tested samples after several hours to confirm that integrations were not changing over time. The overall picture that arises for these self-assembling systems is that hydrazone formation leads directly to dimerization, and that the unassembled hydrazone monomers are energetically far uphill from either the free hydrazide or self-assembled dimeric states.

Understanding the systems that involve precipitating components is nontrivial. The pyridinium arm **D-Py+** is consistently the most stable dimer when all species are in solution. When many components precipitate (e.g. in the presence of high amounts of NaCl, but the absence of urea), the remaining calixarene left in solution is only present as **D-Py+** (and not, for example, as free aldehyde **3.3**). Free aldehyde **3.3** is freely soluble in the presence of NaCl when tested alone. When the same amount of NaCl is added in the presence of solubilizing urea, the proportion of **D-Py+** decreases. This shows how NaCl is not necessarily directly increasing or decreasing the dimerization strength of **D-Py+** but it can also drive changes by the selective precipitation of other competing building blocks.

Ion-solute and solute-solute interactions play an important role in solubility. As described in Chapter 1.3, salt can heavily influence host and protein solubility and we can confer those key lessons to the dimer's responses. Similar to proteins, hosts that bear negatively charged functional groups, like the sulfonates on the calixarene, can associate weakly to monovalent cations, like Na^+, and induce precipitation.[80, 185-186] Furthermore, the dimers enhanced solubility by urea resembles that of proteins but in contrast, the dimers' stability is not compromised as is found when urea interacts with proteins. The denaturation process first involves urea directly interacting with the protein surface through electrostatic interactions. Urea further penetrates the hydrophobic core by making favourable dispersion interactions and ultimately stabilizing a folded state.[187] In the case of the dimers, urea also seems to interact with the surface of the calixarenes, particularly the sulfonates, yet does not create strong enough interactions with the pendant arm to outcompete the dimerization process. This urea-calixarene interaction ultimately seems to shield the sulfonates from Na^+ and limits precipitation.

The SAMPL challenges discussed in Chapter 1.2 provide further context for the challenges in predicting host-guest complexation energies in the presence of salt. The SAMPL4 exercise involved the host cucurbit[7]uril, which is known to interact weakly with Na^+.[188] This small and very well understood host-ion interaction led to significant errors in calculated host-guest binding energies across almost all methods reported.[71] The most recent SAMPL5 exercise showed the best results for host-guest binding predictions arising from explicit solvent free energy simulations, although the "the level of accuracy is still below that sought for reliable computer-aided… design."[72] Considering the complexity of molecular recognition interfaces, it isn't reasonable to predict the energies or structures of their many possible interactions with different co-solutes. Given the barriers to doing and analyzing explicit solvent simulations and incorporating high concentrations of co-solutes, we think that predicting the behaviours of complex systems such as those reported here is currently impossible.

In this work, we purposefully avoid calculations, detailed thermodynamic analysis, and accompanying mechanistic conjecture. The highly charged nature of the recognition systems and the extremely high concentrations of co-solutes would confound any detailed

interpretation. In these experiments, complexes are created and destroyed in response to added solutes in ways that are unpredictable and probably not understandable.

3.4 Conclusions

This work focuses instead on presenting a new method for achieving recognition and self-assembly under highly competitive conditions. Hydrazone exchange is a common tool used in dynamic combinatorial chemistry,[189-190] especially when the goal is to create strong-binding ligands for proteins.[191-193] There are also a few examples that rely on DDC to discover new hosts that form capsules in organic solvents.[194-195] In our current results, self-assembly and precipitation are the selective pressures that control the success of winning building blocks. Frankly, we were surprised that these studies produced compounds that self-assemble faithfully under such extreme urea + salt conditions. We think that dynamic combinatorial methods like these will be invaluable in ongoing efforts to create self-assembled systems that work under extreme conditions.

3.5 Supplementary Information

3.5.1 General information and materials

^{1}H NMR, ^{13}C NMR, 1D DOSY, and 1D NOE were recorded on a Bruker Avance Neo 500 MHz spectrometer unless otherwise indicated, and processed with MestReNova by Mestrelab Research S.L and TopSpin 3.5. All reported chemical shifts were reported in ppm with respect to an internal standard: either maleic acid at 6.2 ppm or 3-(trimethylsilyl)propionic-2,2,3,3-d_4 acid sodium salt (TSP) at 0.0 ppm. Deuterated solvents were purchased from Sigma Aldrich. Sodium citrate buffer ($C_6H_8O_7$/$Na_3C_6H_5O_7$, 50 mM, pD 5) in D_2O was prepared with pD adjustments using NaOD/DCl solutions. Urea was dissolved in D_2O before lyophilizing to a powder to afford d_4-urea, which was used as isolated in all NMR experiments in order to minimize signals from exchangeable NH protons. NaCl, 4-methoxybenzhydrazide (**H-MeO**), **3.7** and hydrazine hydrate were purchased from Sigma-Aldrich. 4-ethylbenzhydrazide (**H-Bz**) was purchased from Enamine.

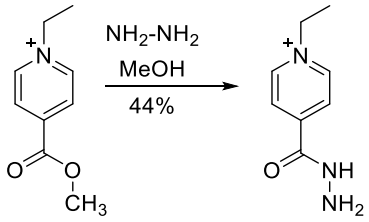

3.7 **H-Py+**

The following protocol was adapted from previous literature. **3.7** (0.290 g, 1 mmol) was dissolved in MeOH (25 mL), 50% hydrazine hydrate (186 μL, 3 mmol) was added and the reaction was heated to reflux for 6 h. The orange reaction mixture was concentrated under vacuum and the crude was re-crystallized with EtOH to afford yellow crystals of **H-Py+** (44% yield). Characterization data matched that of reported literature.[196]

3.5.2 Synthesis of novel compounds

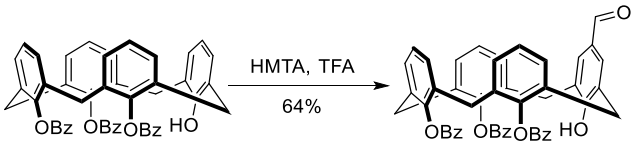

3.4 **3.5**

5-formyl-26,27,28-tribenzoyloxy-calix[4]arene (3.5). 26,27,28-tribenzoyl-calix[4]arene **(3.4)**[176] (3.52 g, 4.7 mmol) was dissolved in TFA (30 mL), followed by the addition of hexamethylenetetramine (HMTA) (4.76 mL 44 mmol) and the pink solution was heated for 4 h at 70°C. The reaction was reduced to a third of the original volume under reduced by vacuum and then diluted with water. The precipitate that formed was dissolved upon addition of CH_2Cl_2. The layers were separated, and the water was extracted with fresh CH_2Cl_2. The organic layers were combined, washed with water, brine, and then dried over Na_2SO_4. The filtered organic layer was concentrated to dryness on a rotary evaporator to afford yellow crystals (2.35 g, 64%). Mp: decomposed > 280 °C. FT-IR (cm^{-1}): 3506 (br), 1726 (m), 1684 (w), 702 (s). ^{1}H NMR (300 MHz, $CDCl_3$): δ 9.69 (s, 1H), 8.01 (d, *J* = 8.8 Hz, 6H), 7.76 (t, *J* = 7.5 Hz, 3H), 7.57 (s, 2H), 7.51 (t, *J* = 7.7 Hz, 6H), 7.24 (m, 2H), 7.02 (dd, *J* = 4.0, 1.0 Hz, 2H), 6.89 (d, *J* = 7.52 Hz, 2H), 6.72 (dd, *J* = 7.5, 1.0 Hz, 1H), 6.61 (m, 4H), 6.17 (s, 1H), 3.90 (d, *J* = 14.6 Hz, 2H), 3.82 (d, *J* = 15.3 Hz, 2H), 3.70 (d, *J* = 15.3 Hz, 2H), 3.62 (d, *J* = 14.3 Hz, 2H). ^{13}C NMR (125 MHz, $CDCl_3$): δ 190.8, 164.3, 163.8, 158.6, 146.9, 134.0, 133.6, 133.3, 133.2, 131.6, 131.3, 130.9, 130.8, 130.7, 129.4, 128.8, 128.6, 128.4, 128.0, 127.8, 126.2, 125.2, 37.4, 32.6. HR-MS ($[M-H]^-$, *m/z*): Calculated for $C_{50}H_{35}O_8^-$ 763.23374, Found 763.23375.

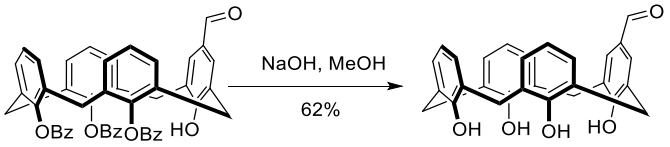

3.5 **3.6**

5-formyl-25,26,27,28-tetrahydroxy-calix[4]arene (3.6). 3.5 (2.35 g, 3.1 mmol) was dissolved in MeOH (40 mL). NaOH pellets (4.46 g, 62 mmol) were added and the green solution was heated at reflux overnight. The reaction volume was reduced by vacuum until

first signs of precipitation. The mixture was quenched with cold 1 M HCl and a precipitate formed. This was collected by vacuum filtration and washed with hexanes. The residue was purified by column chromatography over silica (CH_2Cl_2) (856 mg, 62%). Mp: decomposed > 280 °C. FT-IR (cm^{-1}): 3157 (br), 1684 (w), 1597 (m), 1450 (m), 756 (s). ^1H NMR (300 MHz, d_6-DMSO): δ 9.66 (s, 1H), 7.68 (s, 2H), 7.10 (m, 6H), 5.76 (s, 0.5H), 3.90 (br. d, 8H). ^{13}C NMR (75 MHz, $CDCl_3$): δ 190.6, 154.8, 148.5, 131.1, 129.1, 128.5, 128.0, 127.2, 122.6, 122.4, 31.6. HR-MS ([M−H]$^-$ *m/z*): Calculated for $C_{29}H_{23}O_5^-$ 451.15510, Found 451.15487.

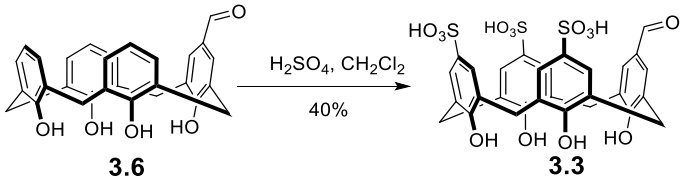

3.6 **3.3**

5-formyl-25,26,27,28-tetrahydroxy-11,17,23-trisulfonatocalix[4]arene (3.3). 3.6 (50 mg, 0.1 mmol) was dissolved in minimum CH_2Cl_2 (2 mL) and was heated at reflux with conc. H_2SO_4 (100 μL, 180 mmol) for 3 h. An insoluble residue formed. The CH_2Cl_2 was decanted, and the residue was rinsed with fresh CH_2Cl_2. The solid was suspended in EtOAc, transferred into a conical tube and diluted with cold Et_2O. The suspension was centrifuged to a pellet, the supernatant was decanted and the resuspension/centrifugation/ decanting process was repeated three times. The pellet was left to air dry overnight and was purified by semi-preparative HPLC (Phenomenex Luna C18, 250 mm x 22 mm, 5 μM, UV detection at 280 nm) with a gradient of 90% H_2O (+0.1% TFA)/10% CH_3CN (+0.1% TFA) to 60% H_2O (+0.1% TFA)/40% CH_3CN (+0.1% TFA) over 20 min. The fractions were collected and lyophilized to yield a white fluffy solid (30 mg, 40%). Mp: decomposed > 280 °C. FT-IR (cm^{-1}): 3173 (br), 1674 (w), 1131 (s) 1035 (s). ^1H NMR (300 MHz, D_2O): δ 9.39 (s, 1H), 7.59 (s, 2H), 7.54 (d, J = 2.3 Hz, 2H), 7.52 (d, J = 2.2 Hz, 2H), 7.44 (s, 2H), 3.95 (d, J = 5.3 Hz, 8H). ^{13}C NMR (75 MHz, D_2O): δ 194.4, 152.1, 135.6, 131.8, 130.0, 128.5, 128.2, 126.5, 30.5, 30.3. HR-MS ([M−2H+Na]$^-$, *m/z*): Calculated for $C_{29}H_{22}NaO_{14}S_3^-$ 713.00749, Found 713.00749.

3.5.3 ^{1}H and ^{13}C of novel compounds

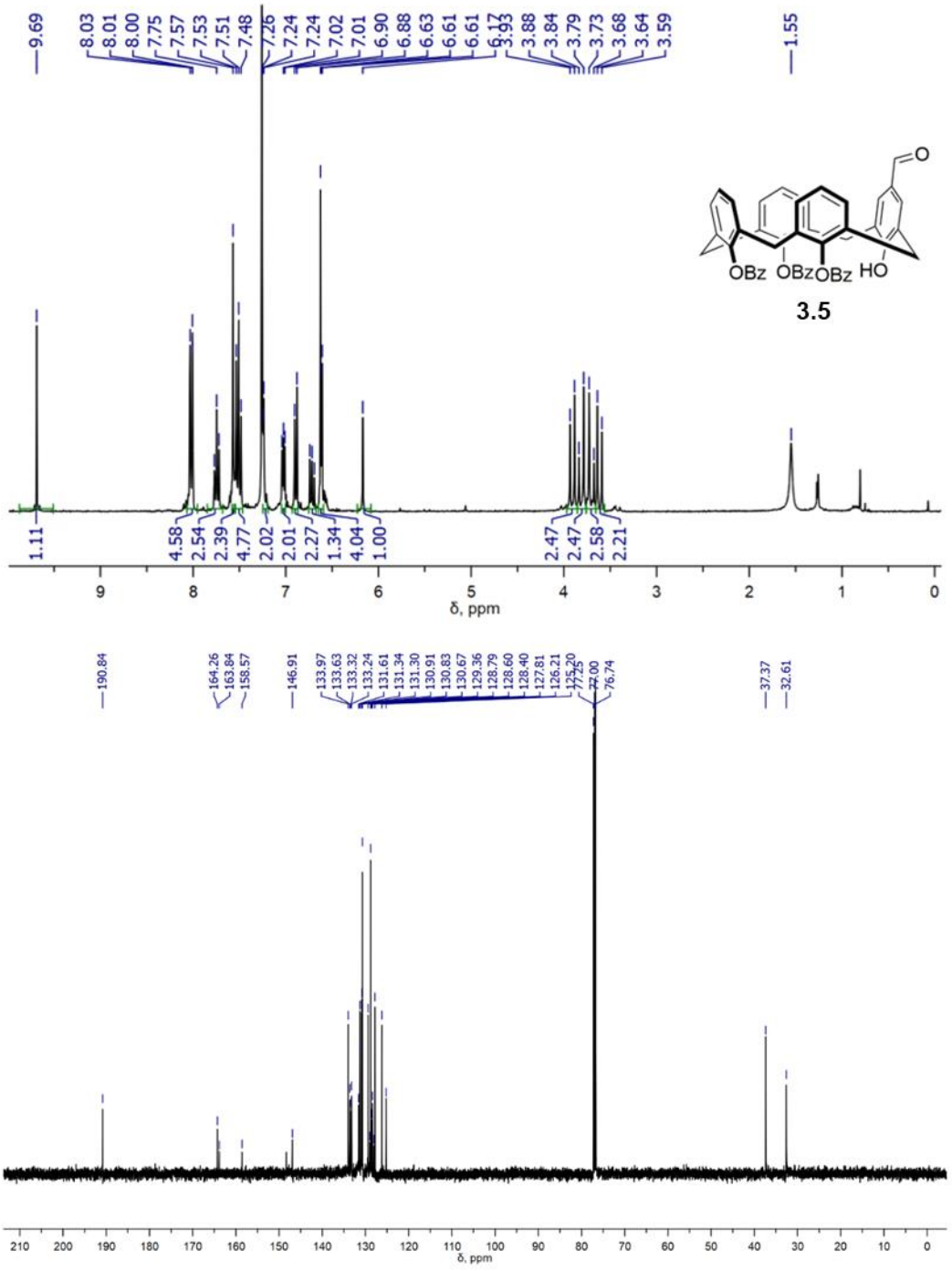

3.5

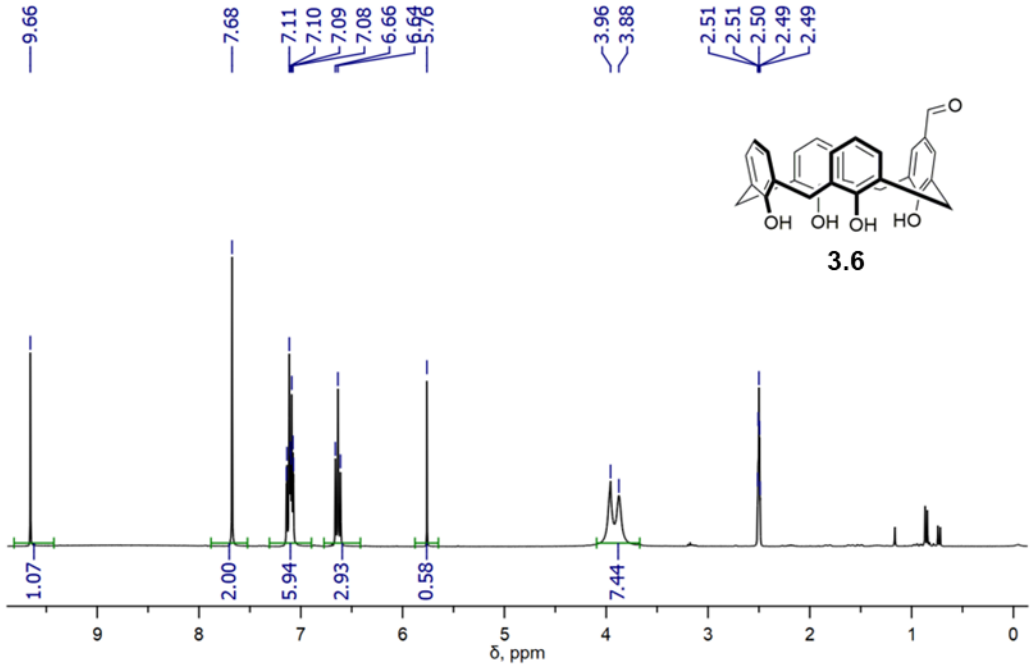
9.66
7.68
7.11
7.10
7.09
7.08
6.66
6.64
5.76
3.96
3.88
2.51
2.51
2.50
2.49
2.49
O
OH
OH
OH
HO
1.07
2.00
5.94
2.93
0.58
7.44
δ, ppm

3.6

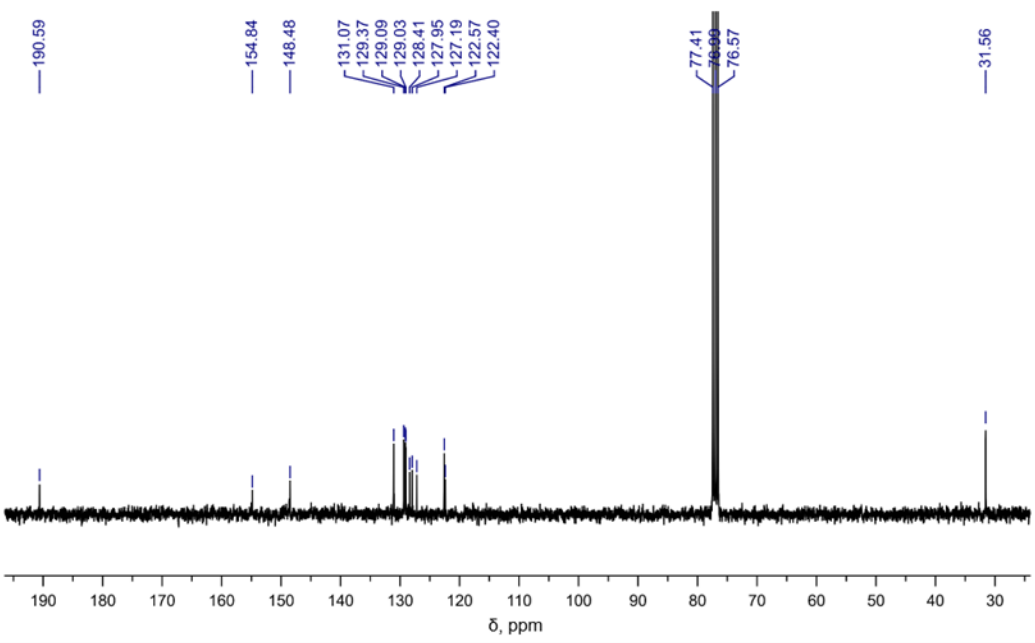
190.59
154.84
148.48
131.07
129.37
129.09
129.03
128.41
127.95
127.19
122.57
122.40
77.41
76.99
76.57
31.56
δ, ppm

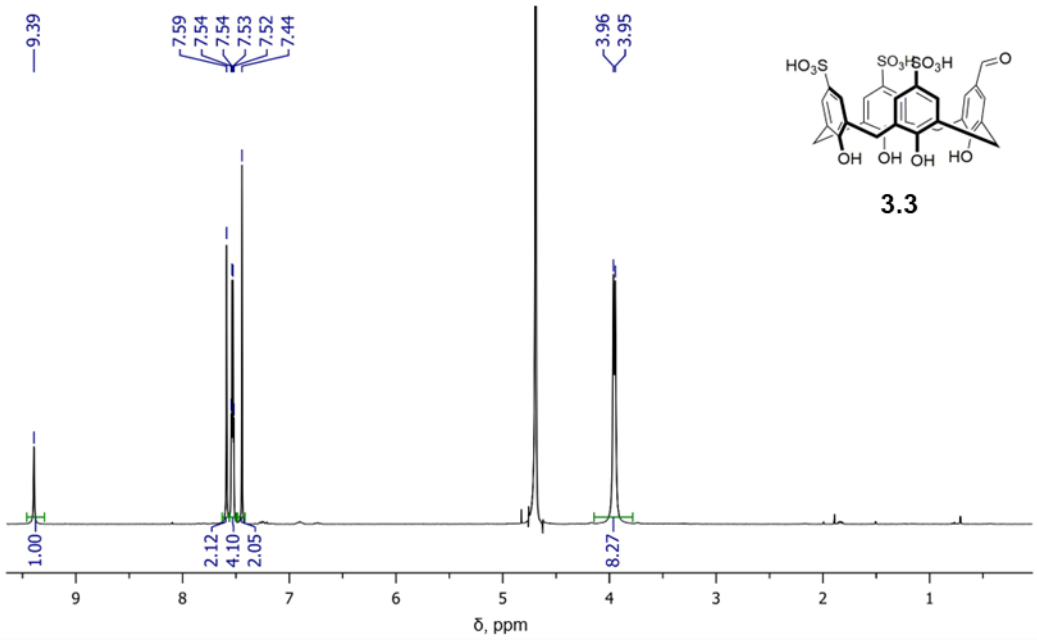
9.39
7.59
7.54
7.54
7.53
7.52
7.44
3.96
3.95
1.00
2.12
4.10
2.05
8.27
δ, ppm

HO3S
SO3H
SO3H
O
OH
OH
OH
HO

3.3

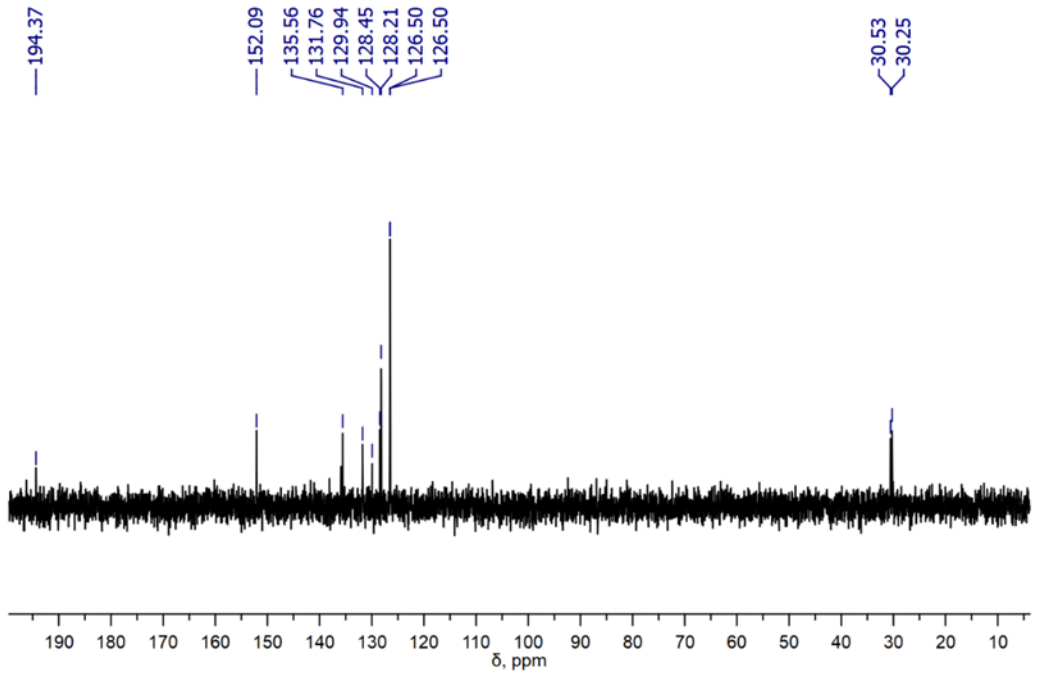
194.37
152.09
135.56
131.76
129.94
128.45
128.21
126.50
126.50
30.53
30.25
δ, ppm

3.5.4 Quantitative NMR protocol, solution prep and sample calculations

General protocol for producing hydrazone dimers

Stock solutions were made in citrate buffer (50 mM, pD 5) containing maleic acid (3 mM) of **3.3** and respective hydrazides were measured by NMR, with sufficient D1 relaxation delay time (25 s) to determine accurate concentrations. Appropriate volumes of each were mixed in an Eppendorf tube to make a 1:1 (5 mM) solution for non-competition experiments or 1:1:1 (4 mM) solutions for competitive experiments with a final volume of 500 μL. The order of addition was as follows: buffer, hydrazide(s), then **3.3**. The hydrazone solutions were allowed to mix at room temperature for 2 h before NMR spectra were taken.

General protocol for the addition of solute to hydrazone dimers

Stock solutions of NaCl (5.8 M) and d_4-urea (14 M) were made in D_2O citrate buffer (50 mM, pD 5). Appropriate volumes were added to hydrazone solutions and the samples were allowed to mix at room temperature for 1 h before NMR spectra were taken. For experiments with both NaCl and urea, the order of addition was as follows: buffer, hydrazide(s), **3.3**, urea then NaCl.

The known concentration of the internal standard was used to calculate the concentration of each species in solution from the average of all visible non-overlapped resonances assigned to that species.

The percent dimer was calculated as follows: % dimer=[Dimer]/[Dimer]+[**3.3**]

The percent dimer left in solution was calculated as follows:

% dimer in sol.=[Dimer]/$[Dimer]_{0mM\text{-}NaCl}$

3.5.5 ^{1}H NMR spectra of D-Bz, D-MeO, D-Py+

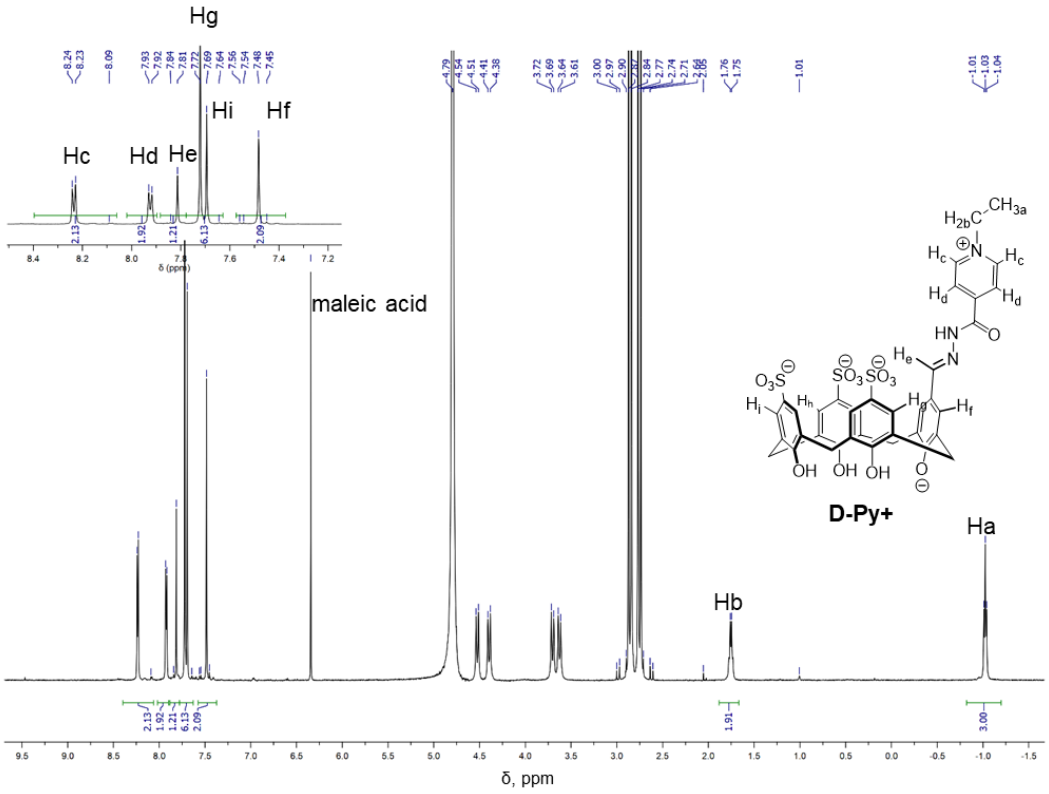

Figure 3. 9 ^{1}H spectrum of **D-Py+** (5 mM, 1:1 **3.3**:**H-Py+**) in citrate buffer (50 mM, pD 5.0).

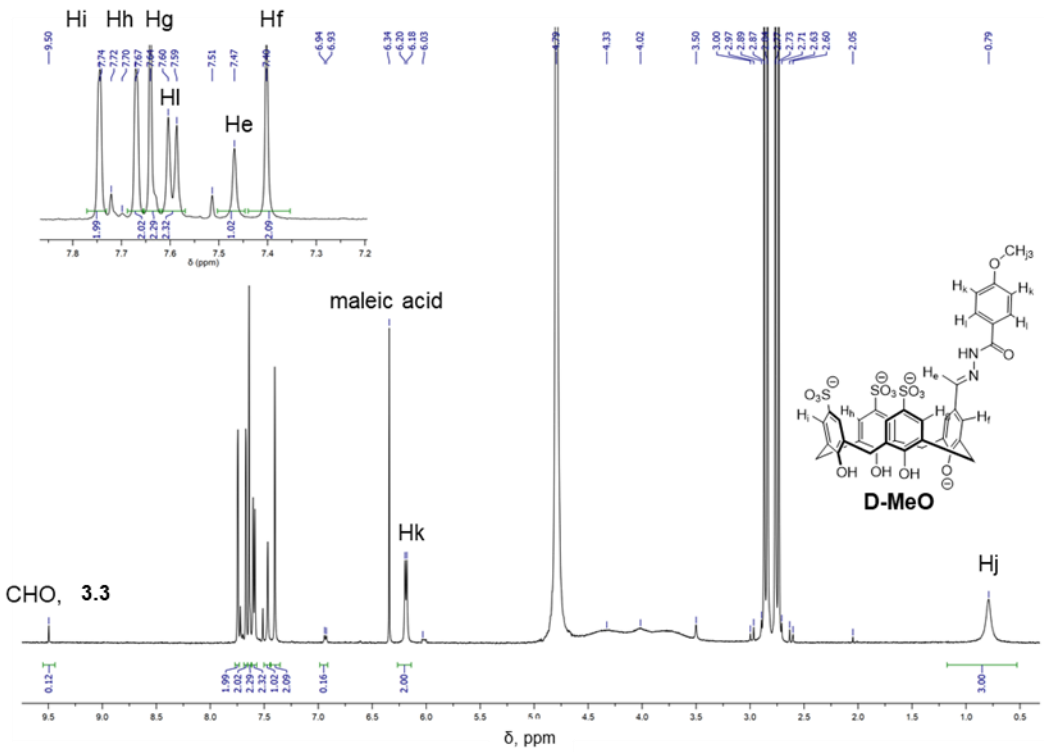

Figure 3. 10 ^{1}H spectrum of **D-MeO** (5 mM, 1:1 **3.3**:**H-MeO**) in citrate buffer (50 mM, pD 5.0).

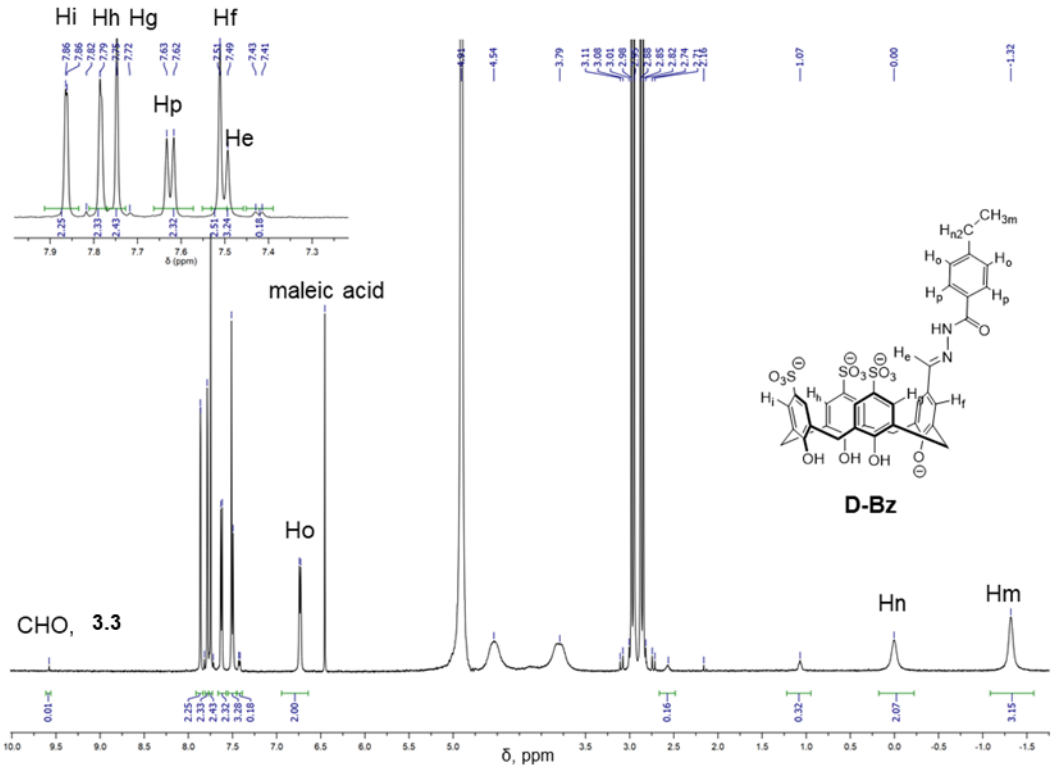

Figure 3. 11 ^{1}H spectrum of **D-Bz** (5 mM, 1:1 **3.3**:**H-Bz**) in citrate buffer (50 mM, pD 5.0).

Table 3. 2 HSQC-assigned carbon and proton hydrazone resonances in **DBz**, **DPy+**, and **DMeO**

Compound	^{13}C chemical shift, ppm	^{1}H chemical shift, ppm
DBz[a)]	149	7.26
DPy+[b)]	150	7.88
DMeO[b)]	148	8.30

a) dimer (30 mM) in citrate buffer (50 mM, pD 5.0) with 15% MeOD. b) dimer (30 mM) in d_6-DMSO

3.5.6 DOSY analysis of D-Py+, D-MeO, D-Bz

Table 3. 3 Parameters used for diffusion analysis of **D-Bz**

Parameters used for diffusion analysis:	
used γ:	26752 rad/(s*Gauss)
used δ:	0.0034000 s
used Δ:	0.049950 s
used gradient strength:	variable
Random error estimation of data:	RMS per spectrum (or trace/plane)
Systematic error estimation of data:	worst case per peak scenario
Fit parameter Error estimation method:	from fit using arbitrary uncertainties

Confidence level:	95%
Used peaks:	automatically picked peaks
Used integrals:	area integral
Used Gradient strength:	all values (including replicates) used

Table 3. 4 Diffusion coefficients calculated for **D-Bz** from 1D DOSY.

Peak name	F2 [ppm]	D [m^2/s]	error
D-Bz	7.741	2.21×10^{-10}	1.581×10^{-12}
D-Bz	7.507	2.23×10^{-10}	1.374×10^{-12}
D-Bz	6.641	2.17×10^{-10}	2.867×10^{-12}
H-Bz	1.108	6.61×10^{-10}	1.580×10^{-11}

Table 3. 5 Parameters used for diffusion analysis of **D-MeO**

Parameters used for diffusion analysis:	
used γ:	26752 rad/(s*Gauss)
used δ:	0.0050000 s
used Δ:	0.049950 s
used gradient strength:	variable
Random error estimation of data:	RMS per spectrum (or trace/plane)
Systematic error estimation of data:	worst case per peak scenario
Fit parameter Error estimation method:	from fit using arbitrary uncertainties
Confidence level:	95%
Used peaks:	automatically picked peaks
Used integrals:	area integral
Used Gradient strength:	all values (including replicates) used

Table 3. 6 Diffusion coefficients calculated for **D-MeO** from 1D DOSY.

Peak name	F2 [ppm]	D [m2/s]	error
D-MeO	7.751	2.22×10^{-10}	3.827×10^{-13}
3.3	7.722	3.27×10^{-10}	4.641×10^{-12}
D-MeO	7.675	2.22×10^{-10}	5.490×10^{-13}
3.3	7.516	3.11×10^{-10}	4.161×10^{-12}
D-MeO	7.466	2.23×10^{-10}	1.406×10^{-12}
D-MeO	7.404	2.25×10^{-10}	6.601×10^{-13}
D-MeO	6.187	2.23×10^{-10}	6.793×10^{-13}
3.3	9.498	3.40×10^{-10}	1.260×10^{-11}
D-MeO	0.781	2.22×10^{-10}	1.424×10^{-12}
D-MeO	0.777	2.24×10^{-10}	1.506×10^{-12}

Table 3. 7 Parameters used for diffusion analysis of **D-Py+**

Parameters used for diffusion analysis:	
used gamma:	26752 rad/(s*Gauss)
used little delta:	0.0050000 s
used big delta:	0.049950 s
used gradient strength:	variable
Random error estimation of data:	RMS per spectrum (or trace/plane)
Systematic error estimation of data:	worst case per peak scenario
Fit parameter Error estimation method:	from fit using arbitrary uncertainties
Confidence level:	95%
Used peaks:	automatically picked peaks
Used integrals:	area integral
Used Gradient strength:	all values (including replicates) used

Table 3. 8 Diffusion coefficients calculated for **D-Py+** from 1D DOSY.

F2 [ppm]	D [m^2/s]	error
8.226	2.38×10^{-10}	2.022×10^{-12}
7.812	2.23×10^{-10}	1.829×10^{-12}
7.719	2.28×10^{-10}	6.549×10^{-13}
7.682	2.37×10^{-10}	8.746×10^{-12}
7.481	2.25×10^{-10}	1.351×10^{-12}
-1.019	2.25×10^{-10}	3.671×10^{-12}
7.919	2.26×10^{-10}	6.528×10^{-12}
1.761	2.24×10^{-10}	4.377×10^{-12}

3.5.7 ^{1}H NMR of competition experiments

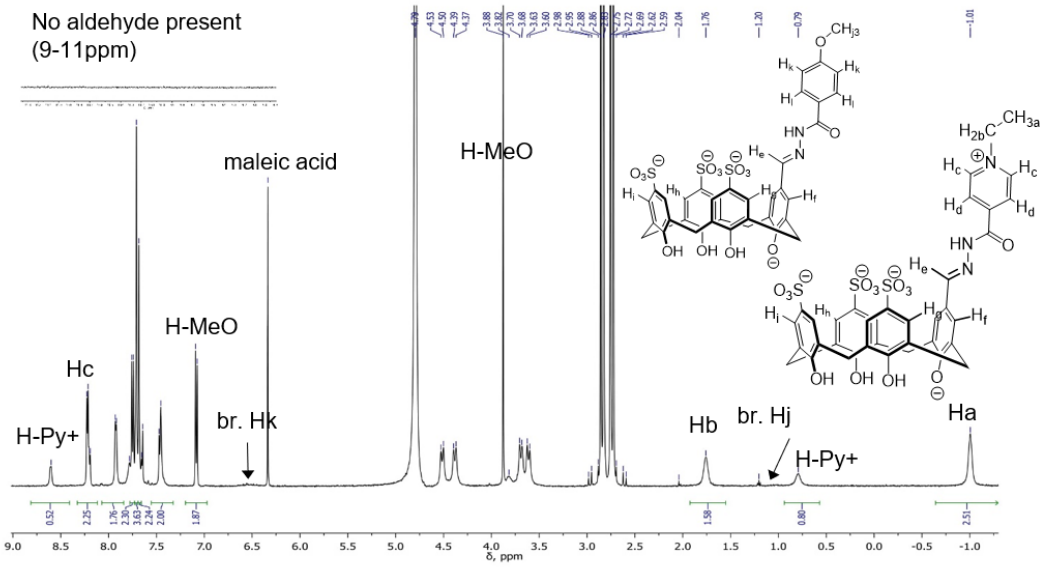

Figure 3. 12 ^{1}H NMR spectrum of 1:1:1 mixture of **3.3**:**H-Py+**:**H-MeO** (4 mM) in citrate buffer (50 mM, pD 5.0)

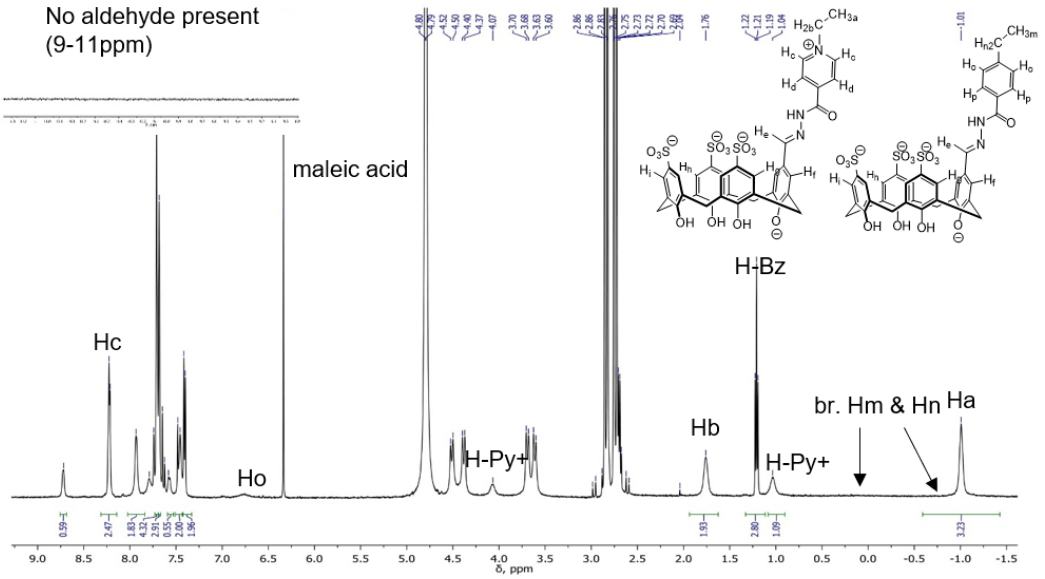

Figure 3. 13 ^{1}H NMR spectrum of 1:1:1 mixture of **3.3**:**H-Py+**:**H-Bz** (4 mM) in citrate buffer (50 mM, pD 5.0)

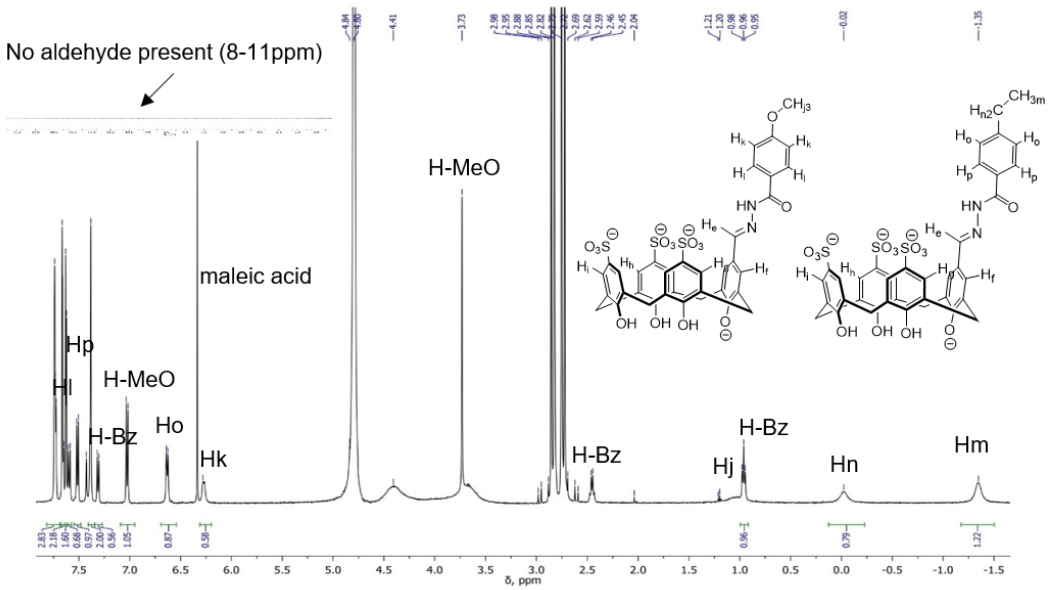

Figure 3. 14 ^{1}H NMR spectrum of 1:1:1 mixture of **3.3**:**H-Bz**:**H-MeO** (4 mM) in citrate buffer (50 mM, pD 5.0)

3.5.8 ^{1}H NMR titrations of co-solutes into D-Bz, D-MeO, D-Py+

3.5.8a Urea (200 mM, 600 mM, 1 M, 2.5 M, 5 M)

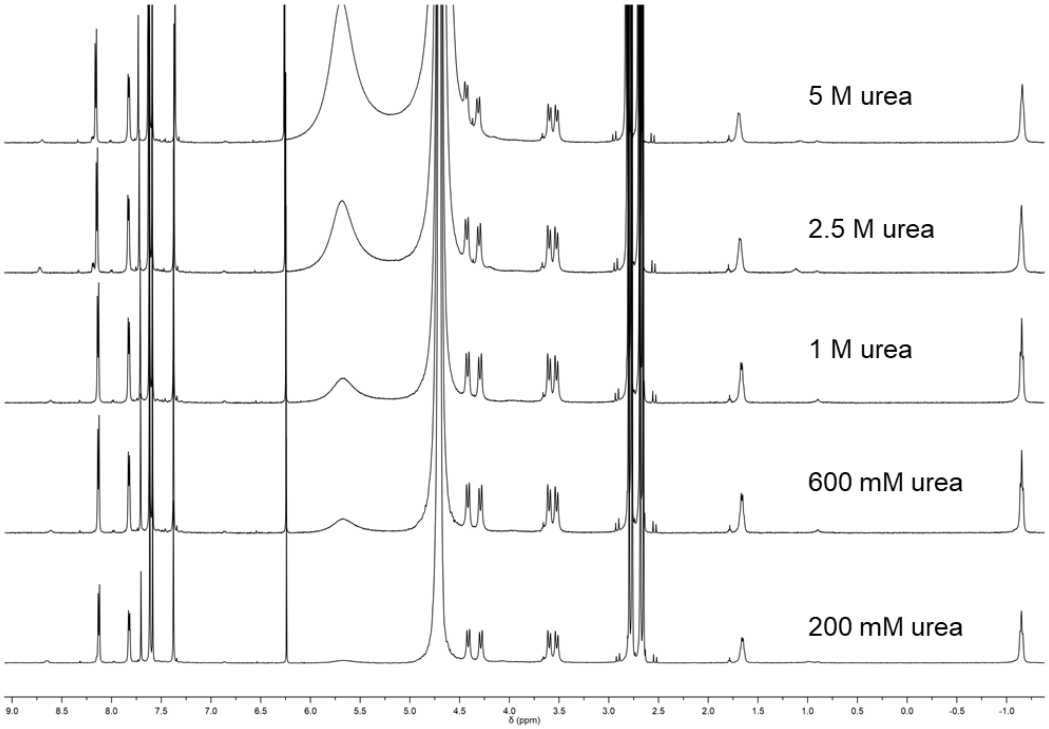

Figure 3. 15 ^{1}H NMR titrations of urea (14 M stock) into **D-Py+** (5 mM) in citrate buffer (50 mM, pD 5) shows very little change in the resonances associated to the dimer (CH_3 – 1.03 ppm, CH_2 1.74 ppm, *ortho*-protons 8.25 ppm), indicating at high concentrations of urea the dimer remains assembled. Solutions contain 1:1 **H-Py+**:**3.3** (5 mM, ea.) and maleic acid as the internal standard (3 mM).

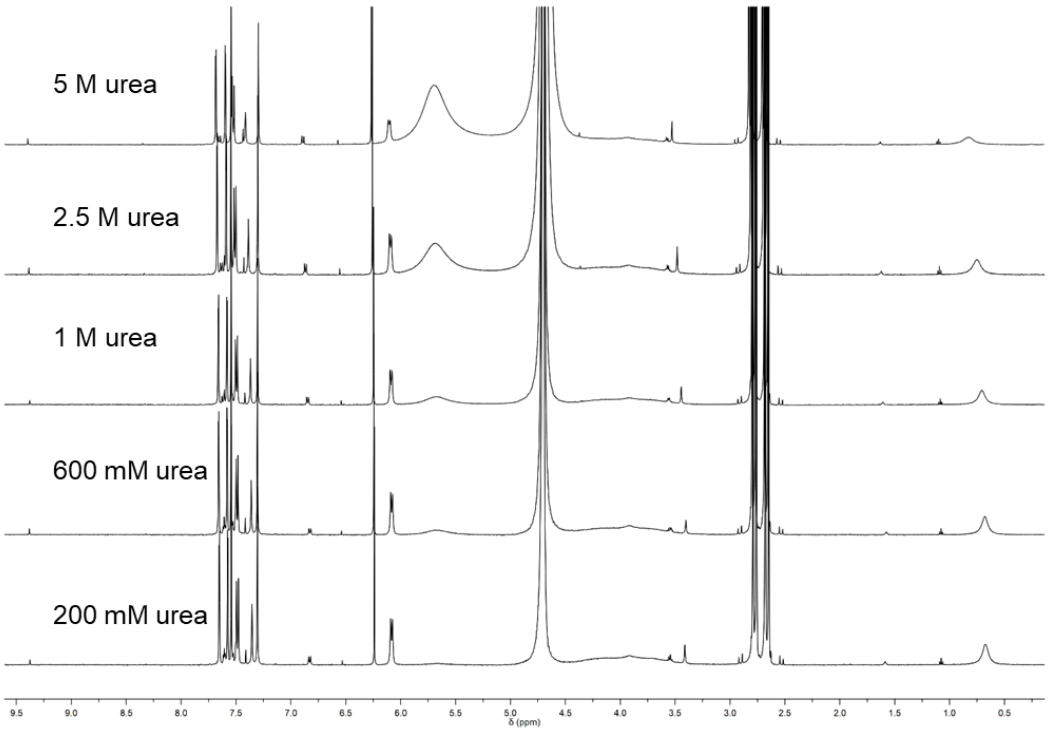

Figure 3. 16 ^{1}H NMR titrations of urea (14 M stock) into **D-MeO** (5 mM) in citrate buffer (50 mM, pD 5) shows very little change in the resonances associated to the dimer (OMe 0.78 ppm, *ortho*-protons 6.20 ppm), indicating at high concentrations of urea the dimer remains assembled. Solutions contain 1:1 **H-MeO**:**3.3** (5 mM, ea.) and maleic acid as the internal standard (3 mM).

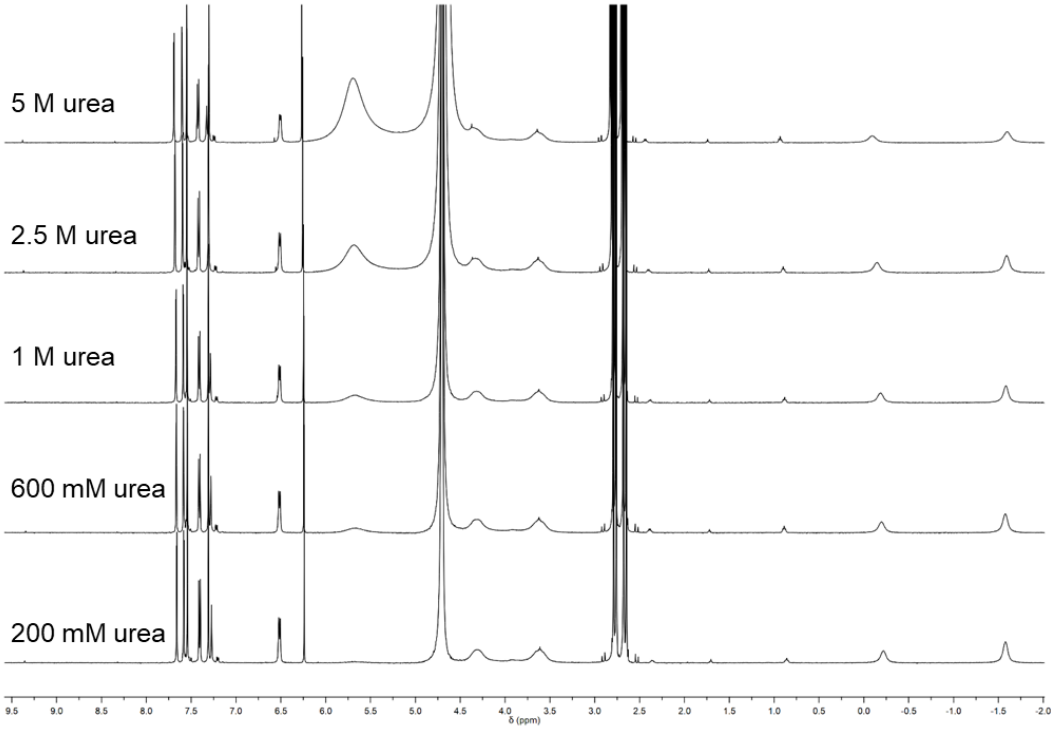

Figure 3. 17 ^{1}H NMR titrations of urea (14 M stock) into **D-Bz** (5 mM) in citrate buffer (50 mM, pD 5) shows very little change in the resonances associated to the dimer (CH_3 – 1.33 ppm, CH_2 –0.21 ppm, *ortho*-protons 6.51 ppm), indicating at high concentrations of urea the dimer remains assembled. Solutions contain 1:1 **H-Bz**:**3.3** (5 mM, ea.) and maleic acid as the internal standard (3 mM).

3.5.8b NaCl (200, 400, 600 mM)

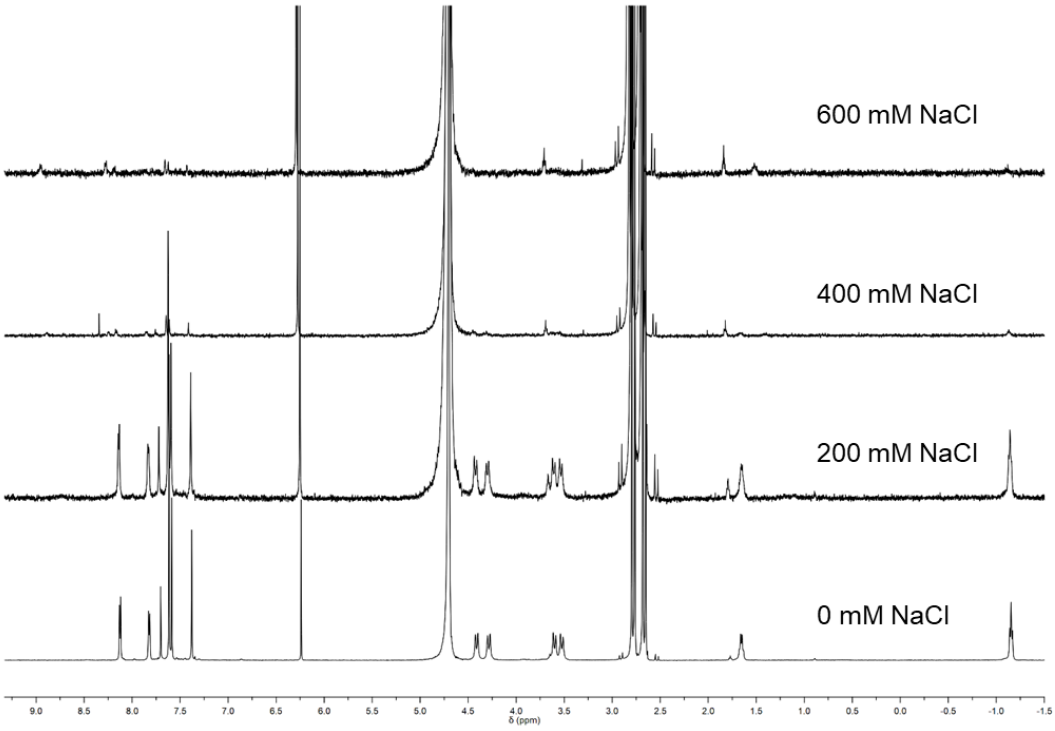

Figure 3. 18 ^{1}H NMR titrations of NaCl (5.8 M) into **D-Py+** (5 mM) in citrate buffer (50 mM, pD 5) shows decreasing signal due to precipitation starting at 200 mM NaCl and nearly all material is lost at 600 mM NaCl. Solutions contain 1:1 **H-Py+**:**3.3** (5 mM, ea.) and maleic acid as the internal standard (3 mM).

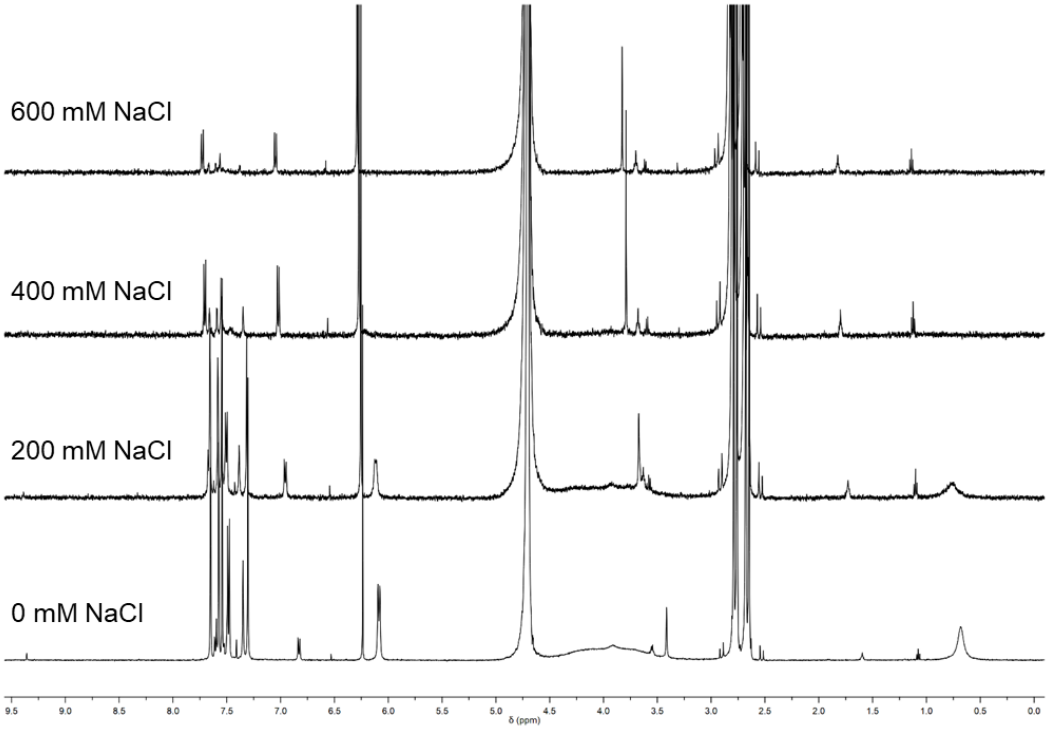

Figure 3. 19 ^{1}H NMR titrations of NaCl (5.8 M) into **D-MeO** (5 mM) in citrate buffer (50 mM, pD 5) shows decrease dimer due to precipitation starting at 200 mM NaCl and nearly all material is lost at 600 mM NaCl, leaving behind **H-MeO**. Solutions contain 1:1 **H-MeO**:**3.3** (5 mM, ea.) and maleic acid as the internal standard (3 mM).

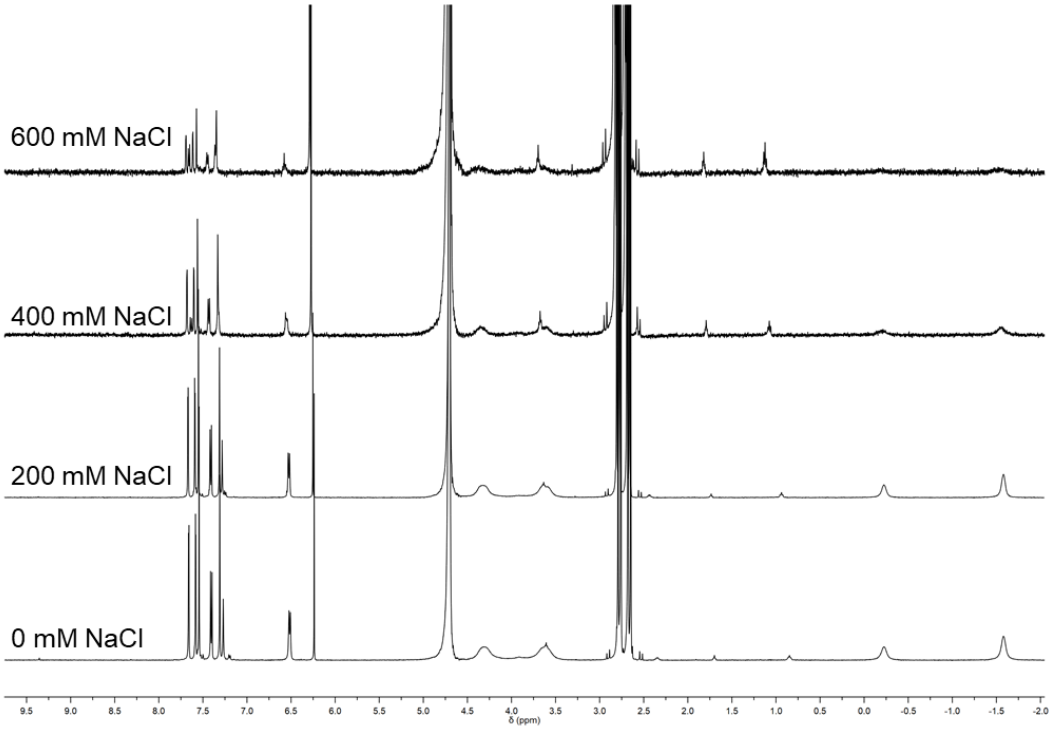

Figure 3. 20 ^{1}H NMR titrations of NaCl (5.8 M) into **D-Bz** (5 mM) in citrate buffer (50 mM, pD 5) shows decrease dimer due to precipitation starting at 200 mM NaCl and nearly all material is lost at 600 mM NaCl, leaving behind **H-Bz**. Solutions contain 1:1 **H-Bz**:**3.3** (5 mM, ea.) and maleic acid as the internal standard (3 mM).

3.5.8c 5 M urea and NaCl (200, 400, 600 mM, 1 M)

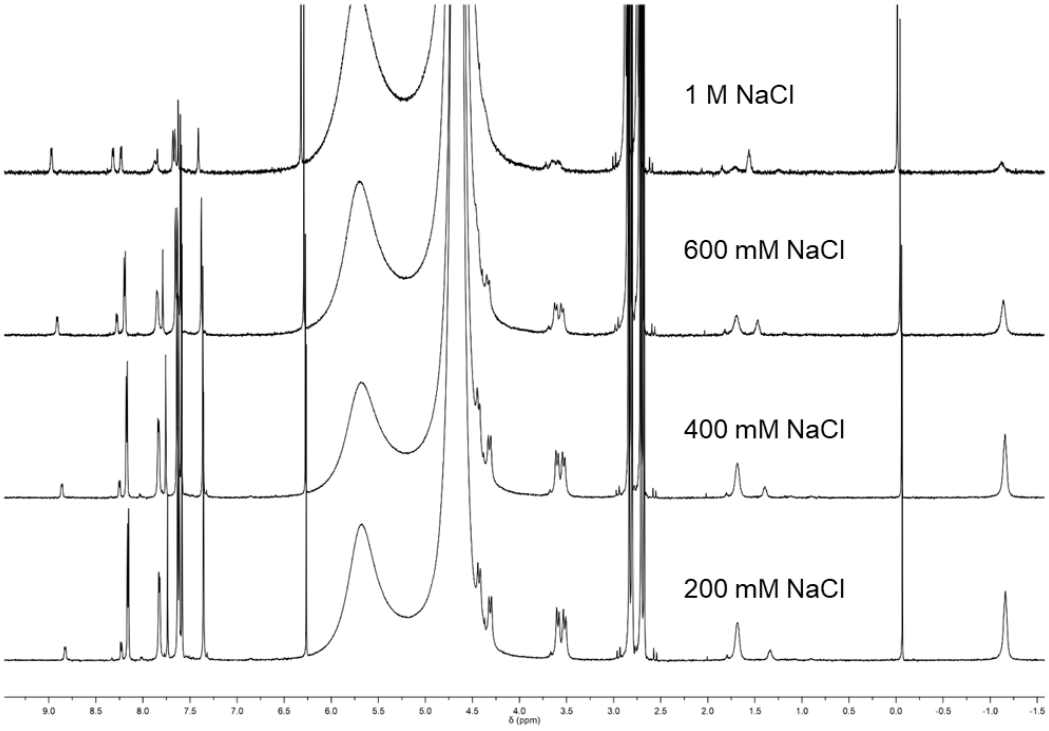

Figure 3. 21 ^{1}H NMR titrations of NaCl (5.8 M) into **D-Py+** (5 mM) with 5 M urea in citrate buffer (50 mM, pD 5) shows the presence of **H-Py+** resonances at 200 mM NaCl, a decrease in dimer intensity due to precipitation starting at 600 mM NaCl yet resonances of dimer remain alongside **H-Py+** at 1 M NaCl. 1:1 **H-Py+**:**3.3** (5 mM, ea.) and TSP as the internal standard (1 mM).

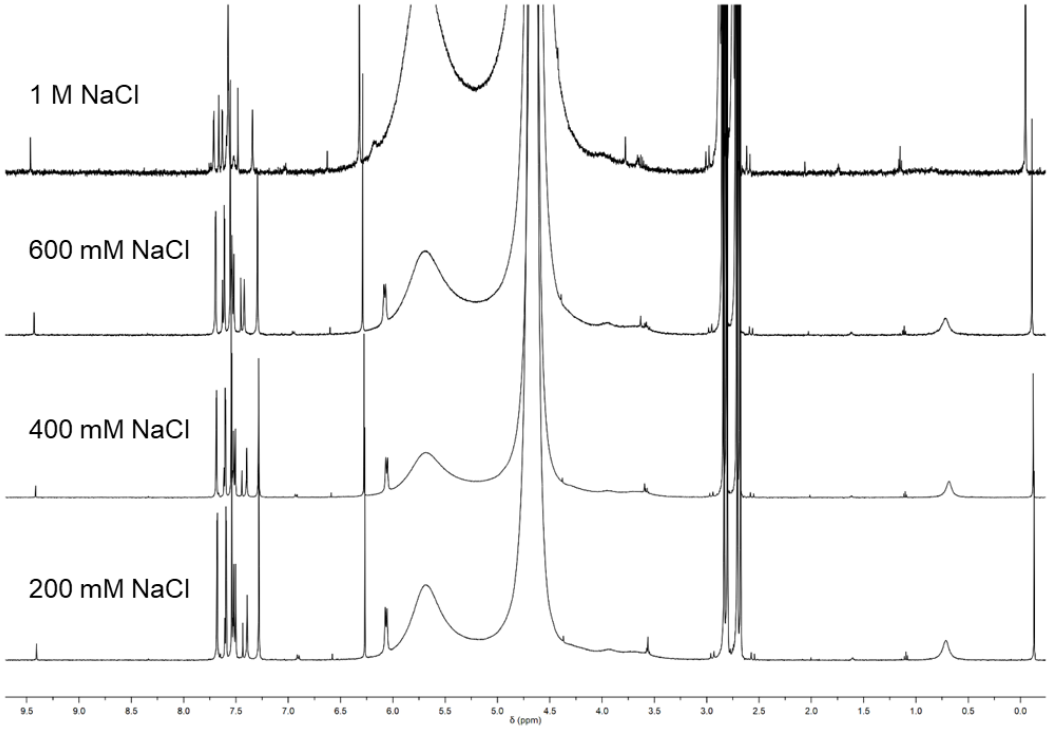

Figure 3. 22 ^{1}H NMR titrations of NaCl (5.8 M) into **D-MeO** (5 mM) with 5 M urea in citrate buffer (50 mM, pD 5) shows the presence of **H-MeO** resonances at 200 mM NaCl, a decrease in dimer intensity due to precipitation starting at 400 mM NaCl yet resonances of dimer remain alongside **H-MeO** at 1 M NaCl. 1:1 **H-MeO**:**3.3** (5 mM, ea.) and TSP as the internal standard (1 mM).

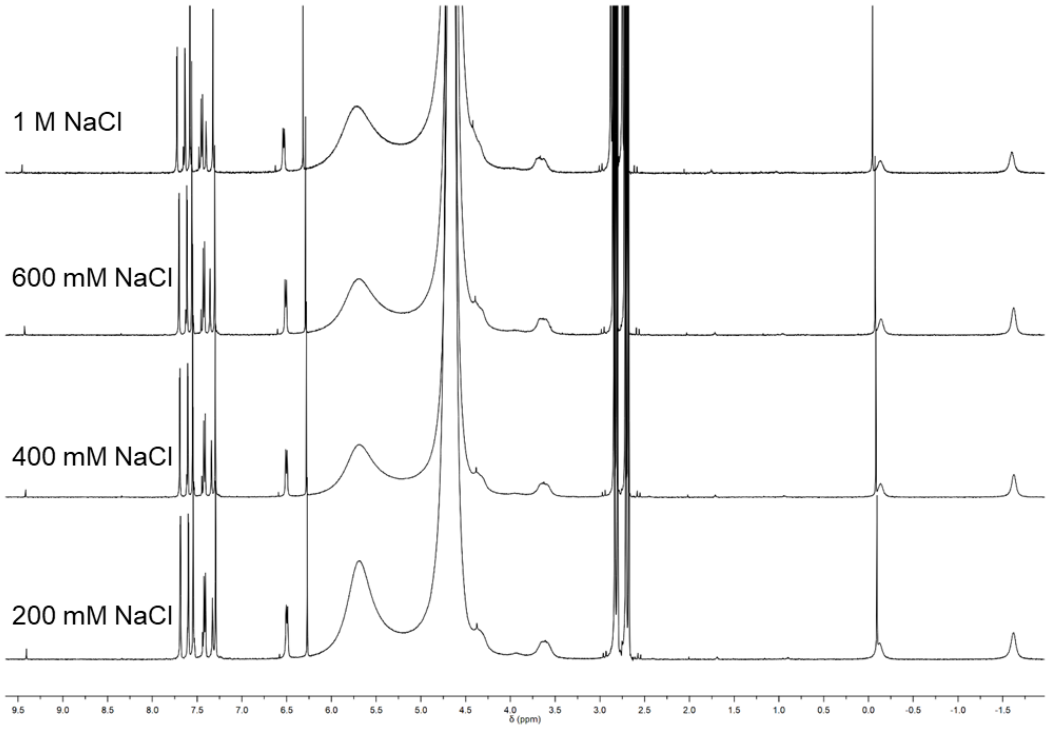

Figure 3. 23 ^{1}H NMR titrations of NaCl (5.8 M) into **D-Bz** (5 mM) with 5 M urea in citrate buffer (50 mM, pD 5) shows a slight decrease in dimer intensity due to precipitation starting at 1 M NaCl yet no new resonances from **H-Bz** become apparent during the titration. 1:1 **H-Bz**:**3.3** (5 mM, ea.) and TSP as the internal standard (1 mM).

3.5.9 ^{1}H NMR stack plots of competition experiments with added co-solutes

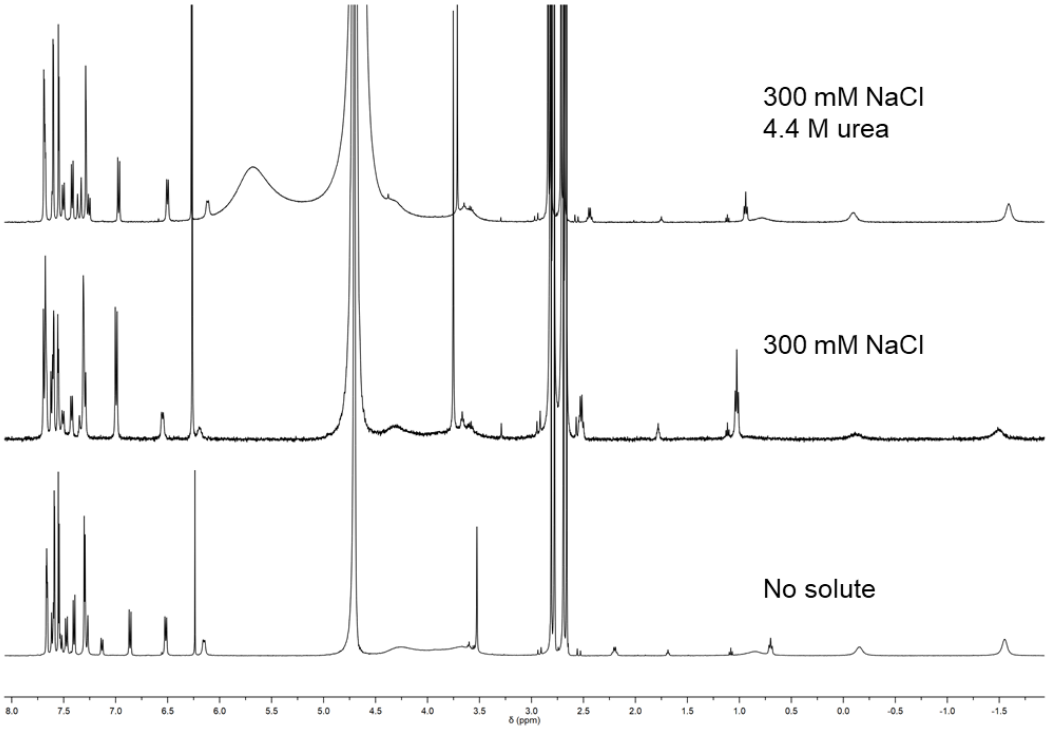

Figure 3. 24 ^{1}H spectra show that neutral hydrophobic, **D-Bz** and neutral polar**, D-MeO** are both equally capable of existing in strongly denaturing conditions. Without solute, **D-Bz** is favoured 60:40, while 300 mM NaCl induces precipitation shown by increased **H-Bz** resonances and decreased **D-MeO** resonances. When both 4.4 M urea and 300 mM NaCl is present the spectra resembles that of no solute present.

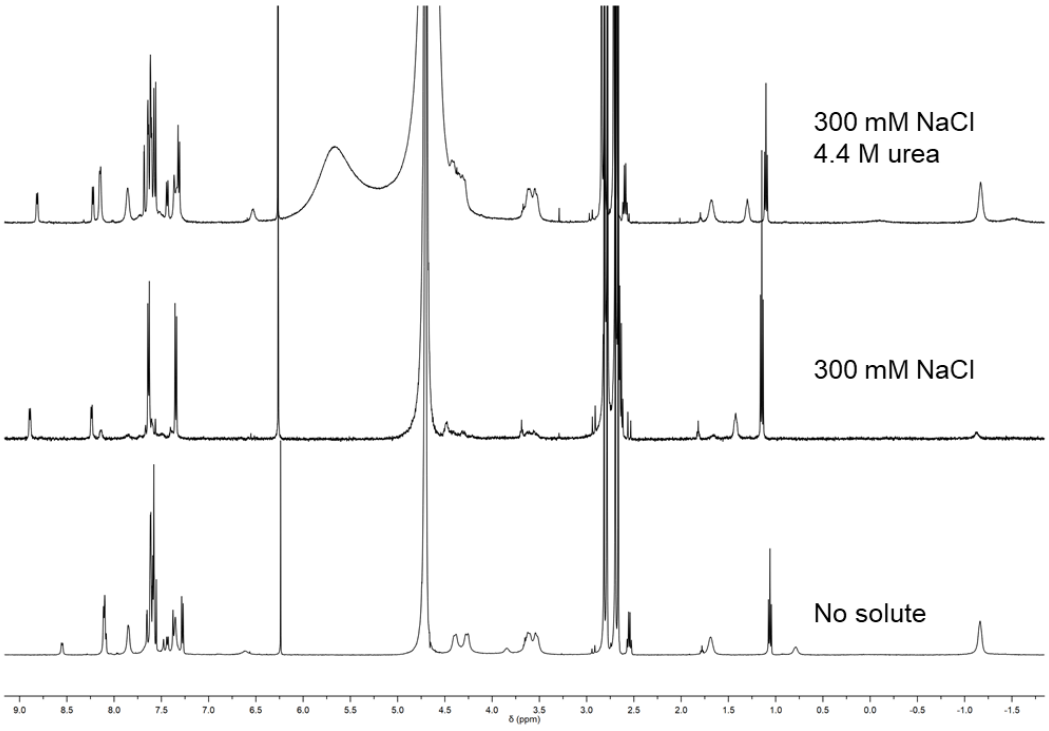

Figure 3. 25 ^{1}H spectra show that neutral hydrophobic, **D-Bz** is more resilient to extreme solute conditions than the charged hydrophobic, **D-Py+** derivative. Without solute, **D-Py+** is favoured 71:29, while 300 mM NaCl induces precipitation of both dimers. When 4.4 M urea and 300 mM NaCl is added, the spectra shows an increase in **D-Bz** resonances (*ortho*-protons, 6.54 ppm) and a proportional decrease in **D-Py+** resonances (*ortho*-protons, 8.13 ppm), shifting the ratio to 64:36.

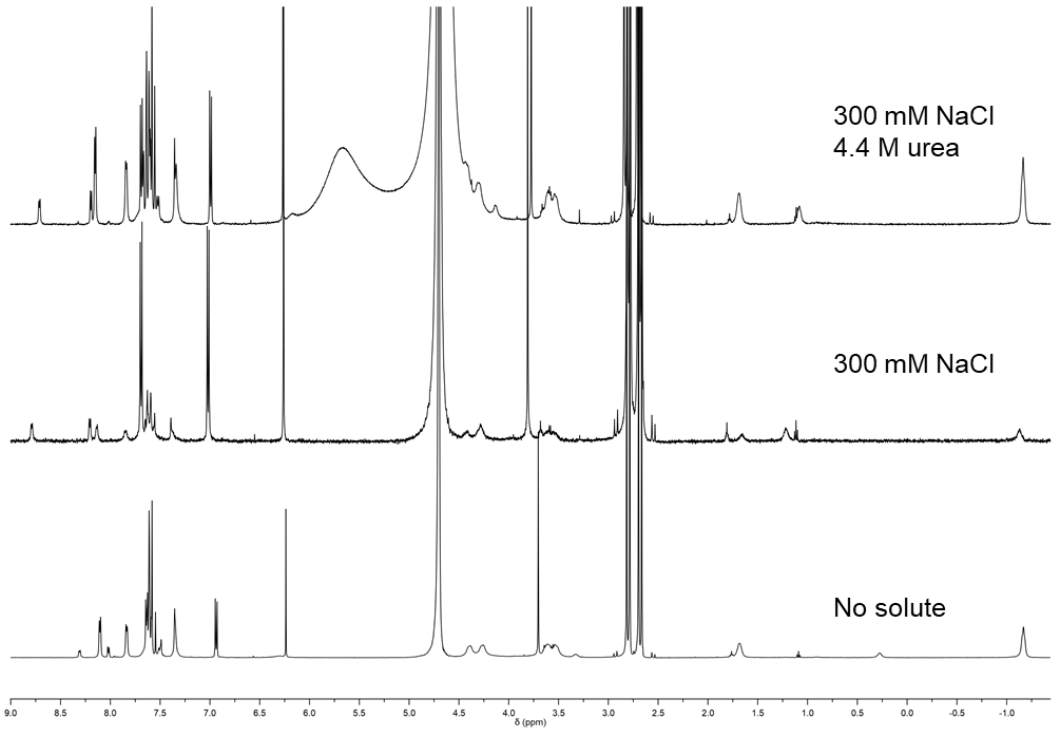

Figure 3. 26 ^{1}H spectra show that neutral polar, **D-OMe** is more resilient to extreme solute conditions than the charged hydrophobic, **D-Py+** derivative. Without solute, **D-Py+** is favoured 84:16, while 300 mM NaCl induces precipitation of both dimers. When 4.4 M urea and 300 mM NaCl is added, the spectra shows an increase in **D-Bz** resonances (*ortho*-protons, 6.2 ppm) and a proportional increase in **H-Py+** resonances (*ortho*-protons, 8.71 ppm), shifting the ratio to 68:32.

Chapter 4: Analyte-driven disassembly and turn-on fluorescent sensing in competitive biological media

This work was adapted from a previously published paper.

Meagan A. Beatty, Jorge Borges-González, Nicholas J. Sinclair, Aidan T. Pye, Fraser Hof.

J. Am. Chem. Soc., **2018**, 140, 3500-3504.

FH conceived of the idea. NS developed synthetic protocols to first synthesize the precursor and the chemosensor. MB supervised the undergraduates JB and AP as they carried out preliminary studies: JB carried out preliminary UV-Vis/fluorescence measurements and ^{1}H NMR dilution and titrations experiments. AP contributed synthesis of starting materials. Shaun MacLean assisted with molecular modeling. MB designed and carried out all assembly characterization and sensing experiments: UV-Vis/fluorescence titrations, 1D DOSY, 2D NOESY, ^{1}H NMR titrations, quantitative NMR, and enzymatic reactions. MB and FH co-wrote the paper. MB coined the term "DimerDye".

4.1 Foreword

Supramolecular chemosensors that detect biological analytes in complex mixtures were introduced in Sections 1.4 and 1.5. These types of sensors operated by indicator displacement, and the examples presented carried out functions that ranged from detecting enzymatic reaction products, to cancer markers in plasma and neurotransmitters inside living cells. The supramolecular complexes involved in these examples all were able to withstand the negative effects of salt that are inevitably present in the respective media. Similarly, our yin-yang self-assemblies in Chapter 3 and Section 1.6 had proven to be tolerant to salts and benefited from large amounts of organic co-solutes. From Chapter 2 we learned that these dimers are responsive and can be disrupted only in the presence of hydrophobic cations.

We wanted to transform the original yin-yang dimers into chemosensors to detect biological cations. We hoped that this new self-assembling chemosensor would inherit the characteristics from dimers in Chapter 2 and Chapter 3. More specifically, that they will disassemble in the presence of a targeted guest yet remain functional in salty solutions.

4.2 Introduction

Indicator displacement assays (IDAs), introduced in Chapter 1.4, are the central mechanism by which supramolecular hosts are converted into sensors.[106, 197-198] This approach has been widely used, having been demonstrated with many different dyes complexed with macrocycles[62, 199-201] or clefts[104, 107, 168] that target analytes of many classes. IDAs that are intended to detect analytes in real biological solutions often need case-by-case optimization. The K_d of host-dye and host-analyte equilibria must be compatible with each other, and both of those equilibria are sensitive to co-solutes.[106, 202]

Real-world solutions contain salts, organic molecules, complex buffers, and biological components that can affect binding equilibria and/or the dye's emission in ways that diminish signal or render the IDA inoperative. There were many examples in Chapter 1 of sulfonatocalix[n]arene hosts (e.g. **SC4A**) paired with the dye lucigenin (**1.29**) (Figure 4. 1), creating IDAs for sensing neurotransmitters, post-translationally modified peptide, and other signaling molecules.[67, 203-205] To re-introduce a key example from Chapter 1, **SC4A** and **1.29** were used inside living cells to successfully detect acetylcholine. However, anions abundantly found in cells such as chloride quench **1.29** fluorescence by up to 95%, reducing the size of signal that can be obtained by this IDA. Furthermore the salts in the cell growth medium ultimately weakened the complex by 100-fold.[109, 117, 206] Cucurbiturils (e.g. **CB7**, Figure 4. 1) have also been paired with a variety of dyes to detect many different amines. [207-209] However, they too operate best in low-Na^+ solutions because Na^+ binds to the oxygen-lined portals and decreases binding of both analytes and indicators.[210-211]

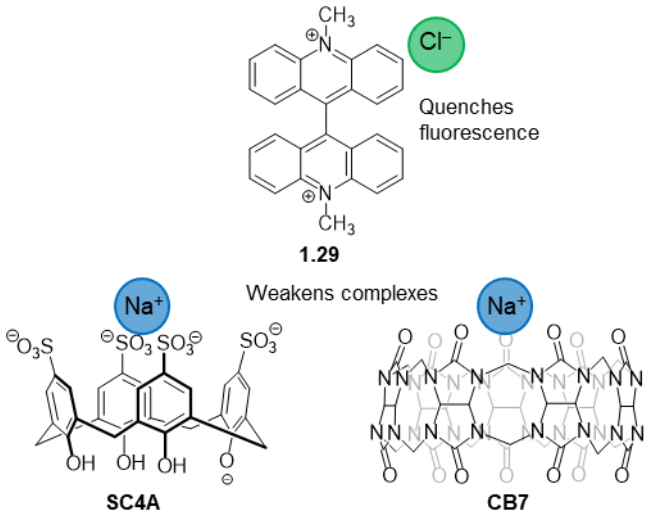

Figure 4. 1 Responses of common IDA assemblies to NaCl. a) Lucigenin (**1.29**), a popular dye used in IDA, is quenched by anions such as chloride. b) Cucurbiturils and **SC4A** have weakened affinities for dyes and guests in the presence of Na^+.

Our collection of self-assembling calix[4]arene hosts are tolerant to salts and other co-solutes yet responsive to hydrophobic cations. As discussed in Chapter 1, these dimers get stronger in the presence of added salt and remain faithfully assembled in real biological fluids.[134] While in Chapter 2, dimers were shown to disassemble and encapsulate hydrophobic cations such as tetramethylammonium but remain inert to hydrophilic cations like methylamine. We sought to translate these unique features to develop a new class of supramolecular chemosensors that can sense analytes in biological solutions.

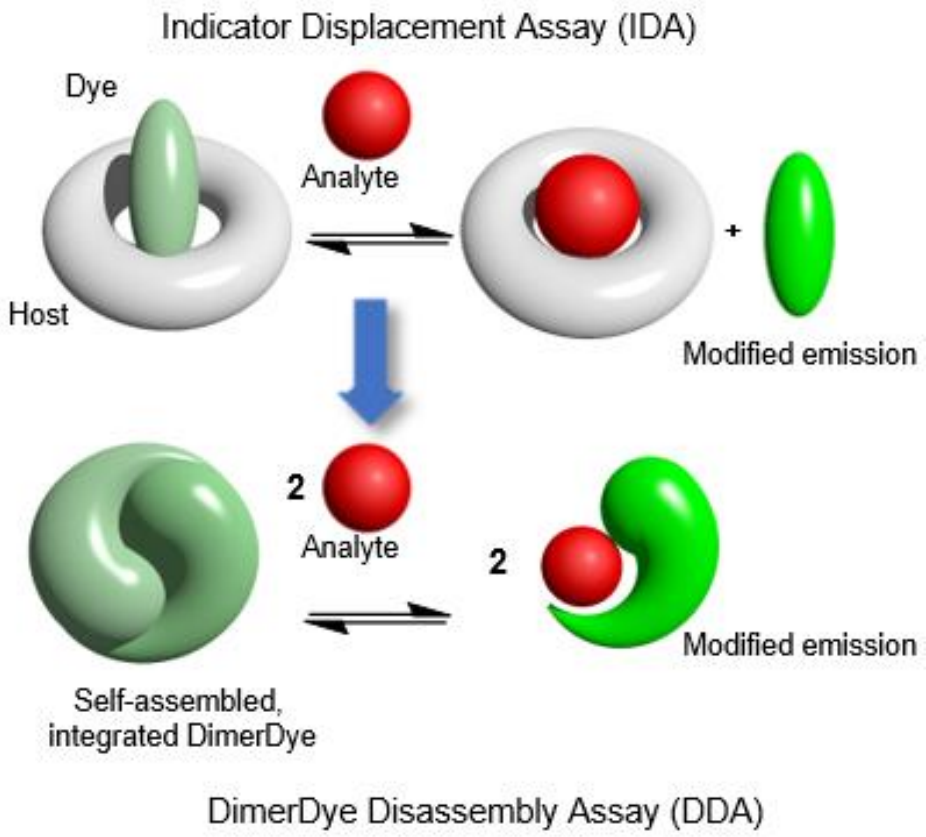

Figure 4. 2 Cartoon depiction of a) an Indicator Displacement Assay and b) a DimerDye Disassembly Assay which involves an integrated host-dye sensor that disassembles in the presence of an analyte to produce a turn-on fluorescence response.

The new chemosensors integrate both host and dye within a single molecular species (a "DimerDye") that homodimerizes in water and can be implemented as a DimerDye Disassembly assay (DDA). DDA would achieve analyte sensing because 1) the self-assembly forces two copies of fluorophore to stack upon each other, and 2) guest binding causes programmed disassembly of the dimers into a host-guest complex, thereby changing the photophysical response (Figure 4. 2).

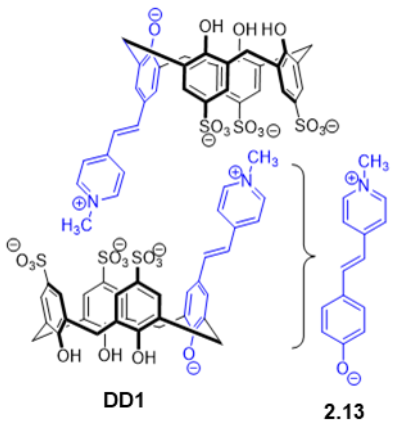

Figure 4. 3 Brooker's Merocyanine (**2.13**) is integrated into the calix[4]arene macrocycle to form **DD1**, which dimerizes in a similar fashion to ***tBu*$_1$-SC4A**.

We designed the integrated host-dye merocyanine calixarene (**DD1**) to test the DDA concept. Brooker's merocyanine (**2.13**) is a styryl dye that displays strong solvatochromism.[99, 212] The design of **DD1** includes the phenolic ring of **2.13** directly within the macrocyclic core of calix[4]arene[213] (Figure 4. 3). We anticipated that the merocyanine arm would serve as hydrophobic element to bind into the calixarene pocket of a second monomer to drive a dimeric self-assembly, wherein each monomer bears a net –3 charge.[152, 214]

4.3 Results and Discussion

DimerDyes were efficiently synthesized by site-specific functionalization of the calix[4]arene skeleton. The aldehyde trisulfonate **3.3** previously discussed in Chapter 3 was used as a key intermediate. Condensation reactions with **3.3** and picolinium derivatives produced the targeted merocyanine calixarenes, **DD1** (*N*-methyl) and **DD2** (*N*-ethyl)**,** with 37% and 30% yield, respectively, after reverse-phase HPLC purification (Scheme 4. 1).

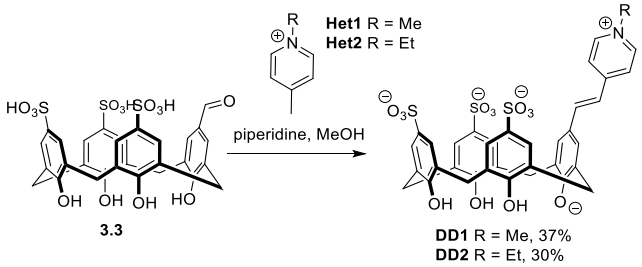

Scheme 4. 1 Synthesis of **DD1** and **DD2**.

NMR studies of **DD1** and **DD2** demonstrate that they self-assemble in water. The pyridinium aryl protons of **DD1** shift upfield by ≥1 ppm relative to chemical shifts observed for free **2.13**, while the *N*-methyl resonance moves >3.5 ppm upfield, which is diagnostic of encapsulation deep within the calixarene macrocycle (Figure 4. 4a). All protons on the merocyanine arm show upfield shifts in D_2O relative to values in d_6-DMSO, consistent with the existence of an assembled state in water and free monomer in DMSO (Table 4. 2). The *N*-ethyl derivative, **DD2,** showed similar upfield chemical shifts in the NMR (Figure 4. 4b and Table 4. 3) while the *N*-ethyl triplet and quartet provided easily assigned protons for structural analysis. 2D NOESY correlations between Et protons (−1.01 ppm) and upper-rim protons (7.64 ppm) are diagnostic of the assembled state (Figure 4. 4c). The rigidity of the *E*-alkene ensures that intramolecular self-inclusion of pyridinium arms is impossible.

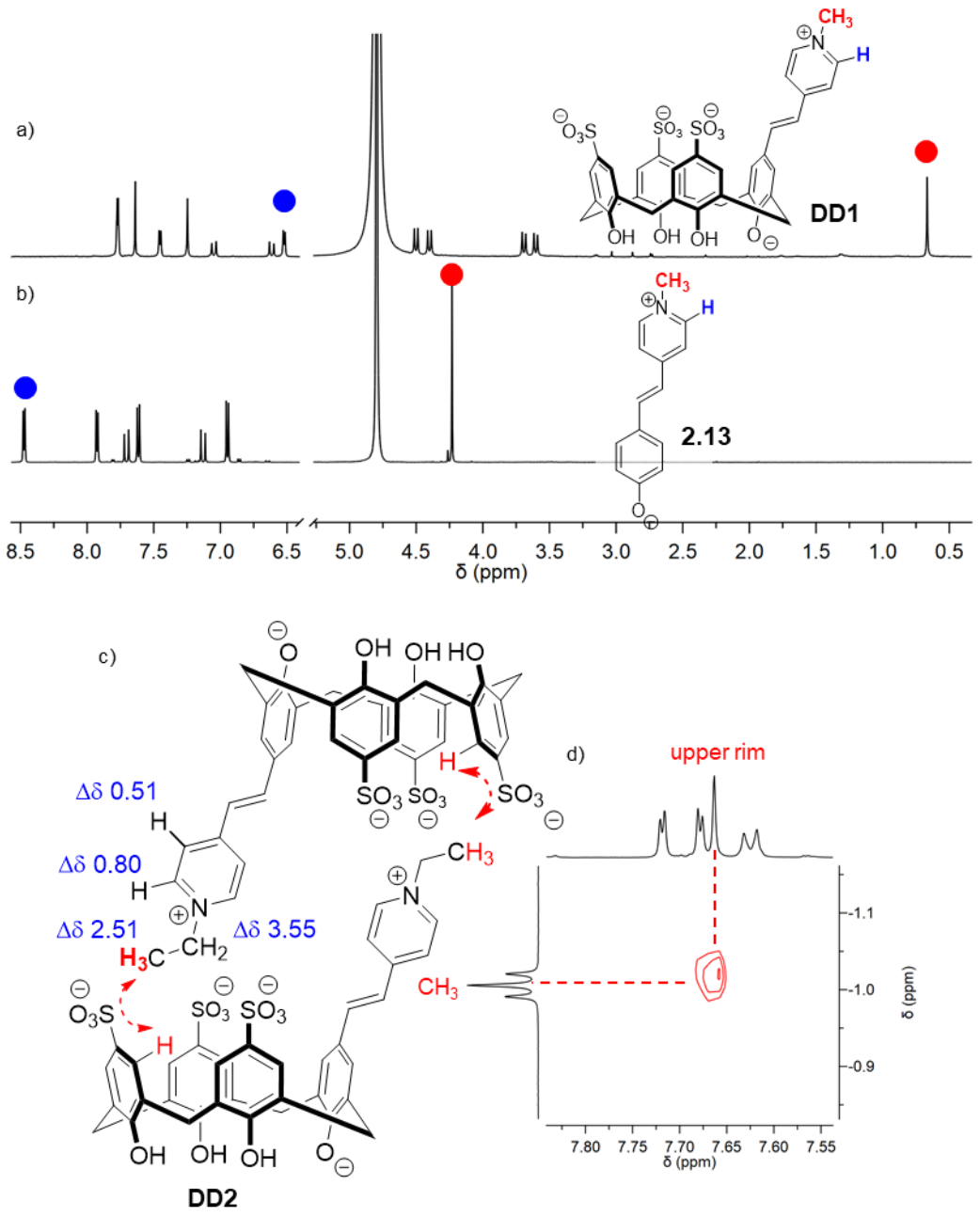

Figure 4. 4 1D and 2D NMR data support the formation of the expected dimers. Key resonances, *N*-CH_3 singlet (red dots) and *ortho*-protons (blue dots), are upfield shifted in a) **DD1** in comparison to the b) parent dye, **2.13**, which is indicative of dimerization. c) *N*-ethylpyridinium protons are upfield-shifted in D_2O (dimer) relative to their normal positions in d_6-DMSO (monomer). d) The upfield-shifted **DD2** ethyl group shows an NOE with calix[4]arene upper rim protons. Solutions all in NaH_2PO_4/Na_2HPO_4 (100 mM, pD 7.8).

DOSY experiments confirm that **DD1** and **DD2** exist as dimers in water. The diffusion coefficient of **DD1**, **DD2** and the monomeric control, **SC4A**, were measured by

1D DOSY, and the hydrodynamic radii (r_H) were calculated using the Stokes-Einstein equation (Table 4. 1). The r_H for both DimerDyes are comparable to predicted radii from simple molecular models (Figure 4. 11 and Figure 4. 12).

Table 4. 1 DOSY characterization of **DD1**, **DD2** dimers and monomeric control calix[4]arene, **SC4A**.

Compound	D (m^2/s)	r_H[a)] (Å)	r (Å)
SC4A	$(3.43 \pm 0.07) \times 10^{-10}$ [a)]	7.1 ± 0.2	6.6[b)]
DD1	$(2.37 \pm 0.04) \times 10^{-10}$	10.3 ± 0.5	11.6[c)]
DD2	$(2.11 \pm 0.08) \times 10^{-10}$	11.5 ± 0.6	11.2[c)]

a) Average of two replicates. b) Values for are from X-ray crystal structure. c) Optimized modeled structures (see Supp. Info.).

Dimerization of **DD1** in water is >500-fold stronger than that of ***tBu*$_1$-SC4A**. ITC dilutions across many different concentration ranges showed little or no heat evolution (data not shown), showing that the dimer dissociation is nearly thermoneutral under these conditions and therefore can't be studied by calorimetry.[215] Instead, upfield-shifted NMR resonances for [**DD1**]$_2$ were identified and integrated for samples containing different total concentrations **DD1**. Free monomer concentration was determined by mass balance, providing a value for K_d of (3.3 ± 2.0) μM from the mean of 3 different experiments at 2 different values of [**DD1**]$_t$ (see Supp. Info.).

The self-assembly of **DD1** gives it photophysical properties that are distinct from those of **2.13**. **DD1** forms a yellow solution in neutral water with an extinction coefficient of 26,500 $M^{-1}cm^{-1}$ as a dimer species (see Supp. Info.). Compound **2.13** is fluorescent in water and in DMSO (see Supp. Info.), while **DD1** is fluorescent in DMSO but is non-emissive in neutral water (see Supp. Info.). Compound **2.13** remained fluorescent when mixed with **SC4A** (see Supp. Info.), showing that the dark state of **DD1** in water arises because of the position of two copies of the chromophore within the **DD1** dimer, and not simply from the binding of a merocyanine dye to a calixarene pocket. Fluorescence and NMR data together demonstrate the structural principles of the DimerDye design: 1) NMR data show that **DD1** is monomeric in DMSO, and dimeric in water. 2) **DD1** is emissive as a monomer, but not emissive as a dimer due to quenching of the fluorophore's excited state by the second adjacent fluorophore.

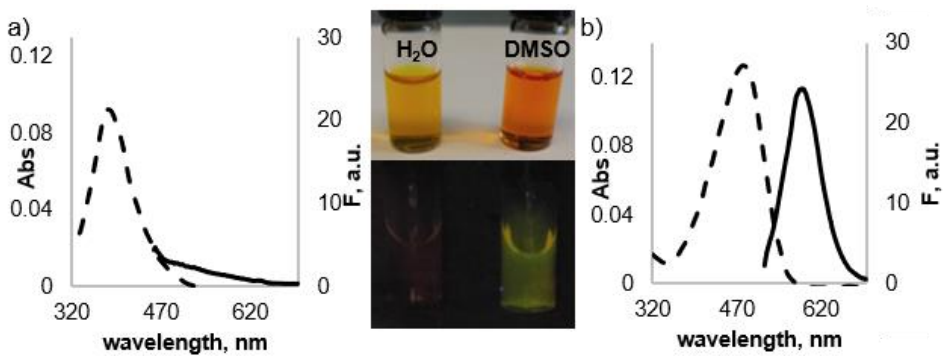

Figure 4. 5 Absorption (dotted line) and fluorescence (solid line) spectra of **DD1** (4 μM) in a) Na_2HPO_4/NaH_2PO_4 buffer (10 mM, pH 7.4, $\lambda_{ex.}$ 382 nm) and b) DMSO ($\lambda_{ex.}$ 482 nm, λ_{em} 585 nm). Pictures of **DD1** show the lack of fluorescence in water (left vials) and visible emission in DMSO (right vials) when irradiated by a handheld UV lamp at 365 nm. All solutions are homogeneous.

DD1 is a turn-on fluorescent sensor for guests in water. A panel of amino acids were studied by fluorescence (Figure 4. 6, Figure 4. 20) and NMR. Sulfonated calixarenes bind Kme3 and other amino acids with K_d values between 30 and 2000 μM, meaning that concentrations of these analytes in this range are needed to disrupt the homodimers.[216] The greatest fluorescence response was observed for Kme3, and a negligible response was seen for K (Figure 4. 6b and c). Added salts are tolerated, causing slightly decreased signal intensity but better Kme3/K selectivity (Figure 4. 21). NMR titrations of Kme3 into **DD1** provided insight into the interactions between analyte and sensor. Most **DD1** resonances broadened with the increase of Kme3 concentration indicating intermediate exchange of [**DD1**]$_2$ and [**DD1**]-Kme3 on the NMR timescale. The resonances that were the most broadened were the protons that experience the largest chemical shift change during the transition from dimer to analyte-sensor complex, in particular the *N*-methyl group, and pyridinium protons (Figure 4. 7). Controls showed that titrating the weaker guest lysine into **DD1** produced only slight broadening at significantly higher lysine concentrations (Figure 4. 8), while titrations of Kme3 into **2.13** caused no changes in chemical shift (Figure 4. 19). These data collectively prove that host-guest recognition within the calixarene pocket causes disassembly of the dimer, which is accompanied by a turn-on fluorescence response.

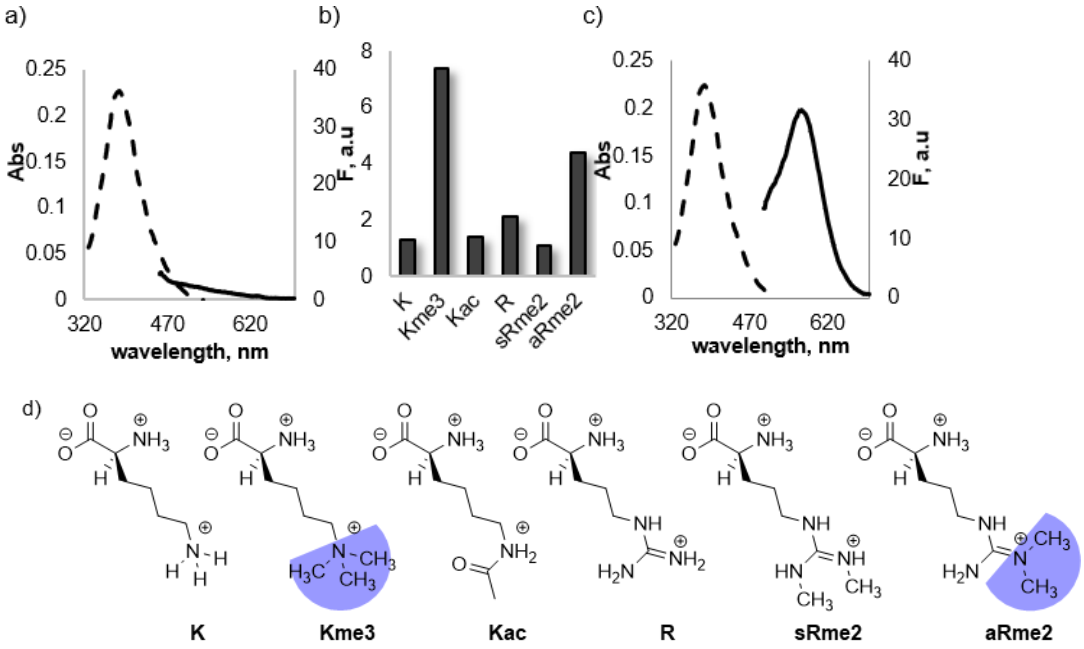

Figure 4. 6 Absorption (dotted line) and fluorescence (solid line) of **DD1** (10 µM) in Na_2HPO_4/NaH_2PO_4 buffer (10 mM, pH 7.4, $\lambda_{ex.}$ 382 nm) a) without guest c) with Kme3 (1 mM, $\lambda_{ex.}$ 382 nm, $\lambda_{em.}$ 575 nm). b) Comparison of fluorescence intensities observed with various amino acids (250 µM, $\lambda_{ex.}$ 382 nm, λ_{em} 575 nm). d) The structures of each analyte tested show the two hydrophobic cations, trimethyllysine (Kme3) and asymmetric dimethyl arginine (aRme2), share a similar shape and induce the strongest responses over the hydrophilic cations lysine (K), *N*-acetyllysine (Kac), arginine (R) and asymmetric dimethylarginine (aRme2).

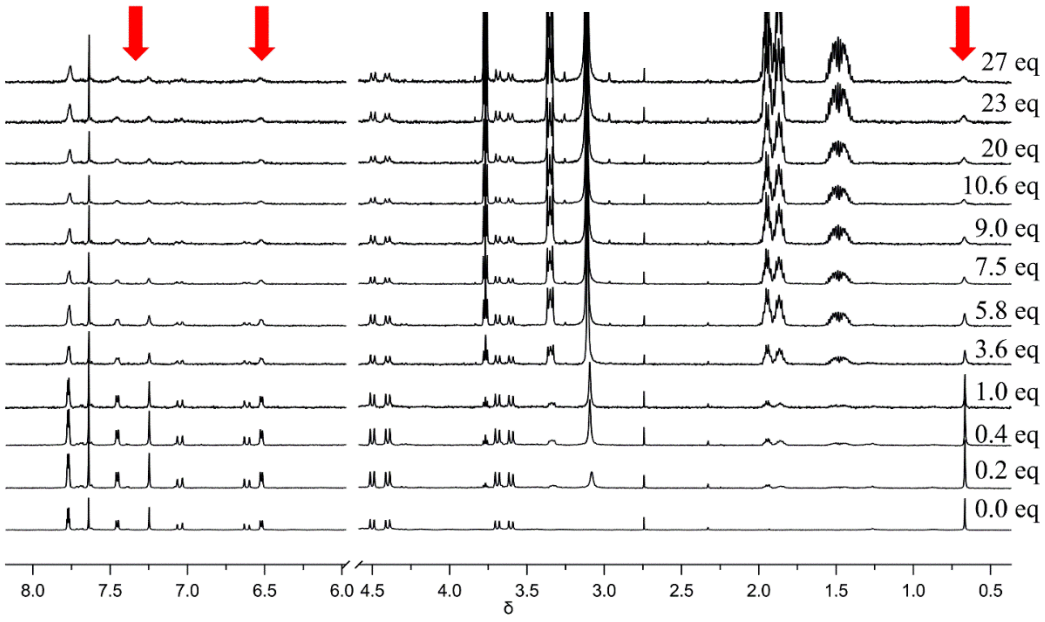

Figure 4. 7 ^{1}H NMR titration of trimethyllysine (Kme3) (10 mM) into **DD1** (250 µM) suggest host-guest complexation. Red arrows indicate **DD1** resonances broadening and decreasing in intensity due to dimer dissociation and complexation with Kme3.

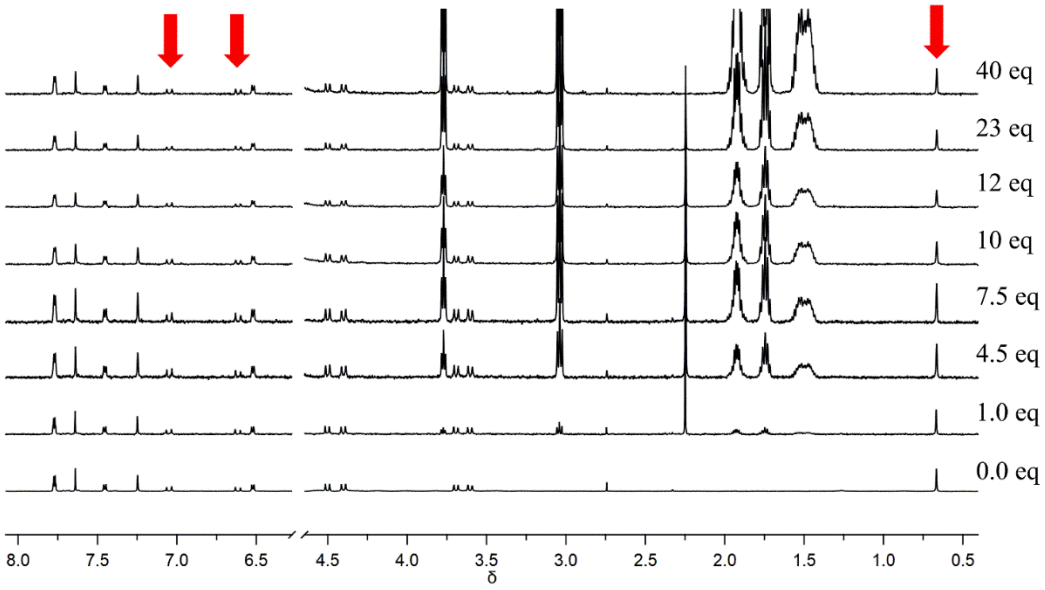

Figure 4. 8 ^{1}H NMR titrations of lysine (K) (10 mM) into **DD1** (250 µM), arrows indicate the lack of change in **DD1** resonances as K does not disrupt the dimer under these conditions.

DD1 operates in complex media and on complex analytes. Histone peptide tails are home to epigenetic methyllysine marks that are under the control of methyltransferases and

demethylases. Calixarenes bearing three sulfonates routinely bind cationic Kme3 peptides with K_d values of 0.17–5 μM, while retaining selectivity over unmethylated peptides.[15] We tested **DD1** with histone tails in typical reaction buffers for *S*-adenyl-methionine (SAM)-dependent methyl transferases (Figure 4. 23) and Fe^{2+}- and cofactor-dependent demethylases (Figure 4. 24). In each case, the methylated histone tail gave a turn-on fluorescent signal that was significantly greater than response to its unmethylated counterpart. We conducted an enzymatic methylation of a H3K4 21-mer histone tail peptide with methyltransferase PRDM9 in 96-well format. **DD1** produced a real-time, turn-on fluorescence signal as the reaction produced methylated product (Figure 4. 9b, c, and Figure 4. 25). The assay is also reversible in that **DD1** was able to monitor the demethylation of a 21-mer H3K9me3 peptide by JMJD2D. In this case, we started with a fluorescent signal as the substrate peptide contained trimethyllysine. As JMJD2D de-methylated the peptide to form the dimethylated product, H3K9me2, the signal decreased as it is a weaker guest for calixarenes (Figure 4. 10 and Figure 4. 26).

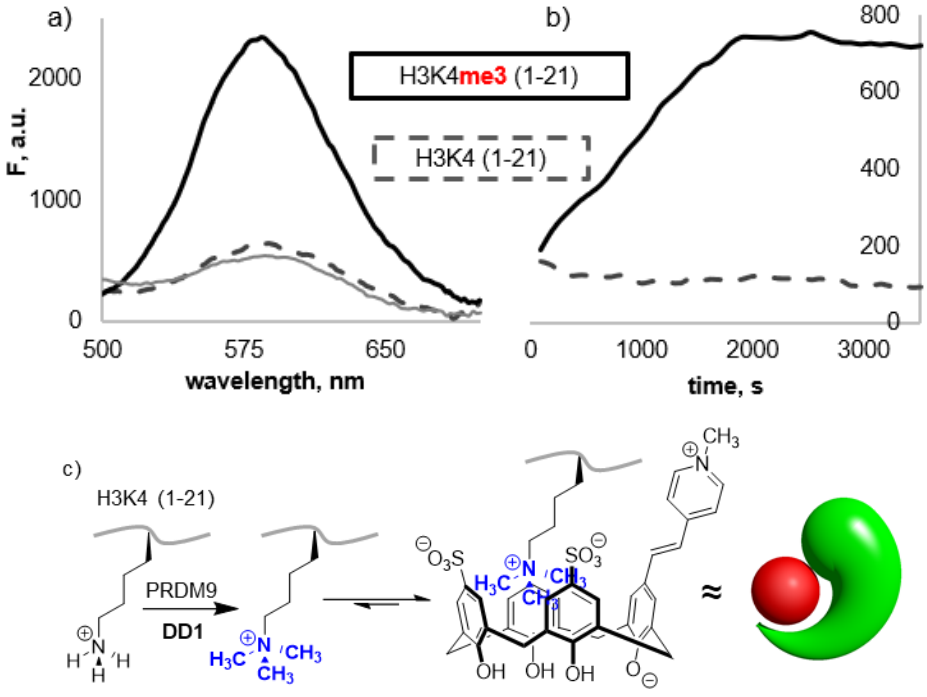

Figure 4. 9 a) Emission spectra of **DD1** (8 μM, $\lambda_{ex.}$ 384 nm) in the reaction conditions (solid gray line), with H3K4me3 (40 μM, solid black line), and H3K4 (40 μM, dotted line). b) Fluorescence increases as methyltransferase, PRDM9 (460 nM), methylates H3K4 (40 μM) with **DD1** (8 μM, $\lambda_{ex.}$ 384 nm, λ_{em} 585 nm) in the reaction conditions: Tris (50 mM, pH 8.5), NaCl (30 mM), DTT (1 mM), SAM (300 μM). c) Reaction scheme

of PRDM9-catalysed conversion of H3K4 to H3K4me3, which complexes with **DD1** inducing a turn-on fluorescence response.

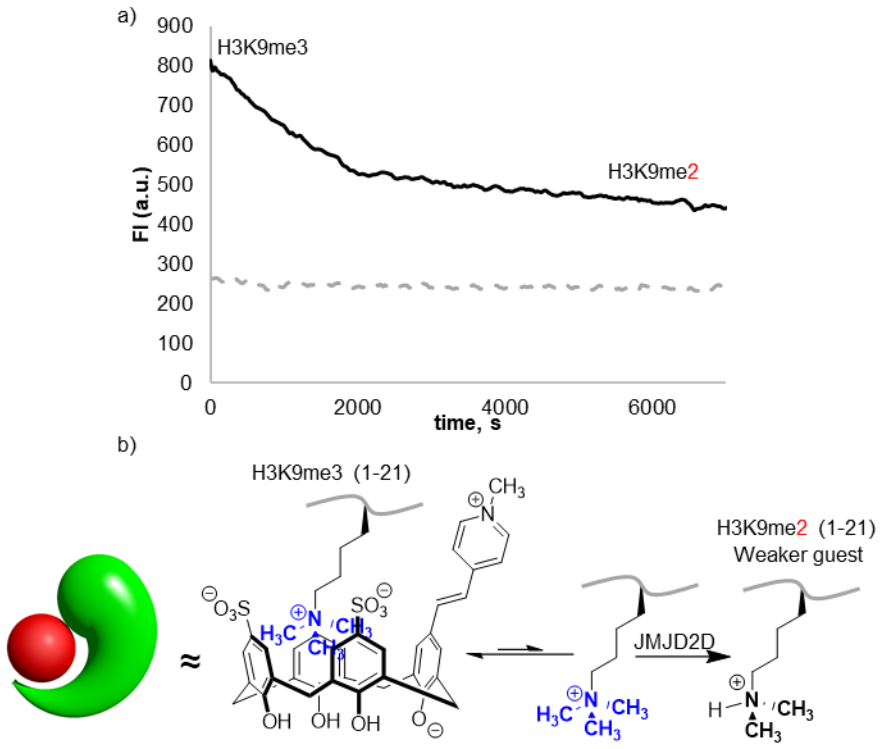

Figure 4. 10 a) Fluorescence decreases as demethyltransferase, JMJD2D (400 nM), removes a single methyl from H3K9me3 (50 μM) to form the dimethylated product (H3K9me2) with **DD1** (8 μM, $\lambda_{ex.}$ 384 nm, λ_{em} 580 nm) in the reaction conditions: NaH_2PO_4/Na_2HPO_4 buffer (50 mM, pH 7.4), $(NH_4)_2Fe(SO_4)_2$ (100 μM), 2-oxoglutaric acid (200 μM), ascorbic acid (500 μM). The dotted line indicates the level of fluorescence response for a control well containing the fully demethylated peptide H3K9 and **DD1** at the same concentrations. b) Reaction scheme of JMJD2D-catalysed conversion of H3K9me3 to H3K9me2, which is a weaker guest for **DD1** and does not induce the same fluorescent response as the substrate peptide.

The sensing of enzymatic reaction by **DD1** is a rare example of real-time analysis of methyltransferase activity. All commercial assays for methyltransferases and demethylases require the reaction to be halted at various times before undergoing separate steps to develop signal through a coupled colorimetric/fluorometric reaction,[217] isolation and detection of an incorporated radioisotope,[218] or by some antibody-mediated binding event.[219] Only a few continuous assays that use supramolecular approaches have been reported. One example introduced in Section 1.4 successfully monitored the trimethyllysine product formation in real-time.[67, 202] Another example mentioned in Section 1.4 operates through the dis-aggregation of a micellar aggregate containing a cavitand and

quenched indicator. This unusual assay reagent gives a turn-off response for a demethylase reaction in the presence of salts, co-solutes and transition metals.[62, 220-221]

This approach incorporates features of other supramolecular sensing schemes in unique ways. Previously published alternatives to IDA fall broadly into three categories: intramolecular indicator displacement assays (IIDAs)[222] and receptor-spacer-reporter (RSR) sensors[223] involve hosts covalently linked to chromophores; another collection of host-type sensors rely on aggregation-induced emission (AIE) arising in various ways from analyte binding.[224-226] DimerDyes relate structurally to IIDAs, but differ in that the dye is included into a recognition pocket in an assembled, intermolecular complex. This dimer assembly is similar to AIE-based sensors in that a change in supramolecular environment induces a photophysical response. But it differs by involving a programmed dimeric assembly with tight control over chromophore-chromophore interactions instead of extended aggregates, and by producing a turn-on response to sensor disassembly that is the opposite of AIE. Unlike RSRs, DimerDyes don't need the analyte to have any direct influence on the excited state of the fluorophore.

4.4 Conclusions

We successfully transformed the original yin-yang structure into a fluorescent chemosensor that operates by disassembly and complexation with select guests. This design is general and adaptable, and we anticipate that this mode of disassembly-induced turn-on sensing will operate for many different dimeric species that include a host and an integrated dye in an appropriate architecture. The DimerDyes reported here have an intrinsic tolerance to diverse biological solutions that we will aim to preserve and exploit as we expand the DimerDye concept to more hosts, dyes, and analytes.

4.5 Supporting information

4.5.1 General information and materials

^{1}H, ^{13}C, 2D NOESY, and 1D DOSY were recorded on a Bruker Avance 500 MHz spectrometer unless otherwise indicated and processed with MestReNova by Mestrelab Research S.L. All reported chemical shifts were reported in ppm with respect to an internal

standard: either *cis*-butenedioic acid (maleic acid) at 6.2 ppm or 2,2,3,3-d_4-3-(trimethylsilyl)propionic acid sodium salt at 0.0 ppm. Deuterated solvents were purchased from Sigma Aldrich and NaH_2PO_4/Na_2HPO_4 (100 mM, pD 7.8) in D_2O were prepared in lab and the pD was adjusted with NaOD/DCl solutions. Mass spectra of novel compounds were collected on a Thermo Scientific Ultimate 3000 ESI-Orbitrap Exactive. All UV-Vis and fluorescence spectra were collected on a Molecular Device Spectra M5 spectrometer in a quartz cuvette. Titrations and dilutions were conducted in a NUNC black walled, optical bottom 96-well plate. Enzyme assay optimization and kinetic experiments were conducted on a Cytation-5 BioTek Imaging Reader. Infrared (IR) spectra were obtained using a Perkin Elmer 1000 FT-IR spectrometer. Data are represented as follows: frequency of absorption (cm^{-1}), intensity of absorption (s = strong, m = medium, w =weak, br = broad). Melting points were collected on a Gallenkamp Melting Point apparatus. Compounds **3.3**, **DD1**, and **DD2** were purified using a Shimadzu Prominence HPLC system with UV detection at 280 nm and 370 nm.

H3K9(7-14) and H3K9me3(7-14) were synthesized on a Liberty 1 solid-phase microwave peptide synthesizer (CEM). The peptides were purified by a 9.4 mm x 250 mm semi-preparative Agilent Eclipse XDB-C18 5 μm on a Shimadzu Prominence HPLC system with UV detection at 280 nm. A gradient ran from 95% H_2O (+0.1% TFA)/5% CH_3CN (+0.1% TFA) to 75% H_2O (+0.1% TFA) /25% CH_3CN (+0.1% TFA) over 18 min. The fractions were collected and lyophilized to a white powder.

H3K4(1-21) and H3K4me3 (1-21) for both enzyme assays were purchased from Anaspec. Recombinant JMJD2D was purchased from Active Motif. Recombinant PRDM9 (191-414) was purchased from Active Motif, and stored as 4 μL (23 μM) aliquots to avoid multiple thaw-freeze cycles. S-(5′-Adenosyl)-L-methionine chloride dihydrochloride (SAM) was purchased from Sigma Aldrich.

Compound **3.3** was synthesized as outlined in Chapter 3. **2.13** was synthesized according to the literature.[227]

4.5.2 Synthesis of DD1 and DD2

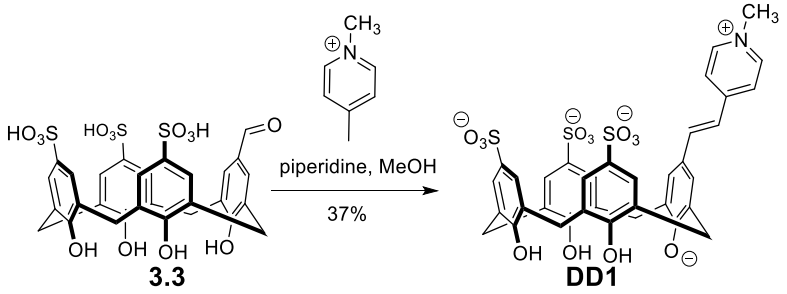

DD1. Compound **3.3** (50 mg, 72 μmol), *N*-methyl-4-methylpyridinium iodide (17 mg, 80 μmol) and piperidine (200 uL, 2.1 mmol) were dissolved in MeOH (3 mL) and heated at reflux overnight. The reaction mixture was reduced to an oil under reduced pressure and purified using a gradient run from 90% H_2O (+0.1% TFA)/10% CH_3CN (+0.1% TFA) to 35% H_2O (+0.1% TFA)/65% CH_3CN (+0.1% TFA) over 25 min the fraction were collected, and lyophilized to a pure yellow solid (20 mg, 37%). Mp: decomposed > 280 °C. FT-IR (cm^{-1}): 3200 (br), 1637 (w), 1625 (w), 1454 (w), 1168 (br), 1112 (m), 1037 (s), 782 (m), 625 (s). ^1H NMR (500 MHz, 100 mM H_2PO_4/HPO_4 in D_2O): δ 7.77 (d, *J* = 3.6 Hz, 4H), 7.64 (s, 2H), 7.45 (d, *J* = 6.7 Hz, 2H), 7.25 (s, 2H), 7.05 (d, *J* = 16.2 Hz, 2H), 6.61 (d, *J* = 16.3 Hz, 2H), 6.52 (d, *J* = 6.6 Hz, 2H), 4.50 (d, *J* = 13.1 Hz, 2H), 4.40 (d, *J* = 13.1 Hz, 2H), 3.69 (d, *J* = 13.3 Hz, 2H), 3.60 (d, *J* = 13.3 Hz, 2H), 0.67 (s, 3H). ^{13}C NMR (125 MHz, d_6-DMSO): δ 153.6, 153.0, 151.3, 144.5, 140.6, 140.5, 140.0, 129.5, 129.4, 128.2, 128.1, 128.0, 127.8, 126.8, 123.4, 120.5, 44.6, 31.1. HR-MS ($[M-2H+Na]^-$, *m/z*): Calculated for $C_{36}H_{29}NNaO_{13}S_3^-$ 802.07042, Found 802.07057.

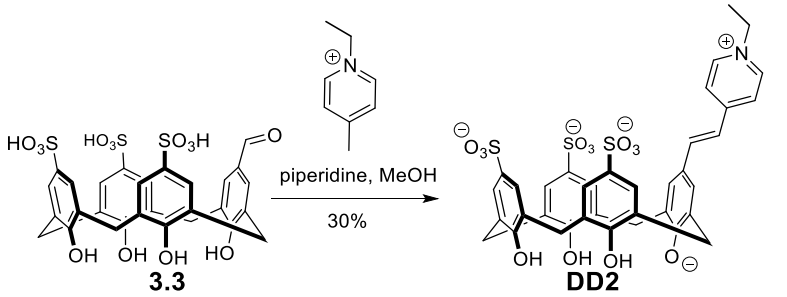

DD2. Compound **3.3** (50 mg,723 μmol), N-ethyl-4-methylpyridinium iodide (19 mg, 80 μmol), and piperidine (200 uL, 2.0 mmol) were dissolved in MeOH (3 mL) and heated at reflux overnight. The reaction mixture was reduced to an oil under reduced pressure and purified by a gradient run from 90% H_2O (+0.1% TFA)/10% CH_3CN (+0.1% TFA) to 35%

H_2O (+0.1% TFA)/65% CH_3CN (+0.1% TFA) over 25 min, the fraction were collected, and lyophilized to a pure yellow solid (20 mg, 30%). Mp: decomposed > 280 °C. FT-IR (cm^{-1}): 3400 (br.), 1644 (w), 1618 (w), 1592 (w), 1457 (w), 1159 (m), 1034 (s), 784 (m), 623 (s). ^{1}H NMR (500 MHz, 100 mM H_2PO_4/HPO_4 in D_2O): δ 7.72 (d, *J* = 2.2 Hz, 2H), 7.68 (d, *J* = 2.6 Hz, 2H), 7.64 (s, 2H), 7.45 (d, *J* = 6.7 Hz, 2H), 7.44 (d, *J* = 6.6 Hz, 2H), 7.25 (s, 2H), 7.05 (d, *J* = 16.2 Hz, 2H), 6.61 (d, *J* = 16.3 Hz, 2H), 4.50 (d, *J* = 13.1 Hz, 2H), 4.40 (d, *J* = 13.1 Hz, 2H), 3.69 (d, *J* = 13.3 Hz, 2H), 3.60 (d, *J* = 13.3 Hz, 2H), 1.16 (q, *J* = 7.4 Hz, 2H), −1.01 (t, *J* = 7.4 Hz, 3H). ^{13}C NMR (125 MHz, d_6-DMSO): δ 154.1, 153.2, 151.9, 150.4, 143.8, 151.1, 143.8, 141.0, 129.3, 128.2, 127.8, 127.7, 127.1, 126.9, 126.6, 123.5, 120.5, 54.0, 31.3, 31.2, 14.8. HR-MS ($[M-2H+Na]^-$, *m/z*): Calculated for $C_{37}H_{31}NNaO_{13}S_3^-$ 816.08607, Found 816.08638.

4.5.3 ^{1}H and ^{13}C NMR spectra of DD1 and DD2

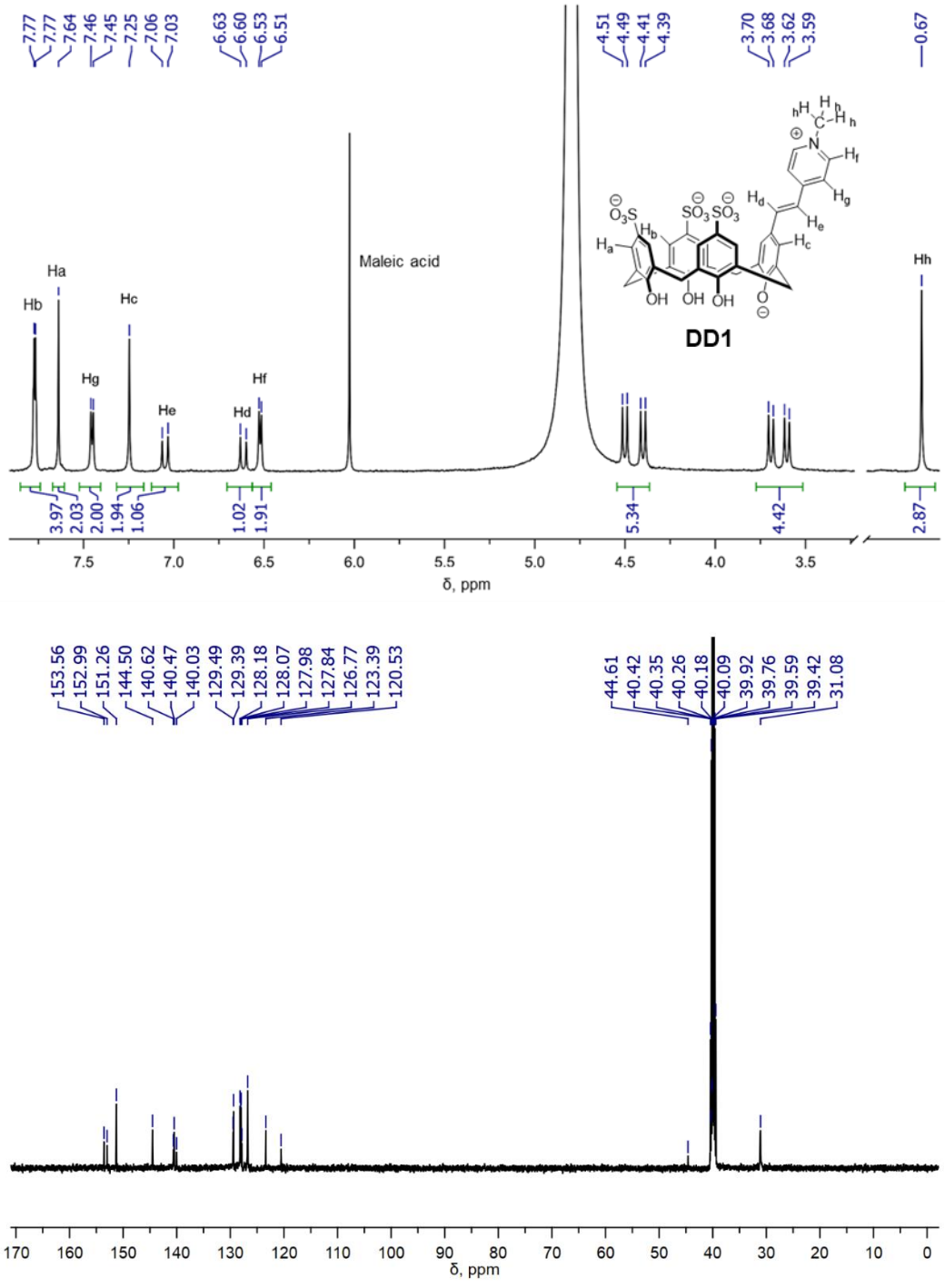

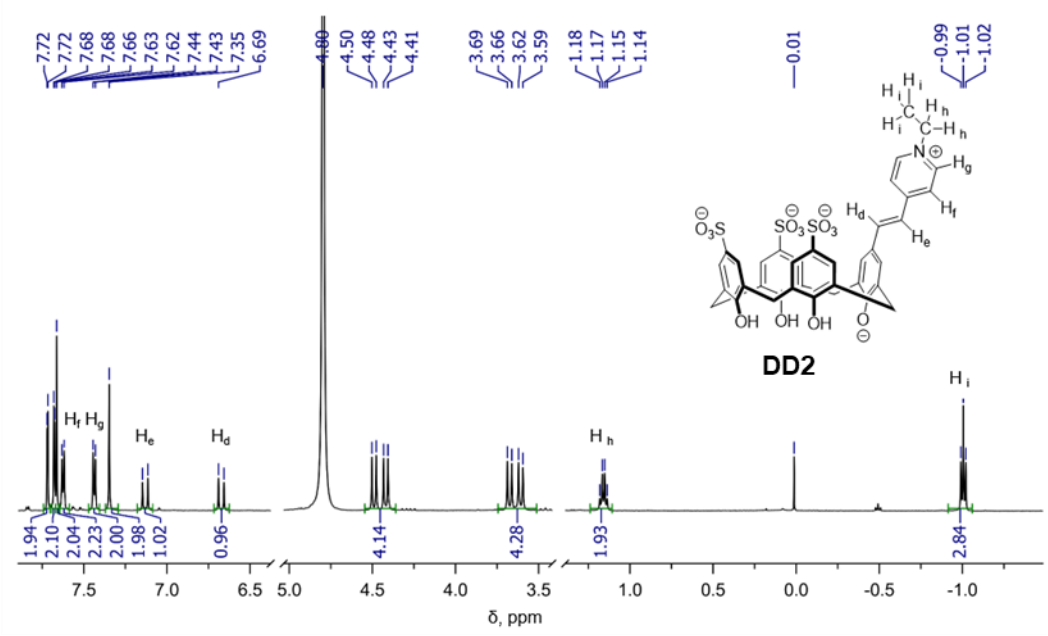
7.72
7.72
7.68
7.68
7.66
7.63
7.62
7.44
7.43
7.35
6.69
4.90
4.50
4.48
4.43
4.41
3.69
3.66
3.62
3.59
1.18
1.17
1.15
1.14
0.01
-0.99
-1.01
-1.02
DD2
H f H g
H e
H d
H h
H i
1.94
2.10
2.04
2.23
2.00
1.98
1.02
0.96
4.14
4.28
1.93
2.84
δ, ppm

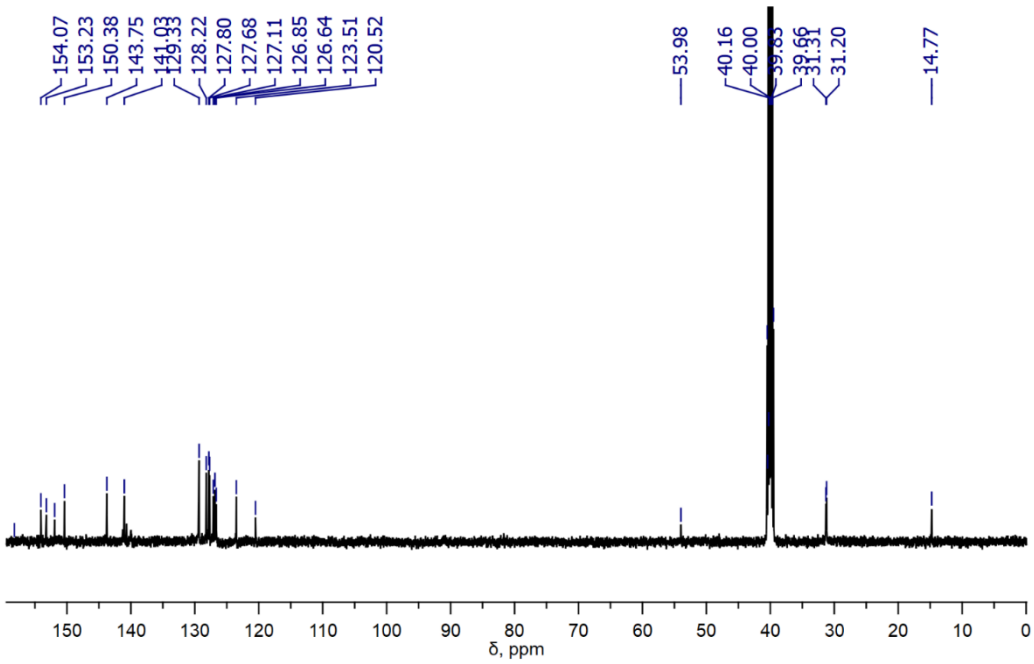
154.07
153.23
150.38
143.75
141.03
129.33
128.22
127.80
127.68
127.11
126.85
126.64
123.51
120.52
53.98
40.16
40.00
39.83
39.66
31.31
31.20
14.77
δ, ppm

4.5.4 Supplementary characterization of self-assembly

4.5.4a ^{1}H NMR of DD1 and DD2 in D_2O and d_6-DMSO

Table 4. 2 Chemical shift comparison of **DD1** in D_2O and d_6-DMSO.

Atom[a)]	D_2O	d_6-DMSO
Hb	7.77	7.45
Ha	7.64	7.38
Hc	7.25	7.33
Hd	6.62	6.95
He	7.04	7.51
Hf	6.52	8.06
Hg	7.45	7.86
Hh	**0.67**	**3.13**

a) See above for atom labels

Table 4. 3 Chemical shift comparison of **DD2** in D_2O and d_6-DMSO.

Atom [a)]	D_2O	d_6-DMSO
Hd	6.67	7.02
He	7.13	7.58
Hf	7.43	7.94
Hg	7.62	8.42
Hh	1.16	4.71
Hi	**-1.01**	**1.51**

a) See above for atom labels

4.5.4b DOSY analysis of DD1 and DD2

Table 4. 4 Parameters used for diffusion analysis of **DD1**

Parameters used for diffusion analysis:	
used γ:	26752 rad/(s*Gauss)
used δ:	0.0054000 s
used Δ:	0.049950 s
used gradient strength:	variable
Random error estimation of data:	RMS per spectrum (or trace/plane)
Systematic error estimation of data:	worst case per peak scenario
Fit parameter Error estimation method:	from fit using arbitrary uncertainties
Confidence level:	95%
Used peaks:	automatically picked peaks
Used integrals:	area integral
Used Gradient strength:	all values (including replicates) used

Table 4. 5 Diffusion coefficients calculated from indicated resonances in **DD1** from 1D DOSY

F2 [ppm]	D [m^2/s]	error
7.768	2.38×10^{-10}	7.431×10^{-13}
7.641	2.40×10^{-10}	1.606×10^{-12}
7.460	2.39×10^{-10}	1.731×10^{-12}
7.247	2.35×10^{-10}	1.907×10^{-12}
6.516	2.34×10^{-10}	1.555×10^{-12}
0.668	2.38×10^{-10}	1.564×10^{-12}

Table 4. 6 Parameters used for diffusion analysis of **DD2**

Parameters used for diffusion analysis:	
used γ:	26752 rad/(s*Gauss)
used δ:	0.0054000 s
used Δ:	0.049950 s
used gradient strength:	variable
Random error estimation of data:	RMS per spectrum (or trace/plane)
Systematic error estimation of data:	worst case per peak scenario
Fit parameter Error estimation method:	from fit using arbitrary uncertainties
Confidence level:	95%
Used peaks:	automatically picked peaks
Used integrals:	peak intensities
Used Gradient strength:	all values (including replicates) used

Table 4. 7 Diffusion coefficients calculated from indicated resonances in **DD2** from 1D DOSY.

F2 [ppm]	D [m^2/s]	error
6.667	2.14×10^{-10}	2.948×10^{-12}
1.148	2.10×10^{-10}	4.696×10^{-12}
1.103	2.10×10^{-10}	6.426×10^{-12}

Table 4. 8 Parameters used for diffusion analysis of **PSC** in buffered water.

Parameters used for diffusion analysis:	
used γ:	26752 rad/(s*Gauss)
used δ:	Replicates 1: 0.0050000 s, 2: 0.0048000 s
used Δ:	Replicates 1: 0.049950 s, 2: 0.049950 s
used gradient strength:	variable
Random error estimation of data:	RMS per spectrum (or trace/plane)
Systematic error estimation of data:	worst case per peak scenario
Fit parameter Error estimation method:	from fit using arbitrary uncertainties
Confidence level:	95%

Used peaks:	automatically picked peaks
Used integrals:	area integral
Used Gradient strength:	all values (including replicates) used

Table 4. 9 Diffusion coefficients calculated from indicated resonances in **PSC** from 1D DOSY.

F2 [ppm]	D [m^2/s]	error
7.571	3.28×10^{-10}	6.395×10^{-13}
7.569	3.58×10^{-10}	5.729×10^{-13}

4.5.4c Molecular models

DD1 was built in GaussView 5.08 starting from the X-ray crystal structure of ***tBu*$_2$-SC4A**. The neutral form of the monomer was optimised in Priroda 16 using the PBE functional, the L11 basis set (equivalent to cc-pCVDZ), and using four-parameter Dirac equation relativistic effects on all atoms. The monomer structure coordinates were then copied and multiplied by –1 to obtain the inverse structure. A dummy atom was placed into the pocket of the monomer structure, and the pyridinium nitrogen from the inverted coordinates was remapped to the location of the dummy atom. The vector of this atom translation was applied to all coordinates of the inverted structure, thereby mutually inserting each monomer into each other's pocket. The dimer of **DD1** was then optimised using Gaussian09 (rev. B) using the PBE functional and 3-21G basis set. **DD2** was then optimised using the same method in Gaussian09 by modifying the **DD1** optimised structure.

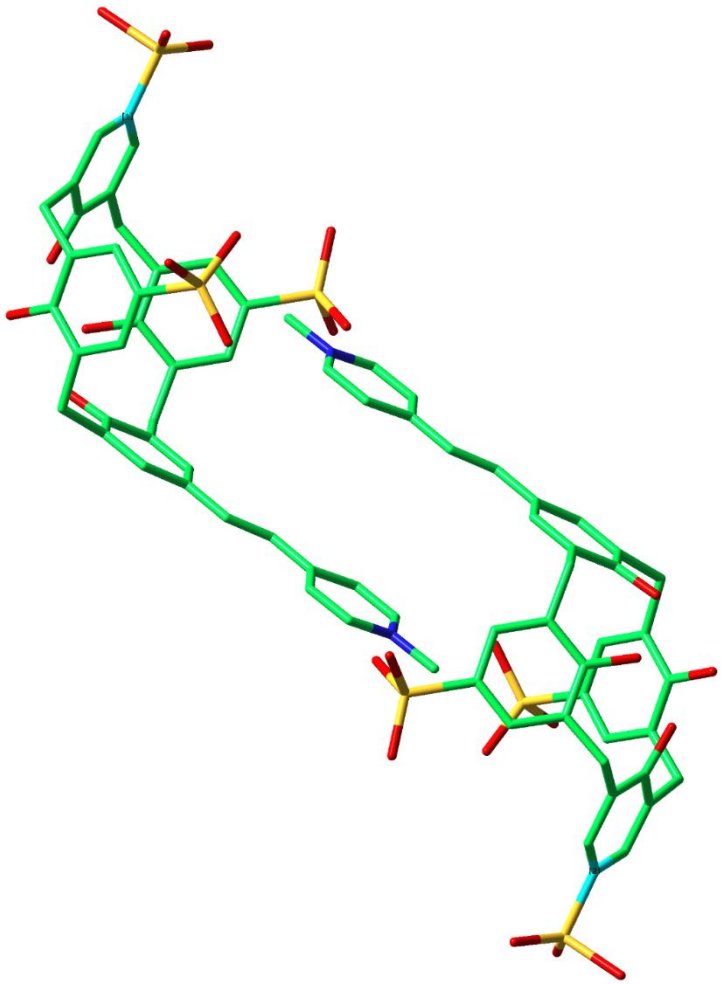

Figure 4. 11 Distance (23.16 Å) between light blue carbons of **DD1** in optimized structure were used to obtain a theoretical radius of 11.58 Å.

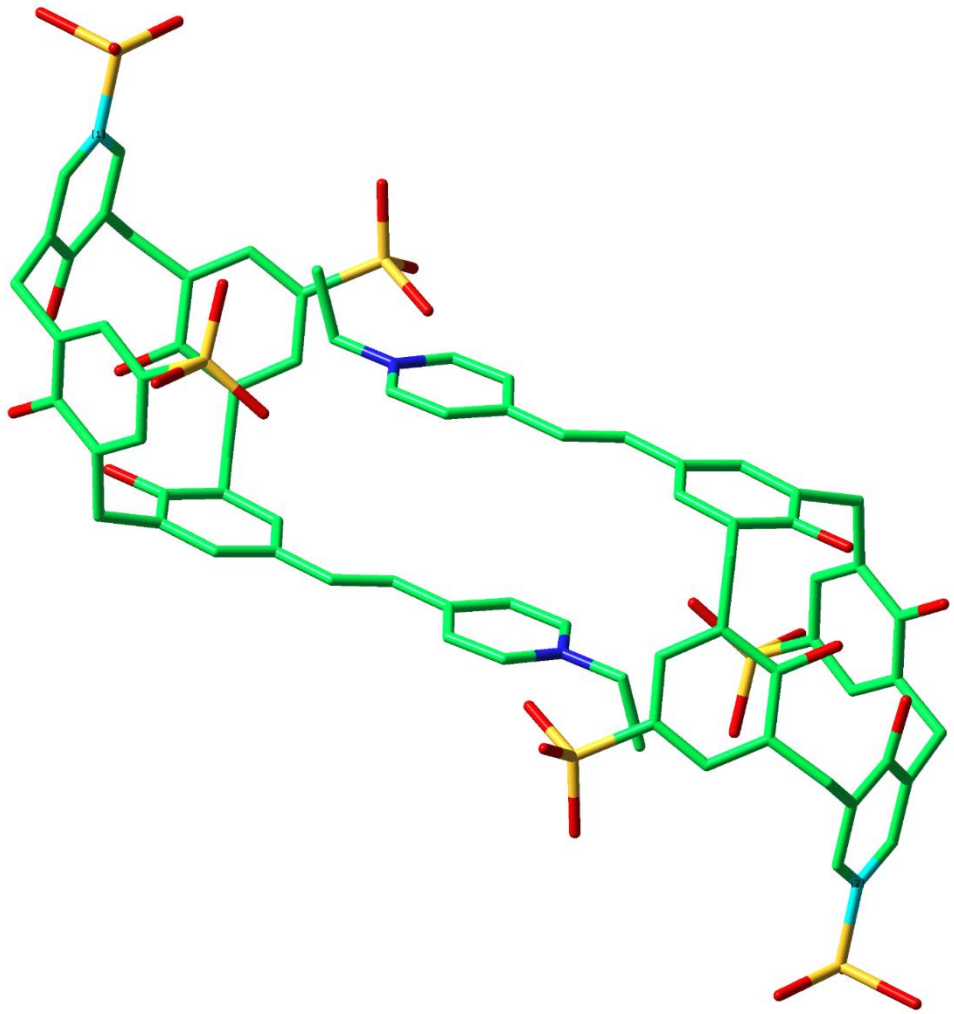

Figure 4. 12 Distance (22.46 Å) between light blue carbons of **DD2** in optimized structure were used to obtain a theoretical radius of 11.23 Å.

4.5.4d K_d values determined by ^{1}H NMR dilutions

Quantitative NMR was conducted as follows: A concentrated stock of **DD1** was prepared in NaH_2PO_4/Na_2HPO_4 (100 mM, pD 7.8 or 10 mM pD 7.5) buffer with maleic acid or 2,2,3,3,-d_4-3-(trimethylsilyl)propionic acid sodium salt (TSP) as internal standards. T1 relaxation of the internal standard was estimated and all following experiments were conducted with D1 = 5*T1 relaxation delay time. An accurate calculation of stock allowed [**DD1**]$_t$ to be determined for all dilution experiments. The singlet at 0.66 ppm was used to calculate [**DD1**]$_2$ (dimer) and through mass balance [**DD1**] (monomer) was calculated.

Table 4. 10 Quantitative concentrations calculated by NMR of **DD1** total, dimer, monomer in NaH_2PO_4/Na_2HPO_4 (100 mM, pD 7.8).

[**DD1**]t[(a)] μM	[**DD1**]2 μM	[**DD1**] μM	K_d μM
355.0	328.8	31.1	3.0
370.5	328.2	42.4	5.5
220.9	203.3	17.5	1.5
K_d	**3.3**	**+/-**	**2.0**

Maleic acid (3 mM and 500 μM) was used as the internal standard and three experiments were used to find the average K_d of 3.3 μM (± 2.0 μM). This low dissociation constant coincides with our fluorescence dilutions experiments as no emission was detected at working concentrations (10 – 4 μM).

Table 4. 11 Quantitative concentrations calculated by NMR of **DD1** total, dimer, monomer NaH_2PO_4/Na_2HPO_4 (10 mM, pD 7.4).

[**DD1**]t μM	[**DD1**]2 μM	[**DD1**] μM	K_d μM
192.6	169.4	23.2	3.2
97.3	83.1	14.1	2.4
K_d	**2.8**	**+/-**	**0.6**

TSP (392 or 196 μM) was used to calculate dimer and total concentrations. Two experiments were used to find the average K_d of 2.8 μM (± 0.6 μM). The dimer dissociation decreases slightly in 10-fold decrease of Na+ concentration from the buffer.

4.5.4e Fluorescence experiments with SC4A and parent dye

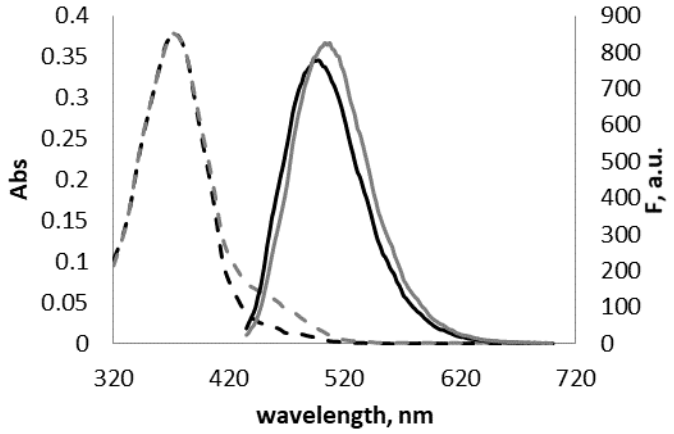

Figure 4. 13 Parent dye **2.13** (10 μM) undergoes minor changes in absorbance (from gray to black dotted line) and upon addition of **SC4A** (100 μM). While there are slight hypochromic and bathochromic shifts (gray solid line without **SC4A**, $\lambda_{ex.}$ 370nm, $\lambda_{em.}$ 505 nm) in fluorescence of **2.13** when encapsulated by **SC4A** (black solid line, $\lambda_{ex.}$ 370 nm, $\lambda_{em.}$ 495 nm).

This fluorescence change is not as significant as the quenching observed by the fluorophore of **DD1** when dimerized in another calixarene pocket. The suggests another photophysical phenomenon is contributing to the fluorescent behavior of **DD1**.

4.5.4f Absorbance and fluorescence spectra of parent dye and DD1 in water and DMSO

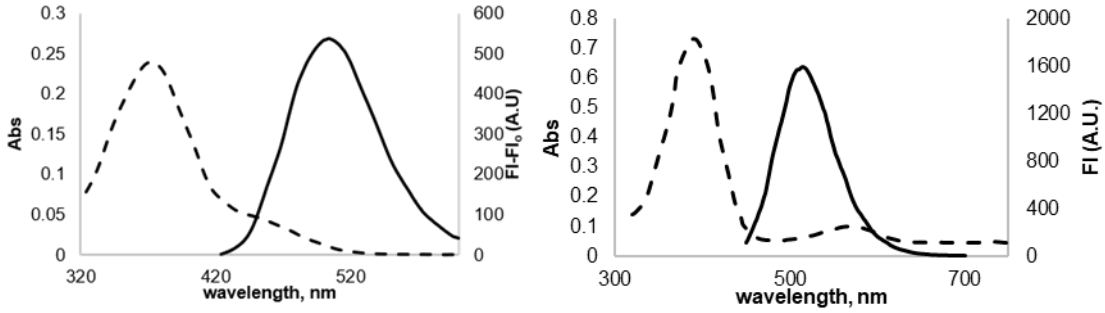

Figure 4. 14 Characterization of the parent dye **2.13** in buffered water and in DMSO. Left: **2.13** (10 μM) is the main species in NaH_2PO_4/Na_2HPO_4 buffer (10 mM, pH 7.4). The absorbance (dotted line, $\lambda_{max.}$ 370 nm) and fluorescence (solid line, $\lambda_{ex.}$ 370 nm, $\lambda_{em.}$ 504 nm) spectra align with literature values for H^+**2.13**.[228-229] Right: absorbance (dotted line) and fluorescence (solid line) spectra indicate that **2.13** (20 μM) exists as both

deprotonated ($\lambda_{max.}$ 572 nm) and protonated ($\lambda_{ex.}$ 394 nm, $\lambda_{em.}$ 516 nm) species in neutral DMSO.[229]

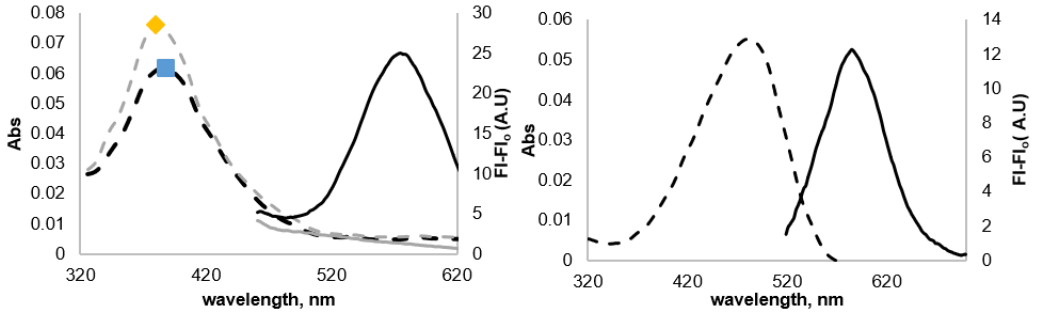

Figure 4. 15 Characterization of **DD1** in buffered water and in DMSO. Left: **DD1** (10 μM) exists as a dimer in NaH_2PO_4/Na_2HPO_4 buffer (10 mM, pH 7.4). This is supported by its absorbance maximum (gray dotted line) of 382 nm and its lack of fluorescence emission (λ_{ex} 382 nm, gray solid line). Addition of H3K9me3 (50 μM) red shifts the **DD1** absorbance (black dotted line, $\lambda_{em.}$ 388 nm) and induces emission (black solid line, λ_{ex} 388 nm, λ_{em} 575 nm). Right: **DD1** (2 μM) photochemical data in DMSO is similar to literature.[229] The absorbance is further red-shifted (black dotted line, λ_{em} 480 nm) — due to the lower pK_a of calixarene phenols, and fluorescent emission (black solid line, λ_{ex} 480 nm, $\lambda_{em.}$ 585 nm) is similar to that of **DD1** water in the presence of a guest.

4.5.4g Extinction coefficients of parent dye and DD1

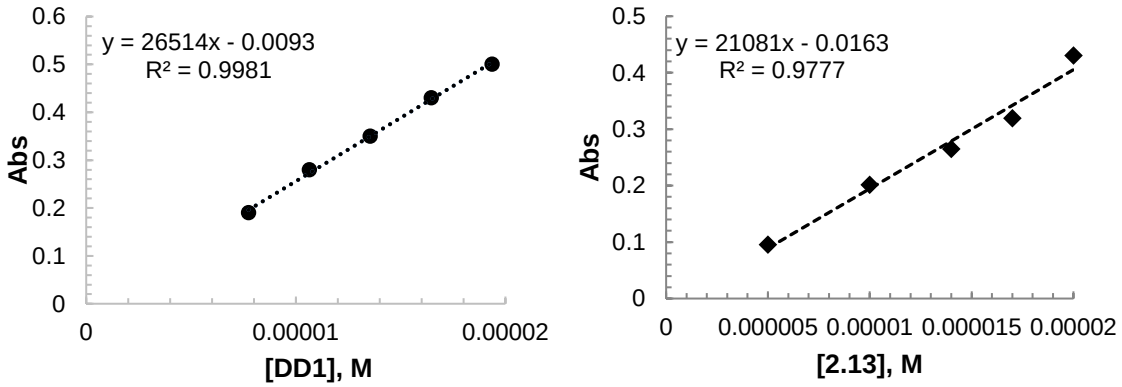

Figure 4. 16 Both **DD1** (left) and **2.13** (right) have similar extinction coefficients in NaH_2PO_4/Na_2HPO_4 (10 mM, pH 7.4) buffer.

DD1: ε_{382nm} = 26,500 M^{-1} cm^{-1}

2.13: ε_{370nm} = 21,000 M^{-1} cm^{-1}

4.5.5 ^{1}H NMR titrations of amino acids into DD2 and parent dye

4.5.5a Titrations with DD2

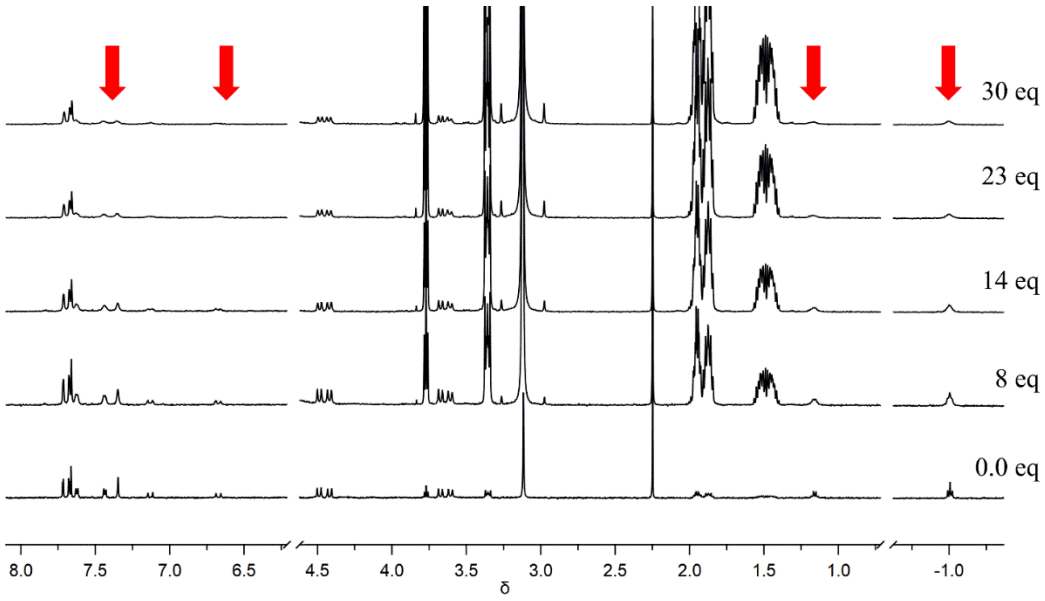

Figure 4. 17 ^{1}H NMR titration of trimethyllysine (Kme3) (20 mM) into **DD2** (250 µM) host-guest complexation, red arrows indicate **DD2** resonances broadening and decreasing in intensity due to dimer dissociation and complexation with Kme3.

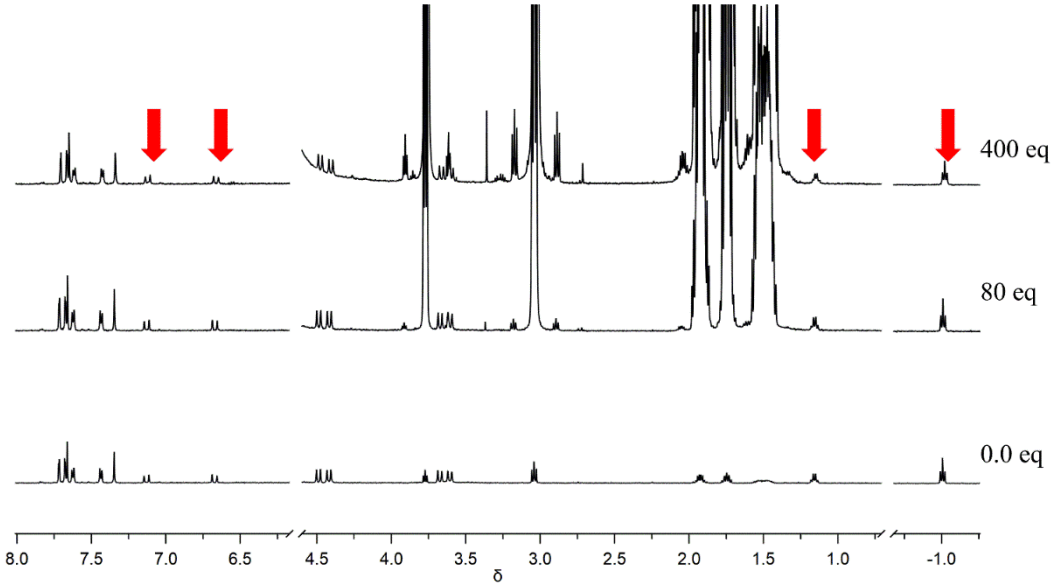

Figure 4. 18 ^{1}H NMR titrations of lysine (K) (20 mM) into **DD2** (250 µM). Red arrows indicate the lack of broadening as K does not disrupt the dimer under these conditions.

4.5.5b Titrations with parent dye

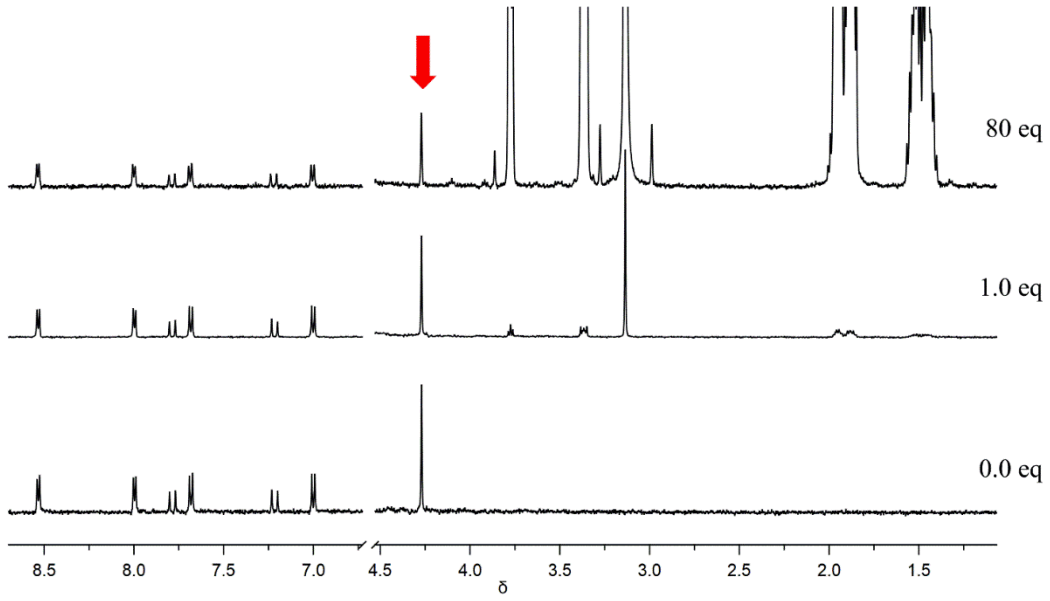

Figure 4. 19 ^{1}H NMR titrations of trimethyllysine (Kme3) into **2.13** (250 µM). Red arrow indicates no change in chemical shift position, intensity, or line shape, indicating no complexation between **2.13** and Kme3.

4.5.6 DD fluorescence response to analytes

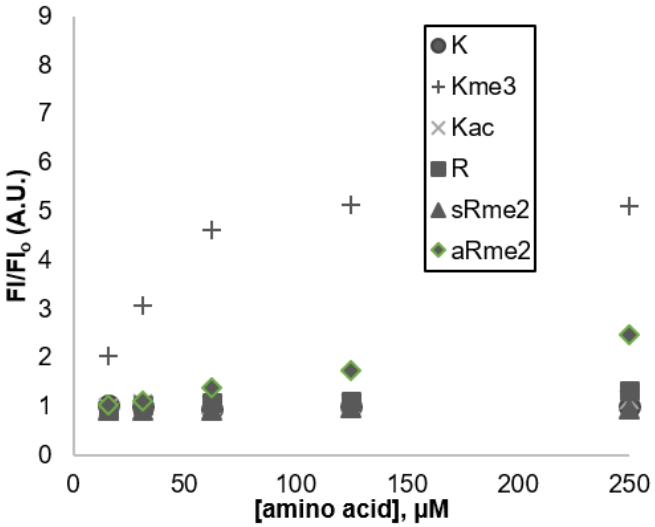

Figure 4. 20 Most intense fluorescence change is from the strongest binding analyte, Kme3. Fluorescence ($\lambda_{ex.}$ 370 nm, $\lambda_{em.}$ 575 nm) titrations of amino acids (lysine (K), trimethyllysine (Kme3), *N*-acetyllysine (Kac), arginine (R), symmetric dimethyl arginine (sRme2) and asymmetric dimethyl arginine (aRme2)) into **DD1** (10 µM) in NaH_2PO_4/Na_2HPO_4 buffer (10 mM, pH 7.4) indicate Kme3 to be the most favourable analyte with the greatest change in fluorescence.

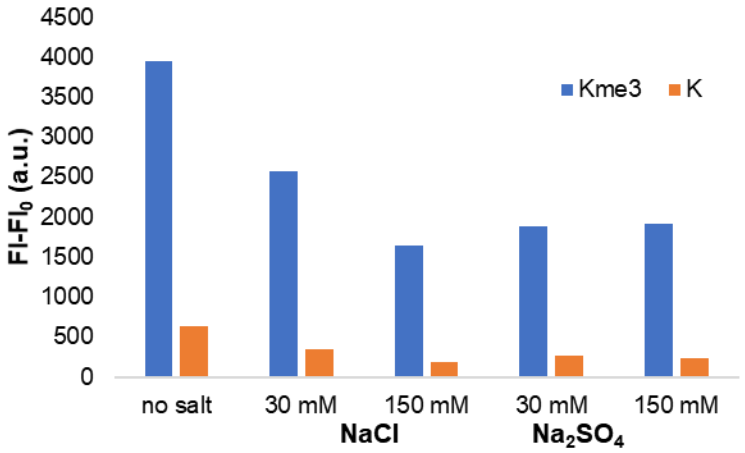

Figure 4. 21 **DD1** fluorescence detection of Kme3 or K in the presence of different salts at varying concentrations. **DD1** (10 μM, $\lambda_{ex.}$ 382 nm, $\lambda_{em.}$ 585 nm) detects trimethyllysine (1 mM, blue bars) in the presence of NaCl (0 mM, 30 mM, 150 mM), and Na_2SO_4 (0 mM, 30 mM, 150 mM) but remains non-emissive in presence of lysine (1 mM, orange bars). All samples run in NaH_2PO_4/Na_2HPO_4 buffer (10 mM, pH 7.4). Selectivity for Kme3 over K increases slightly in presence of the varying salts vs. the 'no salt' phosphate buffered condition.

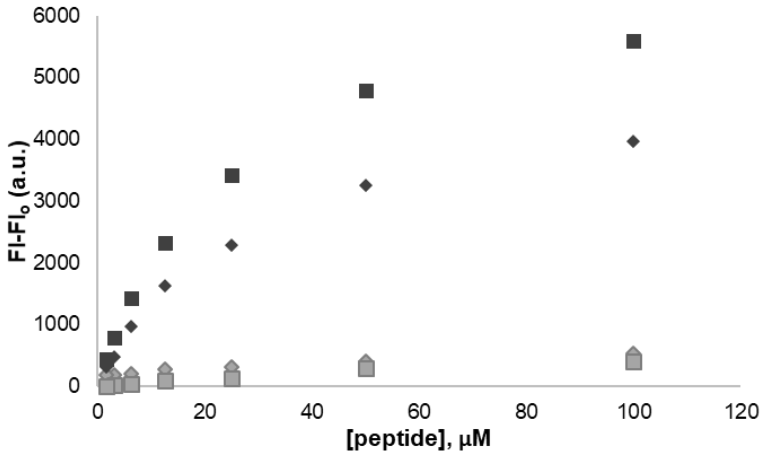

Figure 4. 22 Difference of induced fluorescence between **DD1** and **DD2** in the presence of peptides. **DD1** (square,10 μM, $\lambda_{ex.}$ 385 nm, $\lambda_{em.}$ 585 nm) induces a greater response in the presence of H3K9me3 (black) than **DD2** (diamond, 10 μM, $\lambda_{ex.}$ 385 nm, $\lambda_{em.}$ 585 nm). Both DimerDyes remain non-emissive with H3K9 (gray) in NaH_2PO_4/Na_2HPO_4 buffer (10 mM, pH 7.4).

4.5.7 Histone methyltransferase and demethylase assays

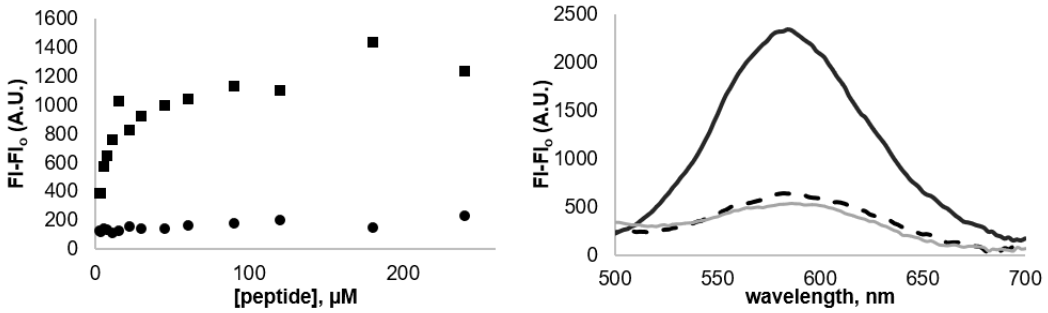

Figure 4. 23 Induced fluorescence of peptide analytes in complex methyltransferase conditions. Left: Fluorescence of **DD1** (8 μM, $\lambda_{ex.}$ 384 nm, $\lambda_{em.}$ 585 nm) in NaH_2PO_4/Na_2HPO_4 buffer (10 mM, pH 7.4) with H3K4 (circles) and H3K4me3 (squares). Right: **DD1** (8 μM, $\lambda_{ex.}$ 384 nm, $\lambda_{em.}$ 585 nm) is non-emissive in enzyme conditions (dotted black line) and with H3K4 (gray solid line, 40 μM) but becomes fluorescent with H3K4me3 (black solid line, 40 μM).

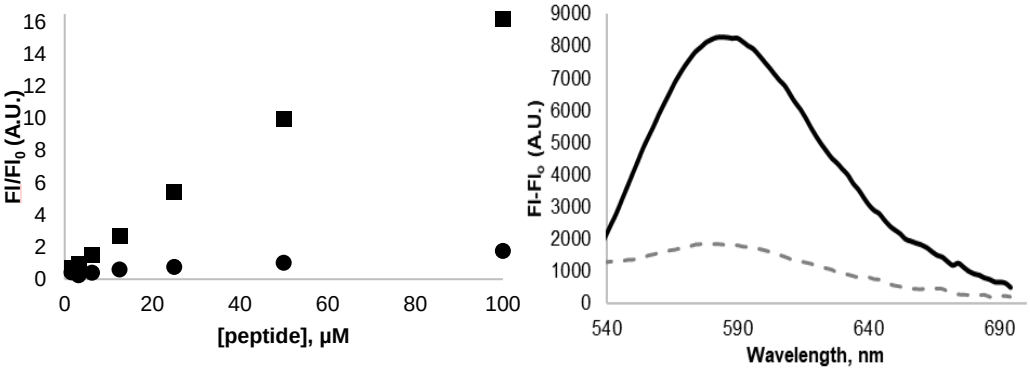

Figure 4. 24 Fluorescence induced by peptide analytes in complex demethylase buffer conditions. Left: Dose-response for fluorescence of **DD1** (8 μM, $\lambda_{ex.}$ 388 nm, $\lambda_{em.}$ 570 nm) with varying concentrations of H3K9 (circles) or H3K9me3 (squares). Right: Emission spectra of **DD1** (8 μM, $\lambda_{ex.}$ 380 nm) in presence of H3K9 (dotted line, 100 μM) or H3K9me3 (solid line, 100 μM).

Protocols

PRDM9: All solutions were made the day of experiment with fresh buffer solution (Tris (50 mM, pH 8.5), NaCl (30 mM)). See Table 4. 12 for stock solution concentrations and volumes. H3K4 and **DD1** solutions were aliquoted into a 96-well plate, immediately followed by freshly made DTT and SAM solutions. The addition of the enzyme initiated the reaction. After the fluorescence kinetic experiment was completed, the reaction was transferred to an Eppendorf and heated to 90°C for 5 min to denature the enzyme.

$\lambda_{ex.}$ 388 nm, $\lambda_{em.}$ 585 nm, temperature 37°C, reaction was read over 1 h, every 90 s.

Table 4. 12 Stock solutions and final concentrations used for PRDM9 methyltransferase assay.

	[final]		[stock]		vol (µL)
H3K4	**40**	µM	400	µM	10
DD1	**8**	µM	100	µM	8
DTT	**1**	mM	10	mM	10
SAM	**300**	µM	5000	µM	6
PRDM9	**0.46**	µM	23	µM	2
buffer					64
				Total Vol:	**100**

JMJD2D: All solutions were made the day of experiment with fresh NaH_2PO_4/Na_2HPO_4 buffer (50 mM, pH 7.4). See Table 4. 13 for stock solution concentrations and volumes. H3K9me3 and **DD1** solutions were aliquoted into a 96-well plate, immediately followed by freshly made 2-oxoglutaric acid (2-OG), ascorbic acid (AA), and $(NH_4)_2Fe(SO_4)_2$ solutions. The addition of the enzyme initiated the reaction. After the fluorescence kinetic experiment was completed, the reaction was transferred to an Eppendorf tube and heated to 90°C for 5 min to denature the enzyme.

$\lambda_{ex.}$ 384 nm, $\lambda_{em.}$ 580 nm, temperature 37°C, reaction was read over 1 h, every 30 s.

Table 4. 13 Stock solutions and final concentrations used for JMJD2D demethylase assay.

	[final]		[stock]		vol (µL)
H3K9me3	**50**	µM	200	µM	25
DD1	**8**	µM	92	µM	9
2-OG	**200**	µM	4	mM	5
AA	**500**	µM	5	mM	10
Fe	**100**	µM	2	mM	5
JMJD2D	**0.4**	µM	4	µM	10
buffer					46
				Total Vol:	**100**

Mass spectrometric analysis of reaction products

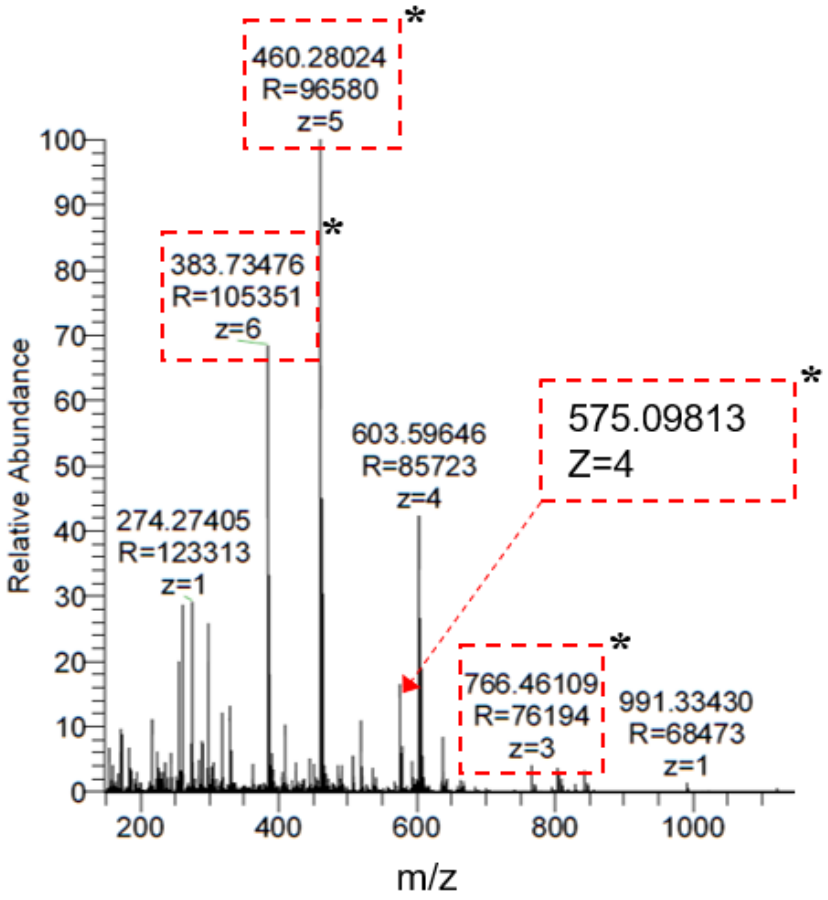

Figure 4. 25 HR-ESI-MS of PRDM9 methyltransferase reaction after 1 h shows the presence of the highly charged H3K4me3 product peptide (ART - K(Me3) – QTARKSTGGKAPRKQLA), as the +3, +4, +5, +6 *m/z* peaks.
The crude reaction mixture was first passed through C18 Zip-Tips before dilution with 1:1 acetonitrile:water (0.1% TFA).

Table 4. 14 Only *m/z* peaks (indicated by *) of H3K4me3 were observed in enzyme reaction mixture from the many possible products that could possibly form.

	H3K4me3 $C_{97}H_{178}N_{36}O_{28}$	H3K4me2 $C_{96}H_{176}N_{36}O_{28}$	H3K4me $C_{95}H_{174}N_{36}O_{28}$	H3K4 $C_{94}H_{172}N_{36}O_{28}$
Exact mass:	2295.36113	2281.34548	2267.32983	2253.31418
$[M+3H^+]^{3+}$	**766.046210***	761.79022	757.11834	752.44645

$[M+4H^+]^{4+}$	**575.09840***	571.59448	568.09057	564.58666
$[M+5H^+]^{5+}$	**460.28017***	457.47704	454.67391	451.87078
$[M+6H^+]^{6+}$	**383.73469***	381.39875	379.06281	376.72687

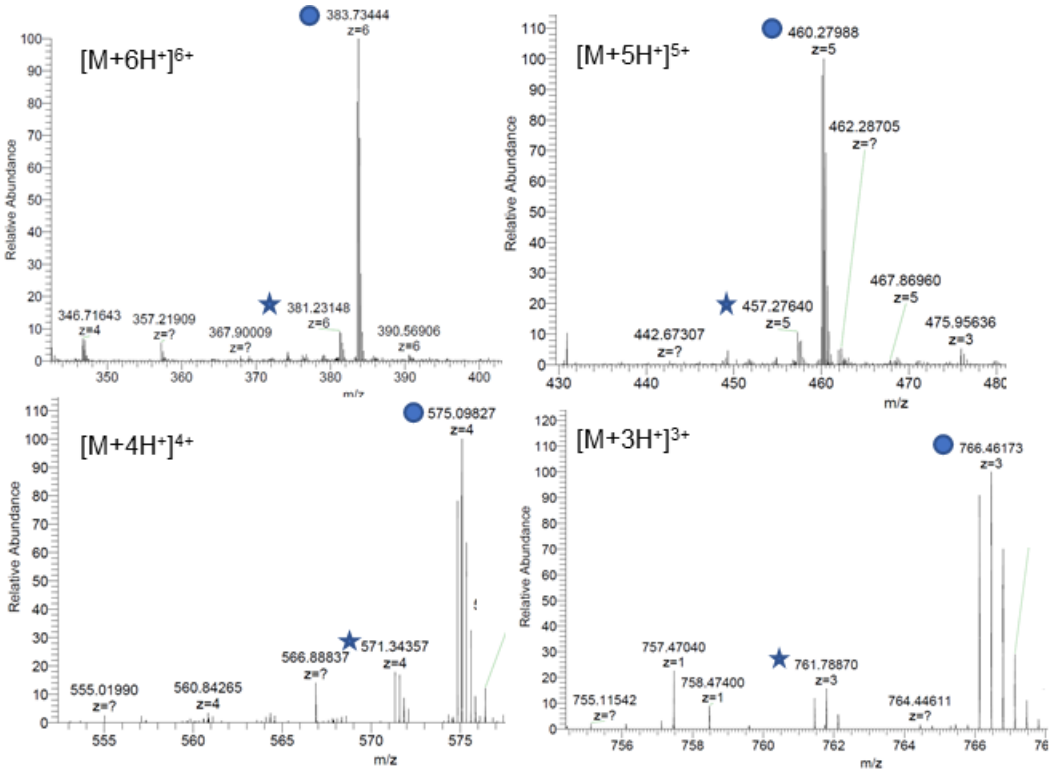

Figure 4. 26 Partial conversion of H3K9me3 is achieved by this enzyme under these conditions. HR-ESI-MS after 1.5 h of enzyme reaction shows the presence of the H3K9me3 substrate and H3K9me2 product peptides as the +3, +4, +5, +6 *m/z* peaks.

Table 4. 15 *m/z* peaks of H3K9me3 and H3K9me2 observed in above MS spectra.

	H3K9me3 $C_{97}H_{178}N_{36}O_{28}$	H3K9me2 $C_{96}H_{176}N_{36}O_{28}$	H3K9me $C_{95}H_{174}N_{36}O_{28}$	H3K9 $C_{94}H_{172}N_{36}O_{28}$
Exact mass:	2295.36113	2281.34548	2267.32983	2253.31418
$[M+3H^+]^{3+}$	**766.04621** ●	**761.79022** ★	757.11834	752.44645
$[M+4H^+]^{4+}$	**575.09840** ●	**571.59448** ★	568.09057	564.58666
$[M+5H^+]^{5+}$	**460.28017** ●	**457.47704** ★	454.67391	451.87078
$[M+6H^+]^{6+}$	**383.73469** ●	**381.39875** ★	379.06281	376.72687

Chapter 5: Parallel Synthesis and Screening of Supramolecular Chemosensors that Achieve Fluorescent Turn-On Detection of Drugs in Saliva

This work was adapted from a submitted paper.

Meagan A. Beatty, Allison J. Selinger, YuQi Li, and Fraser Hof
J. Am. Chem. Soc., **2019** (submitted July 3, 2019)

MB and FH conceived of the idea. YL prepared starting materials. MB designed and optimized parallel synthesis and testing with assistance from AS. MB designed, conducted and analysed data for all UPLC-MS of crude products, NMR characterization of final pure products, ^{1}H NMR titrations, and 1D DOSY. UV-Vis/fluorescence titrations were designed and conducted by MB with assistance from AS. Limits of detection and chemometric analysis were conducted by MB. MB and FH co-wrote the paper.

5.1 Foreword

In Chapter 4 we designed and explored the chemosensing properties of novel supramolecular sensors, DimerDyes, that operated through the disassembly of a quenched homodimer to form an emissive sensor-analyte complex. DimerDyes were tolerant to various salts and co-solutes as predicted by its homodimer predecessor. We successfully implemented DimerDyes as a useful biochemical tool by monitoring enzymatic reactions in real-time.

We wished to expand on this concept to make new DimerDyes that had different photophysical properties, dimerization strengths, and guest selectivities. Through this, we hoped to identify sensors that detect and discriminate between similar analytes in a variety of complex biological solutions. We were also inspired by the combinatorial approach used in Chapter 3 to develop new dimers. Therefore, we wanted to develop a method for quick access to a library of DimerDye sensors, paired with an efficient method to test the new sensors for their differential responses to analytes. Furthermore, we wanted to further challenge the sensors by operating in complex and heterogeneous media like human biofluids.

5.2 Introduction

Supramolecular sensors, once limited to organic solvents and aqueous/organic mixtures, can now detect biologically relevant analytes even in salty aqueous solutions.[105, 147, 197-198, 230-234] Analyte detection in water is made more difficult and less predictable when the target is found in complex biological media. In Chapter 1, highlighted were notable examples of supramolecular sensors that operate in human cells,[98, 149, 203, 235-236] enzyme-supporting buffers,[62, 103, 202, 220, 237-239] bacterial culture,[240] and real biofluids[114, 241-243]. In spite of these significant achievements, the *de novo* design of new sensing systems that work in complex biological media remains non-trivial.

Our novel chemosensor, DimerDye 1 (**DD1**), introduced in Chapter 4 operates via an inherently salt-tolerant supramolecular sensing mechanism. The sensor contains a styryl-type merocyanine dye synthetically integrated into the calix[4]arene macrocycle.[237] In water, the topology of **DD1** leads to self-assembly in water into a non-emissive homodimer. Upon the addition of methyllysine-containing peptides that are good guests, the dimer disassembles and forms a fluorescent DimerDye-methyllysine complex (Figure 5. 1a). We showed that **DD1** was able to monitor the enzymatic methylation and demethylation of peptides in real-time. Due to the intrinsic salt tolerance of this molecular design, the sensor operated in the presence of high concentrations of NaCl, reducing agents, transition metal salts, and other enzyme co-factors.[134]

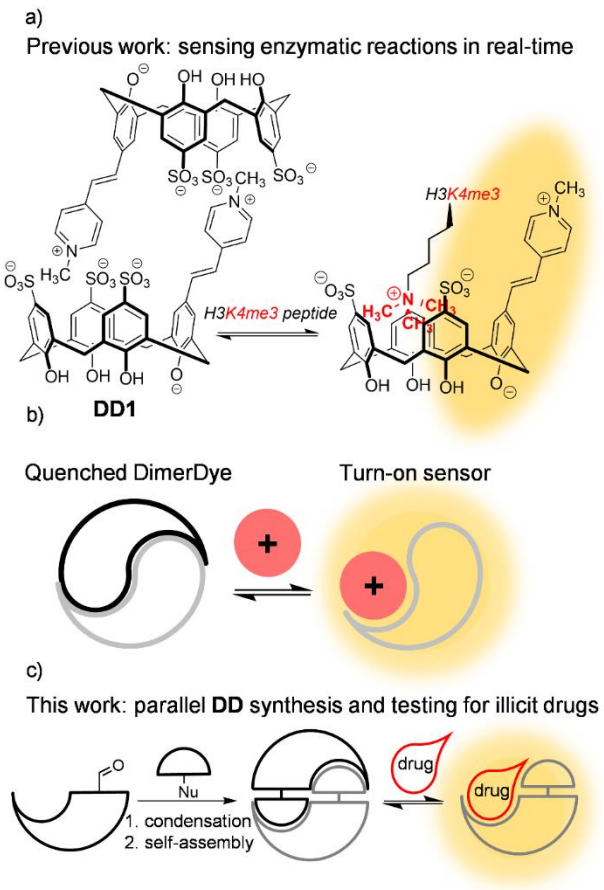

Figure 5. 1 a) Previous work: **DD1** can monitor an enzymatic reaction that produces a trimethyllysine-containing peptide that is bound and detected by **DD1**. b) A cartoon illustrates the guest-induced disassembly and sensing mechanism of the self-assembled DimerDye. c) This work reports the development of a parallel synthesis and screening of diverse new DimerDyes (DDs) to detect cationic drugs in biological media.

Parallel synthesis can give rapid access to sensor molecules. It provides a means to create many products in a quick and combinatorial fashion, and to screen a broad structural space without needing atom-by-atom design. Sensors created by parallel synthesis approaches have typically been inorganic or polymer-based,[244-246] while relatively few examples of discrete organic sensing molecules have been generated in this way.[247-250] One example of particular interest involved the condensation of a set of aromatic aldehydes with a set of heterocyclic nucleophiles to form 276 fluorescent styryl dyes.[251] The reaction mixtures were tested directly in cells for organelle accumulation and 119 dyes were identified as responsive sensors, although no particular sensing mechanism or analyte binding functions had been included in the library design. This approach was attractive to

us as the chromophores in the library resembled those of the styryl-based merocyanine chromophore that is the sensing component of DimerDye.

We report here a parallel synthesis-driven approach to creating new DimerDyes, and its use in a pilot study that rapidly identifies sensors for illicit drugs. Many classes of drugs, including opioids, amphetamines, tropane alkaloids, and anaesthetics, contain a hydrophobic cation in their structure that we hypothesized would be recognized by sulfonatocalix[4]arene-based hosts. Since **DD1**[237] and other related molecules introduced in Chapters 2 and 3[134, 252-253] can assemble and/or bind guests in competitive aqueous buffers, we envisioned that this property could be extended to sensing drugs in biofluids. Unlike most supramolecular host-guest projects, we avoided the atom-by-atom design of sensors that would be highly specific for individual drug molecules. Instead, we developed a parallel synthesis and efficient crude screening process to quickly identify new sensors for the detection of a given analyte in a given solution. We also report the re-synthesis, detailed characterization of sensing mechanisms and limits of detection for a set of structurally diverse "hit" DimerDyes that arose from our screen. To demonstrate the broad scope of this new approach, we describe a sensor array that can identify members of multiple classes of illicit drugs.

5.3 Results

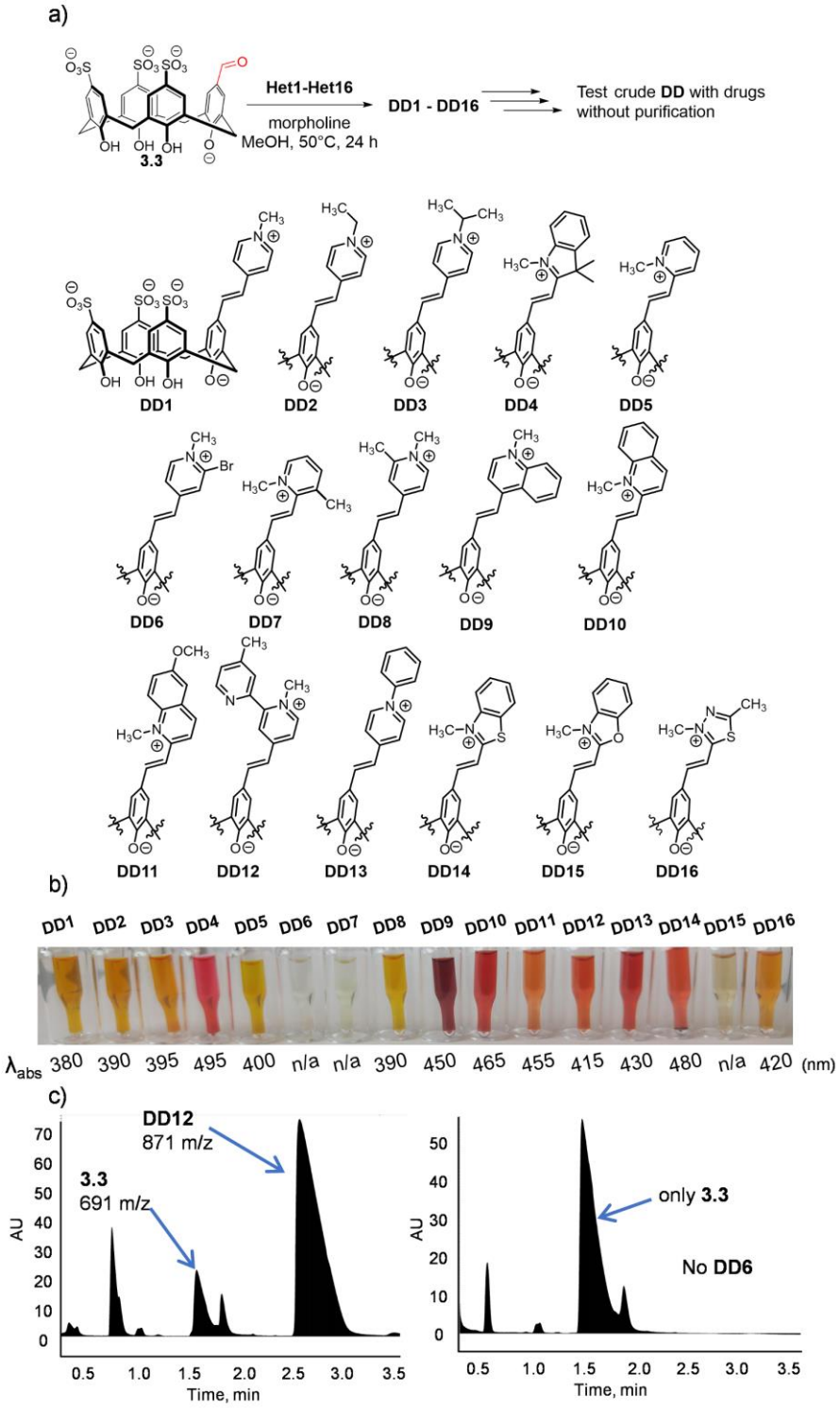

Figure 5. 2 Parallel synthesis provides a library of DimerDye chemosensors. a) Condensation reactions with aldehyde-bearing calix[4]arene, **3.3**, and **Het1–16** give

DimerDyes, **DD1–DD16**. b) Aliquots of crude reaction mixtures show the characteristic colour changes that we use as a visual sign of reaction success for 13 out of 16 DimerDyes after heating mixture at 50°C in methanol for 6 hours. c) Two exemplary traces, showing UPLC-MS data for a successful synthesis (**DD12**) and a failed synthesis (**DD6**). See Supporting information for full UPLC-MS data of all runs.

We first developed an efficient method for the parallel synthesis of new DimerDyes. We anticipated that varying the fluorophore on the edge of the binding pocket would create DDs with diverse homodimerization affinities and guest-binding selectivities, but that would retain the general features of disassembly-driven molecular sensing and salt tolerance that were found in the parent molecule **DD1**. We selected 16 heterocyclic nucleophiles (**Het1–16**) that form merocyanine fluorophores after condensation with the aldehyde precursor, **3.3** (Figure 5. 2a). Our previous synthesis of DimerDyes involved heating at reflux **3.3** and **Het1** with piperidine in methanol overnight.[237] We quickly found that the protonated piperidinium by-product is itself a good guest that interferes with sensor screening. Instead, morpholine was selected as an amine-containing base as its high hydrophilicity would minimize complexation with the hydrophobic binding pockets. Successful condensation reactions are indicated by a colour change after 6 hours at 50°C (Figure 5. 2b). UPLC-MS confirms product formation and reveals the extent of each reaction (Figure 5. 2c and Supporting Information). 13 of the 16 DimerDye syntheses go to full or partial completion, while syntheses of **DD6**, **DD7**, and **DD15** fail under the listed conditions.

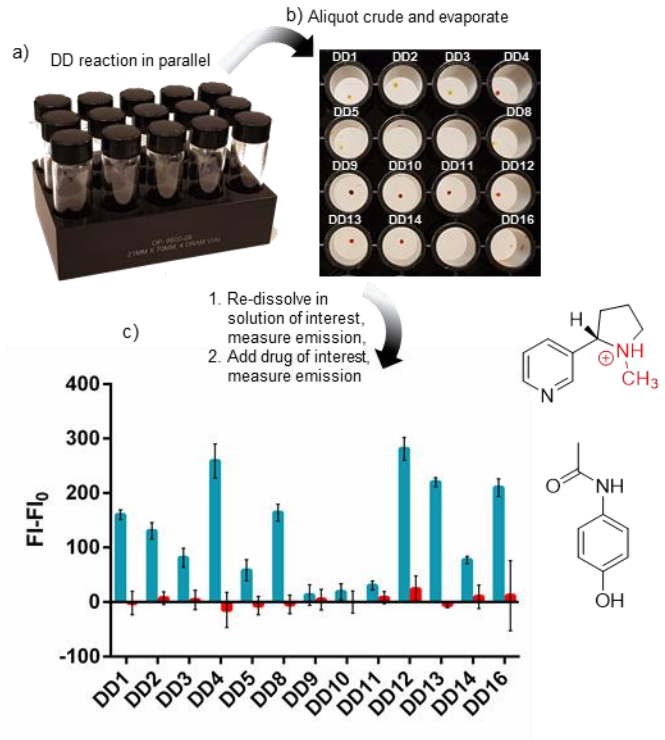

Figure 5. 3 Scheme of parallel DimerDye synthesis and crude screening for nicotine and acetaminophen. a) Each DimerDye reaction occurs in a separate vial, heated in an aluminium block. b) The crude mixture is aliquoted to a black-walled 96-well plate and evaporated. c) The pellets are re-dissolved in buffered water and initial fluorescence is measured. The analyte of interest is added, fluorescence is measured again and the difference in fluorescence is determined. Structures of analytes tested include nicotine with the hydrophobic cation highlighted in red and acetaminophen. Blue bars = 10 μM nicotine, red bars = 10 μM acetaminophen. See Supporting Information for excitation and emission wavelengths used.

A rapid, crude screening process successfully identified DimerDye sensors without first needing to purify each compound. The crude reactions were directly aliquoted into 96-well plates and the reaction solvent was allowed to evaporate (Figure 5. 3a and b). The dried pellets were re-suspended in sodium phosphate buffer (10 mM, pH 7.4). Nicotine was added as a model analyte. The increases in fluorescence in certain wells indicate the creation of good nicotine sensors. To confirm that the fluorescence change arises from host-guest binding, we counter-screened the library against acetaminophen, which is neutral and should not bind DimerDyes. Acetaminophen generates little to no fluorescence in all cases (Figure 5. 3c).

We selected a subset of structurally diverse sensors for follow-up mechanistic studies. From the fluorescence responses to nicotine, we selected **DD1**, **DD4**, **DD8**, **DD12**,

and **DD13** as active sensors to re-synthesize, purify and study (Figure 5. 4). We also selected an inactive sensor, **DD9**, so we could learn more about the parallel synthesis and screening results.

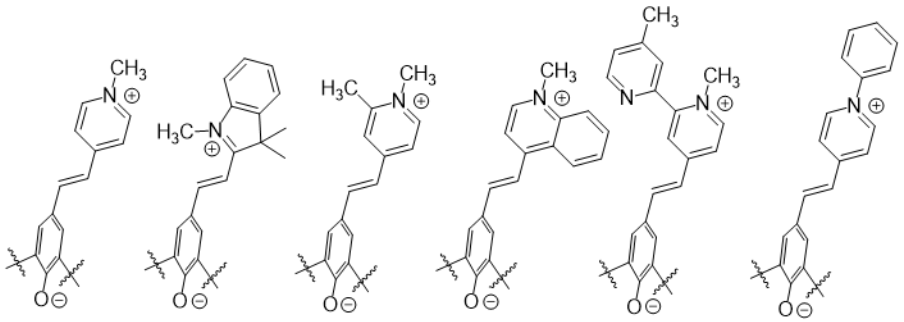

	DD1	DD4	DD8	DD9	DD12	DD13
λex. (nm)	385	475	375	440	415	420
λem. (nm)	590	570	580	660	640	635

Figure 5. 4 "Hit" DimerDyes 1, 4, 8, 12, 13 and control **DD9** selected to be re-synthesized, purified and studied as chemosensors for illicit drugs along with their respective excitation and emission wavelengths.

Each of the selected DimerDyes assembled into homodimers in water in the programmed way, regardless of the structure of the pendant groups. Selected sensors were obtained with modest yields (23–55%) after re-synthesis and purification by reverse-phase HPLC. ^{1}H NMR spectra confirm each sensor exist as homodimers when dissolved in buffered-D_2O. The signature feature of homodimerization is upfield shift and broadening of pendant group resonances due to encapsulation in the electron-rich calix[4]arene pocket. Aromatic resonances in the selected sensors shifted upfield by 1.23-3.69 ppm, while aliphatic (methyl) resonances shifted upfield by 0.46-3.60 ppm (Table 5. 2) compared to the shifts observed for the parent heterocycles. In all cases the protons farthest out on the pendant arm had the greatest upfield shifts. This indicates those protons are the most deeply buried in the pocket of the opposing calixarene in each dimer. 1D DOSY NMR on **DD4** confirmed that its hydrodynamic radius was typical for a dimeric assembly and larger than the non-dimerizing aldehyde precursor, **3.3** (see Supp. Info.). Interestingly, inactive sensor **DD9** also shows clear signs of dimerization with the *N*-CH_3 and *ortho*-proton shifted 2.50 ppm and 2.61 ppm, respectively.

Table 5. 1 1D DOSY obtained diffusion coefficients (D) and hydrodynamic radii (r_H) of **3.3**, **DD4** alone and **DD4** complexed to nicotine

	D (m^2/s)	r_H (Å)
3.3	$(3.29 \pm 0.02) \times 10^{-10}$	7.4 ± 0.3
DD4	$(1.96 \pm 0.05) \times 10^{-10}$	12.4 ± 0.7
DD4 + 20 eq. nicotine	$(2.7 \pm 0.3) \times 10^{-10}$	8 ± 1

The fluorescence responses arise from the disassembly of each DimerDye and host-guest complexation with analyte. ^{1}H NMR titrations of nicotine into each DimerDye show resonances broadening partially or completely, indicating dimer disassembly and nicotine complexation at an intermediate timescale relative to NMR. Nicotine titrations into **DD4** and **DD12** most clearly show the host resonances returning from upfield-shifted locations and/or broadening Figure 5. 5a and Supporting Information). **DD4** resonances stay sharp enough in the presence of 20 eq. nicotine to conduct 1D DOSY experiments, and as expected the hydrodynamic radius of **DD4** decreases to a value expected for a monomeric calixarene-nicotine complex (see Supp. Info.). Comparing the NMR tubes before and after the addition of nicotine shows visible DD fluorescence only for the nicotine-containing samples when irradiated at 365 nm with a hand-held UV lamp Figure 5. 5b and Figure 5. 23). This behaviour is further confirmed with titrations of nicotine into **DD12** monitored by fluorescence spectroscopy. The dimer alone is barely fluorescent when irradiated at 415 nm, but upon addition of nicotine the fluorescence emission at 640 nm increases (Figure 5. 5c and Supporting Information). This turn-on fluorescence response is observed by all selected DimerDyes except for **DD9**, which shows nicotine complexation by NMR yet remains dark when irradiated with the UV hand-held lamp and when studied on a fluorescence spectrometer.

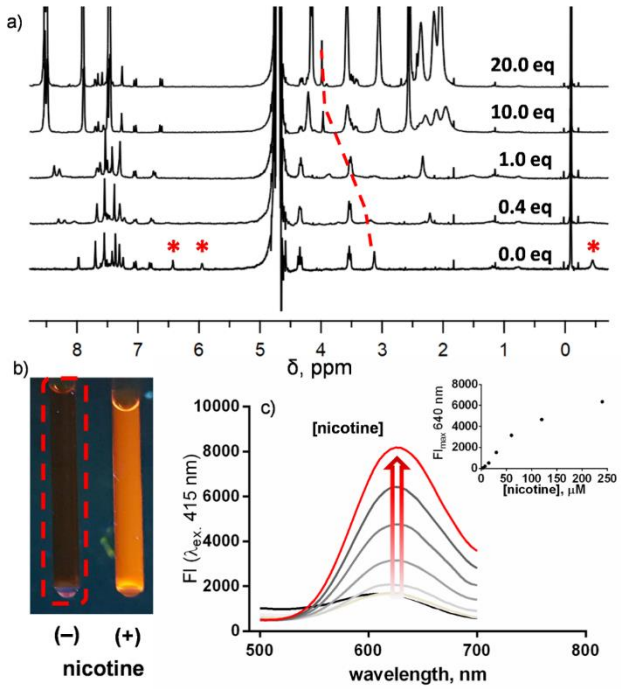

Figure 5. 5 Nicotine titrations reveal disassembly of dimer and formation of fluorescent DD–nicotine complex. a) ^{1}H NMR titrations of nicotine into **DD12** (500 μM) show fluorophore resonances in either fast exchange by shifting downfield (red dotted lines) or in intermediate exchange and broadening (red stars) indicative of disassembly and formation of a nicotine host-guest complex. b) Picture of NMR tubes with **DD12** without nicotine (–) or with nicotine (+) when irradiated by a hand-held UV lamp. c) Fluorescence titrations of nicotine into **DD12** (12 μM) shows a dose-dependent increase in fluorescence. The red trace indicates [nicotine] = 240 μM, while black line indicates no nicotine present. All samples are in NaH_2PO_4/Na_2HPO_4 (10 mM, pH 7.4) buffer.

DimerDyes provide turn-on fluorescence detection of different drugs at low micromolar concentrations in water and in saliva. Three exemplary drugs were chosen from different drug classes: nicotine, methylenedioxymethamphetamine (Ecstasy, or MDMA), and cocaine. In both water and saliva, all five selected DimerDyes detect all three drugs at low μM concentrations (Table 5. 10 and Table 5. 11). **DD8** detects nicotine in water and in saliva with limits of detection at 3.4 μM and 18.6 μM, respectively (Figure 5. 6a and b). Even MDMA, a secondary amine and therefore a weaker guest, induces a response from **DD1** in both water and saliva with limits of detection at 2.7 μM and 41.2 μM, respectively (Figure 5. 6c and d). **DD13** detects cocaine equally well in buffer and in saliva, with limits of detection of 2.7 μM in both fluids (Figure 5. 6e and f).

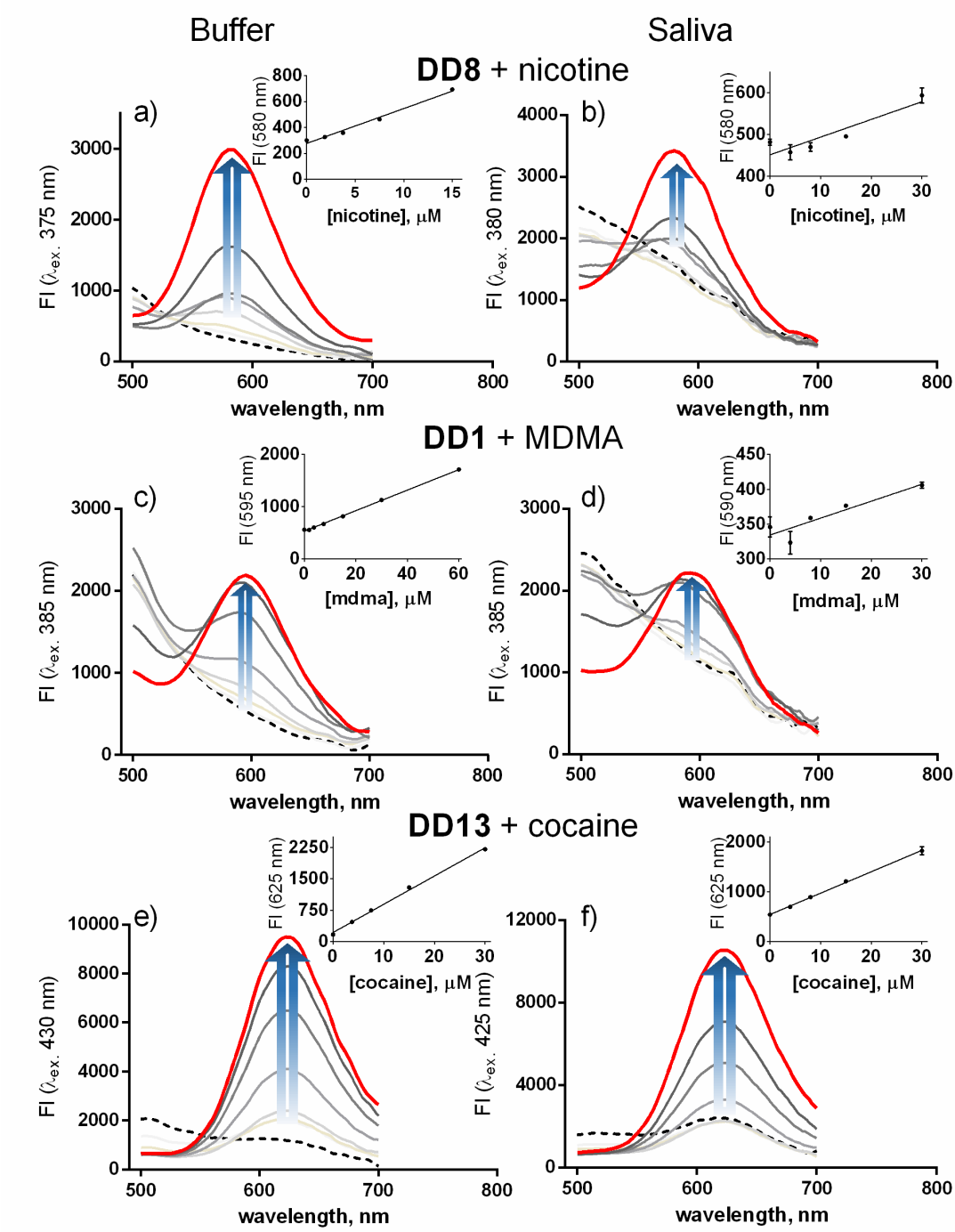

Figure 5. 6 Exemplary fluorescence titrations of different drugs into DimerDyes in buffered water and saliva. Nicotine titrations into **DD8** in a) buffered water and in b) saliva. MDMA titrations into **DD1** in c) buffered water and in d) saliva. Cocaine titrations into **DD13** in e) buffered water and in f) saliva. [**DD**] = 12 µM, red bold trace indicates [drug] = 240 µM, dashed black line indicates no drug present. "Buffer" is NaH_2PO_4/Na_2HPO_4 (10 mM, pH 7.4) and "Saliva" is a 1:1 dilution of saliva with water;

dilution is necessary to allow for accurate, bubble-free pipetting of saliva. See Supporting Information for the complete set of titrations.

We next explored the combination of multiple agents into a sensor array, as initially discussed in Section 1.4. This approach has distinct advantages over the use of single sensors designed for individual analytes. Often chemosensors cross-detect many analytes that are present in a complex mixture. Instead of re-designing a chemosensor to improve selectivity, the original system can be expanded to form an array of chemosensors that cross-react with many analytes but to different extents. This complex output is a unique fingerprint for each analyte. Multivariate analysis, including methods like principal component analysis (PCA) and linear discriminant analysis (LDA), can analyze the 'fingerprints' by both reducing the dimensionality of the data and creating a useful way to represent the differential responses. Anslyn *et al.* first developed these techniques for a wide variation of applications, including sensor arrays that can differentiate flavonoids in wine[254] and those that can classify different cancer cells.[255] Others have used supramolecular array sensors to differentiate chemical marks on histone proteins,[256-257] different anions in toothpaste,[258] and protein recognition from pattern-generating multi-dye probes.[259]

A sensor array of five DimerDyes was successfully able to detect and discriminate between closely related drugs and metabolites in multiple drug families. We studied amphetamines, opiates, and alkaloids, and included nicotine and acetaminophen alongside each different drug family as these two drugs are commonly found in individuals. Figure 5. 7a shows that the active drugs, MDMA and methamphetamine (MA), are discriminated from their respective metabolites, methylenedioxyamphetamine (MDA) and amphetamine (A), even though each differs from its metabolite by only a single methyl group. The array in Figure 5. 7b also differentiated between cocaine, its main metabolite benzoylecgonine, as well as lidocaine and procaine, which are common adulterants found in illegally purchased cocaine.[260] Figure 5. 7c shows a 3D scores plot that highlights the discrimination between heroin and its metabolite 6-monoacetylmorphine (6-MAM), while oxycodone and oxymorphone are not perfectly discriminated as both clusters of replicate data are nearly overlapping.

DimerDyes can function individually or as an array of sensors. Each sensor cross-reacted as expected with each drug, but the uniqueness of the generated fluorescence fingerprint was sometimes limited.[112] This is highlighted by the low variance (< 5%) along the second principal component (F2) in the amphetamines and anaesthetics class. This suggests that in some settings DimerDyes might be able to operate independently and not necessarily within an array. The benefit of the DD array is the easy visualization of the data for drug identification. It is easier to map combinations of drugs with common adulterants or their metabolites by the PCA scores plots rather than fluorescence bar graphs (see Supp. Info).

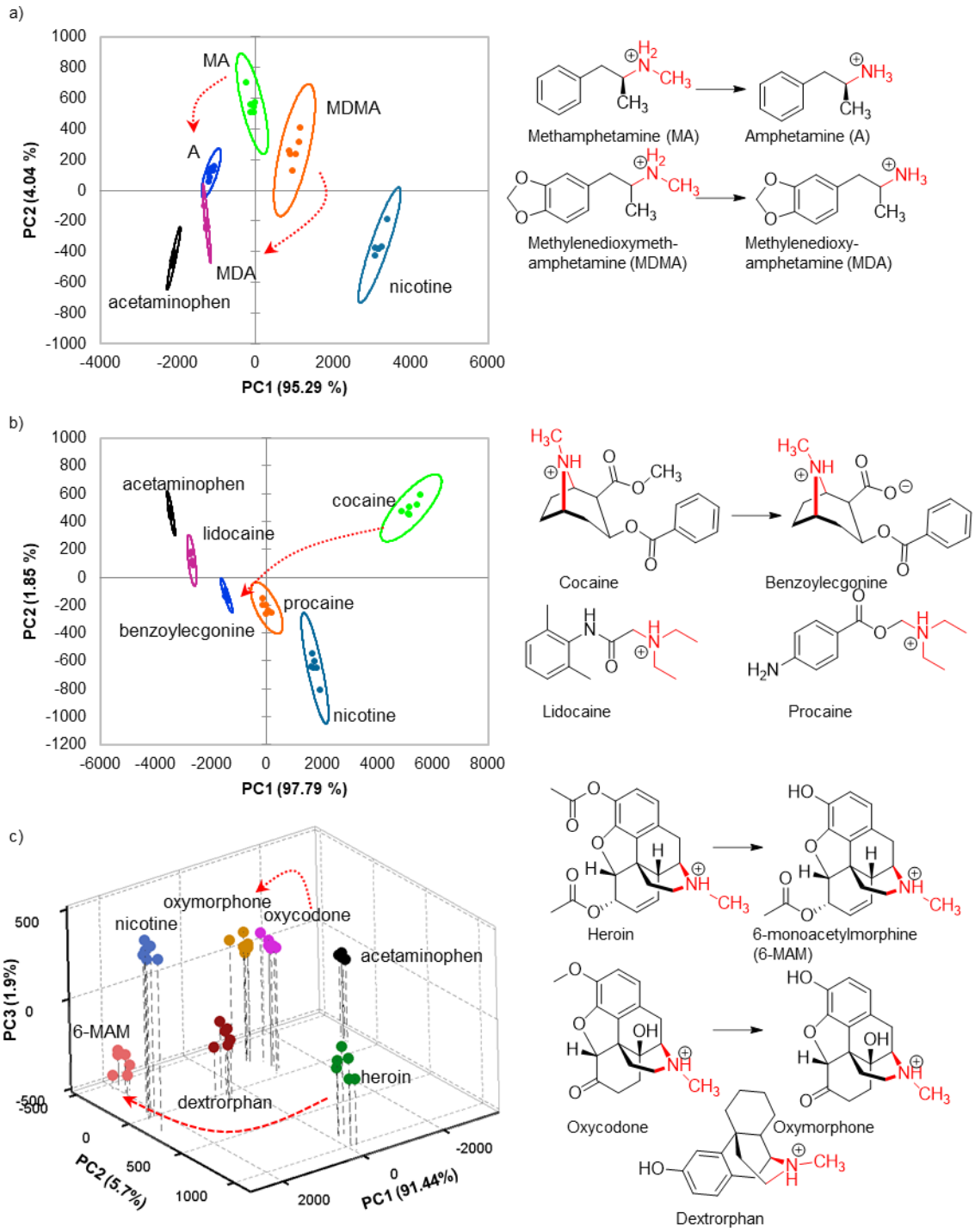

Figure 5. 7 Principal component analysis (PCA) scores plots distinguish between different members and classes of drugs by five DimerDye sensors (**DD1**, **DD4**, **DD8**, **DD12**, **DD13**) operating within an array. a) PCA plot of amphetamines are well discriminated with samples clustered and separated from each other. b) PCA plot of anaesthetics c) 3D PCA plot of opioids. Red dotted lines map the parent drug to its main metabolite. Structures in each class are shown to the right. Red motifs are recognized by

the calixarene pocket. Each sample cluster is enclosed by 95% confidence ellipses. [DD] = 12 μM, [drug] = 100 μM and in a NaH_2PO_4/Na_2HPO_4 (10 mM, pH 7.4) buffer.

5.4 Discussion

The final, parallel synthetic step described here gives access to new agents with a common sensing mechanism, but with varying photophysical properties and guest-binding properties. The successful structures included merocyanines based on *N*-methylpyridinium (**DD1** and **DD8**), indolinium (**DD4**), bipyridinium (**DD12**) and *N*-phenylpyridinium (**DD13**). The new **DD** sensors have tunable excitation and emission wavelengths (λ_{exc} 380-475 nm, λ_{em} 570-640 nm), with Stokes shifts between 95 nm and 215 nm. The variable structures in this small DimerDye library also translated into different binding properties for different drugs. The quinolinium dyes, **DD9** – **DD11**, were not as guest-responsive due to an unpredicted photophysical deficiency rather than poor self-dimerization or guest recognition. This highlights the strength of the parallel synthesis and crude screening process, as it would allow us going forward to avoid the wasted effort in synthesizing, purifying, and characterizing a sensor only to find that it is inoperative for an unknown reason.

These new supramolecular agents have sensitivities in real biological solutions that meet or approach the values seen in real human samples. DimerDyes remain functional in saliva that often contains 3 g/L of proteins and 20 – 100 mM concentrations of various salts.[110] To our knowledge, there are only a few supramolecular chemosensors that operate in biofluids, like urine, which reflects the difficulty of working in such medium.[114, 241, 261] Drug concentrations in saliva reach low μM within an hour of consumption and we have shown that our DimerDye sensors can detect at or near these concentrations.[262-266] For example, MDMA concentrations reach 35 μM in saliva 1.5 hours after consumption,[262] while cocaine can be present in saliva at 1 μM after 2 hours.[263, 266]

The power of a sensor array to detect many analytes without the need for excellent specificity or rational design was demonstrated with the combination of five different DimerDyes (**DD1**, **DD4**, **DD8**, **DD12**, **DD13**). From our nicotine, MDMA, and cocaine titrations, we noticed that subtle changes in drug structure induced small but significant changes in fluorescence responses. Those differences translated into substantial success when the **DD**s were deployed in a sensor array. With the combination of our five sensors,

we were able to reasonably distinguish between each member within a drug class. A jackknife analysis showed that we were also able to successfully classify 100% of members within the opioid and anaesthetics families, and to achieve 96% success in the amphetamines family (see Supporting Information).

5.5 Conclusion

We were successfully able to transform this the original DimerDye concept to include a wide variation of chemosensors that operate through the same supramolecular sensing mechanism. The parallel method for synthesizing and testing new Dimer Dyes is accessible, efficient and flexible. It can easily be expanded upon, enabling the discovery of more DimerDye sensors that work for different cationic analytes, and that operate in different biological solution conditions. The promiscuity of sulfonated calixarenes, coupled with the general success of this approach in salty water, combine to suggest that this concept can be applied to many different cationic analytes in many different aqueous solutions. Expanding the diversity libraries using known synthetic approaches will generate a library of crude sensors that could be quickly tested for the ability to detect any given cationic analyte in its native biological fluid.[251, 267] Furthermore, we envision that this parallel approach can be expanded to include other dye-appended macrocycles to identify sensors for a wider variety of biological analytes.

5.6 Experimental methods and supplementary information

5.6.1 General methods and materials

^{1}H, ^{13}C, and 1D DOSY were recorded on a Bruker Avance Neo 500 MHz spectrometer unless otherwise indicated and processed with MestReNova by Mestrelab Research S.L. Deuterated solvents were purchased from Sigma Aldrich and NaH_2PO_4/Na_2HPO_4 (50 mM, pD 7.4) in D_2O were prepared, and the pD was adjusted with 1 M NaOD/DCl solutions. Accurate mass spectra determinations for novel compounds were done on a Thermo Scientific Ultimate 3000 ESI-Orbitrap Exactive. Purities were determined using a Waters UPLC-MS equipped with UV/Vis and QDa detector, with an

Aquity UPLC BEH C18 1.7 uM (21 x 50 mm) column run with a gradient of 80% H_2O (+0.4% FA)/20% CH_3CN (+0.4% FA) to 50% H_2O (+0.4% FA)/50% CH_3CN (+0.4% FA) over 4 min at 0.6ml/min. All UV-Vis and fluorescence titrations and spectra were collected on a BioTek Cytation-5. Titrations and dilutions were conducted in NUNC black-walled, optical bottom 96-well plates. Infrared (IR) spectra were obtained using a Perkin Elmer 1000 FT-IR spectrometer. Data are represented as follows: frequency of absorption (cm^{-1}), intensity of absorption (s = strong, m = medium, w = weak, br = broad). Melting points were collected on a Gallenkamp Melting Point apparatus.

Compound **3.3** was prepared following literature protocol.[237] Heterocyclic compounds were synthesized from previously reported literature.[251, 268-269]

All drugs except nicotine were purchased through Sigma Aldrich in 1mg/ml ampules dissolved in methanol or acetonitrile. To avoid adding organic solvent to DD array, the ampules were evaporated of organic solvent over a gentle stream of nitrogen overnight. The residue was re-dissolved in water and aliquoted to form stock solutions (1 mM) in NaH_2PO_4/Na_2HPO_4 (10 mM, pH 7.4). *S*-(-)-nicotine was purchased from Alfa Aesar.

Stock solutions of DimerDyes 1, 4, 8, 12, 13 (1 mM) were prepared in NaH_2PO_4/Na_2HPO_4 (10 mM, pH 7.4) with concentrations accurately checked against a reference standard by quantitative NMR before being further diluted to a working stock (200 μM).

5.6.1b Fluorescence titrations in diluted saliva

Saliva was prepared for handling by centrifugation (3400 rpm, 15 min) at 4°C to remove suspended solids. The supernatant was pipetted into a second conical tube containing an equal volume of water to reduce viscosity and foaming. To avoid multiple, foam-inducing transfers of saliva to form stocks, each DimerDye was directly pipetted into empty wells of a NUNC black-walled plate in a set of triplicates. The 1:1 saliva:water mixture was added to form a final [DD] = 12 μM at 100 μL. Separately, each drug (nicotine, MDMA, cocaine) was diluted in the 1:1 saliva:water mixture with a final [DD] = 12 μM and [drug] = 240 μM. This was serial diluted to achieve a [drug] = 240 μM – 4 μM.

5.6.1c General Synthesis of select DimerDyes

The protocol used for parallel synthesis and screening is described below. For all re-synthesized DimerDyes, the synthesis was as follows: **3.3** (50 mg) and Het4/8/9/12/13 (1.1 eq.) were dissolved in methanol (2 mL) along with morpholine (40 eq.) and heated at reflux for 12 hours. Cold ether was added to induce precipitation and the suspension was transferred to a 50 mL conical tube. After centrifugation (3400 rpm, 5 min) a pellet was formed and the supernatant was decanted and discarded. The pellet was re-suspended in fresh cold ether and the centrifugation, decanting process was repeated two more times. The pellet was re-dissolved in the indicated eluent composition and filtered. A Shimadzu HPLC with a 280 nm and 370 nm detector was used to purify the final product with a Phenomenex Luna C18, 250 mm x 22 mm, 5 μM preparative column.

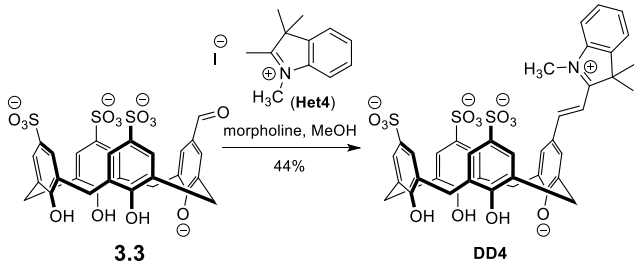

DD4. Het4 was prepared as previously reported.[268] Purified with a gradient of 85% H_2O (+0.1% TFA)/15% CH_3CN (+0.1% TFA) to 50% H_2O (+0.1% TFA)/50% CH_3CN (+0.1% TFA) over 20 min. The fractions were collected and lyophilized to yield a yellow/orange fluffy solid (27 mg, 44%). Mp: decomposed > 260°C. FT-IR (cm^{-1}): 3229 (br), 1585 (m), 1535 (w), 1479 (m), 1447 (w), 1292 (w), 1163 (s), 1135 (s), 1036 (s), 786 (m), 749 (w), 626 (s), 543 (m). ^1H NMR (500 MHz, D_2O): δ 7.79 (s, 1H), 7.78 (s, 1H), 7.63 (d, *J* = 16.3 Hz, 1H), 7.55 (s, 2H), 7.48 (s, 2H), 7.32 (s, 2H), 6.55 (d, *J* = 15.7 Hz, 1H), 6.35 (d, *J* = 6.7 Hz, 1H), 5.90 (br, 1H), 4.57 (d, *J* = 13.7 Hz , 2H), 4.27 (br, 1H), 4.10 (d, *J* = 12.2 Hz, 2H), 3.88 (br, 1H), 3.63 (d, *J* = 12.2 Hz, 2H), 3.54 (s, 3H), 3.43 (d, *J* = 13.7 Hz, 2H), 1.36 (s, 6H). ^{13}C NMR (76 MHz, d_6-DMSO): δ 180.7, 161.2, 153.9, 152.1, 151.4, 143.0, 141.9, 138.7, 138.5, 132.6, 129.7, 128.2, 127.9, 127.8, 127.2, 126.4, 126.2, 125.6, 122.6, 114.2, 108.4, 51.4, 33.7, 31.2, 30.6, 25.8. HR-MS (M^+ *m/z*): Calculated for $C_{41}H_{38}NO_{13}S_3^+$ 848.14998, Found 848.14938.

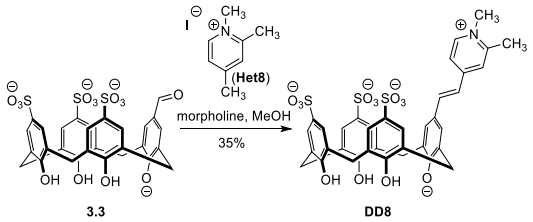

DD8. Het8 was prepared as previously reported.[251] Purified with a gradient of 90% H_2O (+0.1% TFA)/10% CH_3CN (+0.1% TFA) to 70% H_2O (+0.1% TFA)/30% CH_3CN (+0.1% TFA) over 23 min. The fractions were collected and lyophilized to yield a yellow fluffy solid (20 mg, 35%). Mp: decomposed > 300°C. FT-IR (cm^{-1}): 3288 (br), 1621 (m), 1598 (m), 1451 (w), 1132 (s), 1111 (s), 891 (w), 786 (w), 732 (w), 623 (s), 583 (s). ^{1}H NMR (500 MHz, D_2O): δ 7.69 (d, *J* = 1.4 Hz, 2H), 7.63 (d, *J* = 1.8 Hz, 2H), 7.36 (s, 2H), 7.14 (d, *J* = 6.1 Hz, 1H), 7.09 (s, 2H), 6.96 (s, 1H), 6.67 (d, *J* = 6.1 Hz, 1H), 6.67 (d, *J* = 15.5 Hz, 1H), 6.27 (d, *J* = 16.5 Hz, 1H), 4.34 (d, *J* = 3.5 Hz, 2H), 4.32 (d, *J* = 3.1 Hz, 2H), 3.53 (d, *J* = 13.4 Hz, 2H), 3.48 (d, *J* = 13.8 Hz, 2H), 0.79 (s, 3H), 0.54 (s, 3H). ^{13}C NMR (126 MHz, d_6-DMSO): δ 153.9, 152.3, 151.7, 149.6, 140.0, 139.7, 128.8, 127.4, 127.3, 127.2, 126.4, 126.3, 30.4, 18.2. HR-MS (M^+ *m/z*): Calculated for $C_{37}H_{34}NO_{13}S_3^+$ 796.11868, Found 796.11754.

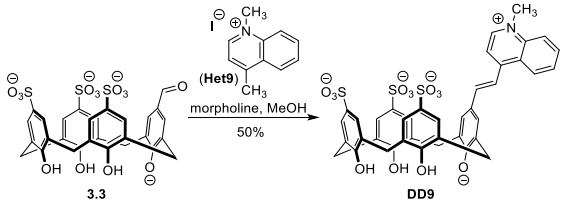

DD9. Het9 was prepared as previously reported.[251] Purified with a gradient of 85% H_2O (+0.1% TFA)/15% CH_3CN (+0.1% TFA) to 50% H_2O (+0.1% TFA)/50% CH_3CN (+0.1% TFA) over 18 min. The fractions were collected and lyophilized to yield an orange fluffy solid (30 mg, 50%). Mp: decomposed > 300°C. FT-IR (cm^{-1}): 3287 (br), 1593 (m), 1567 (m), 1535 (w), 1476 (w), 1449 (w), 1134 (s), 1109 (s), 1035 (s), 626 (s), 544 (s). ^{1}H NMR (500 MHz, D_2O): δ 7.81 (d, *J* = 2.3 Hz, 2H), 7.76 (d, *J* = 1.9 Hz, 2H), 7.67 (d, *J* = 8.6 Hz, 1H), 7.33 (s, 2H), 7.30 (d, *J* = 6.5 Hz, 1H), 7.17 (d, *J* = 6.5 Hz, 1H), 6.97 (s, 2H), 6.68 (br. 1H), 6.64 (d, *J* = 15.6 Hz, 1H), 6.47 (d, *J* = 16.2 Hz, 1H), 6.41 (br. 1H), 5.79 (d, *J* = 9.1 Hz, 1H), 4.45 (d, *J* = 13.6 Hz, 2H), 4.31 (d, *J* = 13.7 Hz, 2H), 3.60 (d, *J* = 13.1 Hz, 2H), 3.53 (d, *J* = 13.1 Hz, 2H), 2.05 (s, 3H). ^{13}C NMR (126 MHz, d_6-DMSO) δ: 153.0, 152.2,

150.5, 140.4, 138.2, 128.8, 128.1, 127.9, 127.7, 127.4, 126.9, 126.7, 125.6, 116.1, 43.6, 31.2, 30.9. HR-MS (M^+ *m/z*): Calculated for $C_{40}H_{34}NO_{13}S_3^+$ 832.11868, Found 832.11788.

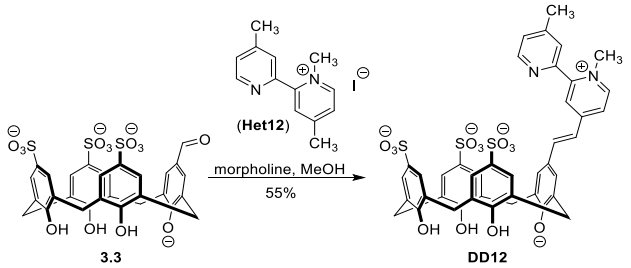

DD12. Het12 was prepared as previously reported.[251] Purified with a gradient of 85% H_2O (+0.01% TFA)/15% CH_3CN (+0.01% TFA) to 50% H_2O (+0.01% TFA)/50% CH_3CN (+0.01% TFA) over 23 min. The fractions were collected and lyophilized to yield an orange fluffy solid (35 mg, 55%). Mp: decomposed > 300°C. FT-IR (cm^{-1}): 3240 (br), 1615 (m), 1591 (m), 1453 (w), 1156 (s), 1111 (s), 1037 (s), 886 (w), 785 (w), 657 (m), 624 (s), 547 (s).). ^1H NMR (500 MHz, D_2O): δ 7.67 (d, *J* = 5.1 Hz, 1H), 7.69 (d, *J* = 2.1 Hz, 2H), 7.58 (br, 1H), 7.55 (d, *J* = 2.1 Hz, 2H), 7.42 (d, *J* = 6.1 Hz, 1H), 7.38 (s, 2H), 7.30 (s, 2H), 7.24 (s, 2H), 7.05 (d, *J* = 16.1 Hz, 1H), 6.80 (d, *J* = 16.1 Hz, 1H), 6.42 (s, 1H), 5.94 (br, 1H), 4.36 (d, *J* = 14.4 Hz, 2H), 4.33 (d, *J* = 14.4 Hz, 2H), 3.55 (d, *J* = 12.4 Hz, 2H), 3.52 (d, *J* = 12.8 Hz, 2H), 3.12 (s, 3H), 0.45 (s, 3H). ^{13}C NMR (126 MHz, d_6-DMSO): δ 154.1, 151.5, 146.9, 142.1, 140.0, 123.0, 129.1, 127.9, 127.7, 127.5, 127.0, 126.9, 125.2, 120.6, 46.1, 31.4, 31.1, 21.1. HR-MS (M^+ *m/z*): Calculated for $C_{42}H_{37}N_2O_{13}S_3^+$ 873.14523, Found 873.14435.

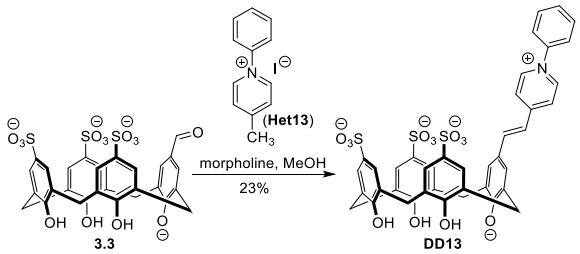

DD13. Het13 was prepared as previously reported.[269] Purified with a gradient of 85% H_2O (+0.1% TFA)/15% CH_3CN (+0.1% TFA) to 50% H_2O (+0.1% TFA)/50% CH_3CN (+0.1% TFA) over 20 min. The fractions were collected and lyophilized to yield an orange fluffy solid (14 mg, 23%). Mp decomposed > 280°C. FT-IR (cm^{-1}): 3229 (br), 1618 (m), 1587

(m), 1489 (w), 1451 (w), 1200 (s), 1133 (s), 1110 (s), 1036 (s), 878 (w), 760 (w), 624 (s), 549 (s). ^{1}H NMR (500 MHz, D_2O): δ 8.28 (d, *J* = 6.8 Hz, 2H), 7.72 (d, *J* = 7.0 Hz, 2H), 7.58 (s, 2H), 7.46 (d, *J* = 2.1 Hz, 2H), 7.40 (d, *J* = 2.1Hz, 2H), 7.30 (d, *J* = 15.8 Hz, 1H), 7.26 (s, 2H), 6.72 (d, *J* = 16.1 Hz, 1H), 6.18 (d, *J* = 6.92 Hz, 2H), 5.10 (br, 2H), 4.45 (d, *J* = 12.7 Hz, 2H), 4.27 (d, *J* = 12.7 Hz, 2H), 4.13 (br, 1H), 3.59 (d, *J* = 13.3 Hz, 2H), 3.45 (d, *J* = 12.7 Hz, 2H). ^{13}C NMR (126 MHz, d_6-DMSO): δ 155.0, 154.6, 151.5, 144.0, 143.3, 142.8, 139.9, 131.2, 130.6, 130.2, 129.3, 127.9, 127.8, 127.7, 127.5, 127.0, 126.9, 124.8, 123.7, 120.6, 31.5, 31.1. HR-MS (M^+ *m/z*): Calculated for $C_{41}H_{34}NO_{13}S_3^+$ 844.11868, Found 844.11786.

5.6.2 ^{1}H and ^{13}C NMR spectra of select DD

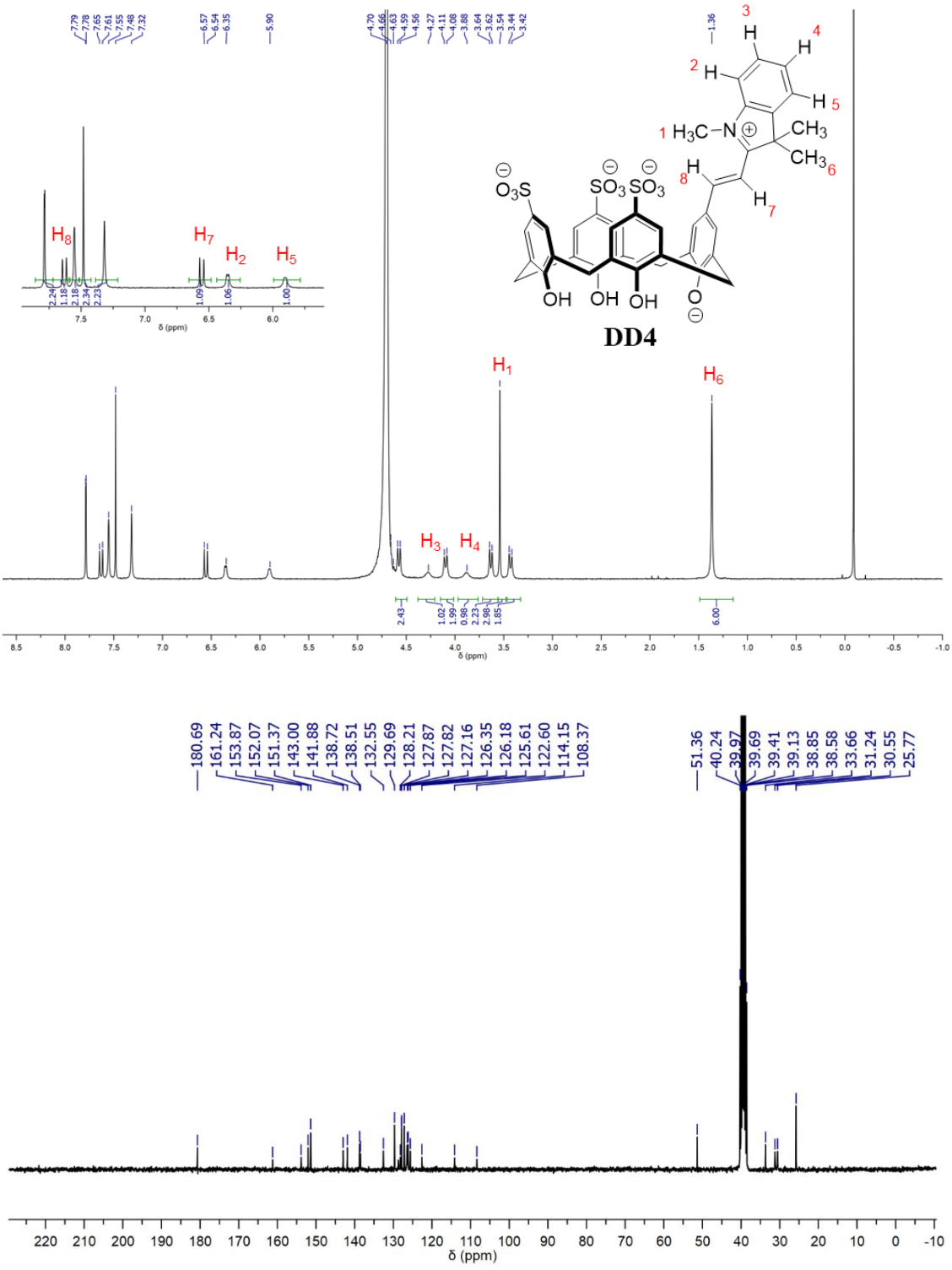

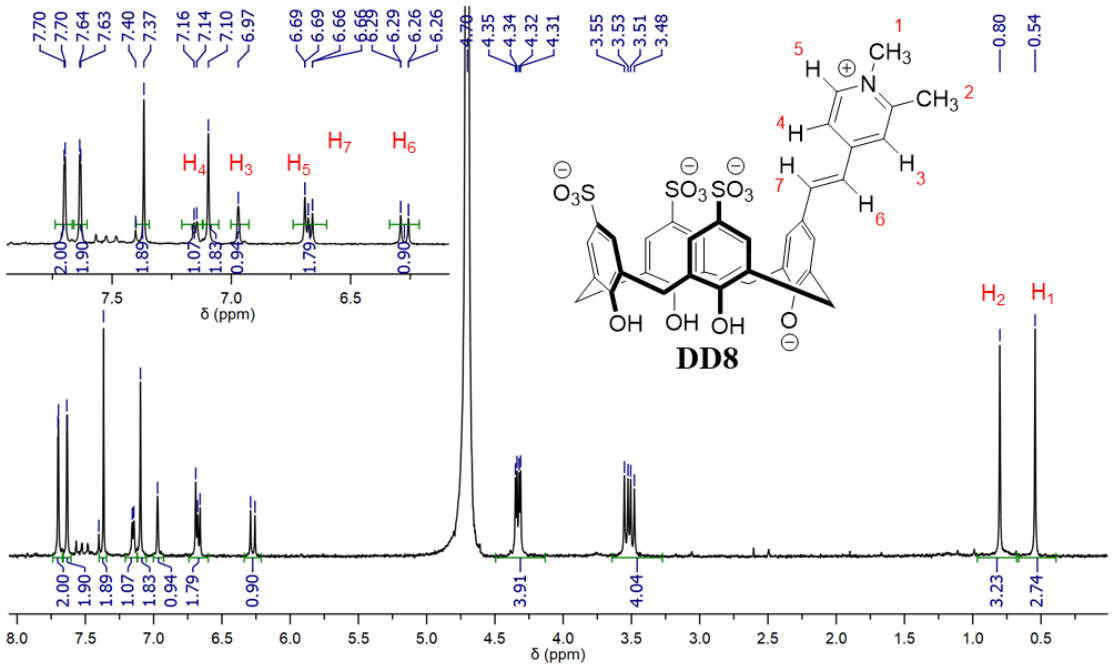
DD8
δ (ppm)

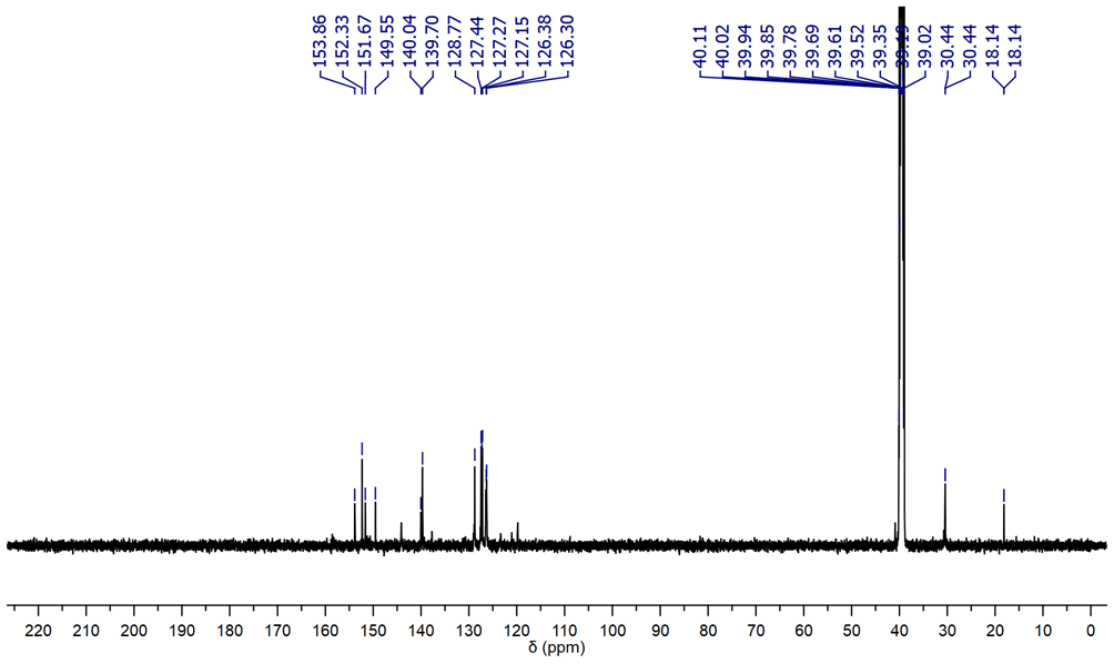
δ (ppm)

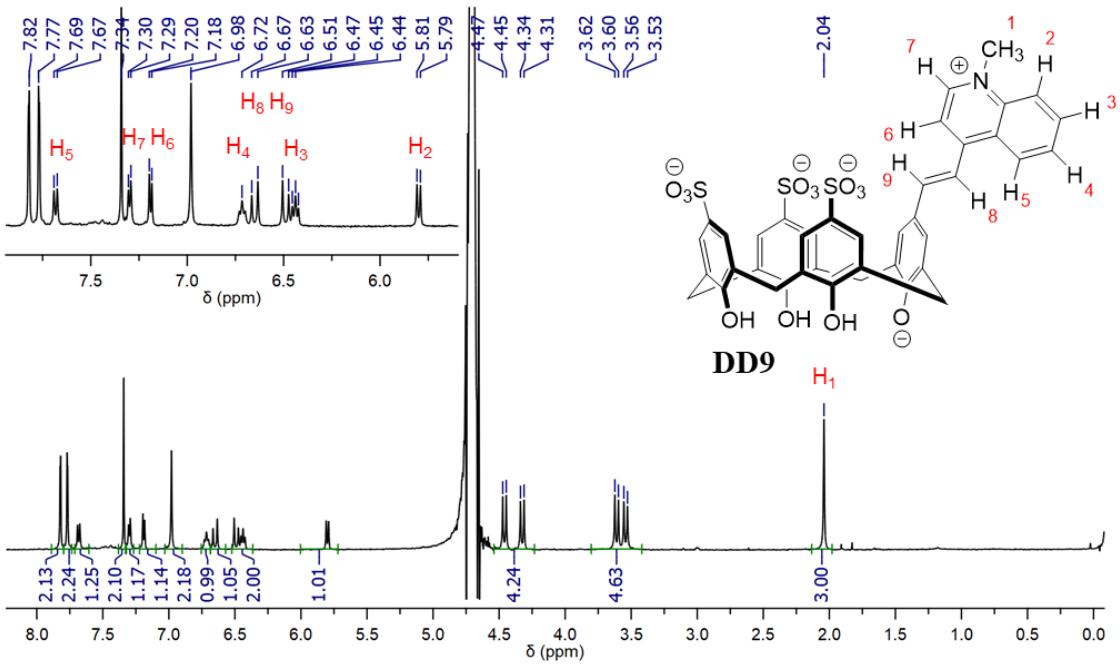
7.82
7.77
7.69
7.67
7.34
7.30
7.29
7.20
7.18
6.98
6.72
6.67
6.63
6.51
6.47
6.45
6.44
5.81
5.79
4.47
4.45
4.34
4.31
3.62
3.60
3.56
3.53
2.04
H5
H7 H6
H4
H3
H2
H8 H9
H1
DD9
2.13
2.24
1.25
2.10
1.17
1.14
2.18
0.99
1.05
2.00
1.01
4.24
4.63
3.00
δ (ppm)

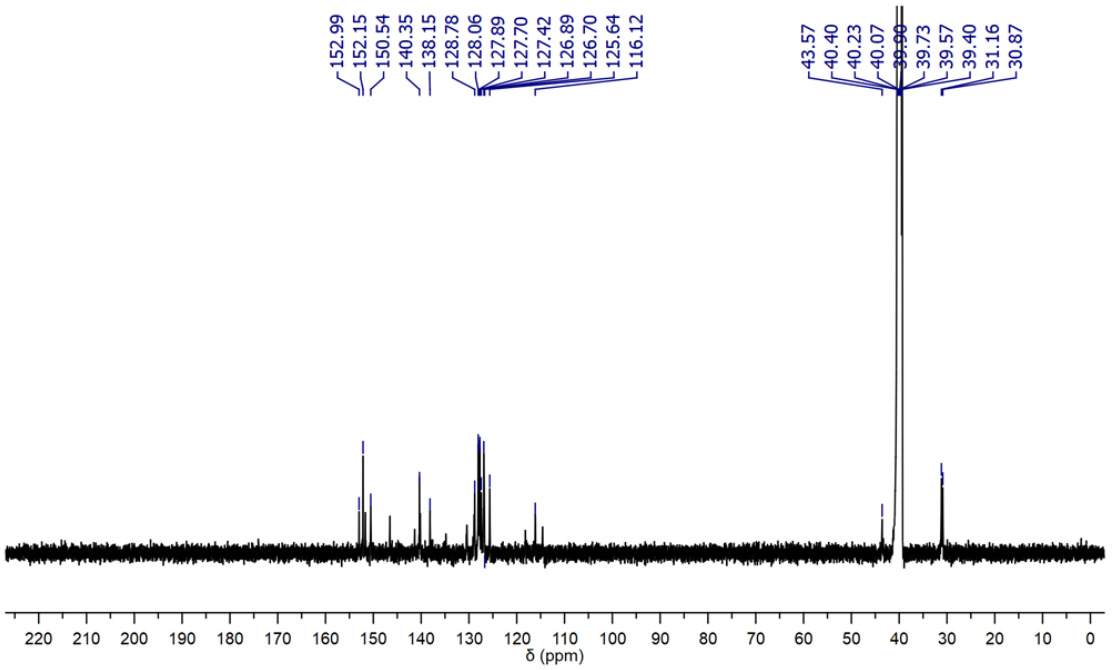
152.99
152.15
150.54
140.35
138.15
128.78
128.06
127.89
127.70
127.42
126.89
126.70
125.64
116.12
43.57
40.40
40.23
40.07
39.90
39.73
39.57
39.40
31.16
30.87
δ (ppm)

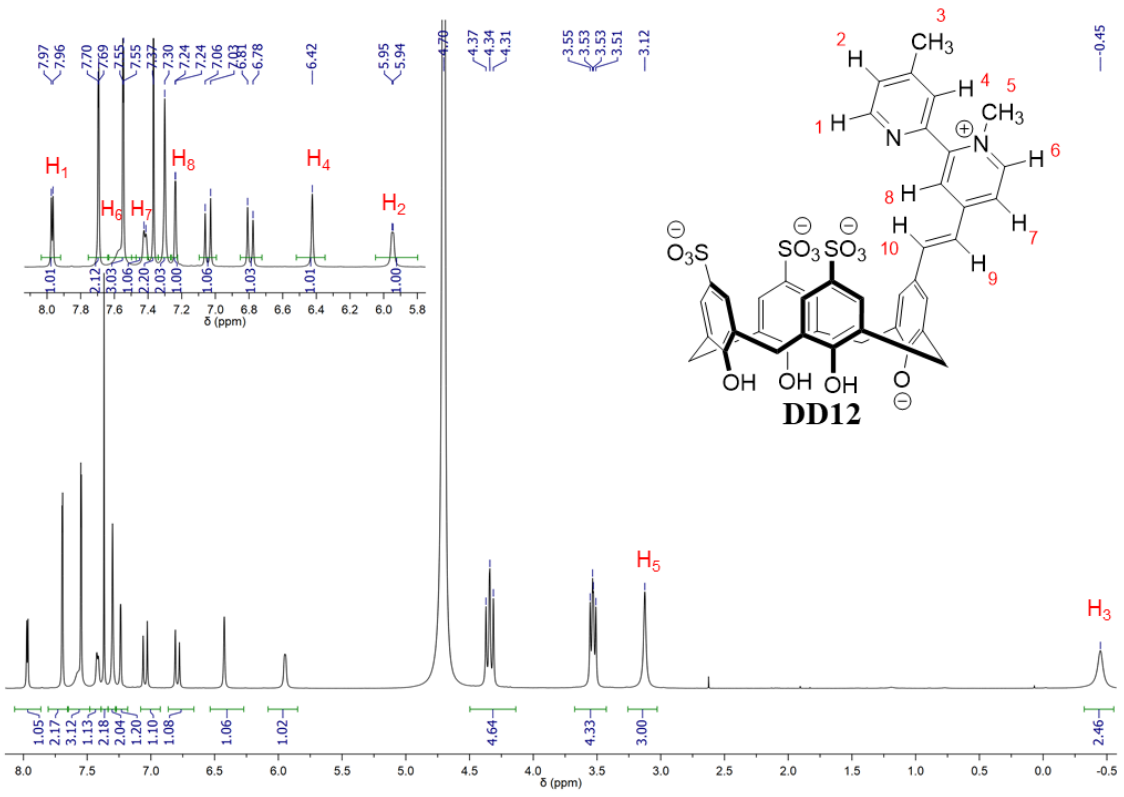
H1
H6
H7
H8
H4
H2
H5
H3
DD12

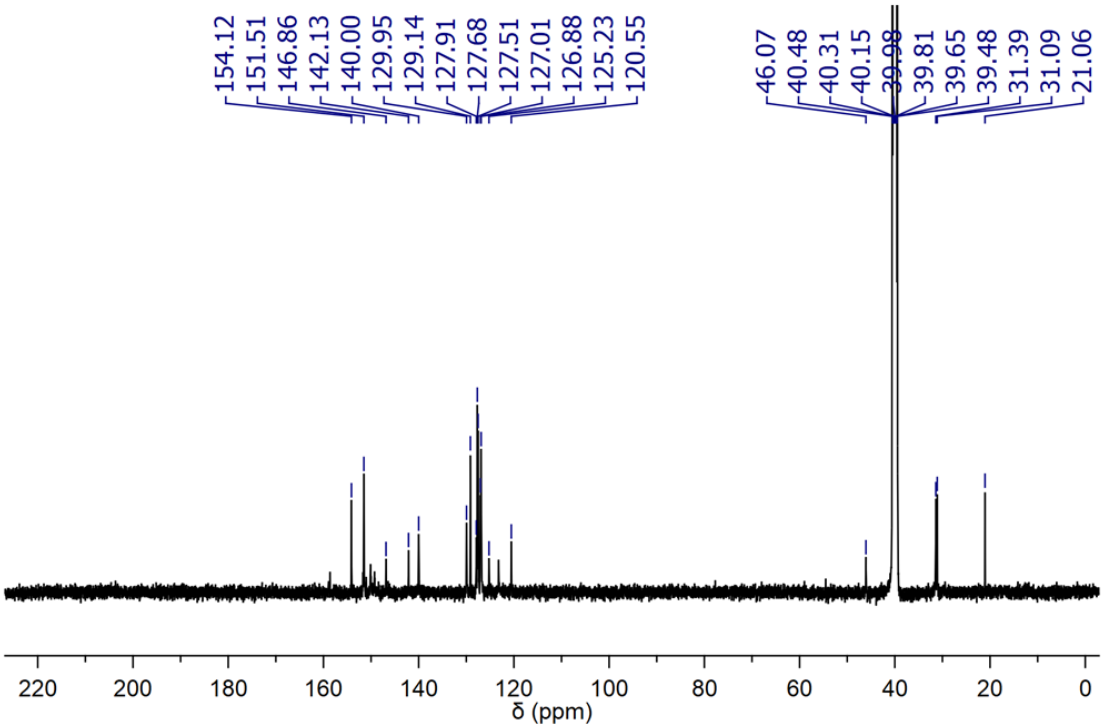
δ (ppm)

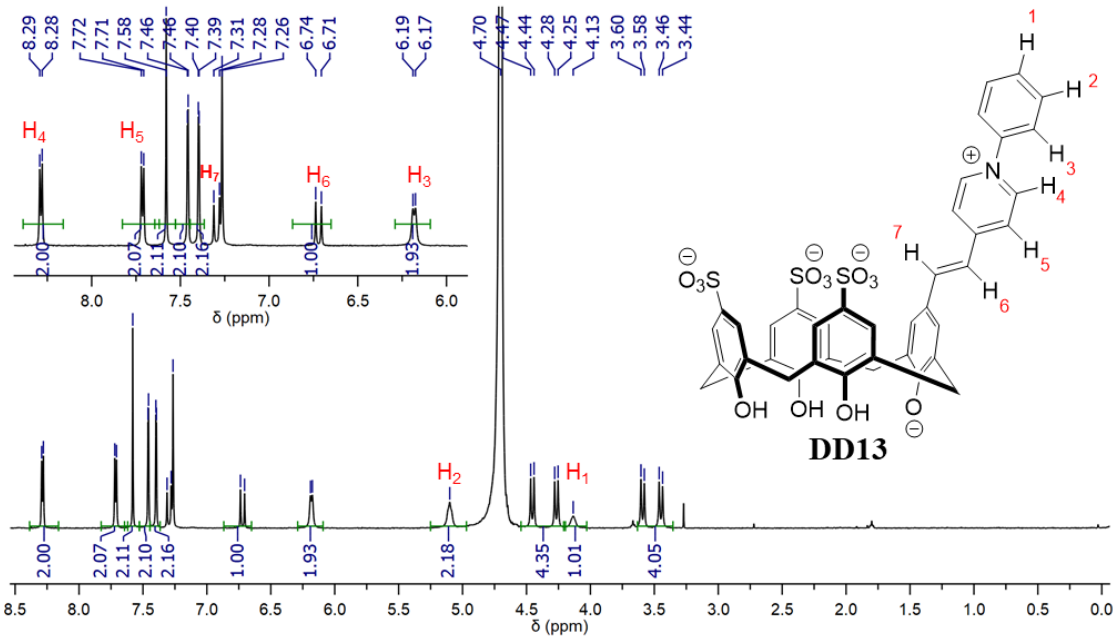
8.29
8.28
7.72
7.71
7.58
7.46
7.40
7.39
7.31
7.28
7.26
6.74
6.71
6.19
6.17
4.70
4.47
4.44
4.28
4.25
4.13
3.60
3.58
3.46
3.44
H4
H5
H7
H6
H3
H2
H1
2.00
2.07
2.11
2.10
2.16
1.00
1.93
2.18
4.35
1.01
4.05
δ (ppm)
DD13

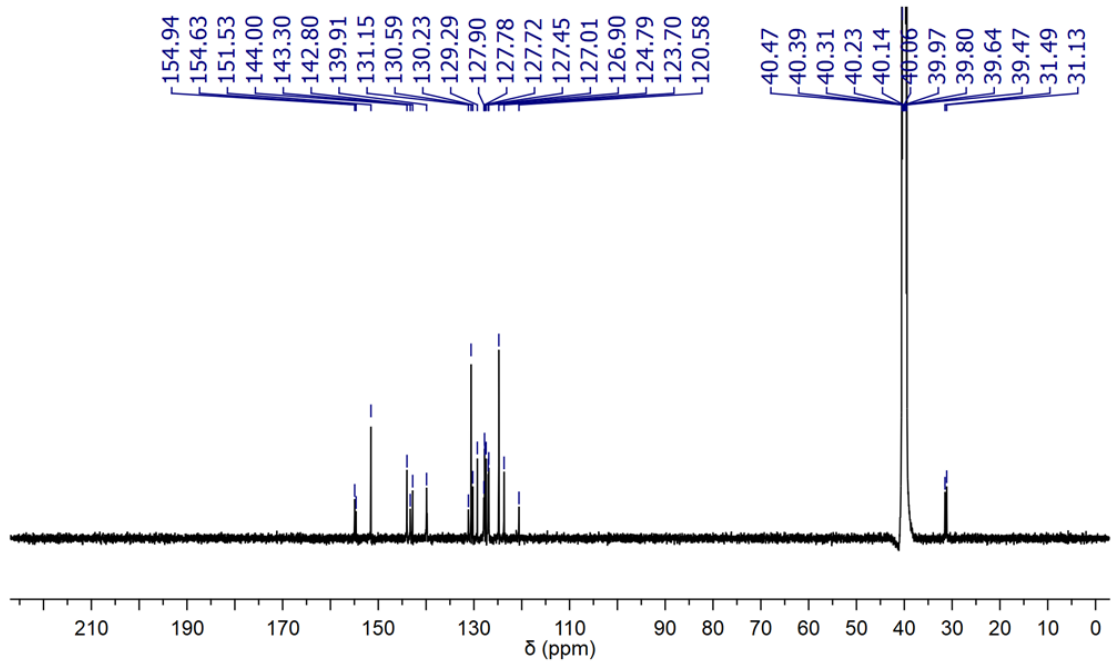
154.94
154.63
151.53
144.00
143.30
142.80
139.91
131.15
130.59
130.23
129.29
127.90
127.78
127.72
127.45
127.01
126.90
124.79
123.70
120.58
40.47
40.39
40.31
40.23
40.14
40.06
39.97
39.80
39.64
39.47
31.49
31.13
δ (ppm)

5.6.3 Additional ^{1}H NMR characterization of dimer assembly

Table 5. 2 Chemical shift differences between key resonances of **DD** and their respective **Het**.

	Het1	**DD1**	Δδ		**Het8**	**DD8**	Δδ
N-CH_3	4.33	0.66	3.67	H1	4.14	0.54	3.60
ortho	8.59	7.35	1.24	H2	2.56	0.79	1.77
meta	7.87	6.42	1.45	H3	8.47	6.66	1.81
				H4	7.62	7.15	0.47
				H5	8.47	6.68	1.79

	Het4	**DD4**	Δδ		**Het12**	**DD12**	Δδ
H1	4.00	3.54	0.46	H1	8.59	7.94	0.65
H6	1.55	1.36	0.19	H2	7.55	5.90	1.65
H2	7.70	6.35	1.35	H3	2.50	0.45	2.05
H3	7.59	4.27	3.32	H4	7.63	6.40	1.23
H4	7.57	3.88	3.69	H5	4.12	3.12	1.00
H5	7.78	5.90	1.88	H6	8.69	7.68	1.01
				H7	7.91	7.41	0.5
				H8	7.93	7.25	0.68

	Het9	**DD9**	Δδ		**Het13**	**DD13**	Δδ
H1	4.54	2.04	2.50	H1	7.59	4.13	3.46
H2	8.41	5.80	2.61	H2	7.59	5.10	2.49
H3	8.17	6.45	1.72	H3	7.59	6.17	1.42
H4	7.96	6.72	1.24	H4	8.79	8.28	0.51
H5	8.29	7.68	0.61				
H6	7.84	7.19	0.65				
H7	8.97	7.30	1.67				

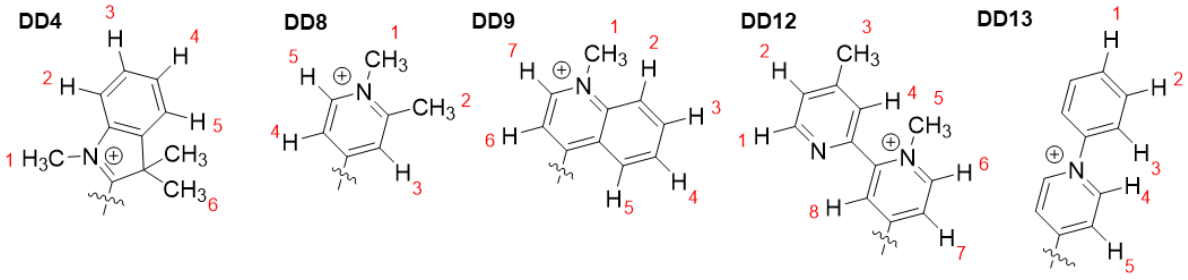

5.6.4 Development of parallel synthesis and screening method

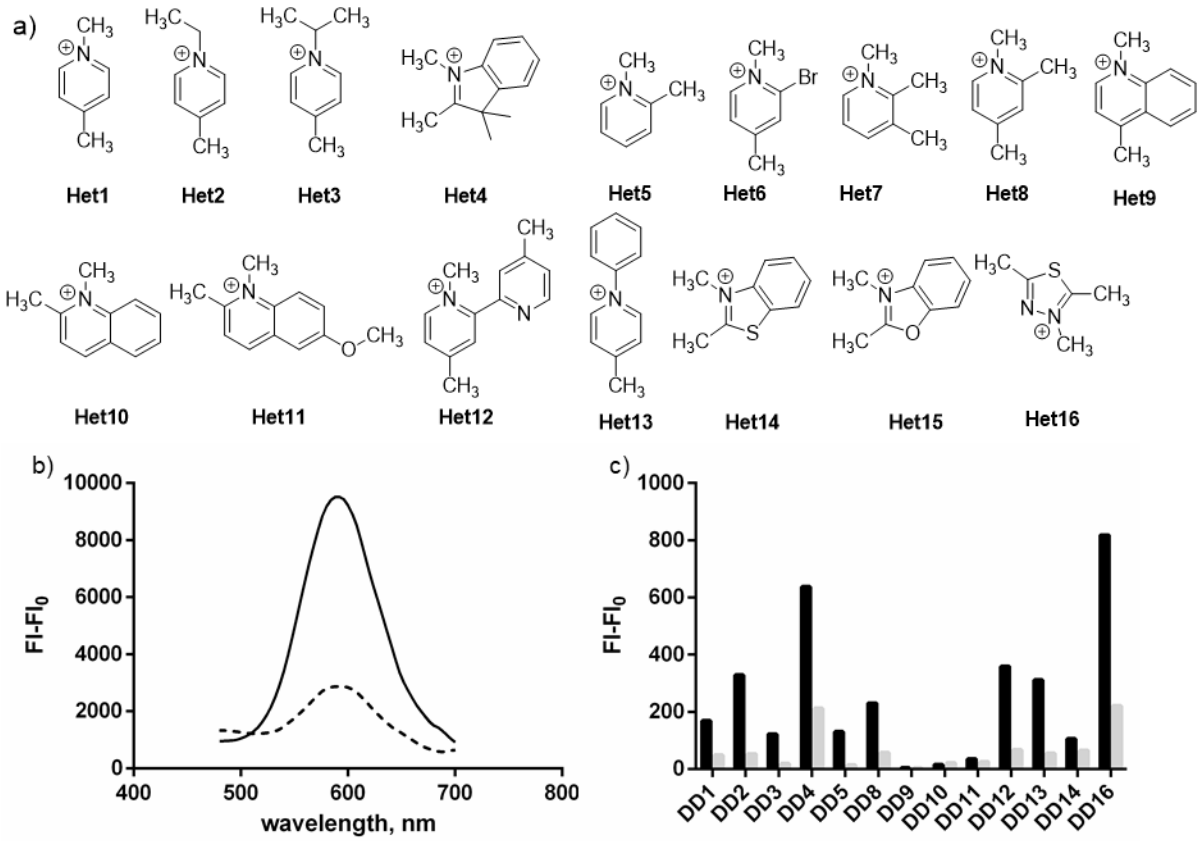

Figure 5. 8 Establishing conditions that allow efficient synthesis of all DDs. a) **Het1-16** used for condensation reactions. b) Fluorescence spectra ($\lambda_{ex.}$ 390 nm) of **DD1** with nicotine (50 μM) increases when changing the reaction time from 1.5 h (dotted line) to 6 h (solid line). c) The response of each crudely synthesized DD to nicotine (10 μM) after reacting with either 40 eq. of morpholine (black bars) or 20 eq. of morpholine (gray bars).

Procedure for parallel synthesis of DDs: An aluminium heating block (CombiBlocks, ChemGlass) held 4 dram vials which each contained a 1:1 mixture of **3.3** and one heterocyclic nucleophile (1.5 mM), along with morpholine (40 eq., 5 μL) in methanol (1 mL). The mixtures were capped, heated and stirred behind a blast shield for 6 hours at 50°C to afford coloured solutions. The solutions were sonicated to re-dissolve dried DimerDyes along the walls. The solutions were aliquoted (10 μL) into NUNC black-walled, clear-bottomed 96-well plates and dried in a 37°C oven for 4 hours. The dried pellets were re-suspended in phosphate buffer (10 mM, pH 7.4), centrifuged and mixed. Each solution was

diluted by transferring aliquots into a separate 96-well plate containing the same phosphate buffer. Fluorescence endpoint measurements were taken for each DimerDye, the $\lambda_{ex.}$ and $\lambda_{em.}$ that were used are listed below. A stock of nicotine prepared in phosphate buffer was added to each well (10 μL for final concentration of 10 μM) and fluorescence endpoint measurements were collected again. The fluorescence differences between after and before nicotine were used to evaluate each DimerDye.

Table 5. 3 Excitation and emission wavelengths used for crude DimerDye screening

	$\lambda_{ex.}$, nm	$\lambda_{em.}$, nm
DD1	380	575
DD2	390	575
DD3	390	575
DD4	480	560
DD5	390	575
DD8	380	575
DD9	440	680
DD10	450	600
DD11	440	630
DD12	410	615
DD13	420	620
DD14	470	565
DD16	420	555

5.6.5 UPLC-MS data of crude DimerDye reactions

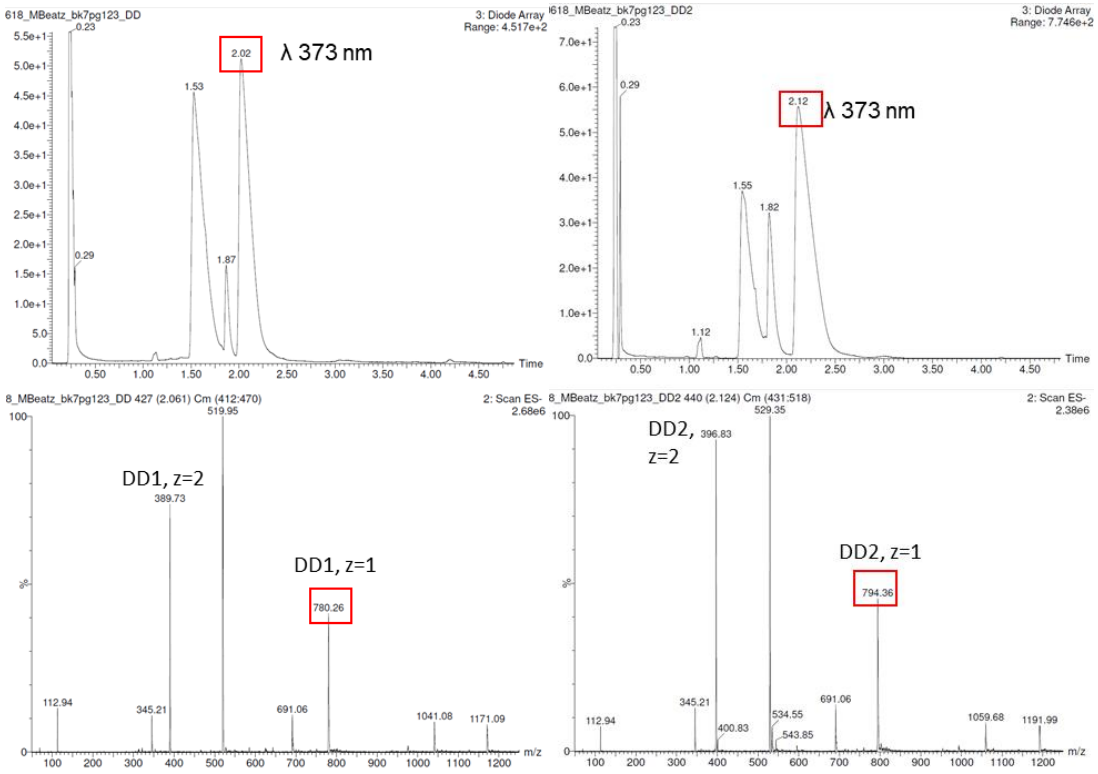

Figure 5. 9 UPLC-MS traces confirm the partial synthesis of **DD1** (left) and **DD2** (right).

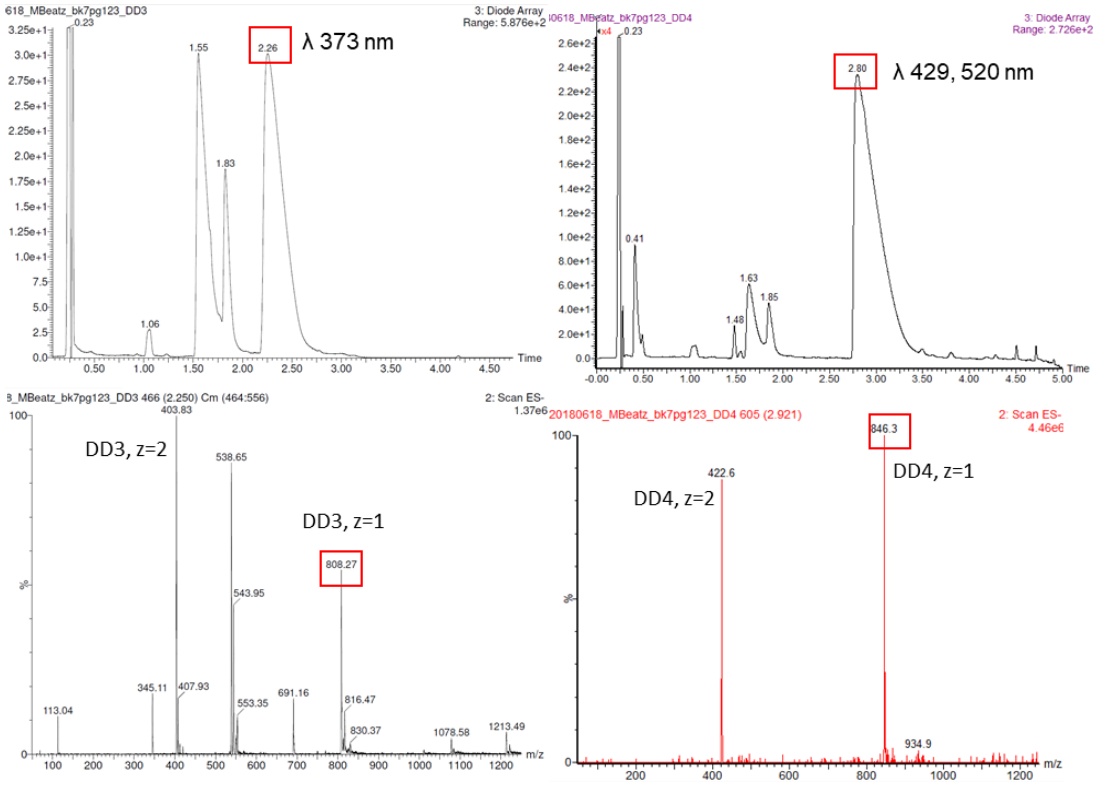

Figure 5. 10 UPLC-MS traces confirm the partial synthesis of **DD3** (left) and **DD4** (right).

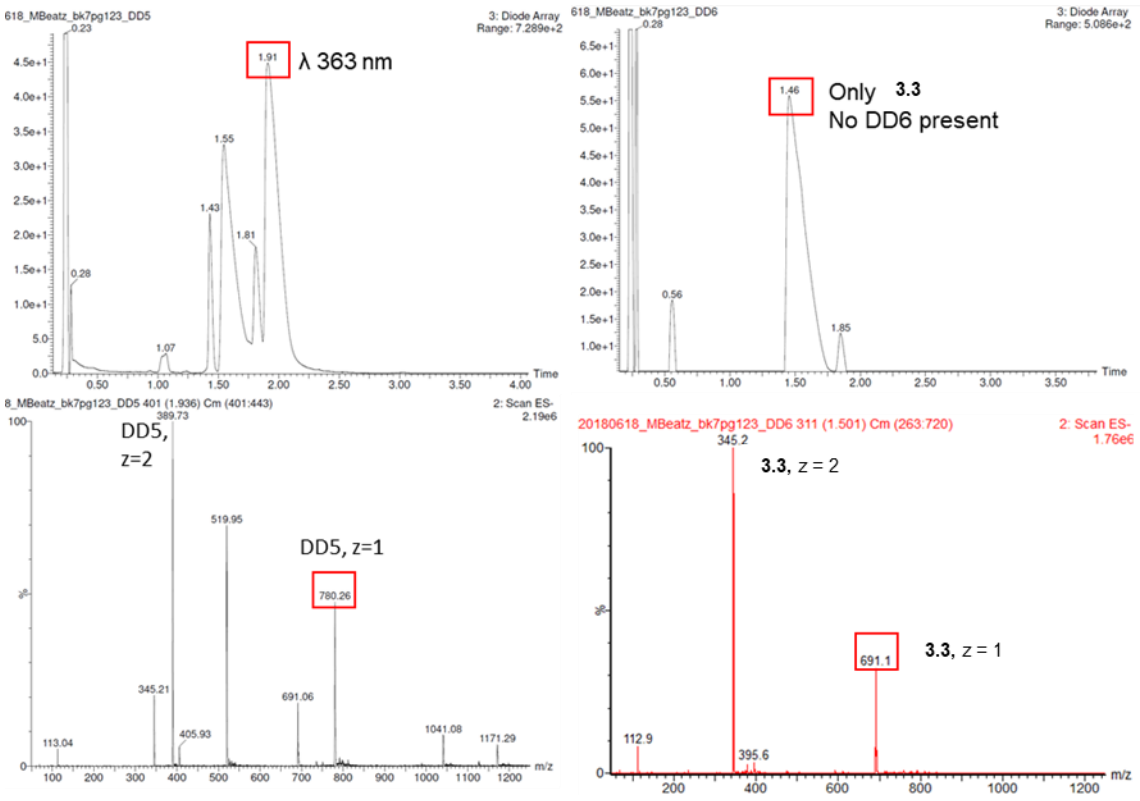

Figure 5. 11 UPLC-MS traces confirm the partial synthesis of **DD5** (left) and a failed **DD6** (right) reaction.

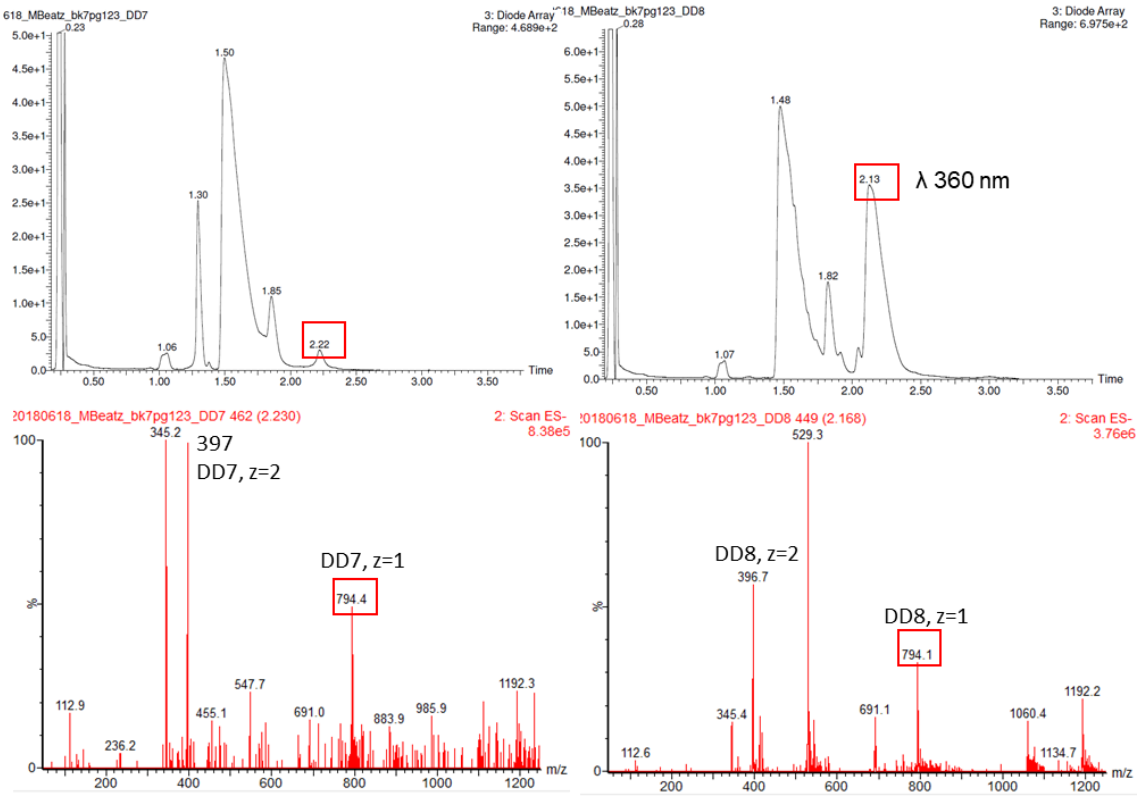

Figure 5. 12 UPLC-MS traces show trace signs of **DD7** (left) and partial formation of **DD8** (right).

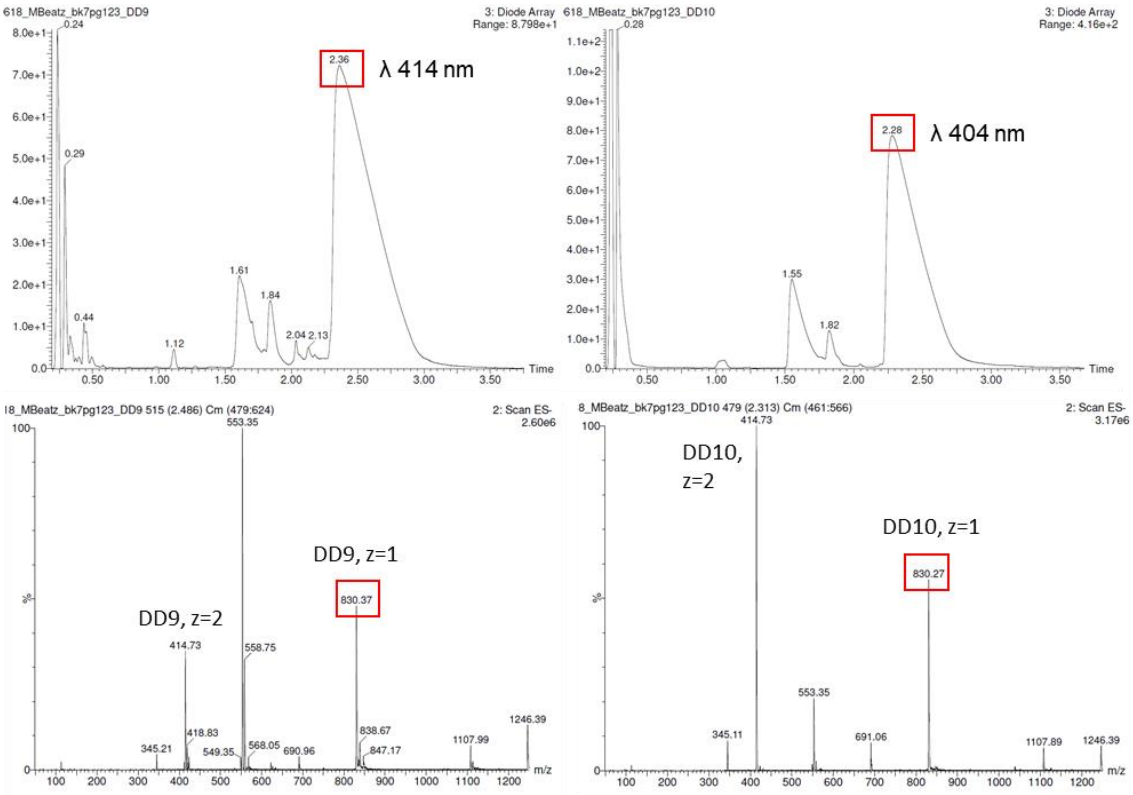

Figure 5. 13 UPLC-MS traces confirm the partial synthesis of **DD9** (left) and **DD10** (right).

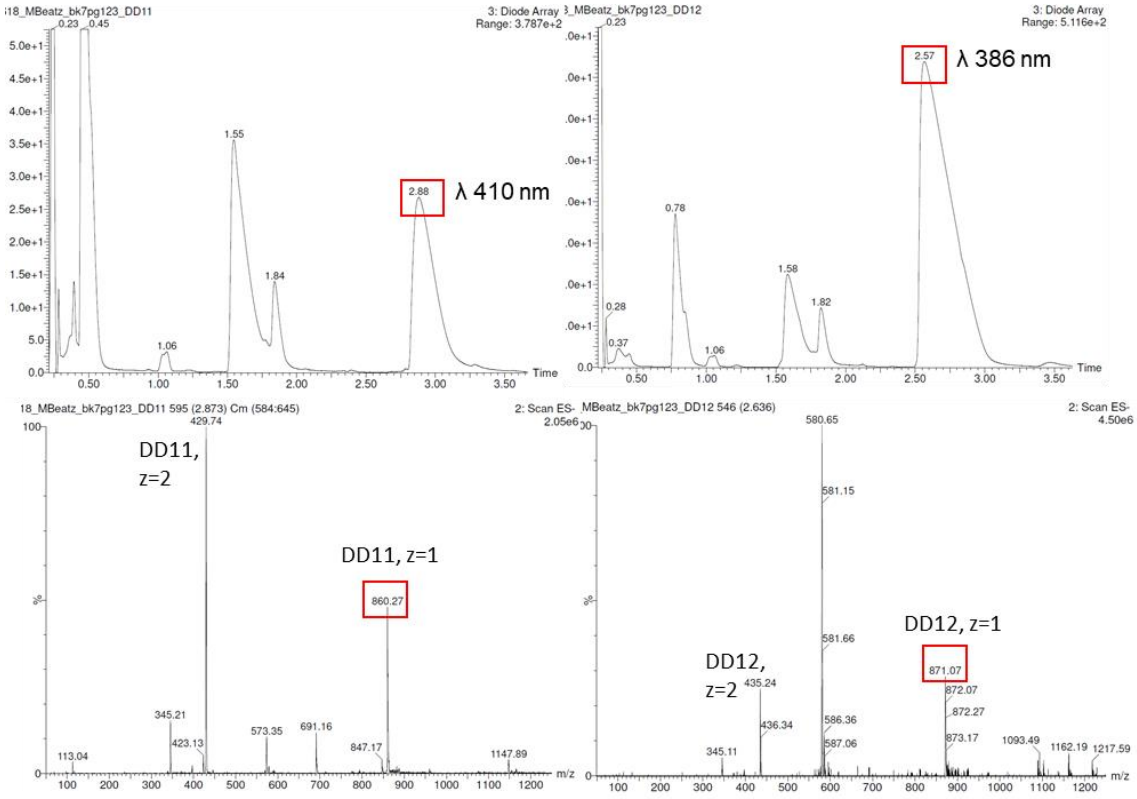

Figure 5. 14 UPLC-MS traces confirm the partial synthesis of **DD11** (left) and **DD12** (right).

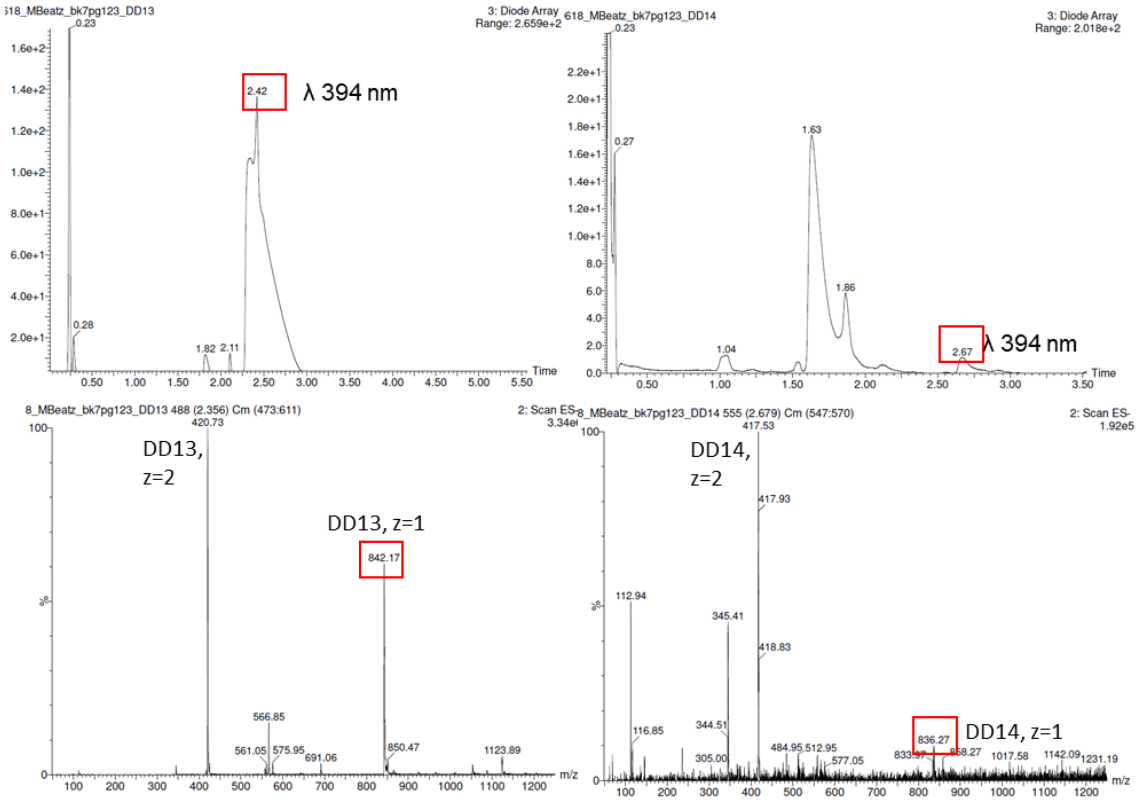

Figure 5. 15 UPLC-MS traces confirm the nearly complete synthesis of **DD13** (left) and trace formation of **DD14** (right).

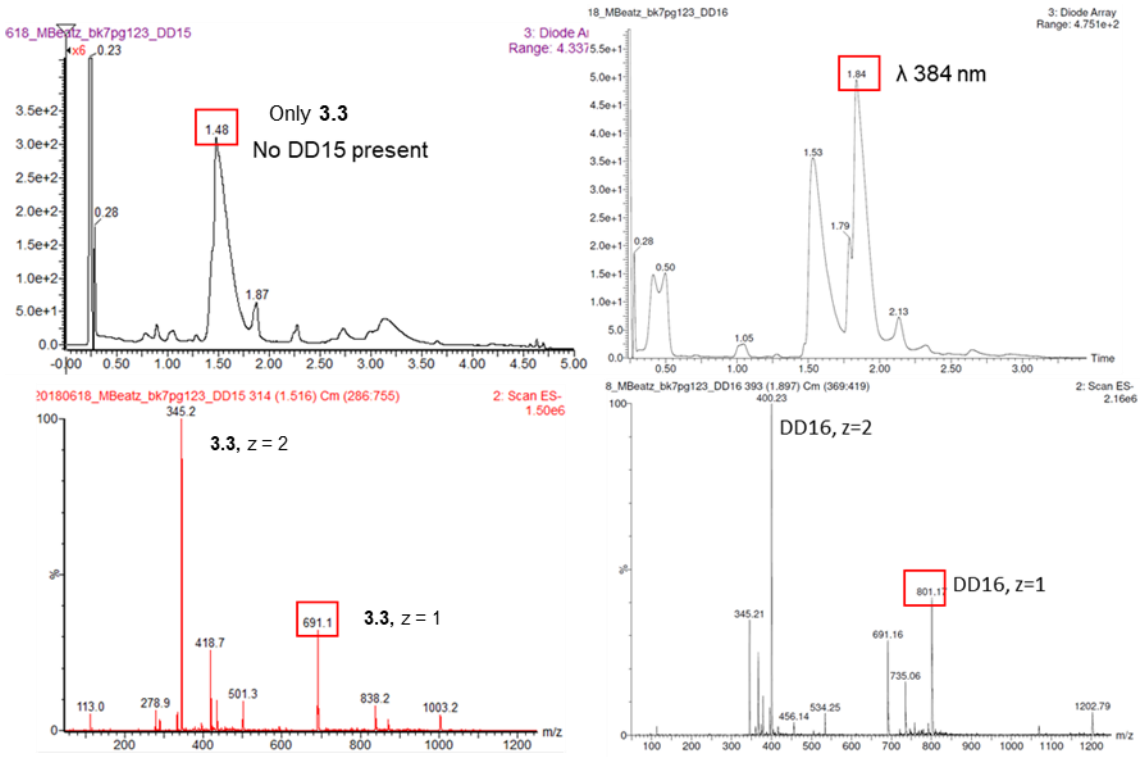

Figure 5. 16 UPLC-MS traces show no conversion of **DD15** (left) and partial conversion of **DD16** (right).

5.5.6 ^{1}H NMR titrations with nicotine

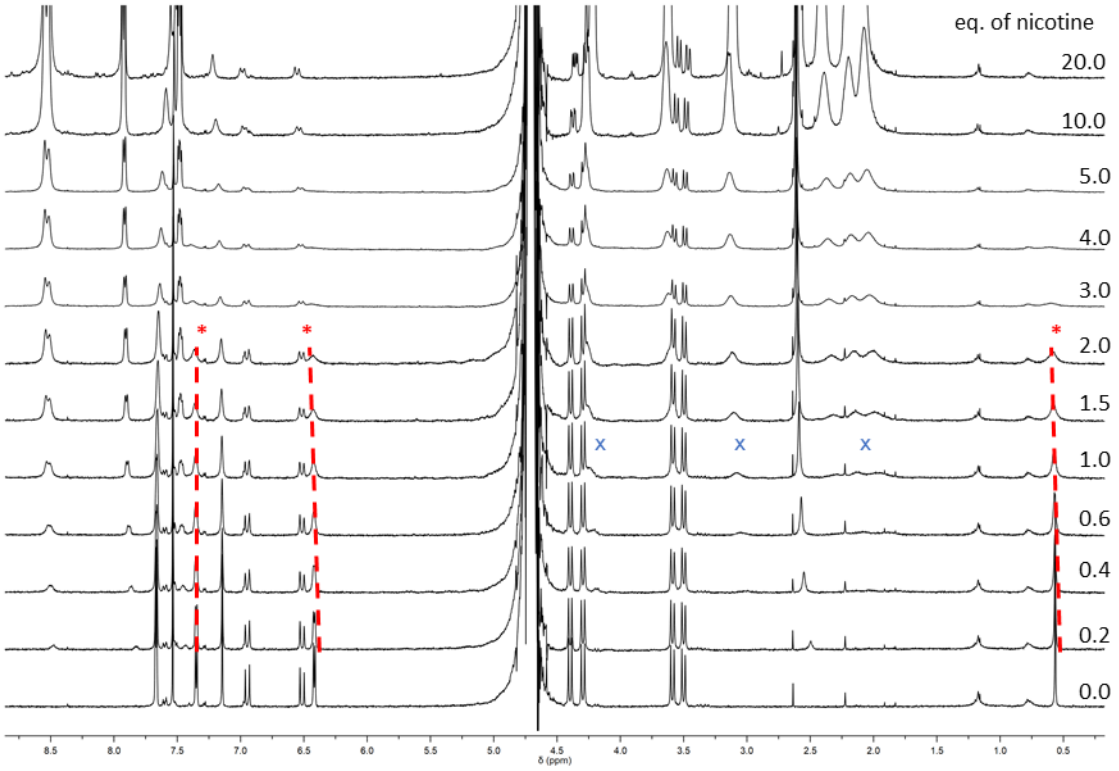

Figure 5. 17 Nicotine titration (10 mM) into **DD1** (500 μM) shows broadening of resonances that support host-guest binding. The resonances of *N*-CH_3, *ortho* and *meta* pyridinium resonances on **DD1**, highlighted by red stars, begin to broaden upon the addition of nicotine. While pyrrolidine protons of nicotine, highlighted with blue cross, barely become visible at 1.0 eq and remain broad throughout the titration. Although resonances of a distinct **DD1**$_{monomer}$-nicotine complex are not present the broadening is evidence of two equilibria (dimer dissociation and nicotine complexation) occurring together in an intermediate timescale relative to the NMR experiment.

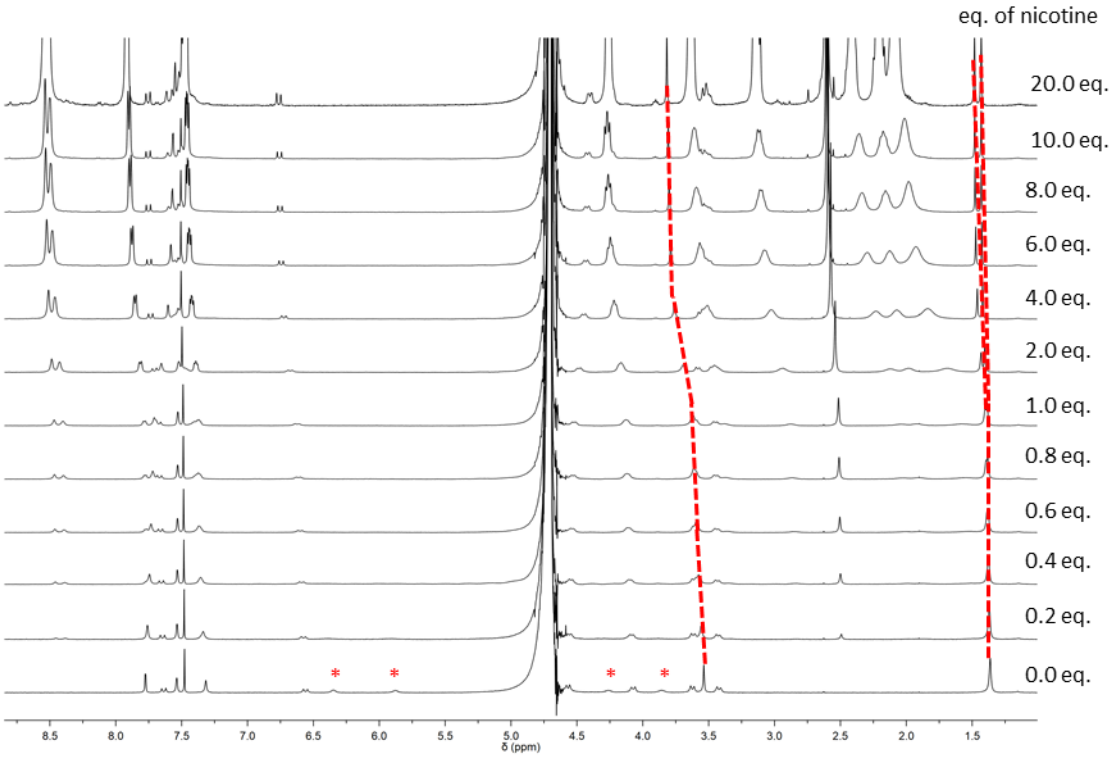

Figure 5. 18 Nicotine titration (10 mM) into **DD4** (500 μM) shows shifts and broadening of resonances that support host-guest binding. The encapsulated aromatic indolinium protons on **DD4**, highlighted by red stars, broaden immediately upon the addition of nicotine. The methyl groups: *N*-CH_3 and the 3-dimethyl protons, can be followed with red dashed lines and are in fast exchange relative to the NMR timescale. The two equivalent dimethyl groups, found as a 6H singlet at 0.0 eq, split into two chemically inequivalent singlets upon the addition of nicotine.

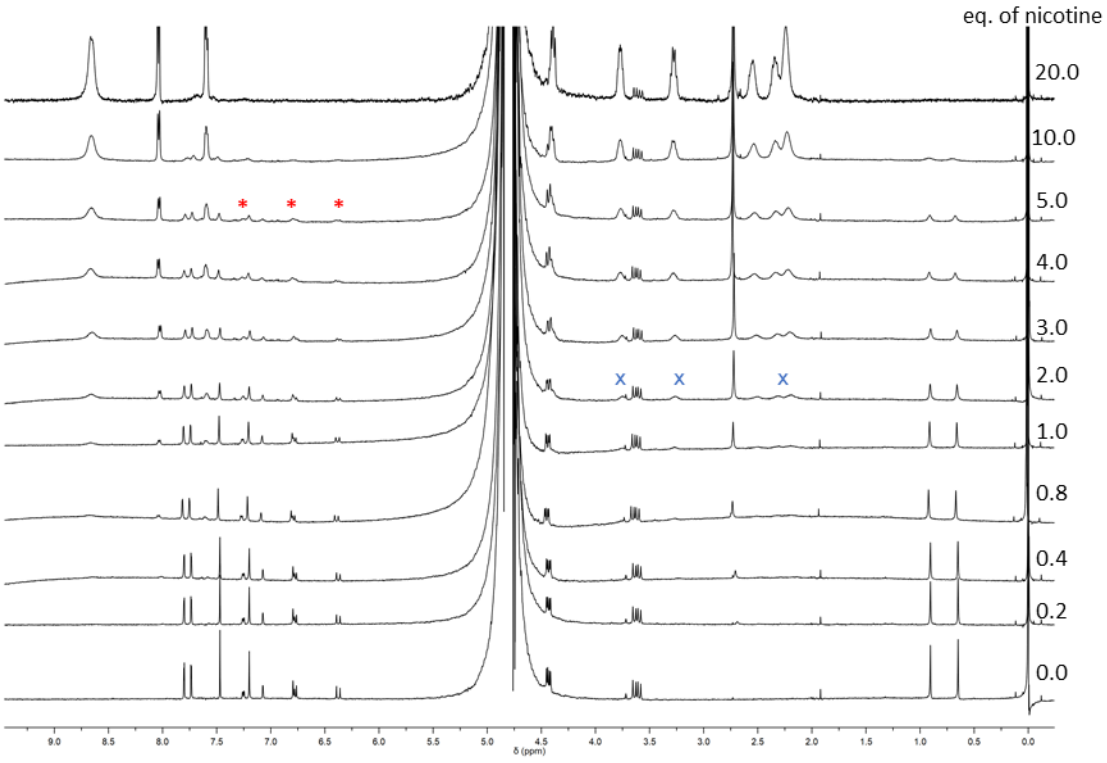

Figure 5. 19 Nicotine titration (4 mM) into **DD8** (200 μM) shows broadening of resonances that supports host-guest binding. **DD8** resonances did not shift but only broadened completely into the baseline, indicated with red stars. Nicotine resonances began to appear at 2.0 eq. and remained broad throughout the titration.

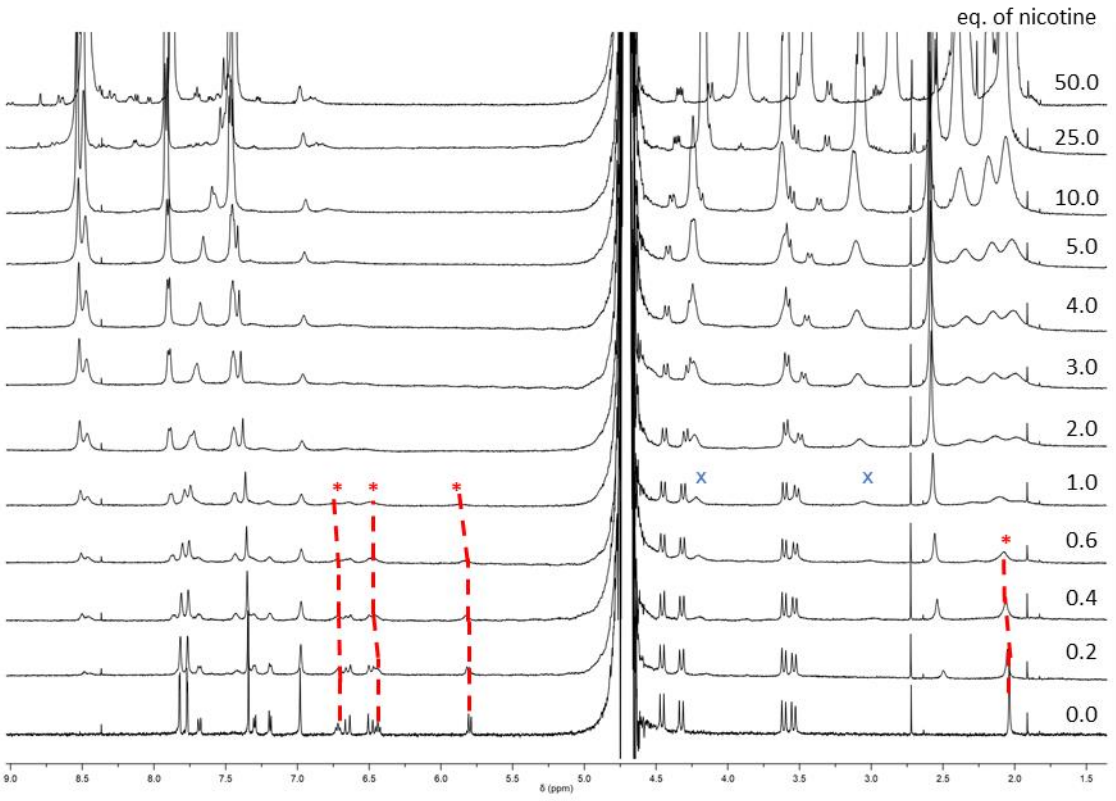

Figure 5. 20 Nicotine titration (25 mM) into **DD9** (500 μM) shows shifts and broadening of resonances that support host-guest binding. **DD9** quinolinium and *N*-CH_3 resonances broadened and shifted downfield slightly (indicated with red stars and dashed lines) and eventually flattened into the baseline after 1.0 eq of nicotine was added. Nicotine pyrrolidine resonances appeared at 1.0 eq (marked with a blue cross) and remained broad throughout the titration.

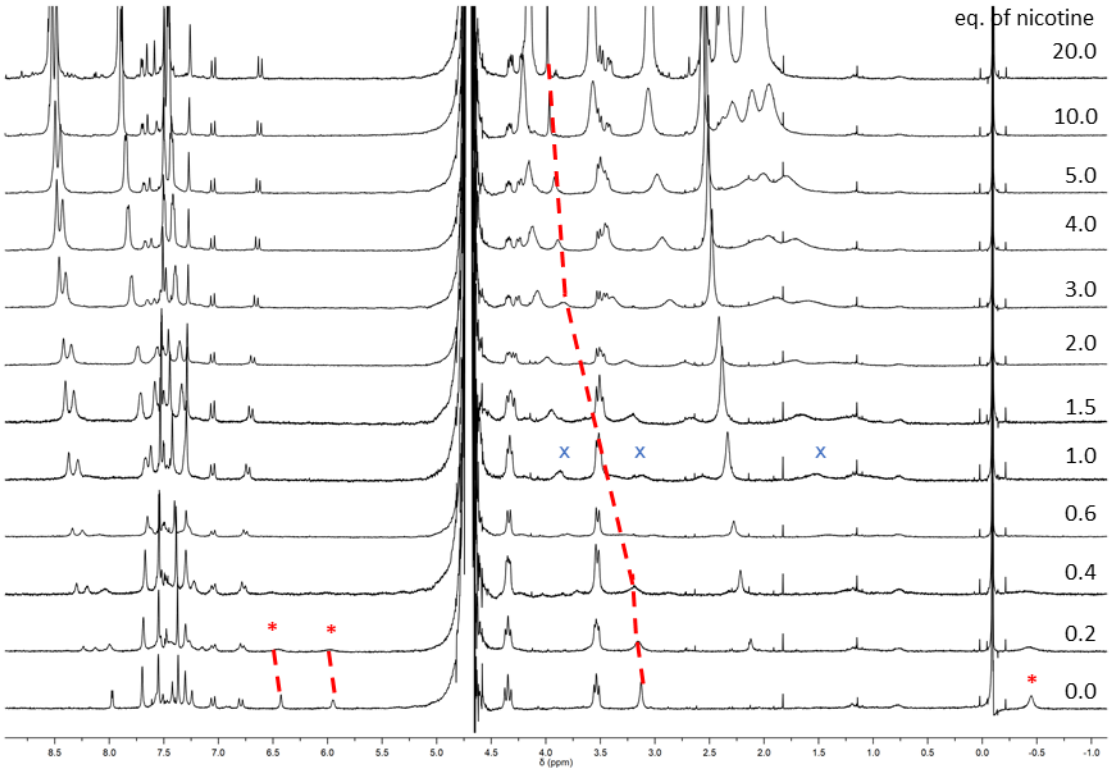

Figure 5. 21 Nicotine titration (10 mM) into **DD12** (500 μM) shows shifts and broadening of resonances that support host-guest binding. The encapsulated aromatic pyridinium protons and 4'-CH_3 on **DD12**, highlighted by red stars, broaden immediately upon the addition of nicotine. However, the less shielded *N*-CH_3, can be followed with red dashed lines and is in fast exchange relative to the NMR timescale, shifting by 0.86 ppm. The nicotine pyrrolidine resonances appear as broad signals near 1.0 eq. and remain broad throughout the titration.

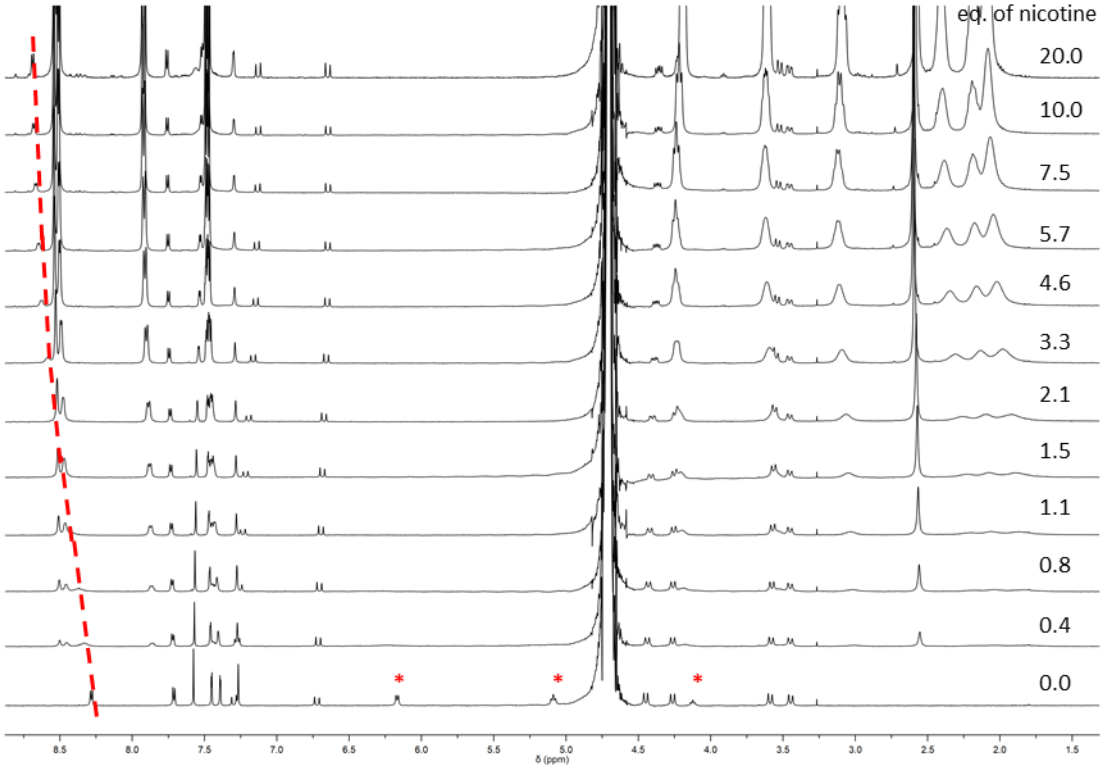

Figure 5. 22 Nicotine titration (10 mM) into **DD13** (500 μM) shows shifts and broadening of resonances that support host-guest binding. The encapsulated *N*-phenyl protons on **DD13**, highlighted by red stars, broaden immediately upon the addition of nicotine. However, the less shielded *ortho*-pyridinium resonances, can be followed with red dashed lines in fast exchange relative to the NMR timescale, shifting by 0.42 ppm.

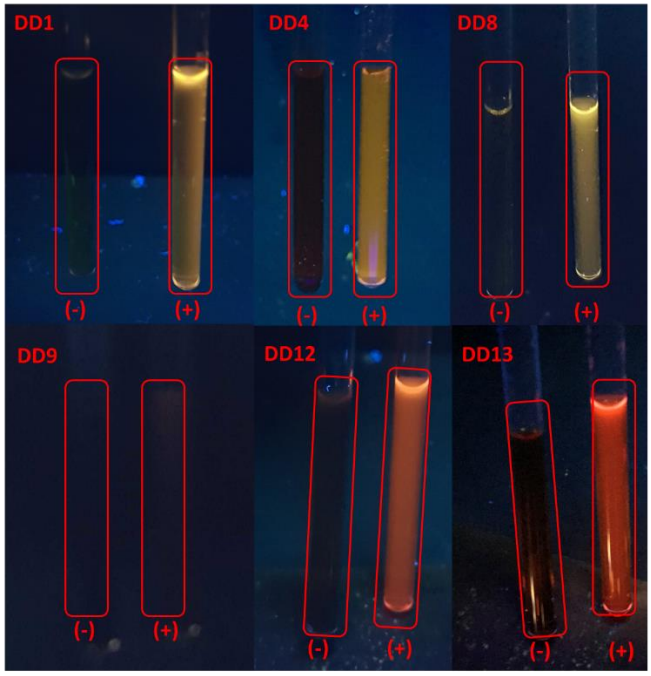

Figure 5. 23 DimerDyes (500 μM) without nicotine (-) are not fluorescent. With addition of 10 mM nicotine (+), DimerDyes 1, 4, 8, 12 and 13 become fluorescent while **DD9** remains dark, as predicted by the screening of crude DD reaction mixtures. Each tube is irradiated with a hand-held UV lamp ($\lambda_{ex.}$ 364 nm ± 20 nm). Solutions are prepared in NaH_2PO_4/Na_2HPO_4 buffered D_2O, (50 mM, pD 7.4).

5.5.7 1D DOSY calculations (3.3, DD4, DD4 + 20 eq. nicotine)

Table 5. 4 Parameters used for diffusion analysis of **DD4** in buffered water.

Parameters used for diffusion analysis:	
used γ:	26752 rad/(s*Gauss)
used δ:	0.0036000 s
used Δ:	0.099900 s
used gradient strength:	variable
Random error estimation of data:	RMS per spectrum (or trace/plane)
Systematic error estimation of data:	worst case per peak scenario
Fit parameter Error estimation method:	from fit using arbitrary uncertainties
Confidence level:	95%
Used peaks:	automatically picked peaks
Used integrals:	area integral
Used Gradient strength:	all values (including replicates) used

Table 5. 5 Diffusion coefficients calculated from indicated resonances in **DD4** from 1D DOSY

F2 [ppm]	D [m^2/s]	error
7.774	1.96×10^{-10}	1.069×10^{-12}
7.313	1.98×10^{-10}	9.863×10^{-13}
3.534	2.00×10^{-10}	1.443×10^{-12}
1.360	1.89×10^{-10}	1.073×10^{-12}
7.629	1.95×10^{-10}	3.024×10^{-12}
6.558	1.98×10^{-10}	2.726×10^{-12}

Table 5. 6 Parameters used for diffusion analysis of **DD4**+20 eq. nicotine in buffered water.

Parameters used for diffusion analysis:	
used gamma:	26752 rad/(s*Gauss)
used little delta:	0.0024000 s
used big delta:	0.099900 s
used gradient strength:	variable
Random error estimation of data:	RMS per spectrum (or trace/plane)
Systematic error estimation of data:	worst case per peak scenario
Fit parameter Error estimation method:	from fit using arbitrary uncertainties
Confidence level:	95%
Used peaks:	automatically picked peaks
Used integrals:	area integral
Used Gradient strength:	all values (including replicates) used

Table 5. 7 Diffusion coefficients calculated from indicated resonances in **DD4**-nicotine complex from 1D DOSY.

F2 [ppm]	D [m^2/s]	error
7.767	3.06×10^{-10}	3.306×10^{-11}
3.821	2.32×10^{-10}	6.292×10^{-12}

Table 5. 8 Parameters used for diffusion analysis of **3.3** in buffered water.

Parameters used for diffusion analysis:	
used γ:	26752 rad/(s*Gauss)
used δ:	0.0046000 s
used Δ:	0.049950 s
used gradient strength:	variable
Random error estimation of data:	RMS per spectrum (or trace/plane)
Systematic error estimation of data:	worst case per peak scenario
Fit parameter Error estimation method:	from fit using arbitrary uncertainties
Confidence level:	95%

Used peaks:	automatically picked peaks
Used integrals:	area integral
Used Gradient strength:	all values (including replicates) used

Table 5. 9 Diffusion coefficients calculated from indicated resonances in **3.3** from 1D DOSY.

F2 [ppm]	D [m^2/s]	error
9.505	3.31×10^{-10}	1.272×10^{-12}
7.723	3.28×10^{-10}	6.311×10^{-13}
7.620	3.28×10^{-10}	7.151×10^{-13}
7.588	3.29×10^{-10}	7.270×10^{-13}
7.506	3.29×10^{-10}	5.165×10^{-13}

5.5.8 Fluorescence titrations of DDs 1, 4, 8, 12, and 13 with nicotine, MDMA and cocaine

All intensity values are plotted as the mean of duplicate experiments. Error bars corresponding to the standard deviation are present on all data points in all dose-response graphs (but in many cases are similar in size to the data point markers themselves). Spectra represent mean of duplicate experiments and are processed with second order smoothing function.

5.5.8a Nicotine

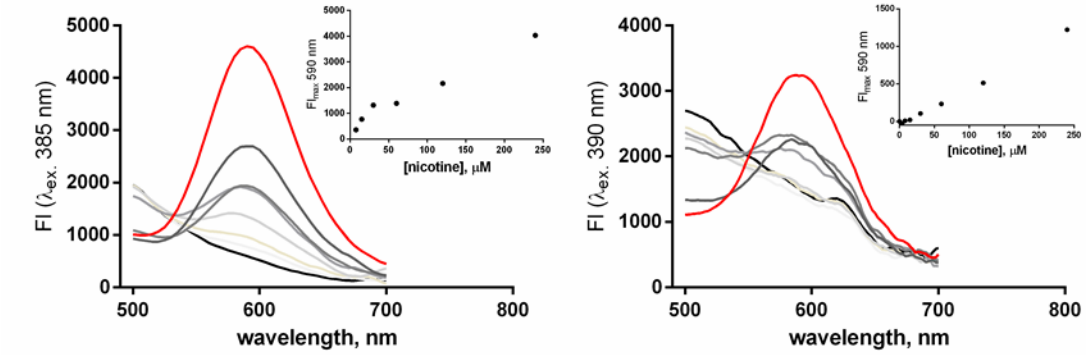

Figure 5. 24 **DD1** turns-on fluorescence upon the addition of nicotine in buffered water and diluted saliva. Nicotine titration into **DD1** (12 μM) monitored by fluorescence spectroscopy in (left) NaH_2PO_4/Na_2HPO_4 buffered water (10 mM, pH 7.4, $\lambda_{ex.}$ = 385 nm) and in (right) diluted saliva (1:1, saliva:water, $\lambda_{ex.}$ = 390 nm) show **DD1** is capable of detecting nicotine in both media. Red line indicates maximum nicotine concentration =

240 μM and black line indicates no nicotine added. Insets show binding isotherms monitored at fluorescence maximum, $\lambda_{max.}$ = 590 nm in both saliva and water.

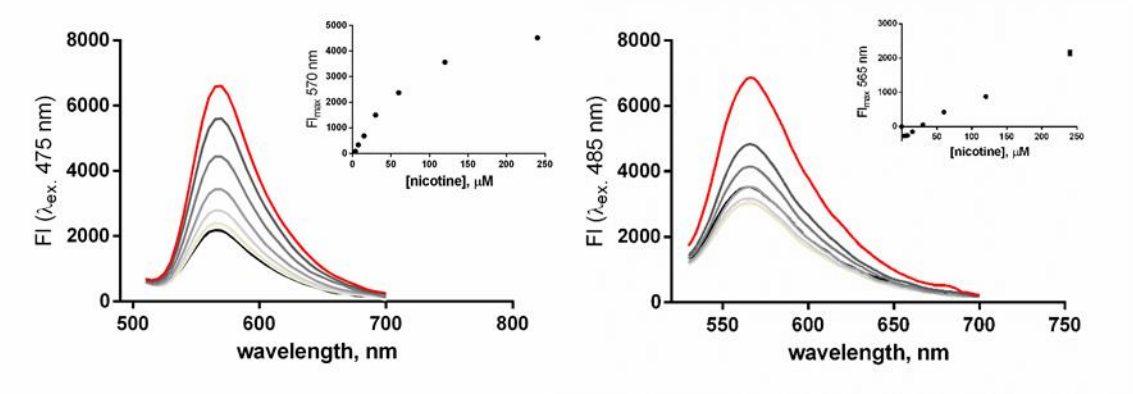

Figure 5. 25 **DD4** turns-on fluorescence upon the addition of nicotine in buffered water and diluted saliva. Nicotine titration into **DD4** (12 μM) monitored by fluorescence spectroscopy in (left) NaH_2PO_4/Na_2HPO_4 buffered water (10 mM, pH 7.4, $\lambda_{ex.}$ = 475 nm) and in (right) diluted saliva (1:1, saliva:water, $\lambda_{ex.}$ = 485 nm), show **DD4** is capable of detecting nicotine in both media. Red line indicates maximum nicotine concentration = 240 μM and black line indicates no nicotine added. Insets show binding isotherms monitored at fluorescence maximum, $\lambda_{max.}$ = 570 nm in buffered water and $\lambda_{max.}$ = 585 nm in diluted saliva.

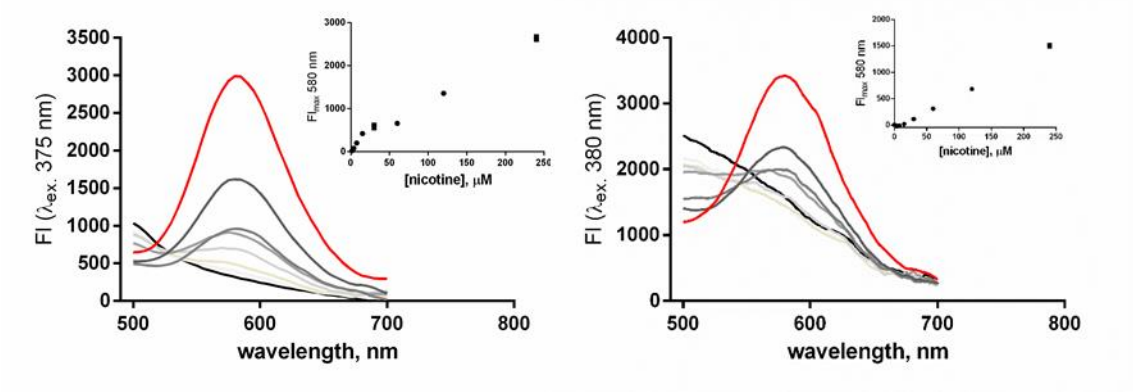

Figure 5. 26 **DD8** turns-on fluorescence upon the addition of nicotine in buffered water and diluted saliva. Nicotine titration into **DD8** (12 μM) monitored by fluorescence spectroscopy in (left) NaH_2PO_4/Na_2HPO_4 buffered water (10 mM, pH 7.4, $\lambda_{ex.}$ = 375 nm) and in (right) diluted saliva (1:1, saliva:water, $\lambda_{ex.}$ = 380 nm) show **DD8** is capable of detecting nicotine in both media. Red line indicates maximum nicotine concentration = 240 μM and black line indicates no nicotine added. Insets show binding isotherms monitored at fluorescence maximum, $\lambda_{max.}$ = 580 nm in both buffered water and diluted saliva.

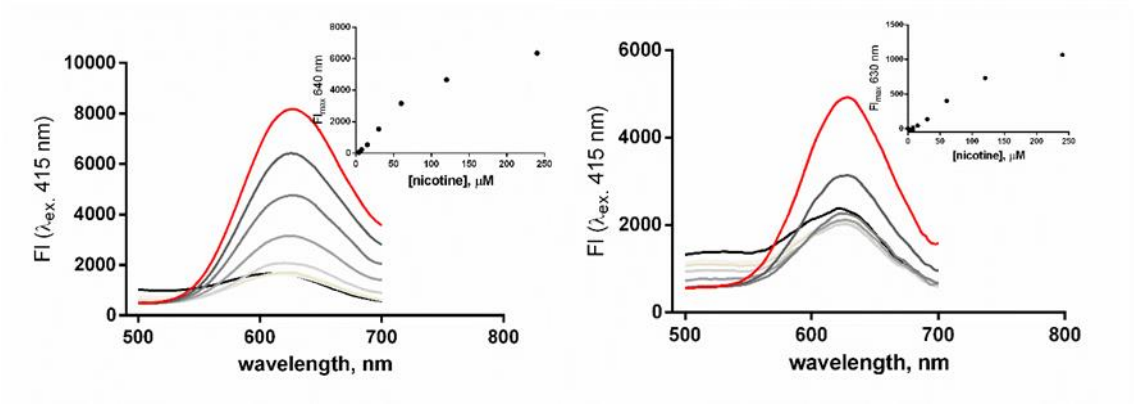

Figure 5. 27 **DD12** turns-on fluorescence upon the addition of nicotine in buffered water and diluted saliva. Nicotine titration into **DD12** (12 μM) monitored by fluorescence spectroscopy in (left) NaH_2PO_4/Na_2HPO_4 buffered water (10 mM, pH 7.4, $\lambda_{ex.}$ = 415 nm) and in (right) diluted saliva (1:1, saliva:water, $\lambda_{ex.}$ = 415 nm) show **DD12** is capable of detecting nicotine in both media. Red line indicates maximum nicotine concentration = 240 μM and black line indicates no nicotine added. Insets show binding isotherms monitored at fluorescence maximum, $\lambda_{max.}$ = 640 nm in both buffered water and diluted saliva.

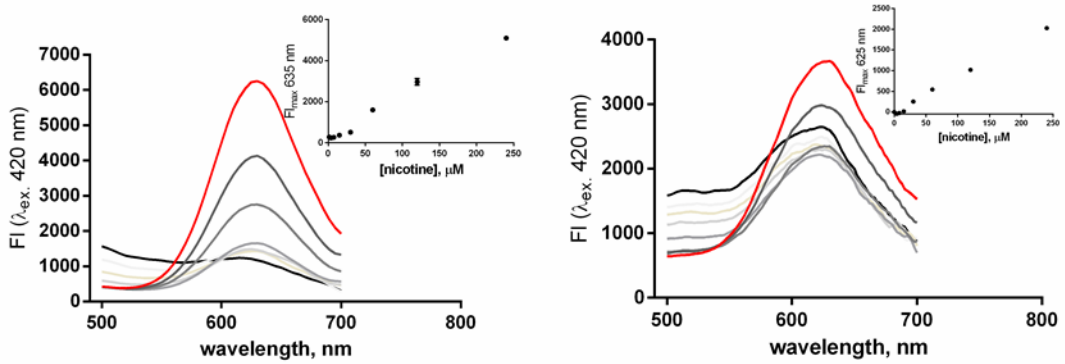

Figure 5. 28 **DD13** turns-on fluorescence upon the addition of nicotine in buffered water and diluted saliva. Nicotine titration into **DD13** (12 μM) monitored by fluorescence spectroscopy in (left) NaH_2PO_4/Na_2HPO_4 buffered water (10 mM, pH 7.4, $\lambda_{ex.}$ = 420 nm) and in (right) diluted saliva (1:1, saliva:water, $\lambda_{ex.}$ = 420 nm) show **DD12** is capable of detecting nicotine in both media. Red line indicates maximum nicotine concentration = 240 μM and black line indicates no nicotine added. Insets show binding isotherms monitored at fluorescence maximum, $\lambda_{max.}$ = 635 nm in buffered water and $\lambda_{max.}$ = 625 nm in diluted saliva.

5.5.8b MDMA

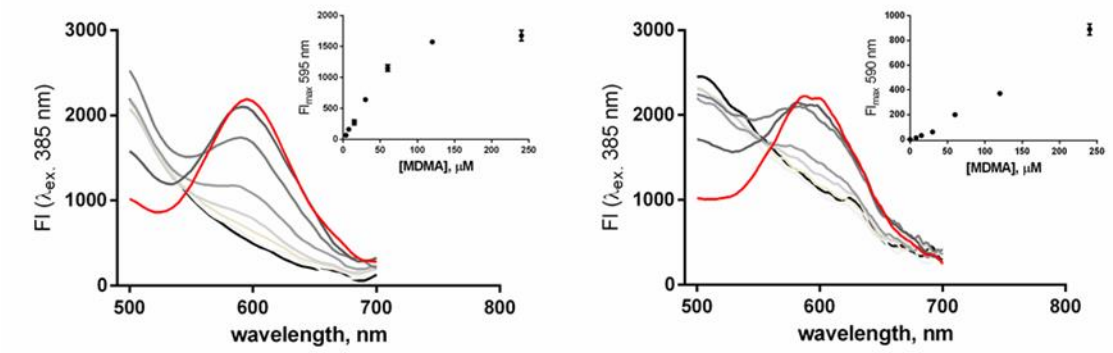

Figure 5. 29 **DD1** turns-on fluorescence upon the addition of MDMA in buffered water and diluted saliva. MDMA titration into **DD1** (12 μM) monitored by fluorescence spectroscopy in (left) NaH_2PO_4/Na_2HPO_4 buffered water (10 mM, pH 7.4, $\lambda_{ex.}$ = 385 nm) and in (right) diluted saliva (1:1, saliva:water, $\lambda_{ex.}$ = 385 nm) show **DD1** is capable of detecting MDMA in both media. Red line indicates maximum MDMA concentration = 240 μM and black line indicates no MDMA added. Insets show binding isotherms monitored at fluorescence maximum, $\lambda_{max.}$ = 595 nm in buffered water and $\lambda_{max.}$ = 590 nm in diluted saliva.

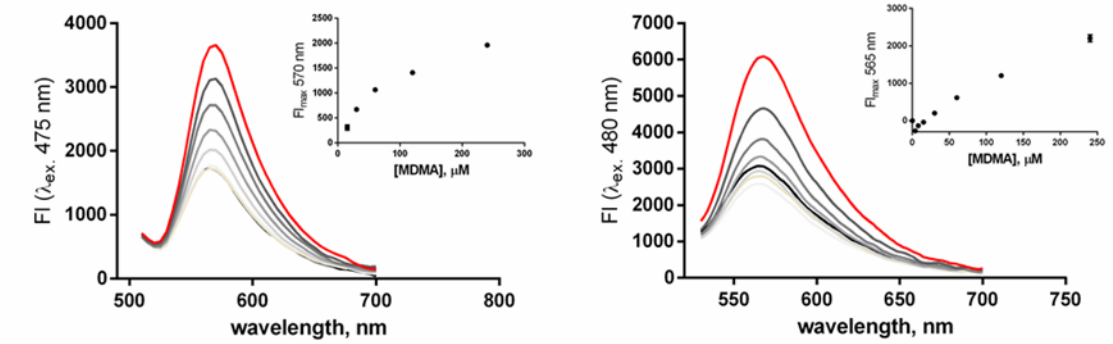

Figure 5. 30 **DD4** turns-on fluorescence upon the addition of MDMA in buffered water and diluted saliva. MDMA titration into **DD4** (12 μM) monitored by fluorescence spectroscopy in (left) NaH_2PO_4/Na_2HPO_4 buffered water (10 mM, pH 7.4, $\lambda_{ex.}$ = 475 nm) and in (right) diluted saliva (1:1, saliva:water, $\lambda_{ex.}$ = 480 nm) show **DD4** is capable of detecting MDMA in both media. Red line indicates maximum MDMA concentration = 240 μM and black line indicates no MDMA added. Insets show binding isotherms monitored at fluorescence maximum, $\lambda_{max.}$ = 595 nm in buffered water and $\lambda_{max.}$ = 590 nm in diluted saliva.

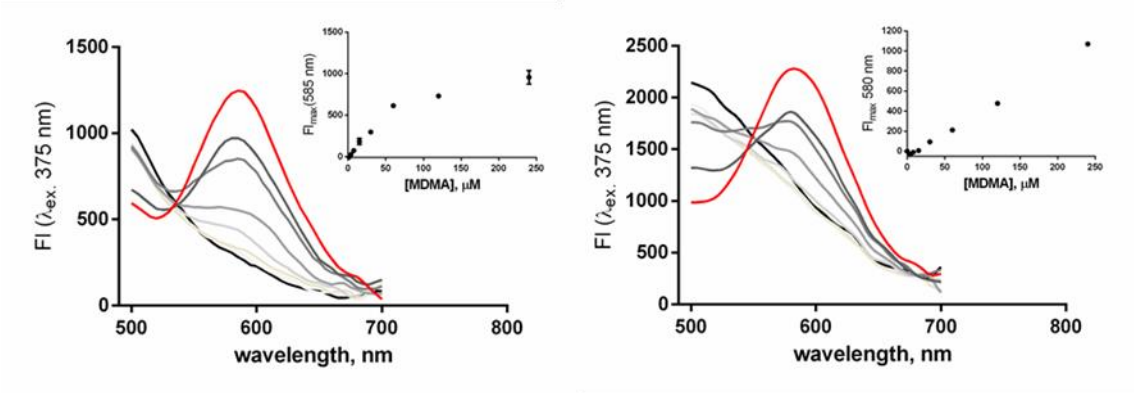

Figure 5. 31 **DD8** turns-on fluorescence upon the addition of MDMA in buffered water and diluted saliva. MDMA titration into **DD8** (12 μM) monitored by fluorescence spectroscopy in (left) NaH_2PO_4/Na_2HPO_4 buffered water (10 mM, pH 7.4, $\lambda_{ex.}$ = 375 nm) and in (right) diluted saliva (1:1, saliva:water, $\lambda_{ex.}$ = 375 nm) show **DD8** is capable of detecting MDMA in both media. Red line indicates maximum MDMA concentration = 240 μM and black line indicates no MDMA added. Insets show binding isotherms monitored at fluorescence maximum, $\lambda_{max.}$ = 585 nm in buffered water and $\lambda_{max.}$ = 580 nm in diluted saliva.

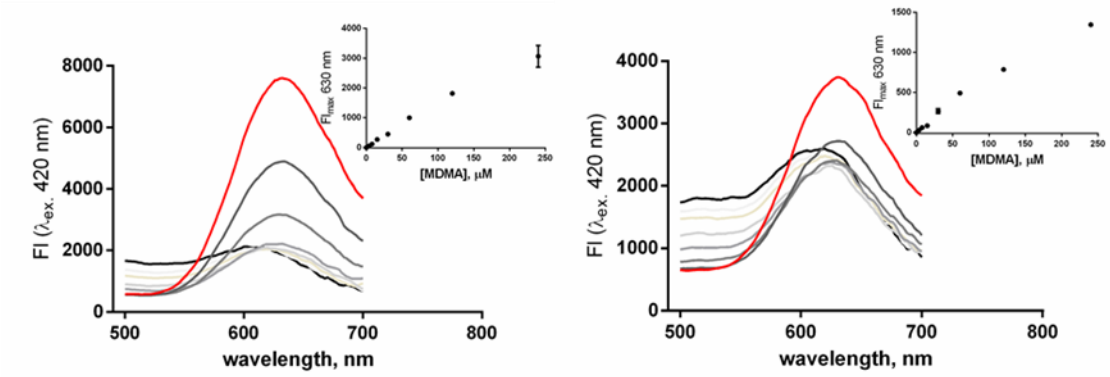

Figure 5. 32 **DD12** turns-on fluorescence upon the addition of MDMA in buffered water and diluted saliva. MDMA titration into **DD12** (12 μM) monitored by fluorescence spectroscopy in (left) NaH_2PO_4/Na_2HPO_4 buffered water (10 mM, pH 7.4, $\lambda_{ex.}$ = 420 nm) and in (right) diluted saliva (1:1, saliva:water, $\lambda_{ex.}$ = 420 nm) show **DD12** is capable of detecting MDMA in both media. Red line indicates maximum MDMA concentration = 240 μM and black line indicates no MDMA added. Insets show binding isotherms monitored at fluorescence maximum, $\lambda_{max.}$ = 630 nm in both buffered water and in diluted saliva.

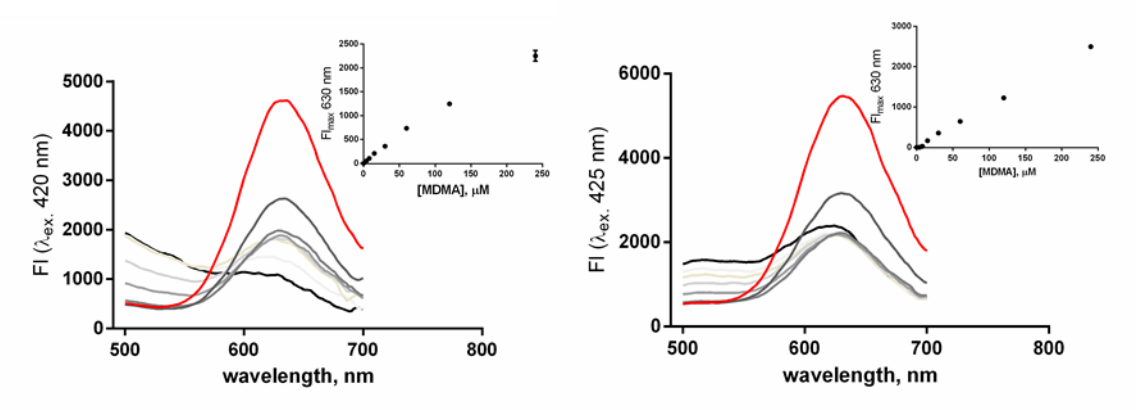

Figure 5. 33 **DD13** turns-on fluorescence upon the addition of MDMA in buffered water and diluted saliva. MDMA titration into **DD13** (12 μM) monitored by fluorescence spectroscopy in (left) NaH_2PO_4/Na_2HPO_4 buffered water (10 mM, pH 7.4, $\lambda_{ex.}$ = 420 nm) and in (right) diluted saliva (1:1, saliva:water, $\lambda_{ex.}$ = 420 nm) show **DD13** is capable of detecting MDMA in both media. Red line indicates maximum MDMA concentration = 240 μM and black line indicates no MDMA added. Insets show binding isotherms monitored at fluorescence maximum, $\lambda_{max.}$ = 630 nm in both buffered water and in diluted saliva.

5.5.8c Cocaine

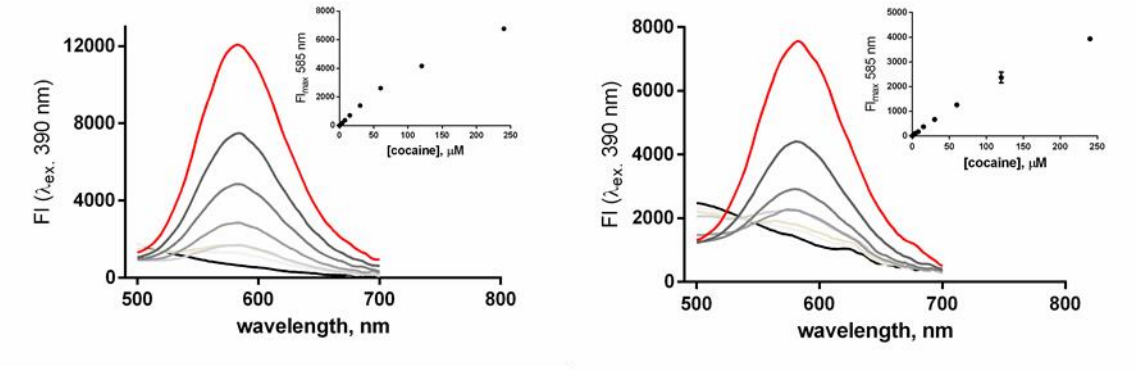

Figure 5. 34 **DD1** turns-on fluorescence upon the addition of cocaine in buffered water and diluted saliva. Cocaine titration into **DD1** (12 μM) monitored by fluorescence spectroscopy in (left) NaH_2PO_4/Na_2HPO_4 buffered water (10 mM, pH 7.4, $\lambda_{ex.}$ = 390 nm) and in (right) diluted saliva (1:1, saliva:water, $\lambda_{ex.}$ = 390 nm) show **DD1** is capable of detecting cocaine in both media. Red line indicates maximum cocaine concentration = 240 μM and black line indicates no cocaine added. Insets show binding isotherms monitored at fluorescence maximum, $\lambda_{max.}$ = 585 nm in both buffered water and in diluted saliva.

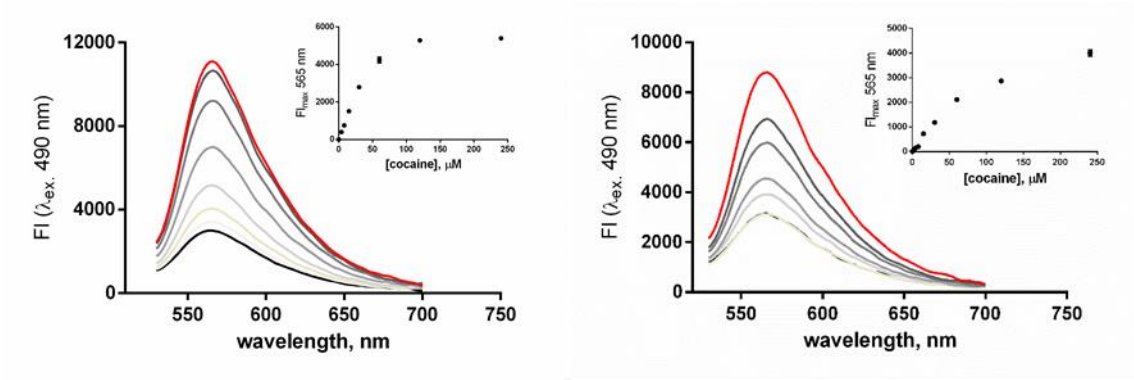

Figure 5. 35 **DD4** turns-on fluorescence upon the addition of cocaine in buffered water and diluted saliva. Cocaine titration into **DD4** (12 μM) monitored by fluorescence spectroscopy in (left) NaH_2PO_4/Na_2HPO_4 buffered water (10 mM, pH 7.4, $\lambda_{ex.}$ = 490 nm) and in (right) diluted saliva (1:1, saliva:water, $\lambda_{ex.}$ = 490 nm) show **DD4** is capable of detecting cocaine in both media. Red line indicates maximum cocaine concentration = 240 μM and black line indicates no cocaine added. Insets show binding isotherms monitored at fluorescence maximum, $\lambda_{max.}$ = 565 nm in both buffered water and in diluted saliva.

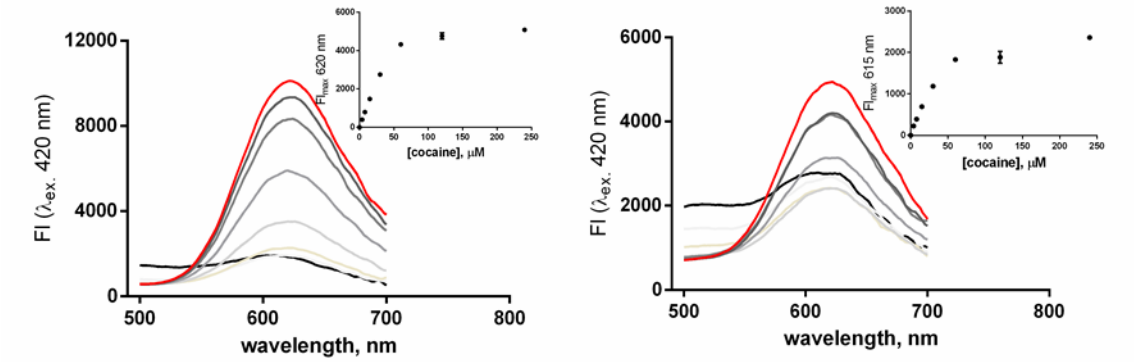

Figure 5. 36 **DD8** turns-on fluorescence upon the addition of cocaine in buffered water and diluted saliva. Cocaine titration into **DD8** (12 μM) monitored by fluorescence spectroscopy in (left) NaH_2PO_4/Na_2HPO_4 buffered water (10 mM, pH 7.4, $\lambda_{ex.}$ = 390 nm) and in (right) diluted saliva (1:1, saliva:water, $\lambda_{ex.}$ = 380 nm) show **DD4** is capable of detecting cocaine in both media. Red line indicates maximum cocaine concentration = 240 μM and black line indicates no cocaine added. Insets show binding isotherms monitored at fluorescence maximum, $\lambda_{max.}$ = 575 nm in both buffered water and in diluted saliva.

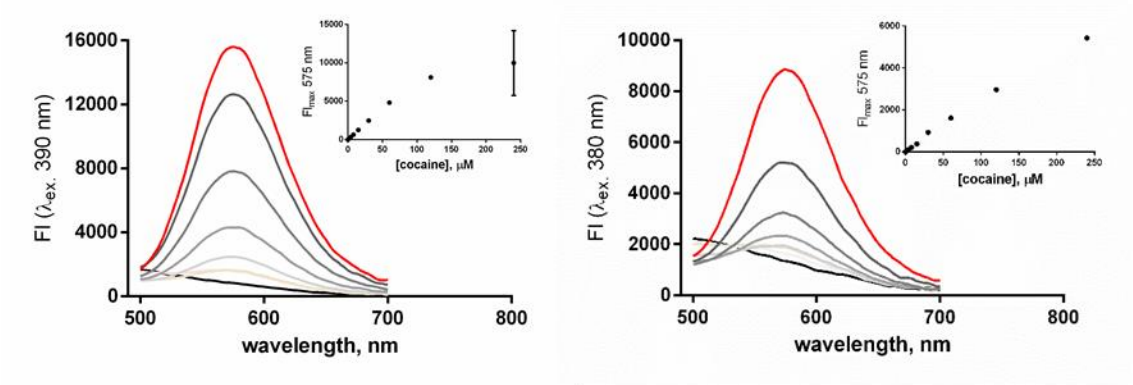

Figure 5. 37 **DD12** turns-on fluorescence upon the addition of cocaine in buffered water and diluted saliva. Cocaine titration into **DD12** (12 μM) monitored by fluorescence spectroscopy in (left) NaH_2PO_4/Na_2HPO_4 buffered water (10 mM, pH 7.4, $\lambda_{ex.}$ = 420 nm) and in (right) diluted saliva (1:1, saliva:water, $\lambda_{ex.}$ = 420 nm) show **DD12** is capable of detecting cocaine in both media. Red line indicates maximum cocaine concentration = 240 μM and black line indicates no cocaine added. Insets show binding isotherms monitored at fluorescence maximum, $\lambda_{max.}$ = 620 nm in buffered water and $\lambda_{max.}$ = 615 nm in diluted saliva.

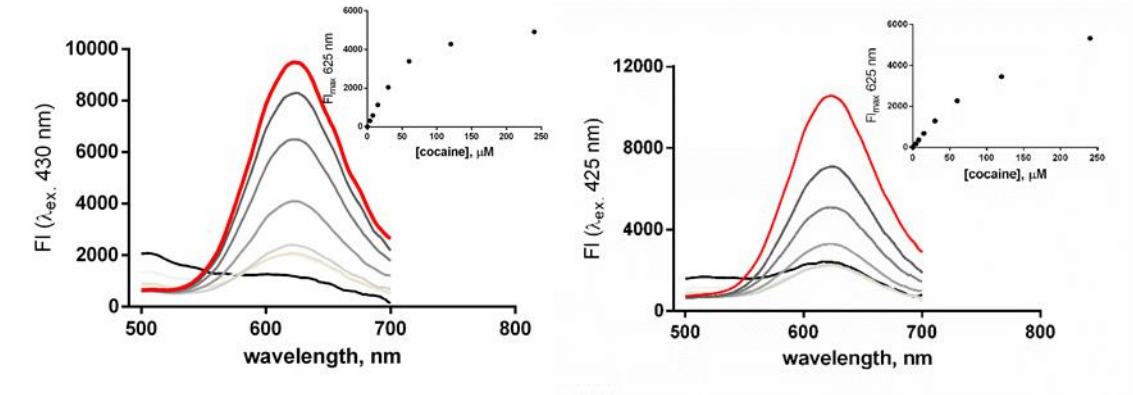

Figure 5. 38 **DD13** turns-on fluorescence upon the addition of cocaine in buffered water and diluted saliva. Cocaine titration into **DD13** (12 μM) monitored by fluorescence spectroscopy in (left) NaH_2PO_4/Na_2HPO_4 buffered water (10 mM, pH 7.4, $\lambda_{ex.}$ = 430 nm) and in (right) diluted saliva (1:1, saliva:water, $\lambda_{ex.}$ = 425 nm) show **DD13** is capable of detecting cocaine in both media. Red line indicates maximum cocaine concentration = 240 μM and black line indicates no cocaine added. Insets show binding isotherms monitored at fluorescence maximum, $\lambda_{max.}$ = 625 nm in both buffered water and in diluted saliva.

5.5.9 Limits of Detection

Limits of detection (LOD) were found through the linear regression of each data set (only linear region of the curve is considered) and calculating:

LOD = σ/slope*3.3

Where, σ and slope are the standard deviation and slope obtained from the regression line

All LOD were measured with purified **DD**s, [**DD**] = 12 μM.

Table 5. 10 Limits of detection determined of each DimerDye for nicotine, MDMA and cocaine in sodium phosphate buffer

	Nicotine			MDMA			Cocaine		
	σ	Slope	LOD (μM)	σ	Slope	LOD (μM)	σ	Slope	LOD (μM)
DD1	45.91	43.42	3.489	16.20	19.65	2.721	12.87	46.51	0.9132
DD4	64.27	44.19	4.800	90.93	18.82	15.94	52.02	92.76	1.851
DD8	21.43	26.94	2.625	15.25	10.07	4.998	32.12	80.26	1.321
DD12	82.56	33.99	8.016	82.56	33.99	8.016	57.65	91.09	2.089
DD13	58.65	97.59	1.983	12.15	12.08	3.319	54.44	67.62	2.657

Table 5. 11 Limits of detection determined of each DimerDye for nicotine, MDMA and cocaine in diluted saliva

	Nicotine			MDMA			Cocaine		
	σ	Slope	LOD (μM)	σ	Slope	LOD (μM)	σ	Slope	LOD (μM)
DD1	17.38	2.08	27.57	30.36	2.428	41.26	28.54	22.23	4.237
DD4	134.8	6.003	74.10	120.8	10.97	36.34	94.71	41.11	7.603
DD8	23.88	4.233	18.62	22.43	3.682	20.104	45.95	30.63	4.951
DD12	26.85	5.149	17.21	26.26	8.699	9.962	47.81	38.76	4.071
DD13	52.71	9.283	18.74	32.75	12.68	8.523	35.11	43.05	2.691

5.5.10 PCA and LDA analysis

Stocks of each DimerDye (13.4 μM) were prepared in NaH_2PO_4/Na_2HPO_4 (10 mM, pH 7.4) and aliquoted (90 μL) into a 96-well plate to account for 5 replicates of each drug and 2 blanks. This was followed by additions of each drug/buffer (10 μL) to make a final [DD] = 12 μM, [drug] = 100 μM or 0 μM (blank) with a final volume of 100 μL. The fluorescence was measured with $\lambda_{ex.}$ and $\lambda_{em.}$ tabulated below. The raw fluorescence was subtracted from the blank before analysis. The PCA (type: covariance) and LDA analysis (cross-validation) were conducted with XLSTAT and Minitab 18.

Table 5. 12 Excitation and fluorescence emission wavelengths used for each DimerDye

	$\lambda_{ex.}$ (nm)	$\lambda_{em.}$ (nm)
DD1	385	590
DD4	475	570
DD8	375	580
DD12	415	640
DD13	420	635

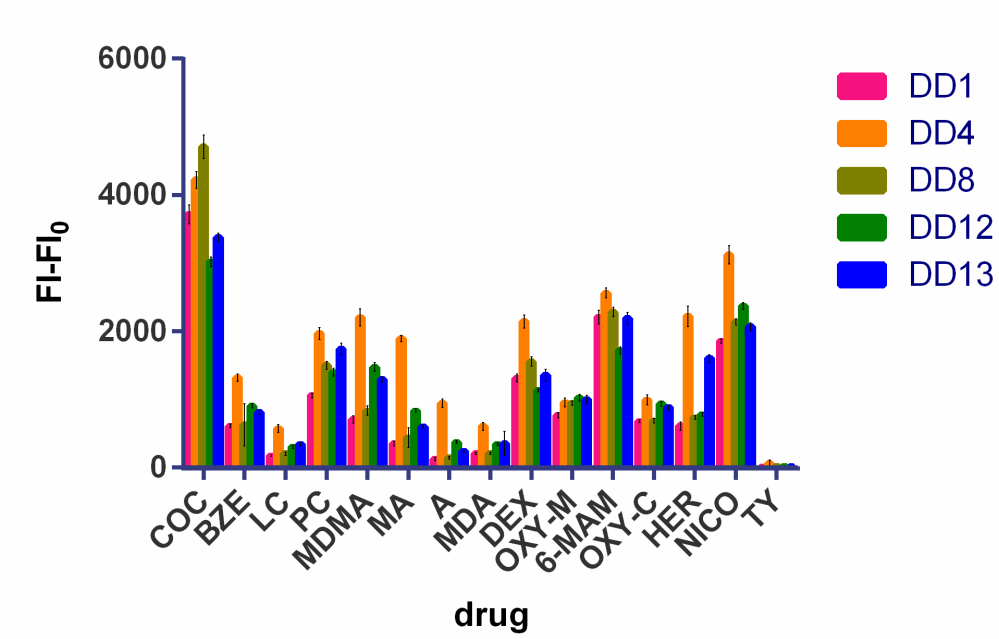

Figure 5. 39 Average fluorescence data from each DD with respect to COC (cocaine), BZE (benzoylecgonine), LC (lidocaine), PC (procaine), MDMA (3,4-methylenedioxymethamphatamine), MA (methamphetamine), A (amphetamine), MDA (3,4-methylenedioxoamphetamine), DEX (dextrorphan), OXY-M (oxymorphone), 6-MAM (6-acetylmorphine), OXY-C (oxycodone), HER (heroin), NICO (nicotine), TY (acetaminophen).

Discriminant Analysis: C7 versus DD1, DD4, DD8, DD12, DD13

Linear Method for Response: C7

Predictors: DD1, DD4, DD8, DD12, DD13

Groups

Group	6-MAM	DEX	HER	OXY-C	OXY-M
Count	6	6	6	6	6

Summary of Classification

	True Group				
Put into Group	6-MAM	DEX	HER	OXY-C	OXY-M
6-MAM	6	0	0	0	0
DEX	0	6	0	0	0
HER	0	0	6	0	0
OXY-C	0	0	0	6	0
OXY-M	0	0	0	0	6
Total N	6	6	6	6	6
N correct	6	6	6	6	6
Proportion	1.000	1.000	1.000	1.000	1.000

Correct Classifications

N	Correct	Proportion
30	30	1.000

Summary of Classification with Cross-validation

	True Group				
Put into Group	6-MAM	DEX	HER	OXY-C	OXY-M
6-MAM	6	0	0	0	0
DEX	0	6	0	0	0
HER	0	0	6	0	0
OXY-C	0	0	0	6	0
OXY-M	0	0	0	0	6
Total N	6	6	6	6	6
N correct	6	6	6	6	6
Proportion	1.000	1.000	1.000	1.000	1.000

Correct Classifications with Cross-validation

N	Correct	Proportion
30	30	1.000

Squared Distance Between Groups

	6-MAM	DEX	HER	OXY-C	OXY-M
6-MAM	0.00	512.96	1700.60	1538.17	1221.73
DEX	512.96	0.00	524.66	390.45	259.67
HER	1700.60	524.66	0.00	278.79	361.25
OXY-C	1538.17	390.45	278.79	0.00	31.07
OXY-M	1221.73	259.67	361.25	31.07	0.00

Linear Discriminant Function for Groups

	6-MAM	DEX	HER	OXY-C	OXY-M
Constant	-2044.5	-925.2	-565.4	-383.1	-480.5
DD1	0.4	0.2	0.0	0.1	0.1
DD4	0.1	0.1	0.2	0.1	0.1
DD8	0.5	0.4	-0.0	0.1	0.2
DD12	0.9	0.6	0.5	0.6	0.6
DD13	0.1	0.0	0.2	0.1	0.1

Summary of Misclassified Observations

					Squared Distance		Probability	
Observation	True Group	Pred Group	X-val Group	Group	Pred	X-val	Pred	X-val

Discriminant Analysis: C10 versus DD1_1, DD4_1, DD8_1, ... 12_1, DD13_1

Linear Method for Response: C10

Predictors: DD1_1, DD4_1, DD8_1, DD12_1, DD13_1

Groups

Group	BZE	COC	LC	PC
Count	6	6	6	6

Summary of Classification

	True Group			
Put into Group	BZE	COC	LC	PC
BZE	6	0	0	0
COC	0	6	0	0
LC	0	0	6	0
PC	0	0	0	6
Total N	6	6	6	6
N correct	6	6	6	6
Proportion	1.000	1.000	1.000	1.000

Correct Classifications

N	Correct	Proportion
24	24	1.000

Summary of Classification with Cross-validation

	True Group			
Put into Group	BZE	COC	LC	PC
BZE	6	0	0	0
COC	0	6	0	0
LC	0	0	6	0
PC	0	0	0	6
Total N	6	6	6	6
N correct	6	6	6	6
Proportion	1.000	1.000	1.000	1.000

Correct Classifications with Cross-validation

N	Correct	Proportion
24	24	1.000

Squared Distance Between Groups

	BZE	COC	LC	PC
BZE	0.00	2751.04	200.06	299.07
COC	2751.04	0.00	4006.46	1520.15
LC	200.06	4006.46	0.00	862.35
PC	299.07	1520.15	862.35	0.00

Linear Discriminant Function for Groups

	BZE	COC	LC	PC
Constant	-261.7	-2462.1	-42.7	-710.5
DD1_1	-0.2	0.0	-0.1	-0.3
DD4_1	0.1	0.1	0.1	0.1
DD8_1	-0.0	-0.0	-0.0	-0.0
DD12_1	0.5	0.8	0.1	0.6
DD13_1	0.1	0.7	0.1	0.4

Summary of Misclassified Observations

					Squared Distance		Probability	
Observation	True Group	Pred Group	X-val Group	Group	Pred	X-val	Pred	X-val

Discriminant Analysis: C18 versus DD1_2, DD4_2, DD8_2, ... _2, DD13_2

Linear Method for Response: C18

Predictors: DD1_2, DD4_2, DD8_2, DD12_2, DD13_2

Groups

Group	A	MA	MDA	MDMA
Count	6	6	6	6

Summary of Classification

	True Group			
Put into Group	A	MA	MDA	MDMA
A	6	0	0	0
MA	0	6	0	0
MDA	0	0	6	0
MDMA	0	0	0	6
Total N	6	6	6	6
N correct	6	6	6	6
Proportion	1.000	1.000	1.000	1.000

Correct Classifications

N	Correct	Proportion
24	24	1.000

Summary of Classification with Cross-validation

	True Group			
Put into Group	A	MA	MDA	MDMA
A	6	0	1	0
MA	0	6	0	0
MDA	0	0	5	0
MDMA	0	0	0	6
Total N	6	6	6	6
N correct	6	6	5	6
Proportion	1.000	1.000	0.833	1.000

Correct Classifications with Cross-validation

N	Correct	Proportion
24	23	0.958

Squared Distance Between Groups

	A	MA	MDA	MDMA
A	0.00	262.02	68.18	984.61
MA	262.02	0.00	468.55	404.44
MDA	68.18	468.55	0.00	1056.58
MDMA	984.61	404.44	1056.58	0.00

Linear Discriminant Function for Groups

	A	MA	MDA	MDMA
Constant	-120.91	-493.59	-60.77	-936.50
DD1_2	-0.27	-0.40	-0.00	-0.12
DD4_2	0.25	0.46	0.10	0.31
DD8_2	0.07	0.15	0.05	0.16
DD12_2	0.04	0.12	0.08	0.58
DD13_2	0.07	0.16	0.06	0.23

Summary of Misclassified Observations

					Squared Distance		Probability	
Observation	True Group	Pred Group	X-val Group	Group	Pred	X-val	Pred	X-val
19**	MDA	MDA	A	A	70.25	286.84	0.00	1.00
				MA	478.81	915.10	0.00	0.00
				MDA	16.30	1020.77	1.00	0.00
				MDMA	1110.96	4313.67	0.00	0.00

Chapter 6: Conclusions and future directions

6.1 Contributions to the field of supramolecular chemistry in salty solutions

At the start of this thesis work, a few supramolecular systems had been studied in-depth and functioned in complex aqueous solutions. Recently, the community has taken a closer look at how salts interact with hosts and how it affects host-guest binding. However, more research is needed to fully understand molecular recognition in salty solutions.

Before this thesis work, the design of supramolecular sensors working in biologically relevant solutions was primarily focused on pairing known hosts with dyes. A few examples of these sensors functioned in complex solutions, but their performance was greatly affected by the salts present. Furthermore, self-assembly operated sensors were less explored and reported.

One example of self-assembly in salty conditions arose from the serendipitous discovery of the salt-tolerant, calix[4]arene-based homodimers that this work was inspired from. The prior research focused only on a narrow range of host motifs and tolerated moderately challenging conditions. From my research I have expanded the calixarene motif, tested the assembly to extreme conditions and implemented the self-assembly into a useful supramolecular sensor which I outline below.

I furthered the field of molecular recognition in salty water by developing calixarenes that self-assembled in the presence of molar concentrations of NaCl and urea, two co-solutes known to strongly perturb molecular recognition. From my best knowledge, no one has ever studied molecular recognition in such extreme conditions.

I furthered the field of supramolecular sensing by reporting DimerDyes that operate through a novel self-assembly sensing mechanism. I demonstrated that they can operate despite the presence of competitive salts, co-factors and proteins. Most often the discovery of new sensors requires rational design and here I report new DimerDye scaffolds identified by supramolecular parallel synthesis and testing. Only a few host systems are able to target a wide breadth of guest analytes in real biological fluid. I added to this field by implementing DimerDyes in real saliva by the detection of multiple classes of drugs.

6.2 Future directions for the yin-yang dimer

Expanding the structural diversity of the yin-yang scaffold is a lead for future development of this technology. Both upper and lower rim modifications need to be explored and homodimerization tested. For example, if dimerization is preserved with an alkyl chain appended to the lower rim, two levels of self-assembly can occur: dimerization and amphiphilic aggregation.

DimerDyes' strengths stem from both their tolerance to environmental conditions and accommodating structural diversity of the pendant group. This inspires many opportunities that can and are currently being explored. I will mention here a few improvements and ideas towards the DimerDye concept. To improve the sensing capabilities, DimerDyes need to become more sensitive. This can be achieved by integrating completely different fluorophores within the pocket. These fluorophores can be intrinsically brighter and modulate the dimerization strength which ultimately improves sensitivity. DimerDyes operating on paper-based test strips are currently being pursued and an increase in sensitivity will greatly improve the applicability of the test strips to real-world analytical problems.

In order to improve the sensing quality from the DimerDye array, a richer set of photophysical information is needed. This can be achieved by creating DimerDyes that undergo alternative sensing mechanisms. For example, currently bring pursued are DimerDyes that work by aggregation-induced emission would emit upon dimerization and turn-off upon complexation to a guest. Another possibility is to integrate a second fluorophore within the pocket. Upon dimerization the two fluorophores will fluoresce *via* resonance energy transfer yet emit differently upon complexation with a guest. Another method to increase sensitivity is to incorporate covalent bond formation with the target analyte and sensor instead of relying solely on non-covalent interactions.

The calixarene-based dimers described in this work are unique in both their resilience to environmental pressures and work elegantly as supramolecular tools. I hope my extensive research regarding this privileged structure will inspire the development of functional supramolecular systems that thrive in complex media.

Bibliography

1. Lehn, J. M., Cryptates: inclusion complexes of macropolycyclic receptor molecules. In *Pure Appl. Chem.*, 1978; Vol. 50, p 871.
2. Huang, F.; Anslyn, E. V. Introduction: Supramolecular Chemistry. *Chem. Rev.* **2015**, *115*, 6999-7000.
3. Astumian, R. D. How molecular motors work – insights from the molecular machinist's toolbox: the Nobel prize in Chemistry 2016. *Chem. Sci.* **2017**, *8*, 840-845.
4. Moss, G. P.; Smith, P. A. S.; Tavernier, D., Glossary of class names of organic compounds and reactivity intermediates based on structure (IUPAC Recommendations 1995). In *Pure Appl. Chem.*, 1995; Vol. 67, p 1307.
5. A. Beatty, M.; Hof, F., *New Technologies Powered by Protein-Binding Calixarenes*. 2016; p 601-625.
6. Saenger, W. Cyclodextrin inclusion compounds in research and industry. *Angew. Chem. Int. Ed.* **1980**, *19*, 344-362.
7. Lai, C.-F.; Odashima, K.; Koga, K. Synthesis and properties of water-soluble bis-paracyclophanes. *Tetrahedron Lett.* **1985**, *26*, 5179-5182.
8. Shepodd, T. J.; Petti, M. A.; Dougherty, D. A. Tight, oriented binding of an aliphatic guest by a new class of water-soluble molecules with hydrophobic binding sites. *J. Am. Chem. Soc.* **1986**, *108*, 6085-6087.
9. Corbett, P. T.; Sanders, J. K. M.; Otto, S. Exploring the Relation between Amplification and Binding in Dynamic Combinatorial Libraries of Macrocyclic Synthetic Receptors in Water. *Chem. Eur. J.* **2008**, *14*, 2153-2166.
10. Ingerman, L. A.; Cuellar, M. E.; Waters, M. L. A small molecule receptor that selectively recognizes trimethyl lysine in a histone peptide with native protein-like affinity. *Chem. Commun.* **2010**, *46*, 1839-1841.
11. Corbett, P. T.; Sanders, J. K. M.; Otto, S. Systems Chemistry: Pattern Formation in Random Dynamic Combinatorial Libraries. *Angew. Chem. Int. Ed.* **2007**, *119*, 9014-9017.
12. Shinkai, S.; Araki, K.; Tsubaki, T.; Arimura, T.; Manabe, O. New syntheses of calixarene-*p*-sulphonates and *p*-nitrocalixarenes. *J. Chem. Soc., Perkin Trans. 1* **1987**, 2297-2299.
13. Arena, G.; Gentile, S.; Gulino, F. G.; Sciotto, D.; Sgarlata, C. Water-soluble pentasulfonatocalix[5]arene: selective recognition of ditopic trimethylammonium cations by a triple non-covalent interaction. *Tetrahedron Lett.* **2004**, *45*, 7091-7094.
14. Arena, G.; Casnati, A.; Contino, A.; Gulino, F. G.; Sciotto, D.; Ungaro, R. Entropic origin of the sulfonate groups' electrostatic assistance in the complexation of quaternary ammonium cations by water soluble calix[4]arenes. *J. Chem. Soc., Perkin Trans. 2* **2000**, 419-423.
15. Alex, J. M.; Rennie, M. L.; Volpi, S.; Sansone, F.; Casnati, A.; Crowley, P. B. Phosphonated Calixarene as a "Molecular Glue" for Protein Crystallization. *Cryst. Growth Des.* **2018**, *18*, 2467-2473.
16. Gutsche, C. D.; Alam, I. Calixarenes. 23. the complexation and catalytic properties of water soluble calixarenes. *Tetrahedron Lett.* **1988**, *44*, 4689-4694.
17. Martin, A. D.; Raston, C. L. Multifunctional *p*-phosphonated calixarenes. *Chem. Commun.* **2011**, *47*, 9764-9772.

18. Biros, S. M.; Rebek, J. J. Structure and binding properties of water-soluble cavitands and capsules. *Chem. Soc. Rev.* **2007**, *36*, 93-104.
19. Oshovsky, G. V.; Reinhoudt, D. N.; Verboom, W. Supramolecular Chemistry in Water. *Angew. Chem. Int. Ed.* **2007**, *46*, 2366-2393.
20. Ogoshi, T.; Takashima, S.; Yamagishi, T.-a. Molecular Recognition with Microporous Multilayer Films Prepared by Layer-by-Layer Assembly of Pillar[5]arenes. *J. Am. Chem. Soc.* **2015**, *137*, 10962-10964.
21. Zhang, H.; Ma, X.; Nguyen, K. T.; Zhao, Y. Biocompatible Pillararene-Assembly-Based Carriers for Dual Bioimaging. *ACS Nano* **2013**, *7*, 7853-7863.
22. Kim, K.; Selvapalam, N.; Oh, D. H. Cucurbiturils–a New Family of Host Molecules. *J. Inclusion Phenom. Macrocyclic Chem.* **2004**, *50*, 31-36.
23. Vinciguerra, B.; Cao, L.; Cannon, J. R.; Zavalij, P. Y.; Fenselau, C.; Isaacs, L. Synthesis and Self-Assembly Processes of Monofunctionalized Cucurbit[7]uril. *J. Am. Chem. Soc.* **2012**, *134*, 13133-13140.
24. Guo, D.-S.; Liu, Y. Calixarene-based supramolecular polymerization in solution. *Chem. Soc. Rev.* **2012**, *41*, 5907-5921.
25. Guo, D.-S.; Liu, Y. Supramolecular Chemistry of *p*-Sulfonatocalix[n]arenes and Its Biological Applications. *Acc. Chem. Res.* **2014**, *47*, 1925-1934.
26. Wang, K.; Guo, D.-S.; Wang, X.; Liu, Y. Multistimuli Responsive Supramolecular Vesicles Based on the Recognition of *p*-Sulfonatocalixarene and its Controllable Release of Doxorubicin. *ACS Nano* **2011**, *5*, 2880-2894.
27. Fiammengo, R.; Timmerman, P.; Huskens, J.; Versluis, K.; Heck, A. J. R.; Reinhoudt, D. N. Non-covalent synthesis of calix[4]arene-capped porphyrins in polar solvents via ionic interactions. *Tetrahedron Lett.* **2002**, *58*, 757-764.
28. Corbellini, F.; Di Costanzo, L.; Crego-Calama, M.; Geremia, S.; Reinhoudt, D. N. Guest Encapsulation in a Water-Soluble Molecular Capsule Based on Ionic Interactions. *J. Am. Chem. Soc.* **2003**, *125*, 9946-9947.
29. Evan-Salem, T.; Baruch, I.; Avram, L.; Cohen, Y.; Palmer, L. C.; Rebek, J., Jr. Resorcinarenes are hexameric capsules in solution. *Proc Natl Acad Sci U S A* **2006**, *103*, 12296-12300.
30. Katiyar, A.; Freire Sovierzoski, J. C.; Calio, P. B.; Vartia, A. A.; Thompson, W. H. Water plays a diverse role in a hydrogen-bonded, hexameric supramolecular assembly. *Chem. Commun.* **2019**, *55*, 6591-6594.
31. Shivanyuk, A.; Rebek, J. Assembly of Resorcinarene Capsules in Wet Solvents. *J. Am. Chem. Soc.* **2003**, *125*, 3432-3433.
32. Jia, C.; Zuo, W.; Zhang, D.; Yang, X.-J.; Wu, B. Anion recognition by oligo-(thio)urea-based receptors. *Chem. Commun.* **2016**, *52*, 9614-9627.
33. Jia, C.; Wu, B.; Li, S.; Huang, X.; Yang, X.-J. Tetraureas versus Triureas in Sulfate Binding. *Org. Lett.* **2010**, *12*, 5612-5615.
34. Qin, L.; Hartley, A.; Turner, P.; Elmes, R. B. P.; Jolliffe, K. A. Macrocyclic squaramides: anion receptors with high sulfate binding affinity and selectivity in aqueous media. *Chem. Sci.* **2016**, *7*, 4563-4572.
35. Liu, Y.; Sengupta, A.; Raghavachari, K.; Flood, A. H. Anion Binding in Solution: Beyond the Electrostatic Regime. *Chem.* **2017**, *3*, 411-427.

36. Langton, M. J.; Serpell, C. J.; Beer, P. D. Anion Recognition in Water: Recent Advances from a Supramolecular and Macromolecular Perspective. *Angew. Chem. Int. Ed.* **2016**, *55*, 1974-1987.
37. Jia, C.; Wang, Q.-Q.; Begum, R. A.; Day, V. W.; Bowman-James, K. Chelate effects in sulfate binding by amide/urea-based ligands. *Org. Biomol. Chem.* **2015**, *13*, 6953-6957.
38. Liu, Y.; Zhao, W.; Chen, C.-H.; Flood, A. H. Chloride capture using a C–H hydrogen bonding cage. *Science* **2019**, *365*, 159-161.
39. Murray, J.; Kim, K.; Ogoshi, T.; Yao, W.; Gibb, B. C. The aqueous supramolecular chemistry of cucurbit[n]urils, pillar[n]arenes and deep-cavity cavitands. *Chem. Soc. Rev.* **2017**, *46*, 2479-2496.
40. Dougherty, D. A. The Cation−π Interaction. *Acc. Chem. Res.* **2013**, *46*, 885-893.
41. Ma, J. C.; Dougherty, D. A. The Cation−π Interaction. *Chem. Rev.* **1997**, *97*, 1303-1324.
42. Petti, M. A.; Shepodd, T. J.; Barrans, R. E.; Dougherty, D. A. "Hydrophobic" binding of water-soluble guests by high-symmetry, chiral hosts. An electron-rich receptor site with a general affinity for quaternary ammonium compounds and electron-deficient π systems. *J. Am. Chem. Soc.* **1988**, *110*, 6825-6840.
43. Li, C.; Ma, J.; Zhao, L.; Zhang, Y.; Yu, Y.; Shu, X.; Li, J.; Jia, X. Molecular selective binding of basic amino acids by a water-soluble pillar[5]arene. *Chem. Commun.* **2013**, *49*, 1924-1926.
44. Ogoshi, T.; Hashizume, M.; Yamagishi, T.-a.; Nakamoto, Y. Synthesis, conformational and host–guest properties of water-soluble pillar[5]arene. *Chem. Commun.* **2010**, *46*, 3708-3710.
45. Kazakova, E. K.; Makarova, N. A.; Ziganshina, A. U.; Muslinkina, L. A.; Muslinkin, A. A.; Habicher, W. D. Novel water-soluble tetrasulfonatomethylcalix[4]resorcinarenes. *Tetrahedron Lett.* **2000**, *41*, 10111-10115.
46. Beyeh, N. K.; Jo, H. H.; Kolesnichenko, I.; Pan, F.; Kalenius, E.; Anslyn, E. V.; Ras, R. H. A.; Rissanen, K. Recognition of Viologen Derivatives in Water by *N*-Alkyl Ammonium Resorcinarene Chlorides. *J. Org. Chem.* **2017**, *82*, 5198-5203.
47. Hong, M.; Zhang, Y.-M.; Liu, Y. Selective Binding Affinity between Quaternary Ammonium Cations and Water-Soluble Calix[4]resorcinarene. *J. Org. Chem.* **2015**, *80*, 1849-1855.
48. Dumartin, M.-L.; Givelet, C.; Meyrand, P.; Bibal, B.; Gosse, I. A fluorescent cyclotriveratrylene: synthesis, emission properties and acetylcholine recognition in water. *Org. Biomol. Chem.* **2009**, *7*, 2725-2728.
49. Xia, D.; Li, Y.; Jie, K.; Shi, B.; Yao, Y. A Water-Soluble Cyclotriveratrylene-Based Supra-amphiphile: Synthesis, pH-Responsive Self-Assembly in Water, and Its Application in Controlled Drug Release. *Org. Lett.* **2016**, *18*, 2910-2913.
50. Perret, F.; Morel, J.-P.; Morel-Desrosiers, N. Thermodynamics of the Complexation of the p-Sulfonatocalix[4]arene with Simple Model Guests in Water: a Microcalorimetric Study. *Supramol. Chem.* **2003**, *15*, 199-206.
51. Arnecke, R.; Böhmer, V.; Cacciapaglia, R.; Dalla Cort, A.; Mandolini, L. Cation-π interactions between neutral calix[5]arene hosts and cationic organic guests. *Tetrahedron Lett.* **1997**, *53*, 4901-4908.

52. Hanauer, T.; Hopkinson, R. J.; Patel, K.; Li, Y.; Correddu, D.; Kawamura, A.; Sarojini, V.; Leung, I. K. H.; Gruber, T. Selective recognition of the di/trimethylammonium motif by an artificial carboxycalixarene receptor. *Org. Biomol. Chem.* **2017**, *15*, 1100-1105.
53. Cao, L.; Šekutor, M.; Zavalij, P. Y.; Mlinarić-Majerski, K.; Glaser, R.; Isaacs, L. Cucurbit[7]uril·Guest Pair with an Attomolar Dissociation Constant. *Angew. Chem. Int. Ed.* **2014**, *53*, 988-993.
54. Gibb, C. L. D.; Gibb, B. C. Well-Defined, Organic Nanoenvironments in Water: The Hydrophobic Effect Drives a Capsular Assembly. *J. Am. Chem. Soc.* **2004**, *126*, 11408-11409.
55. Widom, B.; Bhimalapuram, P.; Koga, K. The hydrophobic effect. *Phys. Chem. Chem. Phys.* **2003**, *5*, 3085-3093.
56. Hillyer, M. B.; Gibb, B. C. Molecular Shape and the Hydrophobic Effect. *Annu. Rev. Phys. Chem.* **2016**, *67*, 307-329.
57. Biedermann, F.; Nau, W. M.; Schneider, H. J. The Hydrophobic Effect Revisited—Studies with Supramolecular Complexes Imply High-Energy Water as a Noncovalent Driving Force. *Angew. Chem. Int. Ed.* **2014**, *53*, 11158-11171.
58. He, S.; Biedermann, F.; Vankova, N.; Zhechkov, L.; Heine, T.; Hoffman, R. E.; De Simone, A.; Duignan, T. T.; Nau, W. M. Cavitation energies can outperform dispersion interactions. *Nat. Chem.* **2018**, *10*, 1252-1257.
59. Beshara, C. S.; Jones, C. E.; Daze, K. D.; Lilgert, B. J.; Hof, F. A Simple Calixarene Recognizes Post-translationally Methylated Lysine. *ChemBioChem* **2010**, *11*, 63-66.
60. Peacock, H.; Thinnes, C. C.; Kawamura, A.; Hamilton, A. D. Tetracyanoresorcin[4]arene selectively recognises trimethyllysine and inhibits its enzyme-catalysed demethylation. *Supramol. Chem.* **2016**, *28*, 575-581.
61. Pinkin, N. K.; Waters, M. L. Development and mechanistic studies of an optimized receptor for trimethyllysine using iterative redesign by dynamic combinatorial chemistry. *Org. Biomol. Chem.* **2014**, *12*, 7059-7067.
62. Liu, Y.; Perez, L.; Mettry, M.; Easley, C. J.; Hooley, R. J.; Zhong, W. Self-Aggregating Deep Cavitand Acts as a Fluorescence Displacement Sensor for Lysine Methylation. *J. Am. Chem. Soc.* **2016**, *138*, 10746-9.
63. Daze, K. D.; Jones, C. E.; Lilgert, B. J.; Beshara, C. S.; Hof, F. Determining the effects of salt, buffer, and temperature on the complexation of methylated ammonium ions and methyllysines by sulfonated calixarenes. *Can. J. Chem.* **2013**, *91*, 1072-1076.
64. Rekharsky, M. V.; Mori, T.; Yang, C.; Ko, Y. H.; Selvapalam, N.; Kim, H.; Sobransingh, D.; Kaifer, A. E.; Liu, S.; Isaacs, L.; Chen, W.; Moghaddam, S.; Gilson, M. K.; Kim, K.; Inoue, Y. A synthetic host-guest system achieves avidin-biotin affinity by overcoming enthalpy–entropy compensation. *Proc Natl Acad Sci U S A* **2007**, *104*, 20737-20742.
65. Ganapati, S.; Grabitz, S. D.; Murkli, S.; Scheffenbichler, F.; Rudolph, M. I.; Zavalij, P. Y.; Eikermann, M.; Isaacs, L. Molecular Containers Bind Drugs of Abuse in Vitro and Reverse the Hyperlocomotive Effect of Methamphetamine in Rats. *ChemBioChem* **2017**, *18*, 1583-1588.

66. Zebaze Ndendjio, S. A.; Isaacs, L. Molecular recognition properties of acyclic cucurbiturils toward amino acids, peptides, and a protein. *Supramol. Chem.* **2019**, *31*, 432-441.
67. Guo, D.-S.; Uzunova, V. D.; Su, X.; Liu, Y.; Nau, W. M. Operational calixarene-based fluorescent sensing systems for choline and acetylcholine and their application to enzymatic reactions. *Chem. Sci.* **2011**, *2*, 1722-1734.
68. Lavande, N.; Acuña, A.; Basílio, N.; Francisco, V.; Malkhede, D. D.; Garcia-Rio, L. A journey from calix[4]arene to calix[6] and calix[8]arene reveals more than a matter of size. Receptor concentration affects the stability and stoichiometric nature of the complexes. *Phys. Chem. Chem. Phys.* **2017**, *19*, 13640-13649.
69. James, L. I.; Beaver, J. E.; Rice, N. W.; Waters, M. L. A Synthetic Receptor for Asymmetric Dimethyl Arginine. *J. Am. Chem. Soc.* **2013**, *135*, 6450-6455.
70. Skillman, A. G. SAMPL3: blinded prediction of host–guest binding affinities, hydration free energies, and trypsin inhibitors. *J. Comput.-Aided Mol. Des.* **2012**, *26*, 473-474.
71. Muddana, H. S.; Fenley, A. T.; Mobley, D. L.; Gilson, M. K. The SAMPL4 host–guest blind prediction challenge: an overview. *J. Comput.-Aided Mol. Des.* **2014**, *28*, 305-317.
72. Yin, J.; Henriksen, N. M.; Slochower, D. R.; Shirts, M. R.; Chiu, M. W.; Mobley, D. L.; Gilson, M. K. Overview of the SAMPL5 host–guest challenge: Are we doing better? *J. Comput.-Aided Mol. Des.* **2017**, *31*, 1-19.
73. Rizzi, A.; Murkli, S.; McNeill, J. N.; Yao, W.; Sullivan, M.; Gilson, M. K.; Chiu, M. W.; Isaacs, L.; Gibb, B. C.; Mobley, D. L.; Chodera, J. D. Overview of the SAMPL6 host–guest binding affinity prediction challenge. *J. Comput.-Aided Mol. Des.* **2018**, *32*, 937-963.
74. Francisco, V.; Piñeiro, A.; Nau, W. M.; García-Río, L. The "True" Affinities of Metal Cations to *p*-Sulfonatocalix[4]arene: A Thermodynamic Study at Neutral pH Reveals a Pitfall Due to Salt Effects in Microcalorimetry. *Chem. Eur. J.* **2013**, *19*, 17809-17820.
75. Mock, W. L.; Shih, N. Y. Host-guest binding capacity of cucurbituril. *J. Org. Chem.* **1983**, *48*, 3618-3619.
76. Márquez, C.; Hudgins, R. R.; Nau, W. M. Mechanism of Host−Guest Complexation by Cucurbituril. *J. Am. Chem. Soc.* **2004**, *126*, 5806-5816.
77. Tang, H.; Fuentealba, D.; Ko, Y. H.; Selvapalam, N.; Kim, K.; Bohne, C. Guest Binding Dynamics with Cucurbit[7]uril in the Presence of Cations. *J. Am. Chem. Soc.* **2011**, *133*, 20623-20633.
78. Ong, W.; Kaifer, A. E. Salt Effects on the Apparent Stability of the Cucurbit[7]uril−Methyl Viologen Inclusion Complex. *J. Org. Chem.* **2004**, *69*, 1383-1385.
79. Thomas, S. S.; Tang, H.; Bohne, C. Noninnocent Role of Na^+ Ions in the Binding of the *N*-Phenyl-2-naphthylammonium Cation as a Ditopic Guest with Cucurbit[7]uril. *J. Am. Chem. Soc.* **2019**, *141*, 9645-9654.
80. Okur, H. I.; Hladílková, J.; Rembert, K. B.; Cho, Y.; Heyda, J.; Dzubiella, J.; Cremer, P. S.; Jungwirth, P. Beyond the Hofmeister series: ion-specific effects on proteins and their biological functions. *J. Phys. Chem. B* **2017**, *121*, 1997-2014.

81. Paterová, J.; Rembert, K. B.; Heyda, J.; Kurra, Y.; Okur, H. I.; Liu, W. R.; Hilty, C.; Cremer, P. S.; Jungwirth, P. Reversal of the Hofmeister Series: Specific Ion Effects on Peptides. *J. Phys. Chem. B* **2013**, *117*, 8150-8158.
82. Zhang, Y.; Furyk, S.; Bergbreiter, D. E.; Cremer, P. S. Specific Ion Effects on the Water Solubility of Macromolecules: PNIPAM and the Hofmeister Series. *J. Am. Chem. Soc.* **2005**, *127*, 14505-14510.
83. Carnegie, R. S.; Gibb, C. L. D.; Gibb, B. C. Anion Complexation and The Hofmeister Effect. *Angew. Chem. Int. Ed.* **2014**, *53*, 11498-11500.
84. Gibb, C. L. D.; Gibb, B. C. Anion Binding to Hydrophobic Concavity Is Central to the Salting-in Effects of Hofmeister Chaotropes. *J. Am. Chem. Soc.* **2011**, *133*, 7344-7347.
85. Assaf, K. I.; Nau, W. M. The Chaotropic Effect as an Assembly Motif in Chemistry. *Angew. Chem. Int. Ed.* **2018**, *57*, 13968-13981.
86. Assaf, K. I.; Hennig, A.; Peng, S.; Guo, D.-S.; Gabel, D.; Nau, W. M. Hierarchical host–guest assemblies formed on dodecaborate-coated gold nanoparticles. *Chem. Commun.* **2017**, *53*, 4616-4619.
87. Iki, N.; Suzuki, T.; Koyama, K.; Kabuto, C.; Miyano, S. Inclusion Behavior of Thiacalix[4]arenetetrasulfonate toward Water-Miscible Organic Molecules Studied by Salting-Out and X-ray Crystallography. *Org. Lett.* **2002**, *4*, 509-512.
88. Yuan, D.; Zhu, W. X.; Ma, S.; Yan, X. Bilayer structure of tetrasodium thiacalix[4]arene tetrasulfonate. *J. Mol. Struct.* **2002**, *616*, 241-246.
89. Shinkai, S.; Kawaguchi, H.; Manabe, O. Selective adsorption of UO_2^{2+} to a polymer resin immobilizing calixarene-based uranophiles. *J. Polym. Sci., Part C: Polym. Lett.* **1988**, *26*, 391-396.
90. Kon, N.; Iki, N.; Miyano, S. Inclusion behavior of water-soluble thiacalix- and calix[4]arenes towards substituted benzenes in aqueous solution. *Org. Biomol. Chem.* **2003**, *1*, 751-755.
91. Allen, Hillary F.; Daze, Kevin D.; Shimbo, T.; Lai, A.; Musselman, Catherine A.; Sims, Jennifer K.; Wade, Paul A.; Hof, F.; Kutateladze, Tatiana G. Inhibition of histone binding by supramolecular hosts. *Biochem. J* **2014**, *459*, 505-512.
92. Ali, M.; Daze, K. D.; Strongin, D. E.; Rothbart, S. B.; Rincon-Arano, H.; Allen, H. F.; Li, J.; Strahl, B. D.; Hof, F.; Kutateladze, T. G. Molecular insights into inhibition of the methylated histone-plant homeodomain complexes by calixarenes. *J. Biol. Chem.* **2015**, *290*, 22919-22930.
93. Lee, H. H.; Choi, T. S.; Lee, S. J. C.; Lee, J. W.; Park, J.; Ko, Y. H.; Kim, W. J.; Kim, K.; Kim, H. I. Supramolecular Inhibition of Amyloid Fibrillation by Cucurbit[7]uril. *Angew. Chem. Int. Ed.* **2014**, *53*, 7461-7465.
94. Chinai, J. M.; Taylor, A. B.; Ryno, L. M.; Hargreaves, N. D.; Morris, C. A.; Hart, P. J.; Urbach, A. R. Molecular recognition of insulin by a synthetic receptor. *J. Am. Chem. Soc.* **2011**, *133*, 8810-3.
95. Matar-Merheb, R.; Rhimi, M.; Leydier, A.; Huché, F.; Galián, C.; Desuzinges-Mandon, E.; Ficheux, D.; Flot, D.; Aghajari, N.; Kahn, R.; Di Pietro, A.; Jault, J.-M.; Coleman, A. W.; Falson, P. Structuring Detergents for Extracting and Stabilizing Functional Membrane Proteins. *PLOS ONE* **2011**, *6*, e18036.

96. Shinde, M. N.; Barooah, N.; Bhasikuttan, A. C.; Mohanty, J. Inhibition and disintegration of insulin amyloid fibrils: a facile supramolecular strategy with *p*-sulfonatocalixarenes. *Chem. Commun.* **2016**, *52*, 2992-2995.
97. Goor, O. J.; Hendrikse, S. I.; Dankers, P. Y.; Meijer, E. From supramolecular polymers to multi-component biomaterials. *Chem. Soc. Rev.* **2017**, *46*, 6621-6637.
98. Peng, S.; Pan, Y.-C.; Wang, Y.; Xu, Z.; Chen, C.; Ding, D.; Wang, Y.; Guo, D.-S. Sequentially Programmable and Cellularly Selective Assembly of Fluorescent Polymerized Vesicles for Monitoring Cell Apoptosis. *Adv. Sci.* **2017**, *4*, 1700310.
99. Miskolczy, Z.; Biczok, L. Photochromism of a merocyanine dye bound to sulfonatocalixarenes: effect of pH and the size of macrocycle on the kinetics. *J. Phys. Chem. B.* **2013**, *117*, 648-53.
100. Wang, K.; Cai, X.; Yao, W.; Tang, D.; Kataria, R.; Ashbaugh, H. S.; Byers, L. D.; Gibb, B. C. Electrostatic Control of Macrocyclization Reactions within Nanospaces. *J. Am. Chem. Soc.* **2019**, *141*, 6740-6747.
101. Ramamurthy, V. Photochemistry within a Water-Soluble Organic Capsule. *Acc. Chem. Res.* **2015**, *48*, 2904-2917.
102. Garnett, G. A. E.; Starke, M. J.; Shaurya, A.; Li, J.; Hof, F. Supramolecular Affinity Chromatography for Methylation-Targeted Proteomics. *Anal. Chem.* **2016**, *88*, 3697-3703.
103. Biedermann, F.; Hathazi, D.; Nau, W. M. Associative chemosensing by fluorescent macrocycle-dye complexes - a versatile enzyme assay platform beyond indicator displacement. *Chem. Commun.* **2015**, *51*, 4977-80.
104. Kumar, V.; Anslyn, E. V. A selective turn-on fluorescent sensor for sulfur mustard simulants. *J. Am. Chem. Soc.* **2013**, *135*, 6338-44.
105. Minami, T.; Esipenko, N. A.; Zhang, B.; Isaacs, L.; Anzenbacher, P. "Turn-on" fluorescent sensor array for basic amino acids in water. *Chem. Commun.* **2014**, *50*, 61-63.
106. Dsouza, R. N.; Pischel, U.; Nau, W. M. Fluorescent dyes and their supramolecular host/guest complexes with macrocycles in aqueous solution. *Chem. Rev.* **2011**, *111*, 7941-80.
107. Wiskur, S. L.; Ait-Haddou, H.; Lavigne, J. J.; Anslyn, E. V. Teaching old indicators new tricks. *Acc. Chem. Res.* **2001**, *34*, 963-72.
108. Florea, M.; Kudithipudi, S.; Rei, A.; González-Álvarez, M. J.; Jeltsch, A.; Nau, W. M. A Fluorescence-Based Supramolecular Tandem Assay for Monitoring Lysine Methyltransferase Activity in Homogeneous Solution. *Chem. Eur. J.* **2012**, *18*, 3521-3528.
109. Legg, K. D.; Hercules, D. M. Quenching of lucigenin fluorescence. *J. Phys. Chem.* **1970**, *74*, 2114-2118.
110. Aps, J. K. M.; Martens, L. C. Review: The physiology of saliva and transfer of drugs into saliva. *Forensic Sci. Int.* **2005**, *150*, 119-131.
111. Bouatra, S.; Aziat, F.; Mandal, R.; Guo, A. C.; Wilson, M. R.; Knox, C.; Bjorndahl, T. C.; Krishnamurthy, R.; Saleem, F.; Liu, P.; Dame, Z. T.; Poelzer, J.; Huynh, J.; Yallou, F. S.; Psychogios, N.; Dong, E.; Bogumil, R.; Roehring, C.; Wishart, D. S. The human urine metabolome. *PloS one* **2013**, *8*, e73076-e73076.
112. Stewart, S.; Ivy, M. A.; Anslyn, E. V. The use of principal component analysis and discriminant analysis in differential sensing routines. *Chem. Soc. Rev.* **2014**, *43*, 70-84.

113. Zheng, Z.; Geng, W.-C.; Gao, J.; Wang, Y.-Y.; Sun, H.; Guo, D.-S. Ultrasensitive and specific fluorescence detection of a cancer biomarker via nanomolar binding to a guanidinium-modified calixarene. *Chem. Sci.* **2018**, *9*, 2087-2091.
114. Minami, T.; Esipenko, N. A.; Akdeniz, A.; Zhang, B.; Isaacs, L.; Anzenbacher, P. Multianalyte Sensing of Addictive Over-the-Counter (OTC) Drugs. *J. Am. Chem. Soc.* **2013**, *135*, 15238-15243.
115. Lee, D.-W.; Park, K. M.; Banerjee, M.; Ha, S. H.; Lee, T.; Suh, K.; Paul, S.; Jung, H.; Kim, J.; Selvapalam, N.; Ryu, S. H.; Kim, K. Supramolecular fishing for plasma membrane proteins using an ultrastable synthetic host–guest binding pair. *Nat. Chem.* **2010**, *3*, 154.
116. Bagnacani, V.; Franceschi, V.; Bassi, M.; Lomazzi, M.; Donofrio, G.; Sansone, F.; Casnati, A.; Ungaro, R. Arginine clustering on calix[4]arene macrocycles for improved cell penetration and DNA delivery. *Nat. Commun.* **2013**, *4*, 1721.
117. Norouzy, A.; Azizi, Z.; Nau, W. M. Indicator Displacement Assays Inside Live Cells. *Angew. Chem. Int. Ed.* **2015**, *54*, 792-795.
118. Coleman, A. W.; Jebors, S.; Cecillon, S.; Perret, P.; Garin, D.; Marti-Battle, D.; Moulin, M. Toxicity and biodistribution of *para*-sulfonato-calix[4]arene in mice. *New J. Chem.* **2008**, *32*, 780-782.
119. Uzunova, V. D.; Cullinane, C.; Brix, K.; Nau, W. M.; Day, A. I. Toxicity of cucurbit[7]uril and cucurbit[8]uril: an exploratory in vitro and in vivo study. *Org. Biomol. Chem.* **2010**, *8*, 2037-2042.
120. Munro, I. C.; Newberne, P. M.; Young, V. R.; Bär, A. Safety assessment of γ-cyclodextrin. *Regul. Toxicol. Pharm.* **2004**, *39*, 3-13.
121. Haerter, F.; Simons, J. C. P.; Foerster, U.; Moreno Duarte, I.; Diaz-Gil, D.; Ganapati, S.; Eikermann-Haerter, K.; Ayata, C.; Zhang, B.; Blobner, M.; Isaacs, L.; Eikermann, M. Comparative Effectiveness of Calabadion and Sugammadex to Reverse Non-depolarizing Neuromuscular-blocking Agents. *Anesthesiology* **2015**, *123*, 1337-1349.
122. Naguib, M. Sugammadex: another milestone in clinical neuromuscular pharmacology. *Anesthesia & Analgesia* **2007**, *104*, 575-581.
123. Wang, G.-F.; Ren, X.-L.; Zhao, M.; Qiu, X.-L.; Qi, A.-D. Paraquat Detoxification with *p*-Sulfonatocalix-[4]arene by a Pharmacokinetic Study. *J. Agric. Food. Chem.* **2011**, *59*, 4294-4299.
124. Yu, G.; Zhou, X.; Zhang, Z.; Han, C.; Mao, Z.; Gao, C.; Huang, F. Pillar[6]arene/Paraquat Molecular Recognition in Water: High Binding Strength, pH-Responsiveness, and Application in Controllable Self-Assembly, Controlled Release, and Treatment of Paraquat Poisoning. *J. Am. Chem. Soc.* **2012**, *134*, 19489-19497.
125. Dai, X.; Zhou, X.; Liao, C.; Yao, Y.; Yu, Y.; Zhang, S. A nanodrug to combat cisplatin-resistance by protecting cisplatin with *p*-sulfonatocalix[4]arene and regulating glutathione S-transferases with loaded 5-fluorouracil. *Chem. Commun.* **2019**, *55*, 7199-7202.
126. Shetty, D.; Skorjanc, T.; Olson, M. A.; Trabolsi, A. Self-assembly of Stimuli-Responsive Imine-linked Calix[4]arene Nanocapsules for Targeted Camptothecin Delivery. *Chem. Commun.* **2019**.
127. Webber, M. J.; Langer, R. Drug delivery by supramolecular design. *Chem. Soc. Rev.* **2017**, *46*, 6600-6620.

128. Walker, S.; Oun, R.; McInnes, F. J.; Wheate, N. J. The Potential of Cucurbit[n]urils in Drug Delivery. *Isr. J. Chem.* **2011**, *51*, 616-624.
129. Zhou, J.; Yu, G.; Huang, F. Supramolecular chemotherapy based on host–guest molecular recognition: a novel strategy in the battle against cancer with a bright future. *Chem. Soc. Rev.* **2017**, *46*, 7021-7053.
130. Wang, L.; Li, L.-L.; Ma, H. L.; Wang, H. Recent advances in biocompatible supramolecular assemblies for biomolecular detection and delivery. *Chin. Chem. Lett.* **2013**, *24*, 351-358.
131. Li, B.; Meng, Z.; Li, Q.; Huang, X.; Kang, Z.; Dong, H.; Chen, J.; Sun, J.; Dong, Y.; Li, J.; Jia, X.; Sessler, J. L.; Meng, Q.; Li, C. A pH responsive complexation-based drug delivery system for oxaliplatin. *Chem. Sci.* **2017**, *8*, 4458-4464.
132. Gao, J.; Li, J.; Geng, W.-C.; Chen, F.-Y.; Duan, X.; Zheng, Z.; Ding, D.; Guo, D.-S. Biomarker Displacement Activation: A General Host–Guest Strategy for Targeted Phototheranostics in Vivo. *J. Am. Chem. Soc.* **2018**, *140*, 4945-4953.
133. Daze, K. D.; Ma, M. C. F.; Pineux, F.; Hof, F. Synthesis of New Trisulfonated Calix[4]arenes Functionalized at the Upper Rim, and Their Complexation with the Trimethyllysine Epigenetic Mark. *Org. Lett.* **2012**, *14*, 1512-1515.
134. Garnett, G. A.; Daze, K. D.; Pena Diaz, J. A.; Fagen, N.; Shaurya, A.; Ma, M. C.; Collins, M. S.; Johnson, D. W.; Zakharov, L. N.; Hof, F. Attraction by repulsion: compounds with like charges undergo self-assembly in water that improves in high salt and persists in real biological fluids. *Chem. Commun.* **2016**, *52*, 2768-71.
135. Ma, D.; Zavalij, P. Y.; Isaacs, L. Acyclic Cucurbit[n]uril Congeners Are High Affinity Hosts. *J. Org. Chem.* **2010**, *75*, 4786-4795.
136. Lucas, D.; Isaacs, L. Recognition Properties of Acyclic Glycoluril Oligomers. *Org. Lett.* **2011**, *13*, 4112-4115.
137. Minami, T.; Esipenko, N. A.; Zhang, B.; Kozelkova, M. E.; Isaacs, L.; Nishiyabu, R.; Kubo, Y.; Anzenbacher, P. Supramolecular Sensor for Cancer-Associated Nitrosamines. *J. Am. Chem. Soc.* **2012**, *134*, 20021-20024.
138. Da, M.; Ben, Z.; Ulrike, H.; Grosse, S. M.; Matthias, E.; Lyle, I. Acyclic Cucurbit[n]uril-Type Molecular Containers Bind Neuromuscular Blocking Agents In Vitro and Reverse Neuromuscular Block In Vivo. *Angew. Chem. Int. Ed.* **2012**, *51*, 11358-11362.
139. Klärner, F.-G.; Schrader, T. Aromatic Interactions by Molecular Tweezers and Clips in Chemical and Biological Systems. *Acc. Chem. Res.* **2013**, *46*, 967-978.
140. Dutt, S.; Wilch, C.; Gersthagen, T.; Talbiersky, P.; Bravo-Rodriguez, K.; Hanni, M.; Sánchez-García, E.; Ochsenfeld, C.; Klärner, F.-G.; Schrader, T. Molecular Tweezers with Varying Anions: A Comparative Study. *J. Org. Chem.* **2013**, *78*, 6721-6734.
141. Bier, D.; Rose, R.; Bravo-Rodriguez, K.; Bartel, M.; Ramirez-Anguita, J. M.; Dutt, S.; Wilch, C.; Klärner, F.-G.; Sanchez-Garcia, E.; Schrader, T.; Ottmann, C. Molecular tweezers modulate 14-3-3 protein–protein interactions. *Nat. Chem.* **2013**, *5*, 234.
142. Ghosh, S.; Wu, A.; Fettinger, J. C.; Zavalij, P. Y.; Isaacs, L. Self-Sorting Molecular Clips. *J. Org. Chem.* **2008**, *73*, 5915-5925.
143. Anxin, W.; Arindam, C.; C., F. J.; A., F. I. R.; Lyle, I. Molecular Clips that Undergo Heterochiral Aggregation and Self-Sorting. *Angew. Chem. Int. Ed.* **2002**, *41*, 4028-4031.

144. Klärner, F.-G.; Kahlert, B.; Nellesen, A.; Zienau, J.; Ochsenfeld, C.; Schrader, T. Molecular Tweezer and Clip in Aqueous Solution: Unexpected Self-Assembly, Powerful Host−Guest Complex Formation, Quantum Chemical ^{1}H NMR Shift Calculation. *J. Am. Chem. Soc.* **2006**, *128*, 4831-4841.
145. Branchi, B.; Ceroni, P.; Balzani, V.; Cartagena, M. C.; Klarner, F.-G.; Schrader, T.; Vogtle, F. Fluorescent water-soluble molecular clips. Self-association and formation of adducts in aqueous and methanol solutions. *New J. Chem.* **2009**, *33*, 397-407.
146. McGovern, R. E.; Snarr, B. D.; Lyons, J. A.; McFarlane, J.; Whiting, A. L.; Paci, I.; Hof, F.; Crowley, P. B. Structural study of a small molecule receptor bound to dimethyllysine in lysozyme. *Chem. Sci.* **2015**, *6*, 442-449.
147. Gober, I. N.; Waters, M. L. Supramolecular Affinity Labeling of Histone Peptides Containing Trimethyllysine and Its Application to Histone Deacetylase Assays. *J. Am. Chem. Soc.* **2016**, *138*, 9452-9459.
148. Hof, F. Host-guest chemistry that directly targets lysine methylation: synthetic host molecules as alternatives to bio-reagents. *Chem. Commun.* **2016**, *52*, 10093-10108.
149. Norouzy, A.; Azizi, Z.; Nau Werner, M. Indicator Displacement Assays Inside Live Cells. *Angew. Chem. Int. Ed.* **2014**, *54*, 792-795.
150. See, K. A.; Fronczek, F. R.; Watson, W. H.; Kashyap, R. P.; Gutsche, C. D. Calixarenes. 26. Selective esterification and selective ester cleavage of calix[4]arenes. *J. Org. Chem.* **1991**, *56*, 7256-7268.
151. Shinkai, S. Calixarenes - the third generation of supramolecules. *Tetrahedron Lett.* **1993**, *49*, 8933-8968.
152. Guo, D.-S.; Wang, K.; Liu, Y. Selective binding behaviors of *p*-sulfonatocalixarenes in aqueous solution. *J. Inclus. Phenom.Macrocyclic Chem.* **2008**, *62*, 1-21.
153. Schneider, C.; Bierwisch, A.; Koller, M.; Worek, F.; Kubik, S. Detoxification of VX and Other V-Type Nerve Agents in Water at 37 °C and pH 7.4 by Substituted Sulfonatocalix[4]arenes. *Angew. Chem. Int. Ed.* **2016**, *55*, 12668-12672.
154. Yasuaki, K.; Nae, S.; Kayo, H.; Jiaan, L.; Takayoshi, O.; A., K. S.; Kenzo, Y.; Motomu, K. Supramolecular Ligands for Histone Tails by Employing a Multivalent Display of Trisulfonated Calix[4]arenes. *ChemBioChem* **2015**, *16*, 2599-2604.
155. Ali, M.; Daze, K.; Strongin, D.; Rothbart, S.; Rincon-Arano, H.; F Allen, H.; Li, J.; Strahl, B.; Hof, F.; G Kutateladze, T., *Molecular Insights into Inhibition of the Methylated Histone-Plant Homeodomain Complexes by Calixarenes*. 2015; Vol. 290.
156. M., D. A.; L., R. M.; B., C. P. Protein Recognition by Functionalized Sulfonatocalix[4]arenes. *Chem. Eur. J.* **2018**, *24*, 984-991.
157. Thompson, J. W.; Kaiser, T. J.; Jorgenson, J. W. Viscosity measurements of methanol–water and acetonitrile–water mixtures at pressures up to 3500 bar using a novel capillary time-of-flight viscometer. *J. Chromatogr. A* **2006**, *1134*, 201-209.
158. Cremer, P. S.; Flood, A. H.; Gibb, B. C.; Mobley, D. L. Collaborative routes to clarifying the murky waters of aqueous supramolecular chemistry. *Nat. Chem.* **2018**, *10*, 8.
159. Neri, P.; Sessler, J. L.; Wang, M.-X., *Calixarenes and Beyond*. Springer: 2016.
160. Tu, Y.; Peng, F.; Adawy, A.; Men, Y.; Abdelmohsen, L. K. E. A.; Wilson, D. A. Mimicking the Cell: Bio-Inspired Functions of Supramolecular Assemblies. *Chem. Rev.* **2016**, *116*, 2023-2078.

161. Liu, S.; Ruspic, C.; Mukhopadhyay, P.; Chakrabarti, S.; Zavalij, P. Y.; Isaacs, L. The Cucurbit[n]uril Family: Prime Components for Self-Sorting Systems. *J. Am. Chem. Soc.* **2005**, *127*, 15959-15967.
162. Jordan, J. H.; Gibb, B. C. Molecular containers assembled through the hydrophobic effect. *Chem. Soc. Rev.* **2015**, *44*, 547-585.
163. Hill, D. J.; Mio, M. J.; Prince, R. B.; Hughes, T. S.; Moore, J. S. A Field Guide to Foldamers. *Chem. Rev.* **2001**, *101*, 3893-4012.
164. Wu, A.; Mukhopadhyay, P.; Chakraborty, A.; Fettinger, J. C.; Isaacs, L. Molecular Clips Form Isostructural Dimeric Aggregates from Benzene to Water. *J. Am. Chem. Soc.* **2004**, *126*, 10035-10043.
165. Gibb, C. L. D.; Oertling, E. E.; Velaga, S.; Gibb, B. C. Thermodynamic Profiles of Salt Effects on a Host–Guest System: New Insight into the Hofmeister Effect. *J. Phys. Chem. B* **2015**, *119*, 5624-5638.
166. Jordan, J. H.; Gibb, C. L. D.; Wishard, A.; Pham, T.; Gibb, B. C. Ion–Hydrocarbon and/or Ion–Ion Interactions: Direct and Reverse Hofmeister Effects in a Synthetic Host. *J. Am. Chem. Soc.* **2018**, *140*, 4092-4099.
167. Aryal, G. H.; Hunter, K. W.; Huang, L. A supramolecular red to near-infrared fluorescent probe for the detection of drugs in urine. *Org. Biomol. Chem.* **2018**, *16*, 7425-7429.
168. Shcherbakova, E. G.; Zhang, B.; Gozem, S.; Minami, T.; Zavalij, P. Y.; Pushina, M.; Isaacs, L. D.; Anzenbacher, P., Jr. Supramolecular Sensors for Opiates and Their Metabolites. *J. Am. Chem. Soc.* **2017**, *139*, 14954-14960.
169. Wang, Y.; Dmochowski, I. J. Cucurbit[6]uril is an ultrasensitive ^{129}Xe NMR contrast agent. *Chem. Commun.* **2015**, *51*, 8982-8985.
170. Tantakitti, F.; Boekhoven, J.; Wang, X.; Kazantsev, R. V.; Yu, T.; Li, J.; Zhuang, E.; Zandi, R.; Ortony, J. H.; Newcomb, C. J. Energy landscapes and functions of supramolecular systems. *Nat. Mater.* **2016**, *15*, 469.
171. Beck, F.; Dörge, A.; Rick, R.; Thurau, K. Intra- and extracellular element concentrations of rat renal papilla in antidiuresis. *Kidney International* **1984**, *25*, 397-403.
172. Rösgen, J.; Pettitt, B. M.; Bolen, D. W. Protein Folding, Stability, and Solvation Structure in Osmolyte Solutions. *Biophys. J.* **2005**, *89*, 2988-2997.
173. MacMillen, R. E.; Lee, A. K. Australian desert mice: independence of exogenous water. *Science* **1967**, *158*, 383-385.
174. Paul, S.; Bag, S. K.; Das, S.; Harvill, E. T.; Dutta, C. Molecular signature of hypersaline adaptation: insights from genome and proteome composition of halophilic prokaryotes. *Genome Biol.* **2008**, *9*, R70.
175. Shortle, D.; Ackerman, M. S. Persistence of Native-Like Topology in a Denatured Protein in 8 M Urea. *Science* **2001**, *293*, 487-489.
176. Arora, V.; Chawla, H. M.; Santra, A. Synthesis of selectively formylated calixarene ethers. *Tetrahedron Lett.* **2002**, *58*, 5591-5597.
177. Kalia, J.; Raines, R. T. Hydrolytic stability of hydrazones and oximes. *Angew. Chem. Int. Ed.* **2008**, *47*, 7523-7526.
178. Beatty, M. A.; Busmann, J. A.; Fagen, N. G.; Garnett, G. A. E.; Hof, F. A clip-like host that undergoes self-assembly and competitive guest-induced disassembly in water. *Supramol. Chem.* **2019**, *31*, 101-107.

179. Corbellini, F.; Fiammengo, R.; Timmerman, P.; Crego-Calama, M.; Versluis, K.; Heck, A. J. R.; Luyten, I.; Reinhoudt, D. N. Guest Encapsulation and Self-Assembly of Molecular Capsules in Polar Solvents via Multiple Ionic Interactions. *J. Am. Chem. Soc.* **2002**, *124*, 6569-6575.
180. Basilio, N.; García-Río, L.; Martín-Pastor, M. Counterion Binding in Solutions of *p*-sulfonatocalix[4]arene. *J. Phys. Chem. B* **2010**, *114*, 7201-7206.
181. Bakirci, H.; Koner, A. L.; Nau, W. M. Binding of inorganic cations by *p*-sulfonatocalix[4]arene monitored through competitive fluorophore displacement in aqueous solution. *Chem. Commun.* **2005**, 5411-5413.
182. Kelly, T. R.; Kim, M. H. Relative binding affinity of carboxylate and its isosteres: Nitro, phosphate, phosphonate, sulfonate, and. delta.-lactone. *J. Am. Chem. Soc.* **1994**, *116*, 7072-7080.
183. Breslow, R.; Halfon, S. Quantitative Effects of Antihydrophobic Agents on Binding Constants and Solubilities in Water. *Proc. Natl. Acad. Sci. U.S.A.* **1992**, *89*, 6916-6918.
184. Grote, Z.; Scopelliti, R.; Severin, K. Adaptive behavior of dynamic combinatorial libraries generated by assembly of different building blocks. *Angew. Chem. Int. Ed.* **2003**, *42*, 3821-3825.
185. Fox, J. M.; Kang, K.; Sherman, W.; Héroux, A.; Sastry, G. M.; Baghbanzadeh, M.; Lockett, M. R.; Whitesides, G. M. Interactions between Hofmeister anions and the binding pocket of a protein. *J. Am. Chem. Soc.* **2015**, *137*, 3859-3866.
186. Kherb, J.; Flores, S. C.; Cremer, P. S. Role of Carboxylate Side Chains in the Cation Hofmeister Series. *J. Phys. Chem. B.* **2012**, *116*, 7389-7397.
187. Das, A.; Mukhopadhyay, C. Urea-Mediated Protein Denaturation: A Consensus View. *J. Phys. Chem. B* **2009**, *113*, 12816-12824.
188. Hoffmann, R.; Knoche, W.; Fenn, C.; Buschmann, H.-J. Host–guest complexes of cucurbituril with the 4-methylbenzylammonium lon, alkali-metal cations and NH_4^+. *J. Chem. Soc., Faraday Trans.* **1994**, *90*, 1507-1511.
189. Belowich, M. E.; Stoddart, J. F. Dynamic imine chemistry. *Chem. Soc. Rev.* **2012**, *41*, 2003-2024.
190. Zhang, W.; Jin, Y., *Dynamic Covalent Chemistry: Principles, Reactions, and Applications*. John Wiley & Sons: 2017.
191. Mondal, M.; Radeva, N.; Fanlo-Virgós, H.; Otto, S.; Klebe, G.; Hirsch, A. K. Fragment Linking and Optimization of Inhibitors of the Aspartic Protease Endothiapepsin: Fragment-Based Drug Design Facilitated by Dynamic Combinatorial Chemistry. *Angew. Chem. Int. Ed.* **2016**, *55*, 9422-9426.
192. Mondal, M.; Hirsch, A. K. Dynamic combinatorial chemistry: a tool to facilitate the identification of inhibitors for protein targets. *Chem. Soc. Rev.* **2015**, *44*, 2455-2488.
193. Fu, J.; Fu, H.; Dieu, M.; Halloum, I.; Kremer, L.; Xia, Y.; Pan, W.; Vincent, S. P. Identification of inhibitors targeting Mycobacterium tuberculosis cell wall biosynthesis via dynamic combinatorial chemistry. *Chem. Commun.* **2017**, *53*, 10632-10635.
194. Jędrzejewska, H.; Szumna, A. Peptide-based capsules with chirality-controlled functionalized interiors – rational design and amplification from dynamic combinatorial libraries. *Chem. Sci.* **2019**, *10*, 4412-4421.

195. Jędrzejewska, H.; Wierzbicki, M.; Cmoch, P.; Rissanen, K.; Szumna, A. Dynamic Formation of Hybrid Peptidic Capsules by Chiral Self-Sorting and Self-Assembly. *Angew. Chem. Int. Ed.* **2014**, *53*, 13760-13764.
196. Ahmad, Y.; Habib, M. S.; Iqbal, M.; Qureshi, M. I.; Craig, J. C.; Garnett, J. L.; Temple, D. M.; Fischer, A.; Happer, D. A. R.; Vaughan, J.; Albert, A.; Willette, R. E.; Daly, J. J.; Banks, R. E.; Haszeldine, R. N.; Sutcliffe, H.; Beer, R. J. S.; Slater, R. A.; Griffith, W. P.; Benn, M. H.; Fields, E. K.; Beard, J. H.; Plesch, P. H.; Carruthers, W.; Douglas, A. G.; Battersby, A. R.; Francis, R. J.; Johnson, A. W.; Oldfield, D.; Rodrigo, R.; Shaw, N.; Clifford, D. R.; Woodcock, D.; Edwards, R. L.; Kale, N.; Birch, A. J.; White, D. A.; Edwards, A. J.; Mouty, M. A.; Peacock, R. D.; Suddens, A. J. Notes. *J. Am. Chem. Soc.* **1964**, 4053-4088.
197. You, L.; Zha, D.; Anslyn, E. V. Recent Advances in Supramolecular Analytical Chemistry Using Optical Sensing. *Chem. Rev.* **2015**, *115*, 7840-92.
198. Ghale, G.; Nau, W. M. Dynamically Analyte-Responsive Macrocyclic Host–Fluorophore Systems. *Acc. Chem. Res.* **2014**, *47*, 2150-2159.
199. Dsouza, R. N.; Nau, W. M. Triple molecular recognition as a directing element in the formation of host-guest complexes with *p*-sulfonatocalix[4]arene and β-cyclodextrin. *J. Org. Chem.* **2008**, *73*, 5305-10.
200. Praetorius, A.; Bailey, D. M.; Schwarzlose, T.; Nau, W. M. Design of a fluorescent dye for indicator displacement from cucurbiturils: a macrocycle-responsive fluorescent switch operating through a pKa shift. *Org. Lett.* **2008**, *10*, 4089-92.
201. Koh, K. N.; Araki, K.; Ikeda, A.; Otsuka, H.; Shinkai, S. Reinvestigation of Calixarene-Based Artificial-Signaling Acetylcholine Receptors Useful in Neutral Aqueous (Water/Methanol) Solution. *J. Am. Chem. Soc.* **1996**, *118*, 755-758.
202. Dsouza, R. N.; Hennig, A.; Nau, W. M. Supramolecular tandem enzyme assays. *Chem.* **2012**, *18*, 3444-59.
203. Ghale, G.; Lanctôt, A. G.; Kreissl, H. T.; Jacob, M. H.; Weingart, H.; Winterhalter, M.; Nau, W. M. Chemosensing Ensembles for Monitoring Biomembrane Transport in Real Time. *Angew. Chem. Int. Ed.* **2014**, *53*, 2762-2765.
204. Florea, M.; Kudithipudi, S.; Rei, A.; Gonzalez-Alvarez, M. J.; Jeltsch, A.; Nau, W. M. A fluorescence-based supramolecular tandem assay for monitoring lysine methyltransferase activity in homogeneous solution. *Chem. Eur. J.* **2012**, *18*, 3521-8.
205. Florea, M.; Kudithipudi, S.; Rei, A.; González-Álvarez, M. J.; Jeltsch, A.; Nau, W. M. A Fluorescence-Based Supramolecular Tandem Assay for Monitoring Lysine Methyltransferase Activity in Homogeneous Solution. *Chem. Eur. J.* **2012**, *18*, 3521-3528.
206. Lakowicz, J. R. Principles of fluorescence spectroscopy. *Springer Science and Business Media, LLC, New York* **2006**, *13*, 978-0.
207. Miskolczy, Z.; Biczók, L.; Megyesi, M.; Jablonkai, I. Inclusion complex formation of ionic liquids and other cationic organic compounds with cucurbit [7] uril studied by 4′, 6-diamidino-2-phenylindole fluorescent probe. *J. Phys. Chem. B* **2009**, *113*, 1645-1651.
208. Zhang, H.-M.; Yang, J.-Y.; Du, L.-M.; Li, C.-F.; Wu, H. Determination of sotalol by fluorescence quenching method. *Anal. Methods* **2011**, *3*, 1156-1162.
209. Hennig, A.; Bakirci, H.; Nau, W. M. Label-free continuous enzyme assays with macrocycle-fluorescent dye complexes. *Nat. Methods* **2007**, *4*, 629-632.

210. Liu, Y.; Li, C.-J.; Guo, D.-S.; Pan, Z.-H.; Li, Z. A Comparative Study of Complexation of β-Cyclodextrin, Calix[4]arenesulfonate and Cucurbit[7]uril with Dye Guests: Fluorescence Behavior and Binding Ability. *Supramol. Chem.* **2007**, *19*, 517-523.
211. Ong, W.; Kaifer, A. E. Salt effects on the apparent stability of the cucurbit [7] uril− methyl viologen inclusion complex. *J. Org. Chem.* **2004**, *69*, 1383-1385.
212. Linn, M. M.; Poncio, D. C.; Machado, V. G. An anionic chromogenic sensor based on the competition between the anion and a merocyanine solvatochromic dye for calix[4]pyrrole as a receptor site. *Tetrahedron Lett.* **2007**, *48*, 4547-4551.
213. Shinkai, S.; Araki, K.; Shibata, J.; Tsugawa, D.; Manabe, O. Diazo-Coupling Reactions with Calix[4]arene. pKa Determination with Chromophoric Azocalix[4]arenes. *Chem. Lett.* **1989**, *18*, 931-934.
214. Lhotak, P.; Nakamura, R.; Shinkai, S. Synthesis and ^{1}H NMR studies of vinyl-substituted calix[4]arene derivatives: Enhanced cation-π interactions with extended calix[4]arene π-systems. *Supramol. Chem.* **1997**, *8*, 333-344.
215. Linton, B. R.; Goodman, M. S.; Fan, E.; van Arman, S. A.; Hamilton, A. D. Thermodynamic Aspects of Dicarboxylate Recognition by Simple Artificial Receptors. *J. Org. Chem.* **2001**, *66*, 7313-7319.
216. Beshara, C. S.; Jones, C. E.; Daze, K. D.; Lilgert, B. J.; Hof, F. A Simple Calixarene Recognizes Post-translationally Methylated Lysine. *ChemBioChem* **2010**, *11*, 63-66.
217. Koh-Stenta, X.; Joy, J.; Poulsen, A.; Li, R.; Tan, Y.; Shim, Y.; Min, J.-H.; Wu, L.; Ngo, A.; Peng, J. Characterization of the histone methyltransferase PRDM9 using biochemical, biophysical and chemical biology techniques. *Biochem. J* **2014**, *461*, 323-334.
218. Eram, M. S.; Bustos, S. P.; Lima-Fernandes, E.; Siarheyeva, A.; Senisterra, G.; Hajian, T.; Chau, I.; Duan, S.; Wu, H.; Dombrovski, L. Trimethylation of histone H3 lysine 36 by human methyltransferase PRDM9 protein. *J. Biol. Chem.* **2014**, *289*, 12177-12188.
219. Jacob, Y.; Voigt, P., In Vitro Assays to Measure Histone Methyltransferase Activity Using Different Chromatin Substrates. In *Plant Chromatin Dynamics: Methods and Protocols*, Bemer, M.; Baroux, C., Eds. Springer New York: New York, NY, 2018; pp 345-360.
220. Liu, Y.; Lee, J.; Perez, L.; Gill, A. D.; Hooley, R. J.; Zhong, W. Selective Sensing of Phosphorylated Peptides and Monitoring Kinase and Phosphatase Activity with a Supramolecular Tandem Assay. *J. Am. Chem. Soc.* **2018**, *140*, 13869-13877.
221. Liu, Y.; Perez, L.; Gill, A. D.; Mettry, M.; Li, L.; Wang, Y.; Hooley, R. J.; Zhong, W. Site-Selective Sensing of Histone Methylation Enzyme Activity via an Arrayed Supramolecular Tandem Assay. *J. Am. Chem. Soc.* **2017**, *139*, 10964-10967.
222. Minami, T.; Liu, Y.; Akdeniz, A.; Koutnik, P.; Esipenko, N. A.; Nishiyabu, R.; Kubo, Y.; Anzenbacher, P., Jr. Intramolecular indicator displacement assay for anions: supramolecular sensor for glyphosate. *J. Am. Chem. Soc.* **2014**, *136*, 11396-401.
223. Liu, Y.; Minami, T.; Nishiyabu, R.; Wang, Z.; Anzenbacher, P. Sensing of Carboxylate Drugs in Urine by a Supramolecular Sensor Array. *J. Am. Chem. Soc.* **2013**, *135*, 7705-7712.
224. Chapin, B. M.; Metola, P.; Vankayala, S. L.; Woodcock, H. L.; Mooibroek, T. J.; Lynch, V. M.; Larkin, J. D.; Anslyn, E. V. Disaggregation is a Mechanism for Emission

Turn-On of ortho-Aminomethylphenylboronic Acid-Based Saccharide Sensors. *J. Am. Chem. Soc.* **2017**, *139*, 5568-5578.
225. Watt, M. M.; Engle, J. M.; Fairley, K. C.; Robitshek, T. E.; Haley, M. M.; Johnson, D. W. "Off-on" aggregation-based fluorescent sensor for the detection of chloride in water. *Org. Biomol. Chem* **2015**, *13*, 4266-4270.
226. Wang, J.; Gu, X.; Zhang, P.; Huang, X.; Zheng, X.; Chen, M.; Feng, H.; Kwok, R. T. K.; Lam, J. W. Y.; Tang, B. Z. Ionization and Anion−π+ Interaction: A New Strategy for Structural Design of Aggregation-Induced Emission Luminogens. *J. Am. Chem. Soc.* **2017**, *139*, 16974-16979.
227. Hayes, K. L.; Lasher, E. M.; Choczynski, J. M.; Crisci, R. R.; Wong, C. Y.; Dragonette, J.; Deschner, J.; Cardenas, A. J. P. Brooker's merocyanine: Comparison of single crystal structures. *J. Mol. Struct.* **2018**, *1161*, 194-198.
228. Kuder, J. E.; Wychick, D. Acid-based equilibria in the ground and excited states of a solvatochromic merocyanine dye. *Chem. Phys. Lett.* **1974**, *24*, 69-72.
229. Cavalli, V.; da Silva, D. C.; Machado, C.; Machado, V. G.; Soldi, V. The Fluorosolvatochromism of Brooker's Merocyanine in Pure and in Mixed Solvents. *J. Fluoresc.* **2006**, *16*, 77-86.
230. Gale, P. A.; Caltagirone, C. Anion sensing by small molecules and molecular ensembles. *Chem. Soc. Rev.* **2015**, *44*, 4212-4227.
231. Wu, D.; Sedgwick, A. C.; Gunnlaugsson, T.; Akkaya, E. U.; Yoon, J.; James, T. D. Fluorescent chemosensors: the past, present and future. *Chem. Soc. Rev.* **2017**, *46*, 7105-7123.
232. Aryal, G. H.; Hunter, K. W.; Huang, L. A supramolecular red to near-infrared fluorescent probe for detection of drugs in urine. *Org. Biomol. Chem.* **2018**.
233. Gill, A. D.; Perez, L.; Salinas, I. N. Q.; Byers, S. R.; Liu, Y.; Hickey, B. L.; Zhong, W.; Hooley, R. J. Selective Array-Based Sensing of Anabolic Steroids in Aqueous Solution by Host–Guest Reporter Complexes. *Chem. Eur. J.* **2019**, *25*, 1740-1745.
234. Kolusheva, S.; Zadmard, R.; Schrader, T.; Jelinek, R. Color Fingerprinting of Proteins by Calixarenes Embedded in Lipid/Polydiacetylene Vesicles. *J. Am. Chem. Soc.* **2006**, *128*, 13592-13598.
235. Wang, K.; Guo, D.-S.; Zhao, M.-Y.; Liu, Y. A Supramolecular Vesicle Based on the Complexation of *p*-Sulfonatocalixarene with Protamine and its Trypsin-Triggered Controllable-Release Properties. *Chem. Eur. J.* **2016**, *22*, 1475-1483.
236. Bockus, A. T.; Smith, L. C.; Grice, A. G.; Ali, O. A.; Young, C. C.; Mobley, W.; Leek, A.; Roberts, J. L.; Vinciguerra, B.; Isaacs, L.; Urbach, A. R. Cucurbit[7]uril–Tetramethylrhodamine Conjugate for Direct Sensing and Cellular Imaging. *J. Am. Chem. Soc.* **2016**, *138*, 16549-16552.
237. Beatty, M. A.; Borges-González, J.; Sinclair, N. J.; Pye, A. T.; Hof, F. Analyte-Driven Disassembly and Turn-On Fluorescent Sensing in Competitive Biological Media. *J. Am. Chem. Soc.* **2018**, *140*, 3500-3504.
238. Florea, M.; Kudithipudi, S.; Rei, A.; Gonzalez-Alvarez, M. J.; Jeltsch, A.; Nau, W. M. A fluorescence-based supramolecular tandem assay for monitoring lysine methyltransferase activity in homogeneous solution. *Chem.* **2012**, *18*, 3521-8.
239. Ghale, G.; Kuhnert, N.; Nau, W. M. Monitoring Stepwise Proteolytic Degradation of Peptides by Supramolecular Domino Tandem Assays and Mass Spectrometry for

Trypsin and Leucine Aminopeptidase. *Nat. Prod. Commun.* **2012**, *7*, 1934578X1200700315.
240. Stahl, A.; Lazar, A. I.; Muchemu, V. N.; Nau, W. M.; Ullrich, M. S.; Hennig, A. A fluorescent, supramolecular chemosensor to follow steroid depletion in bacterial cultures. *Anal. Bioanal.Chem.* **2017**, *409*, 6485-6494.
241. Shcherbakova, E. G.; Zhang, B.; Gozem, S.; Minami, T.; Zavalij, P. Y.; Pushina, M.; Isaacs, L. D.; Anzenbacher Jr, P. Supramolecular Sensors for Opiates and Their Metabolites. *J. Am. Chem. Soc.* **2017**, *139*, 14954-14960.
242. Shah, K.; Hassan, E.; Ahmed, F.; Anis, I.; Rabnawaz, M.; Shah, M. R. Novel fluorene-based supramolecular sensor for selective detection of amoxicillin in water and blood. *Ecotoxicol. Environ. Saf.* **2017**, *141*, 25-29.
243. Sinn, S.; Spuling, E.; Bräse, S.; Biedermann, F. Rational design and implementation of a cucurbit[8]uril-based indicator-displacement assay for application in blood serum. *Chem. Sci.* **2019**.
244. Potyrailo, R. A.; Mirsky, V. M. Combinatorial and High-Throughput Development of Sensing Materials: The First 10 Years. *Chem. Rev.* **2008**, *108*, 770-813.
245. Potyrailo, R.; Rajan, K.; Stoewe, K.; Takeuchi, I.; Chisholm, B.; Lam, H. Combinatorial and High-Throughput Screening of Materials Libraries: Review of State of the Art. *ACS Comb. Sci.* **2011**, *13*, 579-633.
246. Briehn, C. A.; Schiedel, M.-S.; Bonsen, E. M.; Schuhmann, W.; Bäuerle, P. Single-Compound Libraries of Organic Materials: From the Combinatorial Synthesis of Conjugated Oligomers to Structure–Property Relationships. *Angew. Chem. Int. Ed.* **2001**, *40*, 4680-4683.
247. Lee, J.-S.; Kim, H. K.; Feng, S.; Vendrell, M.; Chang, Y.-T. Accelerating fluorescent sensor discovery: unbiased screening of a diversity-oriented BODIPY library. *Chem. Commun.* **2011**, *47*, 2339-2341.
248. Zhai, D.; Lee, S.-C.; Vendrell, M.; Leong, L. P.; Chang, Y.-T. Synthesis of a Novel BODIPY Library and Its Application in the Discovery of a Fructose Sensor. *ACS Comb. Sci.* **2012**, *14*, 81-84.
249. Schiedel, M.-S.; Briehn, C. A.; Bäuerle, P. Single-Compound Libraries of Organic Materials: Parallel Synthesis and Screening of Fluorescent Dyes. *Angew. Chem. Int. Ed.* **2001**, *40*, 4677-4680.
250. Vendrell, M.; Zhai, D.; Er, J. C.; Chang, Y.-T. Combinatorial Strategies in Fluorescent Probe Development. *Chem. Rev.* **2012**, *112*, 4391-4420.
251. Rosania, G. R.; Lee, J. W.; Ding, L.; Yoon, H.-S.; Chang, Y.-T. Combinatorial Approach to Organelle-Targeted Fluorescent Library Based on the Styryl Scaffold. *J. Am. Chem. Soc.* **2003**, *125*, 1130-1131.
252. Beatty, M. A.; Busmann, J. A.; Fagen, N. G.; Garnett, G. A. E.; Hof, F. A clip-like host that undergoes self-assembly and competitive guest-induced disassembly in water. *Supramol. Chem.* **2018**, 1-7.
253. Beatty, M. A.; Pye, A. T.; Shaurya, A.; Kim, B.; Selinger, A. J.; Hof, F. Using reversible non-covalent and covalent bonds to create assemblies and equilibrating molecular networks that survive 5 molar urea. *Org. Biomol. Chem.* **2019**, *17*, 2081-2086.
254. Umali, A. P.; LeBoeuf, S. E.; Newberry, R. W.; Kim, S.; Tran, L.; Rome, W. A.; Tian, T.; Taing, D.; Hong, J.; Kwan, M.; Heymann, H.; Anslyn, E. V. Discrimination of

flavonoids and red wine varietals by arrays of differential peptidic sensors. *Chem. Sci.* **2011**, *2*, 439-445.
255. Gade, A. M.; Meadows, M. K.; Ellington, A. D.; Anslyn, E. V. Differential array sensing for cancer cell classification and novelty detection. *Org. Biomol. Chem.* **2017**, *15*, 9866-9874.
256. Peacor, B. C.; Ramsay, C. M.; Waters, M. L. Fluorogenic sensor platform for the histone code using receptors from dynamic combinatorial libraries. *Chem. Sci.* **2017**, *8*, 1422-1428.
257. Minaker, S. A.; Daze, K. D.; Ma, M. C. F.; Hof, F. Antibody-Free Reading of the Histone Code Using a Simple Chemical Sensor Array. *J. Am. Chem. Soc.* **2012**, *134*, 11674-11680.
258. Palacios, M. A.; Nishiyabu, R.; Marquez, M.; Anzenbacher, P. Supramolecular Chemistry Approach to the Design of a High-Resolution Sensor Array for Multianion Detection in Water. *J. Am. Chem. Soc.* **2007**, *129*, 7538-7544.
259. Pode, Z.; Peri-Naor, R.; Georgeson, J. M.; Ilani, T.; Kiss, V.; Unger, T.; Markus, B.; Barr, H. M.; Motiei, L.; Margulies, D. Protein recognition by a pattern-generating fluorescent molecular probe. *Nat. Nanotechnol.* **2017**, *12*, 1161.
260. Lapachinske, S. F.; Okai, G. G.; dos Santos, A.; de Bairros, A. V.; Yonamine, M. Analysis of cocaine and its adulterants in drugs for international trafficking seized by the Brazilian Federal Police. *Forensic Sci. Int.* **2015**, *247*, 48-53.
261. Sonzini, S.; McCune, J. A.; Ravn, P.; Scherman, O. A.; van der Walle, C. F. A simple supramolecular assay for drug detection in urine. *Chem. Commun.* **2017**, *53*, 8842-8845.
262. Navarro, M.; Pichini, S.; Farré, M.; Ortuño, J.; Roset, P. N.; Segura, J.; de la Torre, R. Usefulness of Saliva for Measurement of 3,4-Methylenedioxymethamphetamine and Its Metabolites: Correlation with Plasma Drug Concentrations and Effect of Salivary pH. *Clin. Chem.* **2001**, *47*, 1788-1795.
263. Ellefsen, K. N.; Concheiro, M.; Pirard, S.; Gorelick, D. A.; Huestis, M. A. Oral fluid cocaine and benzoylecgonine concentrations following controlled intravenous cocaine administration. *Forensic Sci. Int.* **2016**, *260*, 95-101.
264. Jenkins, A. J.; Oyler, J. M.; Cone, E. J. Comparison of Heroin and Cocaine Concentrations in Saliva with Concentrations in Blood and Plasma. *J. Anal. Toxicol.* **1995**, *19*, 359-374.
265. Feyerabend, C.; Higenbottam, T.; Russell, M. A. Nicotine concentrations in urine and saliva of smokers and non-smokers. *Br. Med. J.* **1982**, *284*, 1002-1004.
266. Cone, E. J.; Oyler, J.; Darwin, W. D. Cocaine Disposition in Saliva Following Intravenous, Intranasal, and Smoked Administration. *J. Anal. Toxicol.* **1997**, *21*, 465-475.
267. Hof, F.; Beatty, M.; Sellinger, A. *Compound and dimer complex embodiments for supramolcular sensing* 2019.62/866,473,
268. Song, X.; Bian, H.; Wang, C.; Hu, M.; Li, N.; Xiao, Y. Development and applications of a near-infrared dye–benzylguanine conjugate to specifically label SNAP-tagged proteins. *Org. Biomol. Chem.* **2017**, *15*, 8091-8101.
269. Coe, B. J.; Harris, J. A.; Asselberghs, I.; Clays, K.; Olbrechts, G.; Persoons, A.; Hupp, J. T.; Johnson, R. C.; Coles, S. J.; Hursthouse, M. B.; Nakatani, K. Quadratic Nonlinear Optical Properties of *N*-Aryl Stilbazolium Dyes. *Adv. Funct. Mater.* **2002**, *12*, 110-116.